UNIVERSITÀ DEGLI STUDI DI MILANO

DOCTORAL PROGRAMME IN EARTH SCIENCES

Cycle XXXIII

DIPARTIMENTO DI SCIENZE DELLA TERRA

PhD Dissertation

Wildland surface fire behaviour: a spatial simulation model for operational emergency management

GEO/05 – Engineering Geology

PhD Candidate
DEBORA VOLTOLINA
R11976

Tutor
Prof.ssa TIZIANA APUANI

Co-tutors
Dr. SIMONE STERLACCHINI
Dr. GIACOMO CAPPELLINI

Coordinator of the PhD programme
Prof. FERNANDO CAMARA ARTIGAS

Abstract

Wildfires affect vegetation dynamics, geomorphological processes, biogeochemical cycles, atmospheric chemistry, and climate, posing a severe threat to human lives and activities interacting with the natural system. As both fire activity and wildland-urban interface exposure are expected to increase under future climate projections, the improvement of our ability to promptly predict wildland fire behaviour, in terms of expected intensity and geographic patterns, has become a tangible need.
The general purpose of this PhD research is to investigate on wildland surface fire behaviour simulation models and to support disaster managers in optimizing decision making processes in wildfire risk management in a Mediterranean-type climate region, namely Sardinia, Italy. This project is intended to pursue two major objectives: (i) develop and validate a predictive spatially distributed wildland surface fire behaviour simulation model intended for operational use; (ii) design and implement a geospatial decision support system to provide decision makers with appropriate strategies and tools for an integrated wildland fire risk management.
Predicting wildland surface fire behaviour requires a deep understanding of the influence of environmental parameters that act as drivers of the fire spread, including geomorphometrical variables, meteorological conditions, and fuel characteristics, on fire descriptors, such as the rate and direction of the maximum fire spread, the eccentricity of the ellipse approximating the fire shape, the intensity of the fire front, and the flame length. The Rothermel's mathematical model for predicting surface fire spread in wildland fuels is currently the most extensively used method to estimate fire descriptors, especially for operational purposes. The application of the Rothermel's model for simulating the behaviour of ongoing wildfires calls for the need of a technique for continuous monitoring of the spatiotemporal variability of weather conditions and fuel characteristics, such as fuel height, loading, and moisture content, in the pre-fire environment. Firstly, freely available data sources and remote sensing products and datasets have been investigated to define a pre-processing methodology for the near real-time estimation of the drivers of fire spread. Secondly, the need for flexibility in handling the equations of the Rothermel's and associated models, together with the necessity of integrating corrections and updates, have led to an original implementation of a computer algorithm that evaluates the fire descriptors as defined by the extended Rothermel's mathematical model. Then, a proxy model of this implementation has been developed using a machine learning ensemble method in order to analyse the interdependence of the drivers and to understand their relative importance in predicting fire descriptors. Furthermore, the proxy model for predicting fire spread across heterogeneous landscapes has been integrated into an agent-based simulation model developed to predict the surface fire behaviour and growth with the aim of providing fire management authorities with timely information on the expected progress of the fire front. Finally, the developed simulation model has been applied to and validated against historical wildfire events recorded in Sardinia, Italy, to evaluate its performance in terms of predictive capacity. The effects of fire suppression activities have also been simulated according to the availability of accurate information on timing and location of interventions that effectively extinguished the fire's spread.
As a whole, the developed wildland surface fire behaviour simulation model, together with the preprocessing methodology, have resulted in a satisfying accuracy in terms of quantitative agreement

between modelled and observed patterns of fire growth. The adoption of the proxy model instead of its original implementation has guaranteed a significative reduction of the computing time in the face of a limited loss in accuracy at the scale of the analysis if compared with the original implementation of the Rothermel's equations. Results of the validation suggest the model's suitability for operational uses for predicting wildland surface fire behaviour. The predictive ability of the simulation model could reasonably benefit from the inclusion of some additional mathematical models simulating the potential evolution of the surface fire towards passive or active crown fires or spotting fires. Moreover, major improvements could be granted by implementing in the agent-based simulation model a wider range of fire suppression activities and techniques, ranging from ground to aerial interventions. The proposed predictive model could become a valid tool for the optimization of risk planning, prevention, and management activities. Within the context of the PhD project, three modules of a geospatial decision support system have been designed and implemented with the aim of improving the efficiency of risk management strategies and reducing expected impacts and potential damage. The first module is a dynamic workflow of actions and represents the core of the decision support system. This module aims to guide decision makers in carrying out the procedures of the intervention model compliant with the legislative framework. The workflow is then supported by a second module, a customised version of a geographic information system with dynamic forms designed to support users with limited expertise in geodatabase management. This module will incorporate a structured relational geodatabase storing (i) scenarios of wildfire events, produced by means of the developed predictive wildland surface fire behaviour simulation model, (ii) existing institutional wildfire susceptibility, hazard, and risk maps, (iii) available resources and socioeconomic exposed values, and (iv) real-time data from field surveys. Finally, the decision support system will provide authorities and technicians with a third module composed by web applications for mobile field data collection and sharing.

The PhD project strived to investigate principles and accepted theories on the complex dynamics of wildland surface fire behaviour and to shed light on the need for a better understanding of the difference between real and simulated fire behaviour in terms of the importance of the drivers of fire spread in predicting fire spread and growth. The project also tried proposing solutions integrating remote sensing and machine learning techniques with the aim of improving the applicability of near real-time simulation models as well as the effectiveness of decision-making strategies.

Table of contents

Chapter 1

Introduction

Wildland fires are an ongoing and pervasive global phenomenon whose frequency and severity dynamically respond to interactions among climate regimes, weather conditions, fuels availability, and anthropic influence. Wildfires actively maintain diverse naturally fire-prone ecosystems, nevertheless they pose a growing threat to ecological and socioeconomic values, with detrimental impacts on human lives and activities, especially in the wildland-urban interface, where the urban and rural systems interact with the natural system. Besides, forest fires may assume a remarkable significance in landscape transfiguration with considerable implications for vegetation dynamics (Trabaud, 1994), atmospheric composition (Jaffe and Wigder, 2012; Y. Liu et al., 2014; van der Werf et al., 2017), and geomorphological processes by altering physico-chemical properties of soils and biogeochemical cycles (Certini, 2005; Lainas et al., 2016; Parise and Cannon, 2012; Shakesby, 2011).
Globally 400-500 million ha of the Earth's vegetation are estimated to have burnt annually between 2002 and 2016 (Bowman et al., 2020; Giglio et al., 2018) and the concern over the potential impacts of future climate change on fire activity is intensifying the scientific interest in the complex interactions between wildland fires and climate. Despite the intrinsic uncertainties associated with climate projections, researches at a global and local scale have already pointed out the pivotal influence of climate trends in exacerbating fire activity, in terms of either fire season length, fire density, and intensity (Dupuy et al., 2020; Flannigan et al., 2009, 2016; Forkel et al., 2019; Jolly et al., 2015; Jones et al., 2020; Y. Liu et al., 2010; Moritz et al., 2012; Pechony and Shindell, 2010; Turco et al., 2018; Williams and Abatzoglou, 2016). Mediterranean-type climate regions, i.e. the European Mediterranean Basin, the Southwestern Australia, the West Coast of North America, the central Chile, and the Southwestern tip of South Africa, seem to be particularly prone to suffer for the above-mentioned increase in fire activity under future climate projections (Bowman et al., 2017). Additional uncertainties stem from the incompleteness in the comprehension of the long-term shifts in the potential vegetation under future climate, especially in Mediterranean-type climate regions, where fuel dynamics have been indicated as the most relevant factor in driving fire activity (Costa et al., 2020; Dupuy et al., 2020; Pausas and Paula, 2012). Besides, fire activity is deeply influenced by human-related factors, including fuel load and structure modifications as well as fire ignition and suppression activities (Bowman et al., 2011). The general tendency to a massive abandonment of traditional rural practices is responsible for greater landscape homogeneity, fuel accumulation, continuity and connectivity (Kelley et al., 2019; Mantero et al., 2020; Salis et al., 2019; Turco et al., 2016) and the current global trends in land uses conversions in terms of both extension and speed of replacement highlight the evolutionary drift towards an impressive exposure of the wildland-urban interface. The progressive expansion of these areas has compelled anthropic elements to merge with natural ones, leading to a dramatic growth of wildfire-related vulnerability and risk to which communities are exposed (C.

Miller and Ager, 2013). Wildfire's impact on wildland-urban interface and its inhabiting communities is expected to intensify accordingly. (Caton et al., 2017; Mell et al., 2010).

The recent worldwide profusion of extraordinary wildfire events has drawn major attention to the need for a holistic view of these phenomena which tends to overwhelm suppression capabilities, causing substantial damage and often resulting in fatalities amongst both civilian and firefighters (Tedim et al., 2018). The concept of extreme wildfire event has been recently introduced to indicate exceptionally large and high intensity incidents which result in remarkable ecological impacts and substantial socioeconomic losses and disruptions. A significant example is the Pedrógão Grande wildfire, Portugal, which in June 2017, caused 66 fatalities (45 of whom died on the roads) and burned 45,328 ha, spreading at a reported maximum rate of 4.2 m/s (Tedim et al., 2018). The event damaged 1,042 structures (including 263 residential homes) and completely destroyed 434 of them, leading to direct losses estimated at around 200 million euros (Ribeiro et al., 2020). Another meaningful extreme wildfire event is the Eastern Attica Fire, Greece, which in July 2018 destroyed approximately 3,000 dwellings over a total area of 1,250 ha (Lagouvardos et al., 2019) and resulted in the death of 102 civilians making it the second deadliest wildfire in the 21st century, after the Kilmore East Fire, Australia, which killed 120 people in 2009 (Tedim et al., 2020). The Camp Fire, in northern California, which in October 2018 burned 62,052 ha, can be classified as extreme wildfire event as well. It claimed 85 fatalities and destroyed 18,804 structures, resulting in the deadliest and most destructive wildfire event in the California history (Brewer and Clements, 2020). California also faced a severe fire season in 2020, when 5 of the 20 largest wildfires in the State's history took place, burning an overall surface of 584,022 ha. Among them, the Creek Fire burned 152,847 ha and destroyed 853 structures between September 4, 2020, and December 24, 2020 (CAL FIRE, 2020).

Despite extreme wildfire events have become a very current topic because of their exceptional impact, their characteristics have been delineated only in recent years. However, during the period 2000-2017, the overall impact of forest fires in the European Mediterranean countries has been responsible for 8.5 million ha burned (approximately 480,000 ha/year), 611 fatalities (nearly 34 people/year), and 54 billion euros in damages (approximately 3 billion euros/year) (Costa et al., 2020). Fires in five Southern Europe countries, i.e. Greece, Italy, France, Spain, and Portugal, have been estimated to account for around 85% of the total burnt area in Europe each year (de Rigo et al., 2017).

The latest report by the European Commission's Directorate-General for Research and Innovation (Rego et al., 2018), which was aimed at providing evidence-based scientific support to the European policymaking process, warned about the emerging risk of a climate-induced disproportionate increase in uncontrolled wildfire events and the consequent urgent need for a re-assessment of fire management policies and strategies. Wildfire management policies in Mediterranean-type climate regions are reported to be predominantly focused on reactive fire suppression strategies, while struggling to adequately and proactively address the underlying causes of the increased prevalence of extreme wildfire events (Moreira et al., 2020). The effectiveness of wildfire management actions should be evaluated not merely as a function of the reduction in total burnt area due to fire suppression, but rather as a function of the minimisation in socioeconomic and environmental damage and loss (e.g. human lives lost, direct economic losses, soil erosion, carbon emissions, and biodiversity impacts). Different mitigation strategies have been recommended, including an exacerbation of wildland-urban interface expansion regulations and the introduction of agricultural policies promoting extensive

livestock grazing and adequate fuel management strategies, such as prescribed burning (Moreira and Pe'er, 2018). However, regardless the uncertainties on the applicability of those measures, they might be insufficient alone to prevent fires to evolve beyond a threshold of suppression capability. Indeed, an integrated forest fire risk management requires contribution from different thematic areas, ranging from enhancement in the scientific comprehension of fire behaviour and spatiotemporal patterns to further improvements in early fire detection, fire suppression, and risk mitigation strategies. Accurate predictions of spatiotemporal patterns and behaviour of future forest fire are of prominent importance for planning and optimizing wildfire risk management strategies and emergency response activities. Timely and appropriate intervention strategies, applied since the earliest stages, are essential to bring the fire ignition and spread under control before it could evolve in an extreme and uncontrolled wildfire event.

Rego et al. (2018) stressed the exigence of improving the effectiveness of contemporary wildfire protection programmes across the European Mediterranean countries by: (i) adopting effective science-based forest fire management and risk-informed decision making; (ii) ensuring a balance between fire suppression, with its immediate but short-term results, and the long-term investment effort required for mitigation, prevention, and preparedness actions; (iii) increasing the awareness and preparedness of populations at risk; (iv) promoting resilient landscapes and communities through integrated fire management; and (v) improving firefighting and rescue capacities of first responders in crisis management by optimizing their operations and strategies. Those policies are fully compliant with the more general Sendai Framework for Disaster Risk Reduction 2015-2030 aimed at defining a global strategy directed at enhancing risk-exposed communities' resilience and improving the efficiency of risk management strategies in order to reduce expected impacts and potential damage (UNISDR, 2015).

1.1 Objectives

In agreement with the above-mentioned needs, the general purpose of the PhD research is to investigate on wildland surface fire behaviour simulation modelling and to support disaster managers in optimizing decision-making processes in wildfire risk management in a Mediterranean-type climate region, Sardinia, Italy. The project is intended to pursue two major objectives: (i) develop and validate a predictive spatially distributed agent-based wildland surface fire behaviour simulation model intended for operational use; (ii) design and implement a geospatial decision support system to provide decision makers with appropriate strategies and tools for an integrated wildland fire risk management. The development of a predictive simulation model for wildland surface fire behaviour necessitates tackling the key challenge of handling different sources and types of uncertainties stemming from data inaccuracy or absolute unavailability and also from the incompleteness in the scientific understanding of fire behaviour, even in the presence of impressive modelling advances (Finney et al., 2013; Thompson and Calkin, 2011). When dealing with the complexity of modelling and predicting the behaviour of wildland surface fires, the recent literature reveals an extensive exploration of methodologies capable of integrating the accumulated knowledge with both the growing availability of novel datasets provided by rapidly developing remote sensing technologies and the state of the art in machine learning techniques.

Predicting wildland surface fire behaviour requires a deep understanding of the influence of those parameters that act as drivers of fire spread on the fire descriptors, such as the rate and direction of the maximum fire spread, the eccentricity of the ellipse approximating the fire growth, the intensity of the fire front, and the flame length. The Rothermel's mathematical model for predicting surface fire spread in wildland fuels and subsequent developments (Andrews, 2012; Rothermel, 1972) are currently the most extensively used to estimate fire descriptors, especially for operational purposes which require a short decision time frame (Andrews, 2018; Sullivan, 2009c). Starting from an in-depth study of the Rothermel's mathematical model, the project intends to: (i) propose an original implementation of the Rothermel's mathematical model for the evaluation of fire descriptors; (ii) fit a proxy model for predicting fire spread based on those machine learning techniques which offer major benefits in terms of model's interpretability; (iii) provide exhaustive explanations for the proxy model to clarify the complexity of the interactions between drivers and fire descriptors according to the model itself; (iv) develop an agent-based simulation model based on the estimated fire descriptors and capable of predicting the surface fire spread and growth across heterogeneous landscapes in order to provide fire management authorities with timely information on the progress of the fire front; (v) investigate freely available remote sensing products and datasets to define a methodology for the near real-time estimation of drivers of fire spread; (vi) evaluate the performance of the agent-based simulation model in terms of predictive capacity by validating it against historical wildfire events recorded in Sardinia, Italy, and chosen as case studies.

Besides, the project strives to propose a geospatial decision support system integrating different module and headed towards supporting risk-informed decision-making. In addition to the developed predictive wildland surface fire behavior simulation model, the decision support system means to include: (i) a dynamic workflow of action which aims to guide decision-makers in carrying out those procedures that constitute an integral part of the intervention model compliant with the legislative framework; (ii) a structured relational geodatabase to store existing institutional and research-based information needed, including fire event scenarios, available resources, and socioeconomic exposed values; (iii) a web application for immediate field data collection and sharing.

1.2 Thesis structure

Chapter 1 has highlighted the general purpose and the specific objectives of the research. The remaining of the manuscript can be distinguished into four conceptual parts and organised as follows.

The first part of the thesis summarises the state of the art on those aspects of wildfire sciences that are of greatest interest for the purposes of the project. Chapter 2 reviews the recent literature investigating on causes and effects of the increasing fire activity at a global and regional scale, with a major attention on the current situation in Mediterranean-type climate regions. Chapter 3 introduces the concept of wildland surface fire behaviour illustrating its dynamics and the environmental factors influencing it. Chapter 4 provides an overview of the state of the art in wildland surface fire behaviour simulation modelling, focusing on the Rothermel's quasi-empirical mathematical model for predicting surface fire spread across heterogeneous landscapes. Chapter 5 describes the state of the art for the estimation of the drivers of fire spread that are demanded for wildland surface fire behaviour modelling.

The second part of the thesis is dedicated to the design and implementation of the spatial simulation model developed within the context of the present research. Chapter 6 illustrates the implementation of the Rothermel's quasi-empirical mathematical model for the estimation of the fire descriptors as well as the training of the machine learning proxy model for predicting fire spread. Chapter 7 explains the development of the agent-based model for wildland surface fire growth simulation modelling and verify its conformity with respect to the conceptual model.
The third part of the thesis gives a synopsis of wildfire activity in Sardinia, Italy, and delineates data retrieval and pre-processing needed for the model application. Chapter 8 presents institutional information on historical wildfire events occurred in Sardinia, Italy, between 2005 and 2019, and provides an overview of the selected case studies.
Chapter 9 investigates accessible data sources and describes the pre-processing procedure of the available satellite products and imageries needed to estimate the drivers of fire spread and to recreate the pre-fire environmental conditions of the selected case studies. Finally, it discusses the results of the application of the developed agent-based simulation model to the case studies.
The fourth part of the thesis includes Chapter 10 which reviews the recent efforts to develop wildland fire management decision support systems and proposes a modular geospatial decision support system addressed to support fire managers in optimising decision-making processes and prioritising fire suppression interventions according to potential forest fire impacts and exposed assets.
In conclusion, Chapter 11 summarises the core findings and their implications for the thesis' purposes and emphasises future possible research directions.

1.3 Glossary

Backfire or backburn: a fire set along the inner edge of a fuel-free fireline to consume the fuel in the path of a wildfire or change the direction of force of the fire's convection column (Plucinski, 2019).
Blow-up: sudden increase in fire intensity or rate of spread strong enough to prevent direct control or to upset control plans; often accompanied by violent convection (USDA Forest Service, 2020).
Canopy: stratum containing the crowns of the tallest vegetation present (NWCG, 2006).
Containment: status of a wildfire suppression action signifying that a control line has been completed around the fire, and any associated spot fires, which can reasonably be expected to stop the fire's spread (NWCG, 2006).
Control line: constructed or natural barriers and treated fire edges used to control a fire (NWCG, 2006).
Control time: time at which a fire is declared controlled (NWCG, 2006).
Crown fire: fire spreading through the upper layers of the canopies of a tall timber; it can be further classified into passive, active, or independent crown fire according to the degree of dependence of the crown phase of the fire on the underlying surface phase (Van Wagner, 1977).
Curing: drying and browning of herbaceous vegetation or slash due to mortality or senescence, and also loss of live fuel moisture content of woody fuel following mechanically-caused mortality (NWCG, 2006).
Dead Fuel Moisture Content (**DFMC**): mass of water contained in dead plant tissues (senescent grasses, dry leaves, small twigs, litter, and organic material in the topsoil) relative to its dry mass (Nolan et al., 2016).
Decision Support System (**DSS**): the use of computers to (i) assist managers in their decision processes in semi-structured tasks, (ii) support, rather than replace managerial judgement, and (iii) improve the effectiveness of decision-making rather than its efficiency (Martell, 2011).
Descriptors of surface fire behaviour: parameters that quantify the emerging characteristics of surface fire behaviour as defined by the Rothermel's mathematical model and the associated models, i.e. the rate and direction of the maximum fire spread, the eccentricity of the ellipse approximating the fire shape, the intensity of the fire front, and the flame length (Rothermel, 1983).
Direct attack: either the removal of unburned fuels adjacent to flames or the application of water, or water with suppressant additives, onto burning fuels (Plucinski, 2019).
Drivers of surface fire behaviour: environmental variables that controls the behaviour of wildland surface fires according to the Rothermel's mathematical model, i.e. local geomorphometrical parameters (dip angle and dip direction), meteorological conditions (wind speed and direction), and fuel characteristics (synthesised with the concepts of fuel models and fuel moisture content) (Rothermel, 1983).
Drought: period of relatively long duration with substantially below-normal precipitation, usually occurring over a large area (NWCG, 2006).
Escaped fire: fire which has exceeded or is expected to exceed initial attack capabilities or prescription (NWCG, 2006).

Extreme wildfire events: exceptionally large and high intensity incidents which tends to overwhelm suppression capabilities resulting in remarkable ecological impacts and substantial socioeconomic losses and disruptions (Tedim et al., 2018).
Fire activity: complex of fire characteristics that can by summarized by three main axes: fire density, the number of fires within a given area; fire season length, periods with significant fire density (i.e. with more than 10% of the annual fire density) and closely related to weather conditions and vegetation fire resistance and resilience; fire interannual variability, standard deviation of the average fire density over a period (Chuvieco et al., 2008).
Fire behaviour: study of how a fire reacts to the influences of geo-environmental conditions, including fuel characteristics, weather conditions and geomorphometrical properties (USDA Forest Service, 2020).
Firebrand: piece of hot or burning fuel lofted by the plume of the fire and both spotting ahead of the fire front or rolling downslope (Fernandez-Pello, 2017).
Firebreak, also fuel break: natural or constructed discontinuity in fuel that might be used to stop the spread of a fire or provide a control line (Plucinski, 2019).
Fire flank: portion of a fire's perimeter that is roughly parallel to the main direction of maximum spread (USDA Forest Service, 2020).
Fire frequency: return interval of fire, measured on a time scale (Chuvieco et al., 2008).
Fire front: portion of a fire's perimeter within which continuous flaming combustion takes place and commonly corresponding to be the leading edge of the fire perimeter (USDA Forest Service, 2020).
Fire intensity: general term relating to the heat energy released by a fire front and associated with fire behaviour characteristics (Chuvieco et al., 2008).
Fire perimeter: a series of vertices that collectively define the edge of propagating fire at a particular instant of time (Glasa and Halada, 2011).
Fire-prone ecosystem: ecosystem where fire is the primary disturbance and frequent enough to act as a strong selective pressure (Pausas and Keeley, 2014).
Fire regime: a description of the average fire conditions occurring over a long period by means of parameters of when, where and which fires occur (e.g. fire density, fire frequency, fire intensity, fire seasonality, fire size, and distribution), but in a broader sense it can also include parameters that refer to the conditions of fire occurrence (e.g. fuel characteristics and distribution, meteorological conditions, and anthropogenic influence) and to the immediate effects of fires (both ecological and socioeconomic) (Krebs et al., 2010).
Fire season: period(s) of the year during which wildland fires are likely to occur, spread, and affect resource values sufficient to warrant organized fire management activities (USDA Forest Service, 2020).
Fire severity: degree to which a site has been altered or disrupted by fire; loosely, a product of fire intensity and residence time (NWCG, 2006).
Fire weather: periods with a high likelihood of fire due to a combination of high temperatures, low humidity, low rainfall, and often high winds (Jones et al., 2020).
Fire weather season length: number of days (not necessarily continuous) during each calendar year at a given location that observed high fire danger and thus experienced weather conditions most conducive to ignition and burning (Jolly et al., 2015).

Flame height: average maximum vertical extension of flames at the leading edge of the fire front, without considering occasional flashes that rise above the general level of flames. This distance is less than the flame length if flames are tilted due to wind or slope (USDA Forest Service, 2020).
Flame length: distance between the flame tip and the midpoint of the flame depth at the base of the flame; commonly used as an indicator of fire intensity (USDA Forest Service, 2020).
Flaming combustion: homogeneous combustion, where both the fuel and the oxidiser are usually gaseous, and their reaction typically result in a flame visible to the naked eye at some distance on the top of the surface of the solid fuel (Rein, 2013).
Flare-up: any sudden acceleration of fire spread or intensification of a fire; unlike a blow-up, a flare-up lasts a relatively short time and does not radically change control plans (USDA Forest Service, 2020).
Fuel array: array of fuels usually constructed with specific loading, depth, and particle size to meet experimental requirements (USDA Forest Service, 2020).
Fuel depth: average distance from the bottom of the litter layer to the top of the layer of fuel, usually the surface fuel (NWCG, 2006).
Fuel load: amount of fuel expressed quantitatively in terms of dry weight of fuel per unit area (USDA Forest Service, 2020).
Fuel model: numerical description of the fuel bed and particle properties that characterise a homogeneous unit of vegetation in terms of its influence on the surface fire behaviour (Rothermel, 1972).
Fuel size class: category used to describe the diameter of down dead woody fuels; fuels within the same size class are assumed to have similar wetting and drying properties, and to preheat and ignite at similar rates during the combustion process (NWCG, 2006).
Fuel stick: specially prepared stick or set of sticks of known dry weight continuously exposed to the weather and periodically weighed to determine changes in moisture content as an indication of moisture changes in wildland fuels (NWCG, 2006).
Ground fire: fire that consumes the organic material beneath the surface litter ground as result of the smouldering combustion in organic matter accumulated in the organic horizon of the soil (NWCG, 2006).
Heat transfer: process by which heat is imported from one body to another, through conduction, convection, and radiation (NWCG, 2006).
Indirect attack: manipulation of unburned fuel ahead of the moving fire, either by consuming it in a backfire or by chemically altering it through the application of retardants designed to reduce the flammability of unburned fuel (Plucinski, 2019).
Lazy evaluation: computer science language theory strategy that delays the evaluation of an expression as late as possible or until the value is needed (Watt, 2006).
Live Fuel Moisture Content (LFMC): mass of water contained in live foliage relative to its dry mass (Yebra et al., 2013).
Moisture of extinction: fuel moisture content, weighted over all the fuel classes, at which the fire will not spread (NWCG, 2006).
Mop-up: firefighting operation aimed at reducing residual smoke after the fire has been controlled by extinguishing or removing burning material along or near the control line, felling snags, or moving logs to prevent them to roll downhill (USDA Forest Service, 2020).

Parallel attack: construction of a control line as close to the fire as heat and flame permit (Plucinski, 2019).
Parallel computing: type of calculation where many different operations are executed at the same time, e.g. via multi-threading or multi-processing (Almasi and Gottlieb, 1989).
Pockets of a fire: unburnt indentations in the fire edge formed by fingers or slow burning areas (NWCG, 2006).
Preignition: preliminary phase of combustion in which fuel elements ahead of the fire are heated, causing fuels to dry (NWCG, 2006).
Pyrocumulonimbus: intense convective thunderstorms that develop above highly energetic wildfires, which can reach the stratosphere and create localized weather, including rain, hail, lightning and pyro-tornadoes (Bowman et al., 2020).
Rate of spread: expressed by means of an algebraic relationship between the quantity of heat received by the fuel and the quantity of heat necessary to bring it to the ignition temperature (Rothermel, 1983).
Resilience of an ecosystem: property of an ecosystem that describes its ability to maintain fundamental structures, processes, and functioning following disturbances. It is indicated by an ecosystem's capacity to return to the prior or desired state and/or the recovery time after disturbances. It is a useful concept for describing differences among ecosystems (Chambers et al., 2019).
Resprouting: ability to generate new shoots from dormant buds after stems have been fully scorched by fire (Pausas and Keeley, 2014).
Retardant, also long-term retardants: chemicals, such as diammonium phosphate and ammonium sulphate, typically applied to unburned fuels ahead of fires but also used to reduce the flammability of treated fuels even after the water used to help transport them has dried (Plucinski, 2019).
Seedling recruitment: ability to generate a fire-resistant seed bank with seeds that germinate profusely after fires (Pausas and Keeley, 2014).
Serotiny: persistence of mature cones in the plant crown until an environmental cue triggers seed release, usually fire heat that causes death of the supporting stem (He and Lamont, 2018).
Smouldering combustion: slow, low-temperature, flameless form of combustion, sustained by the heat evolved when oxygen directly attacks the surface of a condensed-phase fuel (Rein, 2013).
Spotting: behaviour of a fire producing firebrands or embers that are carried by the wind and cause secondary outbreaks of surface or crown fire beyond the zone of direct ignition by the main fire (USDA Forest Service, 2020).
Suppressant, also short-term retardants: wet solutions of either plain water or water with additives, such as foam surfactants or gel thickeners, typically applied directly onto burning fuels to cool the fire (Plucinski, 2019).
Surface fire: fire spreading across the surface fuel layer, which lies above the ground fuels, consuming needles, leaves, dead-down woody material, and other undecomposed plant residues in the litter, as well as grass, shrubs, low brushes, short trees, and low branches of tall timber (Rothermel, 1983).
Time lag: time needed under specified conditions for a fuel particle to lose about 63 percent of the difference between its initial moisture content and its equilibrium moisture content; if conditions remain unchanged, a fuel will reach 95 percent of its equilibrium moisture content after 4 time lag periods (USDA Forest Service, 2020).

Torching: envelopment in flames and burning of the foliage of a single tree crown or a small group of trees, from the bottom up (NWCG, 2006).
Wildfire or forest fire: uncontrolled combustion events occurring in the natural environment, where the energy released from exothermic combustion processes invests and ignites the surrounding unburnt fuel (Santoso et al., 2019); complicated combination of energy released due to chemical reactions in the process of combustion and the transport of that energy to surrounding unburnt fuel and the subsequent ignition of said fuel (Sullivan, 2009a).
Wildfire suppression: quelling of flames and containment of the fire perimeter within fuel-free barriers, i.e. firelines, or wet edges, followed by early detection and extinction of residual combustion (Plucinski, 2019).
Wildland-urban interface (WUI): area where humans and their development meet or intermix with wildland fuels; operationally, it is defined by means of three components: human presence, mainly expressed as housing density, wildland vegetation characteristics, such as land cover data, and a buffer distance that represents the potential for effects to extend beyond boundaries and impact neighbouring lands (Stewart et al., 2007).

Chapter 2

Wildland fire activity

2.1 Changing global fire activity

The presence of fossil charcoal in the sedimentary record provides direct evidence that fire turned into a distinctive trait of long-term Earth system's processes as soon as plants colonised lands in the Late Silurian, 420 Ma (He and Lamont, 2018). However, fires became more widespread in the Middle Devonian, 370 Ma, with the evolution of woody stems in terrestrial vascular plants, which represented the first extensive and continuous fuel loads able to sustain and carry fire for significant periods over broad spatial scales. This increase may be also a function of rising atmospheric oxygen levels and the occurrence of fire itself may have contributed to this rise through a positive feedback (Rimmer et al., 2015). Since then, wildland fires have been playing a decisive role in the evolution of the terrestrial floras and in the development of some biomes (Staver et al., 2011), also contributing to the diversification and spread of conifers and angiosperms (Belcher et al., 2021; He et al., 2016). By the Upper Cretaceous, 100-66 Ma, some taxa of land plants were already specialised for fire-prone environments thanks to fire-adaptive traits that are the result of both adaptations or exaptations to particular fire regimes (Keeley et al., 2011).

Fuel, weather, and climate are certainly dominant drivers of fire activity, but it is also true that humans have been shaping global patterns of fire activity for millennia. Bowman et al. (2011) analysed the historical development of humanity's relationship with fire and reported evidences for routine controlled use of fire by the Middle Pleistocene, 790-690 ka. Humans have altered fire regimes by modifying fuel structure and continuity as well as igniting fires in different seasons under various weather conditions. However, the anthropogenic impact on fire activity has become more pronounced since the late eighteenth century, reflecting the effects of industrialization, land clearing for agricultural purposes, human population growth, and replacement of traditional fire management with large-scale firefighting and fuels management in the twentieth century (Bowman et al., 2020). Several researches have outlined the severe human impact on fire frequency, occurrence, and activity at a global scale (Hantson et al., 2015; Kelley et al., 2019; Knorr et al., 2014), suggesting a long-term transition from natural to human dominated fire regimes (Bowman et al., 2011). Human activity is currently regarded as a dominant source of ignition in different ecosystems, such as Mediterranean-type climate regions. However, extreme weather conditions continue to play a relevant role in modulating interannual variations in fire activity and lightning strikes have been associated with unusually large wildfire events, even if rare (Couto et al., 2020; Ganteaume et al., 2013). Lightning strikes are the main natural cause of ignition all over the Earth and they assume significant relevance also in areas characterised by low population densities, such as the boreal forests where they represent the primary cause of ignition (Coogan et al., 2020; Portier et al., 2019; Veraverbeke et al., 2017).

The complex fire-human-climate interactions make it challenging to discern their specific influence on fire dynamics at regional and global scales.

The increased population at the wildland-urban interface, where anthropogenic structures directly interact or intermix with vegetated areas, has been associated to a higher number of human ignitions in Australia (Collins et al., 2015) and in the Mediterranean Basin (Calviño-Cancela et al., 2017; Elia et al., 2019). Ineffectual fuel management practices has been also addressed as a contributing factor to the increasing impact of wildfire in the Western United States (R. K. Miller et al., 2020) and other regions with Mediterranean-type climate (Efthimiou et al., 2020; Moreira et al., 2020; Ribeiro et al., 2020). Nevertheless, demographic and forest management factors alone has been reported to be insufficient to explain the magnitude of the observed extraordinary increase in wildfire size and intensity over the last decades in California and the Western United States (Goss et al., 2020; Westerling, 2016). Similarly, fire risk in southern Europe has been exacerbated in recent years by the extension of the wildland-urban interface combined with anthropogenic climate change (Ganteaume et al., 2021; Ruffault et al., 2020; Turco et al., 2019).

Conversely, some authors have recently pointed out an apparent decline in global burned area over the last two decades (Andela et al., 2017; Chuvieco et al., 2018; Doerr and Santín, 2016; Earl and Simmonds, 2018), sometimes associating it to anthropic factors, such as population growth, pastures, croplands and livestock expansion, improved land management practices, and increased effort in fire prevention, management, and suppression activities, especially in highly capitalized regions. Andela et al. (2017) identified a human-driven decline in global burned area of 1.35 ± 0.49% per year over the period 1998-2015; a decline mostly explained by a decrease in the number of fires rather than by a reduction in fire sizes. Consistently, a slight trend towards a decline in the global burned area has been observed for the period 2001-2016, albeit with substantial geographic variability (Chuvieco et al., 2018). However, Forkel et al. (2019) proved those trends to be not significant and strongly affected by the length of the considered time series, the start and end year chosen for the analysis, and the interannual variability in burned area. Those results rather suggest the impact of human activities can counteract those of climate change, attenuating trends or stabilizing the burned area at least in some regions (Forkel et al., 2019).

Albeit the lack of consensus in the scientific community on the global trend of fire activity (Bowman, 2018), recent literature has seen a significant upsurge in research investigating the influence of Earth's changing climate on global and local fire activity. Earlier studies had warned of potentially significant global increases in fire activities under future climate projections for the 21st century, with most considerable effects, in terms of both fire weather season length and extreme wildfire events occurrence, expected in South America, southern Africa, and Australia (Y. Liu et al., 2010) and in the circumboreal region (Russia, Canada, Alaska) (Flannigan et al., 2013). Jones et al. (2020) and Smith et al. (2020) lately reviewed 116 scientific studies published since the release of the Fifth Assessment Report of the Intergovernmental Panel on Climate Change (IPCC) (Stocker et al., 2013) analysing the linkages between climate change and increased frequency or severity of fire weather (i.e. periods with a high likelihood of fire due to a combination of high temperatures, low humidity, low rainfall, and often high winds). Overall, the 116 research papers support the hypothesis that climate change promotes the conditions on which wildfires depend, enhancing their likelihood. The evidence also emerges that human-induced warming has already had a profound impact on wildland fire activity

and led to a global increase in the frequency and severity of fire weather, increasing the risks of wildfire (Jones et al., 2020). Jolly et al. (2015) analysed daily global fire weather trends from 1979 to 2013 showing that combined surface weather changes over that period have promoted global wildfire weather season lengthening (i.e. an increase in the number of days per year of fire weather). Specifically, they observed (i) an 18.7% increase in global mean fire weather season length, with a statistically significant lengthening across 25.3% of the Earth's vegetated surface, and (ii) an increased frequency of long fire weather seasons across 53.4% of the global vegetated area between 1996 and 2013 if compared with 1979 to 1996. Between 1979 and 2013, South America's ecosystems have recorded a median increase of 33 days in fire weather season length and European Mediterranean forests suffered a fire weather season lengthening of 12 to 29 days. Australia showed no significant changes in biome-level fire season length from 1996 to 2013, but a regional increase in the frequency of anomalously long fire weather seasons has been recorded (Jolly et al., 2015).

Beyond the fire weather season lengthening, the occurrence of objectively defined extreme wildfire events distributed across all flammable biomes has also been investigated. The occurrence of 96% of globally distributed extreme wildfire events between 2002 to 2014 has been proved to be associated with highly anomalous fire weather conditions, mostly strong winds (34.7%) or protracted drought (45%), and approximately 65% of those events occurred on days with a Fire Weather Index above the historical 93% (Bowman et al., 2017). Moreover, a pseudo-climate change experiment predicted an area-weighted 35% global increase in the number of days per year with a Fire Weather Index exceeding the historical 93rd percentile, albeit with sharper increases in the European Mediterranean Basin, subtropical Southern Hemisphere (Eastern Brazil, Southern Africa, and Eastern Australia), and Southwestern USA and Mexico (Bowman et al., 2017). Abatzoglou et al. (2019) used simulations from 17 climate models participating in the Fifth Phase of the Coupled Model Intercomparison Project (CMIP5) (Taylor et al., 2012) of the World Climate Research Programme (WCRP) to evaluate where and when anthropogenic climate change could be expected to cause fire weather conditions to exceed that of natural variability. The study concluded that an anthropogenic increase in the number of days with an extreme Fire Weather Index was already under way for 22% of global burnable land area by 2019, including southern Europe and the Amazon, and warned an expansion of this area, up to 33-62% of global burnable area, by the mid-twenty-first century with continued warming projections (Abatzoglou et al., 2019).

These global findings identifying correlations between climate change and fire weather increase across all vegetated continents are corroborated by several regional and local studies witnessing that climate variability explains a majority of the interannual variability in fire activity (Abatzoglou, Williams, et al., 2018).

Chapter 3

Wildland surface fires

Wildland surface fire behaviour includes “a set of characteristics that describe the rate of the fire’s spread, the fuel strata it consumes, the overall shape of its perimeter, its rate of energy release along the perimeter, its mode of propagation, and perhaps the geometry of the flames along the perimeter” (Albini, 1984).

3.1 The process of combustion

Fire is the visible manifestation of the combustion process, a chemical reaction consisting in the oxidation of a fuel, the reductant, upon contact with an oxidant. In order for a fire to develop, it is also necessary to supply the system with enough activation energy to guarantee ignition.
Wildfires are uncontrolled combustion events occurring in the natural environment, where the energy released from exothermic combustion processes invests and ignites the surrounding unburnt fuel (Santoso et al., 2019). In a wildfire the fuel is represented by a mixture of live and dead plant material, including organic matter of plant origin, while the oxidizer is the atmospheric oxygen. The activation energy usually derives from lightning strikes and volcanic activity in natural systems; however, anthropogenic ignition sources are increasingly becoming prevalent across most of the ecosystems, especially in Mediterranean-type regions (Ganteaume et al., 2013). Once ignited, the combustion releases heat which, by thermal conduction, convection, or radiation, warms the adjacent fuels up to the temperature threshold in a self-sustaining process that becomes independent from the original heat source. The combustion involves a chain of elementary chemical reactions, but the overall process can be distinguished into two consequent phases: pyrolysis and oxidation. Following the exposure to a heat source, solid fuels eventually reach a temperature threshold where they undergo dehydration and **pyrolysis**, which involves both exothermic and endothermic reactions: in the absence of oxygen, the three major components of the plant biomass, i.e. cellulose, hemicellulose (heteropolymers such as xylans and xyloglucans), and lignin (a large group of aromatic polymers rich in phenolic compounds), undergo a thermal decomposition into simpler products consisting of solid charcoal and pyrolytic oils and gases. Pyrolytic oils contain a great amount of water and several organic compounds (e.g. acids, alcohols, ketones, aldehydes, phenols, ethers, esters, sugars, furans, alkenes, nitrogen compounds and miscellaneous oxygenates) whereas thermogenic gases may consist of carbon dioxide (CO_2), carbon monoxide (CO), hydrogen (H_2), low carbon hydrocarbons, such as methane (CH_4), ethane (C_2H_6), and ethylene (C_2H_4), and small amount of other gasses (e.g. propane (C_3H_8), ammonia (NH_3), nitrogen oxides (NO_x), sulphur oxides (SO_x) and low carbon alcohols) (Kan et al., 2016; Yang et al., 2007). The products of the pyrolysis process react with the atmospheric oxygen powering up an exothermic oxidation process: solid products usually undergo an in-situ oxidation

leading to **smouldering combustion**, whereas gaseous products are more prone to an ex-situ oxidation which leads to a **flaming combustion** (Rein, 2013). In a flaming combustion both the fuel and the oxidizer are gaseous (homogeneous combustion) and their reaction typically result in a flame that is visible to the naked eye at some distance on top of the surface of the solid fuel. In a smouldering combustion the atmospheric oxygen directly attacks the surface of the solid fuel (heterogeneous combustion) and the process spreads in-depth inside porous materials (i.e. coal, wood, and peat). The smouldering combustion is defined as a slow, low-temperature, flameless form of combustion (Rein, 2009), since the characteristic temperature and the spread rate are low if compared to those in the flaming combustion: typical values for smouldering are 450-700 °C for the peak temperature and 1 mm/min for the spread rate; whereas typical values for flaming are around 1500-1800 °C and 100 mm/min respectively (Santoso et al., 2019). Both smouldering and flaming combustion are susceptible to evolve one into the other, especially in wildland fuels: some residual smouldering combustion may persist above- or below-ground after the extinction of a flaming combustion (flaming-to-smouldering transition) as well as a smouldering combustion can abruptly ignite or reignite partially exhausted fuels in a flaming combustion (smouldering-to-flaming transition) (Rein, 2013). Santoso et al. (2019) identified in the presence of a vertical channel configuration in permeable fuels one of the main driver of the smouldering-to-flaming transition: vertical channels are susceptible of both increasing the oxygen supply to the smouldering reaction and compensating for the convective heat loss by the external supply of heat flux due to the radiation exchange between the two smouldering surfaces facing each other. Embers are also widely reported to increase the propensity of smouldering-to-flaming transition due to their contribution in the fuel heating process and to the initiation of new flaming sites (i.e. spotting) (Caton et al., 2017; Fernandez-Pello, 2017). Despite the smouldering-to-flaming transition is considered a major threat because of the sudden increase of the spread rate, limited research is currently available on the topic (Santoso et al., 2019).

3.2 Types of wildfire behaviour

In wildland fire science three types of wildfires are traditionally recognised depending on the fuel stratum in which the combustion process is spreading: ground fire, surface fire, and crown fire (Scott and Reinhardt, 2001). **Ground fires** are mainly the result of smouldering combustion in organic matter accumulated in the organic horizon of the soil, including roots, and rotten buried logs. Smouldering combustion is the most persistent type of combustion and is reported to be responsible of the largest and long-lasting ground fire on Earth: some ground fires in peatlands and coalfields in India and United States have been burning for decades and some in Northern China for several centuries (Huang and Rein, 2017; Stracher and Taylor, 2004). Ground fires are extremely difficult to locate, control, and extinguish, and due to the prolonged smouldering combustion (e.g. months and years) they have been proven to have significant detrimental effects on both vegetation and soils (Gabbasova et al., 2019; Rein et al., 2008). However, neither causes and effects, nor behaviour of smouldering combustion in ground fires have been widely investigated thus far (Watts and Kobziar, 2013). **Surface fires** are the most frequent and studied type of wildland fire. Surface fires spread across the surface fuel layer, which lies immediately above the ground fuels, consuming needles, leaves, dead-down woody material, and other undecomposed plant residues in the litter, as well as grass, shrubs,

low brushes, short trees, and low branches of tall timber. These surface fuel layers are regularly consumed by flaming combustion, which could be primary if directly ignited by lightning strikes or anthropogenic sources but also secondary if resulting from a smouldering-to-flaming transition. Surface fires, in turn, may also kindle ground fires because of flaming-to-smouldering combustion transitions. The essential condition for a surface fire to spread is the presence of a horizontal continuity in the fuel bed layer and, typically, there is no interaction with the overstory. However, depending on the vertical continuity in the vegetation cover, a surface fire may extend to the upper layers of the canopies of a tall timber, evolving in a crown fire. **Crown fires** are relatively rare compared to surface fires, but their impact on the canopies can be severe (Rothermel, 1991). Three distinct classes of crown fires can be distinguished according to the degree of dependence of the crown phase of the fire on the underlying surface phase: passive, active, or independent crown fire (Van Wagner, 1977). Passive crown fire occurs in the presence of sparse canopy cover and where the crown base is particularly low, with dead branches hanging from it. The most typical form of passive crown fire is torching, i.e. the sudden envelopment of an entire tree crown in flames, from the base to the very top, and it does not imply the spread of the flaming combustion from one canopy to the other. Active crown fire, contrarily, occurs in the presence of a fairly continuous crown layer with a crown base moderately high aboveground. High intensity surface fires with high spread rates are susceptible to support the development of an actively spreading crown phase, that, however, remains unable to supply the required heat transfer without the support of the underlying surface phase. Occasionally, in the presence of a continuous and dense crown layer the crown phase may acquire the ability to support the spread by itself, no longer depending in any way on the surface phase and evolving into an independent crown fire. Active and independent crown fires are especially frequent in fire-prone ecosystems dominated by fire-adapted highly flammable species, rich in aromatic resins, terpenes, and fatty acids, such as conifers, that often retains dead branches hanging from the crown base. Despite crown fires generally develop as a natural transition from surface fires, they can also originate directly in the canopy as a result of spotting phenomena. In spotting behaviour, firebrands are carried by the wind and ignites new surface or crown fires beyond the active fire front.
Wildland fires in Mediterranean-type climate regions are essentially represented by surface fires, with crown fires being limited to passive or active crown fires but rarely evolving in independent crown fires, that are more typical, if not exclusive, of the coniferous forests of the Boreal climate region. Surface fires henceforth represent the object of major interest within the context of this research.

3.3 Environmental factors influencing surface fire behaviour

A forest fire is a dynamic phenomenon that continues to evolve over space and time. The spatial configuration of the flame front, i.e. the ideal surface that separates the burnt from the not yet burned matter, is influenced by environmental variables that depends on both intrinsic characteristics of an area (i.e. geo-environmental drivers, such as geomorphometrical characteristics, land cover, and vegetation type, but also anthropogenic drivers, such as road network and population density) and local condition insisting on that area (i.e. meteorological factors such as wind speed and direction, temperature, and humidity) (Figure 3-1).

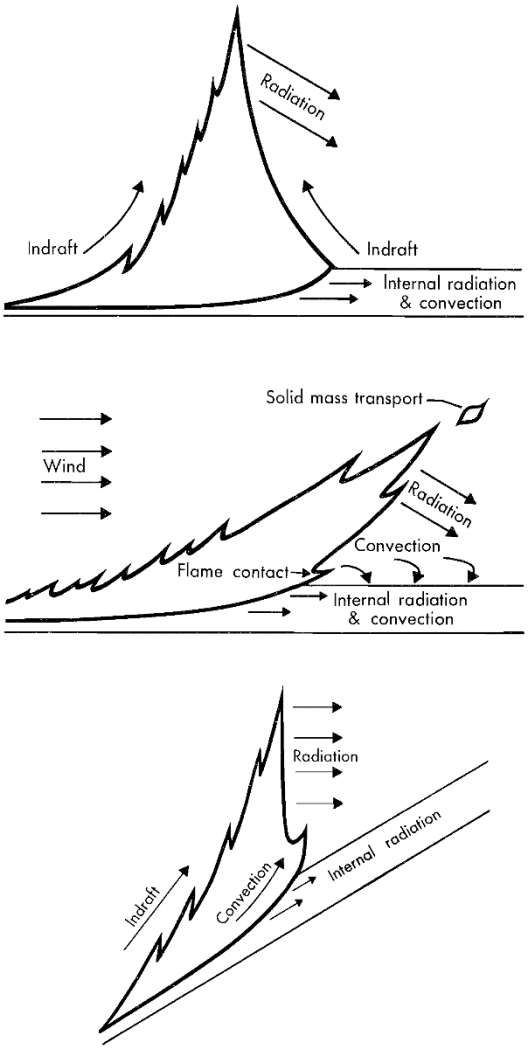

Figure 3-1 Surface fire behaviour: fire spreading in isotropic conditions (upper) or anisotropic conditions, with effects of wind (centre) and dip angle (lower) considered individually. Credits: Rothermel, 1972.

3.3.1 Geomorphometrical characteristics

Surface fire behaviour is primarily conditioned by the local geomorphometrical characteristics in terms of both dip angle and direction.

The effect of the **dip angle** is due to the influence it exerts on the heating of the fuel ahead of the flame front and on the development of the convection column. The heat released by combustion heats up the mass of air above, generating upward convective currents that originate a convection column. If the fire develops along a slope, the upward movements more easily transmit heat by convection to the vegetation present at higher altitudes. It follows that the speed of fire spread increases proportionally with the dip angle. In the absence of other conditioning factors, the surface fire then proceeds more rapidly towards higher altitudes and more slowly towards lower altitudes. The flame front tends to slow down or to arrest its spread as it approaches the ridgeline, because of the close to the ground convective winds blowing from the opposite side of the ridgeline. However, burning embers can roll downstream kindling secondary ignitions in a phaenomenon that is counted under the umbrella of spotting fires.

On the other hand, the **dip direction** directly influences the fire spread direction and indirectly alters the fire spread rate by determining the slope exposure. The differential solar radiation produces different surface energy balances that results in diverse microclimate, with diverse near-surface temperatures, potential evapotranspiration, and soil moisture content. The spatial variation of the amount of available solar radiation may also results in a significant alteration of the vegetation patterns, species distribution, and ecosystem processes (Bennie et al., 2008).

3.3.2 Plant communities

In addition to local geomorphometrical characteristics, the influence of fuel properties is extremely important in the initiation and the spread of forest fires. Wildland fuel is composed of live and dead plant material consisting of a blend of wood, bark, twigs, shrubs, grasses, and litter, with a considerable range of dimensions, physical structures, and chemical components. Wildland fire behaviour and ignition are deeply influenced by the **flammability**, which is the ability of the fuel to ignite in contact with a heat source and to sustain fire, and the **combustibility**, which is the ability of the fuel to sustain a rapid and long-lasting combustion process.

The degree of flammability of vegetal fuel varies from species to species according to their tissues' content in water per dry weight and in substances with a high calorific value (i.e. aromatic resins, tannins, terpenes, fatty acids and lignin). The higher the water content, the lower its flammability, since an higher amount of heat is required to ignite the combustion process, and the lower the calorific value, the heat released by the complete combustion of a unit of weight or volume of the fuel. The excess in moisture content therefore results in reduced intensity and speed.

The combustibility largely depends on fuel dimensions. Bushes, shrubs, and grasses, as well as dead leaves and branches with small diameters, are considered light fuels. Due to their high surface-area-to-volume ratio, light fuels ignite very rapidly, causing the development of fires with low intensity but high spread rates. First order ramifications, trunk, and roots, defined as heavy fuels, have a higher combustibility and can give rise to fires with higher intensity but spreading slower.

Beside their floristic composition, the texture, structure, and phenology of the plant communities take on particular importance in determining the evolution of forest fires as well. Whereas the texture is referred to the composition of morphological elements, the structure and phenology indicate the spatial and temporal arrangement of these morphological elements respectively. In vegetation ecology four overall measurements are commonly used to characterise vegetation: (i) **phytomass**, the total plant biomass in the plant community, expressed as dry-weight (kg/m^2); (ii) **leaf area index**, the total area of leaf surface expressed per surface area (m^2/m^2); (iii) **cover**, the relative area occupied by the vertical projection of all aerial parts of plants, as a percentage of the surface of the unit area; (iv) **stratification**, the vertical arrangement of phytomass in different layers (i.e. low or tall herbs, low or tall shrubs, and low or tall trees. As the vertical continuity in the stratification allows the transition from surface fires to crown fires, the horizontal continuity in either herbaceous fuel or canopy favours the rapid spread of the fire. On the contrary, in sparse formations, with scarce shrub cover, the flames struggle to effectively heat the fuel and therefore to spread, both vertically and horizontally.

Furthermore, at the ecosystem level, the recurrence of forest fires induces the emergence of adaptation strategies which might in turn influence fire behaviour in a deep positive feedback.

Plant communities, which supply the fuel consumed by forest fires, are the expression of the climatic regimes insisting at different spatial scales, ranging from the continental scale of the macroclimate to the local scale of the microclimatic conditions, and are strongly influenced by major disturbances and evolutionary forces, including different anthropic activities and fire itself. Fires represent an environmental disturbance factor which interfere with vegetation dynamics by periodically consuming vegetal biomass. Vegetation dynamics represent a complex sequence of stages, defined successions, aiming at the climax, a self-perpetuating equilibrium between vegetation and climate. Until the 1960s, forest fires have been regarded mainly as a severe economic threat to forest resources and a deleterious environmental factor compelling the plant communities to remain in a sub-climax stage; only in the early 1960s, fire disturbance began to be conceived as a natural evolutionary driving force essential for the maintenance of fire grass climax, i.e. grasslands and savannas (Krebs et al., 2010). Fires are nowadays perceived as an inherent ecosystem disturbance process and the threat is rather identified in perturbations of the natural fire regime (Keeley and Pausas, 2019).
In fire-prone ecosystems, where fire is recurrent enough to exert a strong selective pressure, species evolve survival strategies and traits that represent the adaptive response to fire regimes and can have significant implications on fire behaviour. Species adaptations shape the **resilience** of the ecosystems, i.e. their ability to maintain fundamental structures, processes, and functioning following fire disturbance (Chambers et al., 2019). Two main adaptive response traits are found in resilient Mediterranean-type climate ecosystems: (i) resprouting, that is the ability to generate new shoots from surviving tissues, such as dormant buds, roots, or rhizomes; and (ii) seedling recruitment, that is the ability to nurture new seedlings germinating from fire-resistant seed banks which could remain quiescent for years in serotinous cones (i.e. closed woody reproductive structures still stored in the canopy), which only release their seeds in response to fire (pyriscence), or remain dormant in the soil for decades to centuries waiting for heat or smoke as signals to germinate (He et al., 2016; Pausas and Keeley, 2014). Since fire-prone ecosystems needs for fire in order to regenerate, those adaptive traits usually come together with some other traits that are intended to promote the spread of surface fire or even to foster the transition from surface fire to crown fire. These traits may include the retention of dead hanging branches, the large accumulation of dead organic matter in the litter, or the high concentration in terpenes, resins, volatile oils and other extractives in plant tissues, with a consequent inherently high flammability. Some species instead adopt a strategy of **resistance**, evolving adaptive traits headed to minimise the effects of the fire disturbance rather than promoting a rapid recovery. One of the most typical resistance strategies in Mediterranean-type climate ecosystem is the increased thickness of the bark, often with the production of cork which acts as a thermal insulation of the cambium and buds.
Conversely, non-fire-prone ecosystems are not accustomed to the impact of wildland fires, and recurrent fires here could lead to an insufficient regeneration and result in the conversion of the ecosystem into another one richer in resilient or resistant species (Stevens-Rumann et al., 2018).

3.3.3 Meteorological conditions

While the climatic regime has strong impacts on fire activity, meteorological conditions have a decisive influence on the evolution and behaviour of single fire events. A rise in air temperature favours the heating of the fuel and, together with a reduction in the atmospheric relative humidity, it

determines an intensification of the evapotranspiration process, inducing a reduction in the water content of both plant biomass and necromass increasing their flammability.
What spreads the flames, however, is the wind, which pushes the air generated by the flame onto nearby plants. Winds exert a direct action on the flames, controlling their direction and rate of spread, and an indirect action on the vegetation, promoting its desiccation. The presence of medium to high winds may allow the flame front to propagate at higher speed due to the continuous provision of oxygen and the lengthening of the flame, which, by thermal convection and radiation, favours the heating of the adjacent fuels up to the temperature threshold for the beginning of the combustion process. Furthermore, wind is responsible for the spotting phenomenon, where incandescent materials can be taken over by the wind kindling secondary ignitions even at considerable distances from the original flame front. However, excessively high winds can have an inhibitory effect on flames by extinguishing new ignitions or blowing oppositely to the dip direction lessening its effect on the fire spread.
Extremely large and intense fires are even able to generate winds on their own: hot air rises rapidly and air rushes from the surrounding areas. The result is self-sustaining convective plumes capped by deep cumulus clouds which may form pyrocumulonimbus storms, sometimes described as fire-triggered thunderstorms (Terrasson et al., 2019). Pyrocumulonimbus storms inject aerosols into the stratosphere, where they can be transported globally, impacting radiation budgets and, thus, further facilitating extreme fire behaviour by encouraging lightning ground strikes, which ignite new fires, triggering a positive feedback (Bowman et al., 2020).

3.4 Spatial configuration of the flame front

Surface fire spreads in time and space with continuous movements like a wave expanding on a flat surface. The fire front, analogously to the wave front, can be defined as the geometric locus of the points in space which, at a given time t_n, is reached by the perturbation generated by the source at a given previous time t_{n-1}. In homogeneous environmental conditions, a surface fire would propagate in an **isotropic** and uniform medium, spreading radially with the same speed and intensity in all directions. The fire front would then ideally coincide with the geometric locus of the points equidistant from the ignition point, a circle (Curry and Fons, 1940). Nevertheless, the natural environment in which surface forest fires are expected to spread is characterized by various degrees of inhomogeneous environmental conditions, generated by the interactions amongst geomorphometrical characteristics, meteorological conditions, and structure, texture, composition, and moisture content of the plant communities. The natural environment therefore establishes a directional component in the propagation medium that force the fire front to an **anisotropic** propagation oriented according to one or more preferential directions: (i) the portion of the fire front which advances more rapidly immediately after ignition is designated the **head** of the fire; (ii) the sides of the fire, known as the **flanks**, advances in a direction perpendicular that of the maximum rate of spread; (iii) the portion of the fire front with minimal intensity and speed is the **tail**. As combustion progresses, areas characterized by fuels with different flammability may they generate local slowdowns or accelerations of the fire front propagation speed which consequently undergoes conformational variations. The fire front can

generate elongated extensions of the main body of the fire, called digitation, and unburned indentations, referred to as pockets, which can evolve into unburned areas surrounded by flames, defined islands.

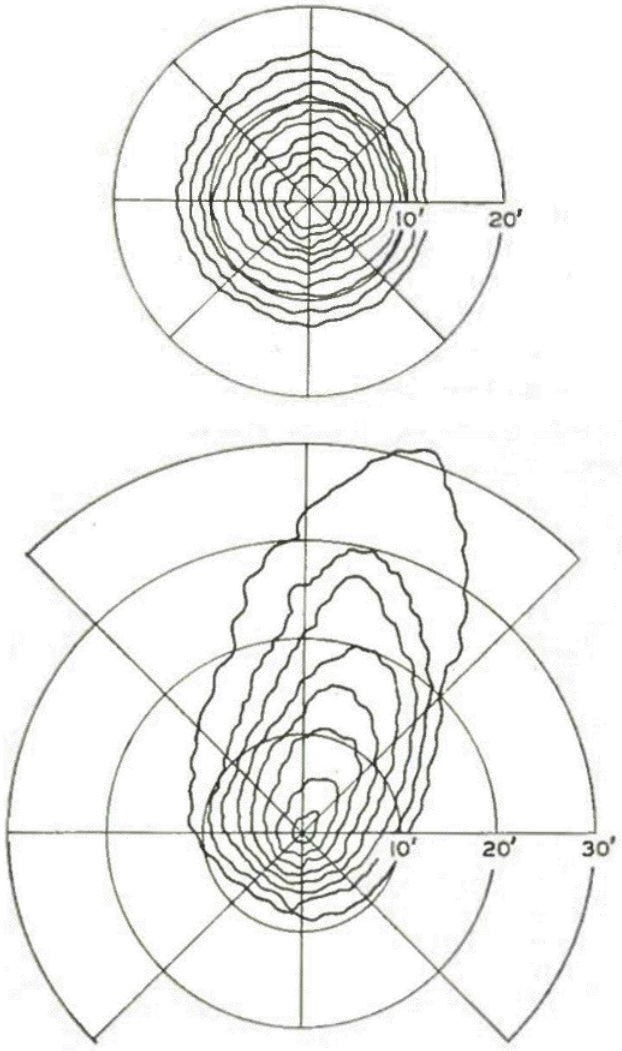

Figure 3-2 Fire spreading in isotropic conditions, with no-wind (upper), and in anisotropic conditions, with wind of constant wind (lower). Credits: Curry and Fons, 1940.

Chapter 4

Wildland surface fire behaviour modelling

The general purpose of fire behaviour modelling and simulation is to provide wildland fire management authorities with practical tools able to provide information on the spatiotemporal progress of fire spread. Wildland surface fire behaviour simulation modelling requires to develop both (i) a **fire spread model**, i.e. a method of converting a multi-dimensional set of drivers into concise parameters describing the fire spread, and (ii) a **fire growth model**, i.e. a spatial simulation model that could simulate the spatial and temporal spread of the entire flame front in two or three dimensions across a landscape. In recent years, the growing availability of computational resources has fuelled the development of a considerable number of wildland surface fire behaviour models, each characterized by different scales of interest and diverse purpose of the study, some intended for operational uses, others of purely academic interest (Sullivan, 2009a).

4.1 Fire spread models

Sullivan (2009a, 2009b) achieved an exhaustive review of the strategies recently adopted and developed to model the spread and behaviour of wildland fire, classifying developed models into two broad categories: (i) physical and quasi-physical models, which are deeply grounded in the fundamental principles of the physics and chemistry of wildland surface fire behaviour, and (ii) empirical models, which are exclusively based upon statistical analysis of fire behaviour observations and laboratory experiments, and quasi-empirical models, which are contextualised in a broader physical framework. Even though some **physical and quasi-physical models** have been developed for specific fire management purposes, the high requisites discourage their operational use: (i) the computational requirements to solve the equations at the desired resolutions, (ii) the level of detail of data needed, either in terms of type, resolution, precision, and accuracy, (iii) the excessive nominal computation times, that varies from close to real time to several order of magnitude slower than real time, and (iv) the complexity in designing laboratory and field experiments suitable for models' validation. On the other hand, in spite of their potentially elevated site-specificity and tight dependence on the environmental condition under which the data for the construction of the model were collected, **empirical and quasi-empirical models** are increasingly being adopted for operational fire suppression purposes. When considering models that can be used as decision support tools for operational fire management, some constraints become evident: (i) short decision time frame, at least less than the duration of the ongoing event; (ii) fine-scale spatial resolution, ideally less than or equal to 100 m; (iii) input data availability in operational environment; (iv) minimum computational requirements. These constraints preclude the application of most physical and quasi-physical models, whereas favours the use of

empirical and quasi-empirical models, primarily the Rothermel's mathematical model (Rothermel, 1972). Amongst the major advantages in using empirical and quasi-empirical simulation models for operational use there are the models' simplicity and calculation promptness and the direct relation to the behaviour of real fires rather than laboratory experiments.

4.1.1 Quasi-empirical models and the Rothermel's equations

The Rothermel's mathematical model for predicting fire spread in wildland fuels (Rothermel, 1972) is undoubtedly one of the most widely used fire spread model and is currently implemented in diverse simulation modelling software (Papadopoulos and Pavlidou, 2011). According to Sullivan (Sullivan, 2009b), the Rothermel's mathematical model adopts a quasi-empirical modelling approach by integrating statistical descriptors of the observed behaviour and considerations on the physical and chemical processes that regulates the combustion of plant biomass and the spread of the flame front. This combined approach of the quasi-empirical models has the advantage to attenuate difficulties of implementing both purely physical and purely empirical models. If the physical models involve issues related to finding the required input data and understanding computational limitations due to the large number of data and variables that contribute to the evolution of the event, the empirical ones are difficult to extrapolate, adapt, and apply outside the peculiar ecological and biogeographical context for which they were developed and calibrated. A quasi-empirical modelling approach, offers a valid alternative particularly suitable for real-time computations, which need to be computed in a short time frames and often with a reduced amount of available data (Papadopoulos and Pavlidou, 2011).
Andrews (2018) has recently reviewed the original Rothermel's surface fire spread model and the associated developments (Albini, 1976b, 1976a; Byram, 1959), providing an up to date reference for the application of an extended version of the Rothermel's mathematical model to wildland surface fire behaviour modelling and prediction. The extended version of the model consists of a non-linear system of equations that relates the **drivers** of surface fire behaviour in the pre-fire environment (input parameters) to a set of **descriptors** that quantifies the emerging characteristics of surface fire behaviour (output parameters). Drivers are variables influencing surface fire behaviour in wildland fuels and include local geomorphometrical parameters, meteorological conditions, and a comprehensive set of fuel characteristics. Descriptors are fire quantities characterising the resultant wildland surface fire in terms of either the rate and direction of the maximum fire spread, the eccentricity of the ellipse approximating the fire shape, the intensity of the fire front, and the flame length.
The formulation of the original Rothermel's model (1972) is based on the assumption that a flame propagates with a constant speed in conditions of spatial homogeneity and in an isotropic medium. In nature, the advancement of the fire front is influenced by the environmental heterogeneity and by the anisotropy of the propagation medium, guaranteed by variations in slope, exposure, intensity, and direction of the wind, as well as composition, structure, and texture of the plant communities. Hence, many factors influence fire behaviour in wildland fuels. The four primary inputs to the fire model are fuels, fuel moisture, wind, and slope. Second-order variables such as temperature, humidity, shading, and sheltering operate through one of the four primary groups (Rothermel, 1983). The primary output of the model is the rate of spread, whose formulation is rooted in the principle of the conservation of energy applied to a unit volume of fuel ahead of an advancing fire in a homogeneous fuel bed, as theorised by Frandsen (1971).

The **rate of spread** can be expressed by means of an algebraic relationship between the quantity of heat received by the fuel, i.e. heat source, and the quantity of heat necessary to bring it to the ignition temperature, i.e. heat sink. The rate of spread R of the fire front for a uniform fuel is therefore regulated by the relationship described in the Equation [4.1]:

$$R = \frac{I_R \xi (1 + \varphi_w + \varphi_s)}{\rho_b \varepsilon Q_{ig}} \quad [4.1]$$

where the numerator $I_R \xi (1 + \varphi_w + \varphi_s)$ indicates the propagating flux, i.e. the heat released from a fire to the fuel ahead of the fire front, and the denominator $\rho_b \varepsilon Q_{ig}$ signifies the heat required to ignite the fuel. A comprehensive summary of the Rothermel's model is provided in Table 4-4.

4.1.1.1 Input parameters

The input variables can be grouped into three categories: environmental values, fuel particle properties, and fuel array properties. **Environmental values** include: fuel moisture M_f, specified as the weight of water divided by the dry weight of the fuel; midflame wind speed U, the wind at the height that affects the surface fire; and slope steepness $tan\varphi$. **Fuel particle properties** are intrinsic parameters to the fuel particle and include: heat content h, which is the heat released during combustion; mineral content total S_t or effective S_e, indicating the quantity and type of inorganic material in the fuel which affects the rate at which it burns; and oven-dry particle density ρ_p. **Fuel array properties** are: surface-area-to-volume ratio σ, which quantifies the fuel particle size; oven-dry fuel load w_0, including the incombustible mineral fraction; fuel bed depth δ; and dead fuel moisture of extinction M_x, that is the moisture at which the dead fuel will not sustain a spreading surface fire.
Fuel bed and particle properties are classified by live and dead category (i) and by size classes (j) as defined by surface-area-to-volume ratio. The size classes are different for live and dead plant material: live fuel components are distinguished in herbaceous (living grasses and forbs, either annual or perennial) and woody (foliage and very fine stems of living shrubs), whereas dead fuel components are classified by ascending sizes (less than $1/4$ inch in diameter, equal or more than $1/4$ inch but less than 1 inch in diameter, and equal or more than 1 inch but less than 3 inches).

Table 4-1 Input parameters. Category is indicated by $i = 1$ for dead and $i = 2$ for live; size class is indicated by j.

		Parameter	Measure unit
Fuel particle	h_{ij}	Heat content	Btu/lb
	$(S_t)_{ij}$	Total mineral content	(fraction)
	$(S_e)_{ij}$	Effective mineral content	(fraction)
	$(\rho_p)_{ij}$	Oven-dry particle density	lb/ft^3
Fuel bed array	σ_{ij}	Surface-area-to-volume ratio	ft^2/ ft^3
	$(w_0)_{ij}$	Oven-dry fuel load	lb/ft^2
	δ	Fuel bed depth	ft
	$(M_x)_{ij}$	Dead fuel moisture of extinction	(fraction)
Environmental	$(M_f)_{ij}$	Moisture content	(fraction)
	U	Wind speed and direction at midflame height	ft/min
	$tan\varphi$	Slope steepness	(fraction)

4.1.1.2 Weighting factors

Fuels are composed of heterogeneous mixtures of fuel types and particle sizes. For the Rothermel's model, these various size fuels are assumed to be uniformly distributed within the fuel array and this assumption is especially critical for the fine fuels (foliage and twigs under $1/4$ inch in diameter). To aid in the understanding of fuel distribution, Rothermel makes use of the concept of unit fuel cell, which permits the mathematical representation of the fuel distribution to be referenced to a unit fuel cell rather than to the heterogeneous mixture of fuels. A **unit fuel cell** is the smallest volume of fuel within a stratum of mean depth that has sufficient fuel to be statistically representative of the entire fuel complex (Rothermel, 1972).

The extended and revised version of the Rothermel's model uses the weighting factors f_{ij} and f_i reported in Rothermel (1972) as well as the g_{ij} weighting factors developed by Albini (1976a).

Weighting factors are based on the surface area of the fuel within each size class j and category i. The mean total surface area per unit fuel cell of each size class within each category A_{ij} is determined from the mean load of that size class $(w_0)_{ij}$, its surface-area-to-volume ratio σ_{ij}, and particle density $(\rho_p)_{ij}$.

$$A_{ij} = \frac{\sigma_{ij}(w_0)_{ij}}{(\rho_p)_{ij}} \qquad [4.2]$$

The weighting factor f_{ij} is calculated as the ratio of the surface area of the jth size class, A_{ij}, to the total surface area of the dead or live categories per unit fuel cell, whereas weighting factor f_i is calculated as the ratio of the total surface area of the dead or live categories to the total surface area per unit fuel cell.

$$f_{ij} = A_{ij} \Big/ \sum_j A_{ij} \qquad [4.3]$$

$$f_i = \sum_j A_{ij} \Big/ \sum_i \sum_j A_{ij} \qquad [4.4]$$

Fuel particle and fuel array properties are used to compute comprehensive descriptions of the fuel bed. The f_{ij} weighting factors are used to find characteristic values for dead and live ith categories, whereas the f_i weighting factors are used to find fuel bed characteristic values. Albini (1976a) developed g_{ij} weighting factors for net fuel load $(w_n)_i$ because f_{ij} factors suffered the logical flaw that the net fuel load is sensitive to the partitioning of the fuel load among nearly equal size classes. Hence, fuels are partitioned by size into six subclasses, with all members of each subclass having the same weighting factor. The weighting factor for a subclass g_{ij} is the fraction of the total fuel surface area contributed by that subclass and is equal to 0 for $\sigma < 16$ ft^2/ft^3.

$$g_{ij} = \sum_{\substack{subclass \\ to\ which \\ j\ belongs}} f_{ij} \qquad [4.5]$$

4.1.1.3 Characteristic values for live and dead categories

The net fuel load $(w_n)_i$ of the live and dead fuel categories is calculated by summing the load of each of the jth size classes in the ith category $(w_n)_{ij}$, multiplied by the weighting factor g_{ij}. The net fuel load $(w_n)_{ij}$ is the oven-dry fuel load $(w_0)_{ij}$ purged of the total mineral content $(S_t)_{ij}$.

$$(w_n)_{ij} = (w_0)_{ij}\left(1 - (S_t)_{ij}\right) \quad [4.6]$$

$$(w_n)_i = \sum_j g_{ij}(w_n)_{ij} \quad [4.7]$$

Fuel particle properties for each category, such as the surface-area-to-volume ratio σ_i, the heat content h_i, the effective mineral $(S_e)_i$ content or the moisture content $\left(M_f\right)_i$ are obtained by summing the particle properties of each of the jth size class in the category multiplied by the weighting factor f_{ij} as shown in The optimum packing ratio β_{op} is a function of the surface-area-to-volume ratio σ of the complex.

$$\beta_{op} = 3.348(\sigma)^{-0.8189} \quad [4.13]$$

The evaluation of fuel particle properties for each category allows for the introduction of two dimensionless damping coefficients having values ranging from 1 to 0, which are used for the definition of the fuel mineral and moisture content of each category: mineral damping coefficient $(\eta_s)_i$ and moisture damping coefficient $(\eta_M)_i$ respectively.

$$(\eta_s)_i = 0.174(S_e)_i^{-0.19} \quad [4.8]$$

$$(\eta_M)_i = 1 - 2.59\frac{\left(M_f\right)_i}{(M_x)_i} + 5.11\left(\frac{\left(M_f\right)_i}{(M_x)_i}\right)^2 - 3.52\left(\frac{\left(M_f\right)_i}{(M_x)_i}\right)^3 \quad [4.9]$$

4.1.1.4 Fuel bed characteristic values

The characteristic surface-area-to-volume ratio σ of the complex is obtained by summing the surface-area-to-volume ratio σ_i for each category and by multiplying it by the weighting factor f_i.

$$\sigma = \sum_i f_i\sigma_i \quad [4.10]$$

Other fuel bed characteristic values are obtained by summing the particle properties of each size class of each category. The oven-dry bulk density ρ_b is the sum of the oven-dry fuel loads $(w_0)_{ij}$ divided by the fuel bed depth δ.

$$\rho_b = \frac{1}{\delta}\sum_i\sum_j (w_0)_{ij} \quad [4.11]$$

The compactness of the fuel bed, which have significant effects upon combustibility, is quantified by the packing ratio β, which is defined as the fraction of the fuel array volume that is occupied by fuel and is computed as the ratio of the oven-dry bulk density ρ_b to the oven-dry particle density $\left(\rho_p\right)_{ij}$.

$$\beta = \rho_b / (\rho_p)_{ij} \quad [4.12]$$

The optimum packing ratio β_{op} is a function of the surface-area-to-volume ratio σ of the complex.

$$\beta_{op} = 3.348(\sigma)^{-0.8189} \quad [4.13]$$

4.1.1.5 Heat source

If computed without considering wind and slope influence, the heat source is defined by the product $I_R\xi$ where I_R is the reaction intensity and ξ is the no-wind no-slope propagating flux ratio. The reaction intensity I_R is the total heat release rate per unit area of fire front, and includes the heat convected, conducted, and radiated in all directions, not just in the direction of the adjacent potential fuel. The reaction intensity I_R is defined as:

$$I_R = \Gamma' \sum_i (w_n)_i h_i (\eta_M)_i (\eta_s)_i \quad [4.14]$$

where Γ' is the optimum potential reaction velocity, $(w_n)_i$ is the net fuel load for the ith category, h_i is the heat content for the ith category, $(\eta_s)_i$ and $(\eta_M)_i$ are the mineral and moisture damping coefficient for the ith category, Equations [4.8] and [4.9]. The optimum potential reaction velocity Γ' is a function of the characteristic surface-area-to-volume ratio σ of the complex, Equation [4.10]:

$$\Gamma' = \Gamma'_{max} (\beta/\beta_{op})^A exp[A(1 - \beta/\beta_{op})] \quad [4.15]$$

where Γ'_{max} is the maximum reaction velocity and A is a correction factor from Albini (1976a).

$$\Gamma'_{max} = \sigma^{1.5}(495 + 0.0594\sigma^{1.5})^{-1} \quad [4.16]$$

$$A = 133\sigma^{-0.7913} \quad [4.17]$$

The propagating flux ratio ξ is the proportion of the total reaction intensity that actually heats adjacent fuel particles to the heat of preignition. The propagating flux ratio ξ is a function of the packing ratio β, Equation [4.12], and of the surface-area-to-volume ratio σ of the complex, Equation [4.10].

$$\xi = (192 + 0.2595\sigma)^{-1} exp[(0.792 + 0.681\sigma^{0.5})(\beta + 0.1)] \quad [4.18]$$

The propagating flux $I_R\xi$ computed for a fire spreading on a flat ground with no wind is then multiplied by empirical correction factors that adjust for the influence of wind φ_w and slope φ_s. The slope and wind factors are again a function of the characteristic surface-area-to-volume ratio σ for the fuel bed, Equation [4.10], and of the relative packing ratio β/β_{op}.

$$\varphi_s = 5.275\beta^{-0.3}(\tan\varphi)^2 \quad [4.19]$$

$$\varphi_w = CU^B (\beta/\beta_{op})^{-E} \quad [4.20]$$

where $tan\varphi$ is the slope steepness, U is the midflame wind speed, whereas C, B, and E are empirical correction factors function of the characteristic surface-area-to-volume ratio σ for the fuel bed.

$$C = 7.47exp(-0.133\sigma^{0.55}) \quad [4.21]$$

$$B = 0.02526\sigma^{0.54} \quad [4.22]$$

$$E = 0.715exp(-0.000359\sigma) \quad [4.23]$$

4.1.1.6 Heat sink

The heat sink $\rho_b \varepsilon Q_{ig}$, Equation [4.24], is the heat required for ignition and depends on the ignition temperature, moisture content of the fuel, and the amount of fuel involved in the ignition process. It is defined as the product of the heat of preignition Q_{ig} and the effective bulk density $\rho_b \varepsilon$. The heat of preignition Q_{ig}, which is the amount of heat required to ignite per unit mass, is evaluated analytically for cellulosic fuels by considering the change in specific heat from ambient to ignition temperature and the latent heat of vaporization of the fuel moisture M_f. The effective bulk density $\rho_b \varepsilon$ is the amount of fuel involved in the ignition process and is computed as the bulk density ρ_b times an effective heating number ε, a dimensionless number that approaches unity for fine fuels and decreases toward 0 as fuel size increases.

$$\rho_b \varepsilon Q_{ig} = \rho_b \sum_i f_i \sum_j f_{ij} \left[exp(-138/\sigma_{ij})\right] \left(Q_{ig}\right)_{ij} \quad [4.24]$$

where $\left(Q_{ig}\right)_{ij}$ is the heat of preignition for the jth size class within the ith category:

$$\left(Q_{ig}\right)_{ij} = 250 + 1116\left(M_f\right)_{ij} \quad [4.25]$$

Table 4-2 Characteristic values for live and dead categories.

Parameter		Measure unit
Net fuel load	$(w_n)_i = \sum_j g_{ij}(w_0)_{ij}\left(1 - (S_t)_{ij}\right)$	lb/ft²
Heat content	$h_i = \sum_j f_{ij} h_{ij}$	Btu/lb
Effective mineral content	$(S_e)_i = \sum_j f_{ij}(S_e)_{ij}$	(dimensionless)
Mineral damping coefficient	$(\eta_s)_i = 0.174(S_e)_i^{-0.19}$	(dimensionless)
Moisture content	$\left(M_f\right)_i = \sum_j f_{ij}\left(M_f\right)_{ij}$	(dimensionless)
Moisture damping coefficient	$(\eta_M)_i = 1 - 2.59(r_M)_i + 5.11(r_M)_i^2 - 3.52(r_M)_i^3$	(dimensionless)
	$(r_M)_i = \left(M_f\right)_i / (M_x)_i$	(dimensionless)
Live fuel moisture of extinction	$(M_x)_2 = 2.9W\left(1 - M_{f,dead}/(M_x)_1\right) - 0.226$	(dimensionless)
Dead-to-live load ratio	$W = \frac{\Sigma_j (w_0)_{1j} exp\left(-138/\sigma_{1j}\right)}{\Sigma_j (w_0)_{2j} exp\left(-500/\sigma_{2j}\right)}$	(dimensionless)
Fine dead fuel moisture	$M_{f,dead} = \frac{\Sigma_j \left(M_f\right)_{1j} (w_0)_{1j} exp\left(-138/\sigma_{1j}\right)}{\Sigma_j (w_0)_{1j} exp\left(-138/\sigma_{1j}\right)}$	(dimensionless)

Table 4-3 Characteristic values for the entire fuel bed

Parameter		Measure unit
Surface-area-to-volume ratio	$\sigma = \sum_i f_i \sum_j f_{ij}\sigma_{ij}$	ft²/ft³
Oven-dry bulk density	$\rho_b = \frac{1}{\delta}\sum_i \sum_j (w_0)_{ij}$	lb/ft³
Packing ratio	$\beta = \rho_b/(\rho_p)_{ij}$	fraction
Optimum packing ratio	$\beta_{op} = 3.348\sigma^{(-0.8189)}$	(dimensionless)

Table 4-4 Summary of the surface fire spread model's equations for heterogeneous wildland fuels.

Parameter		Measure unit
Maximum reaction velocity	$\Gamma'_{max} = \sigma^{1.5}(495 + 0.06\sigma^{1.5})^{-1}$	1/min
Optimum reaction velocity	$\Gamma' = \Gamma'_{max}(\beta/\beta_{op})^{A} exp[A(1-\beta/\beta_{op})]$	1/min
	$A = 133\sigma^{-0.79}$	(dimensionless)
Reaction intensity	$I_R = \Gamma' \sum_i (w_n)_i h_i (\eta_M)_i (\eta_s)_i$	Btu/ft²/min
Propagating flux ratio	$\xi = (192 + 0.26\sigma)^{-1} exp[(0.79 + 0.68\sigma^{0.5})(\beta + 0.1)]$	(dimensionless)
Heat of preignition for each size class	$(Q_{ig})_{ij} = 250 + 1116(M_f)_{ij}$	Btu/lb
Effective heating number	$\varepsilon = exp(-138/\sigma_{ij})$	(dimensionless)
Heat sink	$\rho_b \varepsilon Q_{ig} = \rho_b \sum_i f_i \sum_j f_{ij}\, \varepsilon(Q_{ig})_{ij}$	Btu/ft³
Rate of spread, no-wind no-slope	$R_0 = \frac{I_R \xi}{\rho_b \varepsilon Q_{ig}}$	ft/min
	$R = R_0(1 + \varphi_w + \varphi_s)$	ft/min
Slope factor	$\varphi_s = 5.275\beta^{-0.3}(\tan\varphi)^2$	(dimensionless)
Wind factor	$\varphi_w = CU^B(\beta/\beta_{op})^{-E}$	(dimensionless)
	$C = 7.47exp(-0.133\sigma^{0.55})$	(dimensionless)
	$B = 0.025\sigma^{0.54}$	(dimensionless)
	$E = 0.715exp(-0.000359\sigma)$	(dimensionless)
Rate of spread	$R = \frac{I_R \xi (1 + \varphi_w + \varphi_s)}{\rho_b \varepsilon Q_{ig}}$	ft/min

4.1.1.7 Related model

Diverse mathematical models are commonly associated with the Rothemel's model. Byram (1959) developed a model for estimating the fireline intensity I_B as a function of the rate of spread R, the reaction intensity I_R, and the residence time t_r computed according to H. E. Anderson (1969).

$$I_B = I_R(384/\sigma)\, R/60 \qquad [4.26]$$

From the fireline intensity I_B, Byram (1959) derived the equation for estimating the flame length F_B.

$$F_B = 0.45{I_B}^{0.46} \quad [4.27]$$

Table 4-5 Models related to the Rothermel's surface fire spread model.

Parameter		Measure unit
Residence time	$t_r = 384/\sigma$	min
Fireline intensity	$I_B = I_R t_r R/60$	Btu/ft/s
Flame length	$F_B = 0.45{I_B}^{0.46}$	ft

4.1.2 Directions of fire spread

The Rothermel's model for predicting spread in wildland fuels has been specifically developed for upslope spread with the wind. Adaptations have been made to find maximum rate of spread, fireline intensity, and flame length when the wind is not blowing upslope and the fire spreads in directions other than maximum. Vector addition is mostly used to model fire spread with other than upslope wind.

At a time t after ignition, the magnitude and direction of the vector sum D_h for the two vectors D_s and D_w will represent the rate of spread R_h in the direction α, relative to upslope (Figure 4-1). Let be the vectors D_s and D_w function of the rate of spread for a fire propagating on a flat ground with no wind R_0 (Table 4-4) and of the empirical correction factors for slope φ_s, Equation [4.19], and wind φ_w, Equation [4.20].

$$D_s = R_0 \varphi_s t \quad [4.28]$$

$$D_w = R_0 \varphi_w t \quad [4.29]$$

The magnitude and direction relative to upslope of the resultant vector are defined by D_h and α.

$$D_h = \sqrt{(D_s + D_w \cos\omega)^2 + (D_w \sin\omega)^2} \quad [4.30]$$

$$\alpha = \sin^{-1}(|D_w \sin\omega|/D_h) \quad [4.31]$$

The rate of spread R_h in the direction α, relative to upslope is computed as:

$$R_h = R_0 + D_h/t \quad [4.32]$$

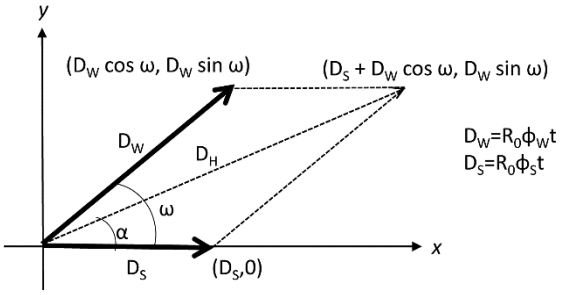

Figure 4-1 Vector addition to compute the fire's spread rate when wind is not blowing upslope. Credits: Andrews, 2018.

The effective wind factor φ_e in the direction of the maximum rate of spread is extrapolated from the rate of spread R_h in the direction α, relative to upslope, according to the Equation [4.41]. Hence, the effective wind speed U_e can be derived from the Equation [4.20] as a function of effective wind factor φ_e and the relative packing ratio β/β_{op}, Equations [4.12] and [4.13].

$$\varphi_e = \varphi_s + \varphi_w \quad [4.33]$$

$$\varphi_e = (R_h/R_0) - 1 \quad [4.34]$$

$$U_e = \left(\frac{\varphi_e (\beta/\beta_{op})^E}{C} \right)^{1/B} \quad [4.35]$$

4.1.2.1 Fire spread from the ignition point

The **ellipse** is traditionally used as growth model for the development of a fire spreading in homogeneous conditions (i.e. constant wind velocity, uniform fuel, flat or uniformly sloping terrain) in either continuous or discontinuous fuels (D. H. Anderson et al., 1982; Catchpole et al., 1992; Glasa and Halada, 2011). An elliptical shape implies a variation in the spread rate at different angles to the prevailing wind direction (Figure 4-2).

The length-to-width ratio of the ellipse Z, which is determined from the effective wind speed U_e, Equation [4.35], allows to compute the eccentricity e of the ellipse:

$$Z = 1 + 0.25 U_e \quad [4.36]$$

$$e = \frac{\sqrt{(Z^2 - 1)}}{Z} \quad [4.37]$$

The rate of spread R_γ in a direction γ from the ignition point depends on the rate of spread R_h in the direction α, relative to upslope, Equation [4.32].

$$R_\gamma = \frac{R_h(1-e)}{(1 - e\cos\gamma)} \quad [4.38]$$

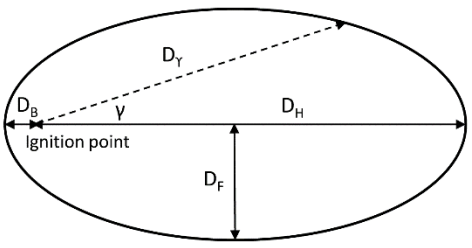

Figure 4-2 Computation of the rate of spread in a direction γ from the ignition point with respect to the direction of maximum spread. Fire spreading from a single ignition point is assumed to be elliptically shaped. Credits: Andrews, 2018.

Two exceptions are represented by the rate of spread of the heading fire which is equal to R_h and the rate of spread of the backing fire R_b.

$$R_b = \frac{R_h(1-e)}{(1+e)} \quad [4.39]$$

4.1.2.2 Fire spread from the fire perimeter

The rate of fire spread and the intensity along the fire perimeter are described by Catchpole et al. (Catchpole et al., 1992) Given the direction from the ignition point γ, it is possible to find the associated direction normal to the perimeter ψ and the rate of spread in that direction R_ψ by means of the direction θ measured from the centre of the ellipse. Let a be the semi-major axis, b the semi-minor axis, and c the distance between the ignition point and the centre of the ellipse:

$$\psi = \tan^{-1}(a/b \tan\theta) \quad [4.40]$$

$$R_\psi = c\cos\psi + (a^2\cos^2\psi + b^2\sin^2\psi)^{0.5} \quad [4.41]$$

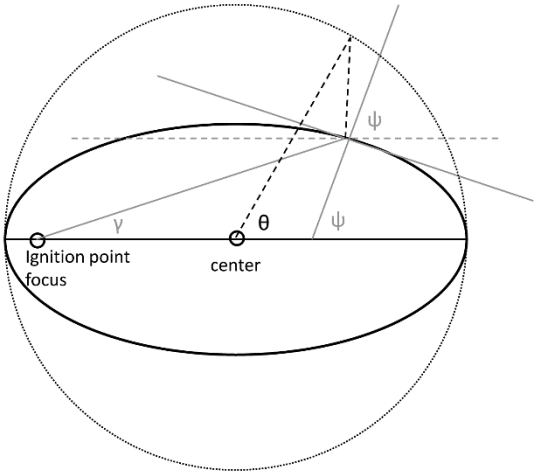

Figure 4-3 Computation of the rate of spread in a direction ψ form the fire growth perimeter with respect to the direction of maximum spread. Credits: Andrews, 2018.

4.2 Fire growth models

Sullivan (2009c) and, then, Papadopoulos and Pavlidou (2011) conducted comparative reviews on simulation and mathematical analogue models, which implement both the previous classes of models, physical and empirical. Fire simulators currently implement fire growth models based on two different approaches for fire growth representation: (i) the first, described in the literature as **vector implementation**, treats the fire perimeter as a closed curve discretised through a number of points, each one expanding based on the given spread model; (ii) the second, described in the literature as **raster implementation**, treats the fire as a group of mainly contiguous independent cells that grows in number simulating the spread mechanism from a cell to its neighbours. The fire propagation across the landscape is then carried out using different expansion algorithms, e.g. the Huygens' wavelet principle or a nearest neighbour algorithm, which are commonly exclusively tied to vector or raster implementations, even though hybrid implementations are equally possible.

4.2.1 Vector implementation

Vector implementations are mainly based on the Huygens' wavelet principle, which states that each point on the flame front becomes a new source of fire spread and growth. New ignitions around the perimeter are assumed to ignite simultaneously and to not interact with each other. The outer shape formed by all individual fires after a given time Δt constitutes the new fire perimeter, which is in turn further discretised into new ignitions and then expanded.

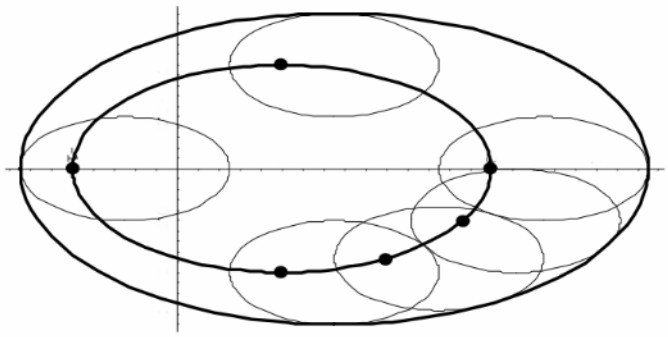

Figure 4-4 Fire growth under constant wind speed and direction conditions according to the Huygens' wavelet principle: initial elliptical fire perimeter (inner) and new fire perimeter (outer) represented by the envelope of the secondary ellipses. Credits: Glasa and Halada, 2008.

The Huygens' wavelet principle has been first proposed in the context of fire growth simulation by D. H. Anderson et al. (1982), who used an ellipse to define the shape of the fire perimeter, with the major axis aligned in the direction of the maximum rate of spread. The ellipse shape has been found to adequately describe the propagation of wildland fires burning unhindered for considerable amount of time (D. H. Anderson et al., 1982). However, Glasa and Halada (2011) recently proved diverse real cases of fire spread to be accurately represented by diverse mathematical shapes, such as single ellipse, double ellipse, oval, tear drop, lemniscate, or other complex shapes. Richards (1995) provided mathematical formulations for the spread rate as a function of the angle from the direction of maximum rate of spread for various observed shapes. Analytical solutions for the modelling approach based on the Huygens' wavelet principle and based on the elliptic template of D. H. Anderson et al. (1982) have been implemented into some of the most commonly used software for fire behaviour modelling, such as FARSITE (Finney, 1998) or the Canadian Wildland Fire Growth Model, Prometheus (Tymstra et al., 2010).

According to Sullivan (2009c), the Huygens' wavelet principle showed only small distortion of the fire perimeter when spreading in homogeneous fuel and weather conditions, while introducing errors and distortions in heterogenous and dynamic environments. Changes in conditions during the propagation period Δt cause the modelled fire perimeter to over- or under-predict the fire growth because those changes are not reflected in the predicted perimeter. Thus, some form of spatial and temporal discretization is required to account for landscape and weather non-homogeneity. Finney (1998) effectively limited the impact of this distortion by reducing the length of the propagation period Δt.

The main weakness of vector implementations is the need for a computationally expensive algorithm for generating the growingly complex convex hull fire-spread perimeter at each time step (Ghisu et al., 2015; Glasa and Halada, 2008).

4.2.2 Raster implementation

Raster implementations represent the fire growth by means of groups of contiguous cells that can be either active or inactive (either burnt or unburnt). An expansion algorithm or a set of rules, usually based on minimum travel time methods, define the mechanism of interactions between cells and the environment, posing the basis for simulating the fire growth. This approach is typically described in terms of cellular automata, discrete computational models which consist of a regular two-dimensional array of cells, each in one of a finite number of states. The complexity of wildland fire spread dynamics is traditionally simulated as a stochastic process, in which the propagation of the fire front towards neighbouring cells is modelled via a probabilistic approach (Alexandridis et al., 2008; Freire and Castro DaCamara, 2018; Ntinas et al., 2017; Trucchia et al., 2020). Less common is the use of deterministic models, where the fire behaviour is controlled by means of the application of pre-existing physical, mathematical, or empirical fire spread models as rules for simulating the fire growth within a cellular automaton (Encinas et al., 2007; Ghisu et al., 2014, 2015; Trunfio et al., 2011).

Approaches based on raster implementations tend to be computationally more efficient but can suffer from significant distortion of the produced fire shape. Under homogeneous geo-environmental conditions, the heading portion of the fire front tends to be angular rather than rounded due to the constraints of the grid cell restriction to a fixed number of directions of movement, which is determined by the chosen neighbourhood (Ghisu et al., 2015; Karafyllidis and Thanailakis, 1997). The use of larger neighbourhoods partly allows to mitigate the distortion of the theoretically elliptic shape but the use of indefinitely large neighbourhoods comes at the cost of larger computational costs and still results in errors under heterogeneous geo-environmental conditions (Finney, 2002). Hexagonal grid cells have been proven to suffer from the same distortion suffered by traditional square grid cells (Encinas et al., 2007). Trunfio et al. (2011) effectively mitigated the problem of distortion and produced shapes more closely resembling the theoretically elliptic shape by proposing a hybrid raster-vector implementation, where local ellipse expands from each cell towards the neighbouring cells without restricting the location of the ignition points to the cell centres. Ghisu et al. (2015) proposed a cellular automaton approach which approximates the expected elliptical fire shapes more closely than other similar techniques by applying to the Rothermel's equations some empirical corrections factors defined as a result of an optimization process. More recently, Trucchia et al. (2020) developed a stochastic cellular automaton model for simulating fire growth with a good overall performance in very heterogeneous geo-environmental conditions. The agreement with real-world test cases is satisfying but the level of conformity to the expected elliptical patterns is not declared.

Advantages of raster implementations over vector implementations include simpler implementation, better portability to parallel computing environments, and higher computational efficiency.

Chapter 5

Drivers of surface fire behaviour

The development of spatial simulation models of wildland surface fire behaviour requires a deep comprehension of the spatiotemporal variability over the landscape of the factors that control the fire behaviour and represent the input parameters for the Rothermel's equations. Most fire behaviour models imply the use of information ideally referring to the conditions existing little before the fire ignition. The **real time estimation** of the drivers of surface fire behaviour poses major challenges to the operational application of the existing models for fire behaviour simulation and prediction. The conventional on-the-spot sampling approach of the models' input parameters is not a viable solution in the emergency context of an ongoing wildland fire event, with the only rare exception of prearranged field sampling campaigns. Rothermel (1972) argued that the application of its mathematical model to forecasting the behaviour of ongoing wildfire calls for the need of a technique for continuous monitoring and rapid updating of fuel characteristics and weather conditions according with their high spatiotemporal variability. Over the last decades, improvements in geospatial technology have catalysed a substantial proliferation of applications in fire sciences (Panda et al., 2016). The application of **remote sensing technologies** for earth observation purposes has turned out to be extremely useful in the development of early fire and smoke detection and warning systems (Alkhatib, 2014; Barmpoutis et al., 2020). Moreover, the huge amount of remotely sensed data and their increasingly higher spatiotemporal resolution, together with the growing diffusion of **machine learning techniques** for their massive analysis, opened the way for a deeper examination and a continuous monitoring of the most critical factor influencing fire ignition and behaviour (Chowdhury and Hassan, 2013; Sayad et al., 2019; Valdez et al., 2017). Remote sensing methodologies, making use of either airborne or spaceborne active and passive sensors, provide exceptional advantages over traditional methods for the estimation of environmental variables, especially in an operational context. Polar orbiting and geostationary weather satellites offer the opportunity to monitor atmospheric conditions with suitable spatiotemporal resolution, independently form the location of weather stations with respect to the site of the fire ignition. Moreover, remotely sensed data coupled with appropriate image processing techniques allow for the production and updating of inventories of fuel characteristics over large regions with unprecedented regularity.

Drivers of fire spread can be distinguished in geomorphometrical variables, meteorological conditions, and a comprehensive set of fuel characteristics. According to the requirements of the Rothermel's model, drivers will be organised and presented here as: (i) fuel models, a mathematical representation of fuel bed and particle properties, (ii) fuel moisture content, the fraction of water content of live and dead components, variously affected by weather conditions, and (iii) wind speed and direction at midflame height, which in turn vary in response to the complexity of the underlying topography and vegetation cover.

5.1 Fuel models

The application of the Rothermel's mathematical model requires the estimation of an ensemble of fuel particles and fuel bed properties which, depending on the variability of environmental conditions can result in a vast amount of arrangements and combinations. However, Rothermel (1972) identified in the existing patterns in the spatial distribution of vegetation the key to simplify the inventory process. The vegetation cover can be interpreted as a juxtaposition of homogeneous areas in terms of structure, texture, and specific composition. The set of chemical and physical properties that characterize these homogeneous units of vegetation can be readily determined in the laboratory and assembled in a mathematical representation of the surface fuels that should have wide applicability.

"On-the-spot sampling of all input parameters is costly, time consuming, and tedious. Cataloguing fuel properties and relating them to observable site characteristics does not eliminate the fuel sampling process, but it will permit a wide application of sampling results. These results can be further refined for use in the mathematical model by assembling them into fuel models that represent typical field situations. Such fuel models contain a complete set of inputs for the mathematical fire spread model." *(Rothermel, 1972)*

5.1.1 Standard fuel models

The concept of fuel model has been introduced by Rothermel (1972) and refers to a numerical description of the fuel properties that characterise a uniform vegetation unit in terms of its influence on the surface fire behaviour. With the assumptions of **homogeneity and continuity of the fuel bed**, Rothermel initially described 11 standard fuel models. This original set has been reviewed and expanded by Albini (1976), who refined those 11 fuel models and added 2 more (Table 5-1). The 13 standard fuel models have been organized into 4 major categories (i.e. grass, shrub, timber, and slash) and later described in detail by H. E. Anderson (1982). Each fuel model is characterised by a set of descriptors that are categorised as fuel particle properties and fuel bed properties. **Fuel particle properties** are generally treated as constants and describe the fuel heat content, its oven-dry particle density, and its total and effective mineral content. **Fuel bed properties** include the thickness or height of the fuel bed depth engulfed by the flame front, the moisture of extinction of the dead fuel (i.e. a value of the percentage moisture content capable of suppressing the rate of spread), and parameters specific for each live and dead size class, such as the oven-dry fuel load and the surface-area-to-volume ratio. Fuels are described for the Rothermel's model by live and dead category and by size classes as defined by surface-area-to-volume ratio. The size classes are different for live and dead plant material: live fuel components are distinguished in herbaceous (living grasses and forbs, either annual or perennial) and woody (foliage and very fine stems of living shrubs), whereas dead fuel components are classified by ascending time lags (1 h, 10 h, and 100 h). The time lag can be defined as the time interval necessary for a dead fuel particle to lose 63% of the difference between its initial moisture content and the equilibrium moisture content, that is a function of the atmospheric temperature and relative humidity. The time lag is equal to 1 h for fuel particles less than 1/4 inch in diameter, 10 h for fuel particles equal or more than 1/4 inch but less than 1 inch in diameter, and 100 h for fuel particles equal or more than 1 inch but less than 3 inches. Fine dead fuels (1 h time lag) have a higher surface-area-to-volume ratio than 10 h and 100 h time lag fuels, and they respond more rapidly to changes in the environmental conditions.

Table 5-1 Standard fuel models (Albini, 1976a; Rothermel, 1972).

Fuel Model	Fuel load 1h [lb/ft²]	Fuel load 10h [lb/ft²]	Fuel load 100h [lb/ft²]	Fuel load live herb [lb/ft²]	Fuel load live wood [lb/ft²]	SAVR 1h [ft²/ft³]	Fuel bed depth [ft]	Dead fuel moisture of extinction [%]	Heat content [Btu/lb]
GRs1	0.034	0.000	0.000	0.000	0.000	3500	1.0	12	8000
GRs2	0.092	0.046	0.023	0.023	0.000	3000	1.0	15	8000
GRs3	0.138	0.000	0.000	0.000	0.000	1500	2.5	25	8000
SHs4	0.230	0.184	0.092	0.000	0.230	2000	6.0	20	8000
SHs5	0.046	0.023	0.000	0.000	0.092	2000	2.0	20	8000
SHs6	0.069	0.115	0.092	0.000	0.000	1750	2.5	25	8000
SHs7	0.052	0.086	0.069	0.000	0.017	1750	2.5	40	8000
TLs8	0.069	0.046	0.115	0.000	0.000	2000	0.2	30	8000
TLs9	0.134	0.019	0.007	0.000	0.000	2500	0.2	25	8000
TLs10	0.138	0.092	0.230	0.000	0.092	2000	1.0	25	8000
SBs11	0.069	0.207	0.253	0.000	0.000	1500	1.0	15	8000
SBs12	0.184	0.644	0.759	0.000	0.000	1500	2.3	20	8000
SBs13	0.322	1.058	1.288	0.000	0.000	1500	3.0	25	8000

The 13 standard fuel models have been originally designed for severe period of the fire season when surface fire events pose major control problems, but Scott and Burgan (2005) called for the necessity of simulating the effects of prescribed burning and fuel treatments on potential fire behaviour as well as of simulating the potential transition to crown fire, especially in timber-dominated conditions. They identified the need for fuel models appropriate for not fully cured grassy fuels and applicable in conditions of relatively high fuel moisture content. Moreover, they focused on developing fuel models leading to an increased precision in crown fire behaviour prediction, according to the conditions for the start and spread of crown fire defined by Van Wagner (1977). Scott and Burgan (2005) therefore expanded the original 13 standard fuel models by developing a comprehensive set of 40 fuel models for use with the Rothermel's surface fire behaviour model (Table 5-2). Among the set of 40 fuel models, those that possess a live herbaceous component are defined as dynamic. In **dynamic fuel models**, a fraction of fuel herbaceous load, ranging from 0 to 1, is transferred from the live to the dead category depending on the live herbaceous moisture content in order to represent curing. The portion of fuel load transferred is inversely proportional to the live herbaceous moisture content if it assumes values between 30% and 120%, indicating that fuel is partly cured. No live herbaceous fuel is transferred if live herbaceous moisture content is equal to 120% or higher, meaning that fuel is uncured, whereas all live herbaceous fuel is transferred to dead if live herbaceous moisture content is 30% or lower, meaning that fuel is fully cured. Based on the physiognomy of the plant communities and the type of plant material mainly involved in surface fire spread, the 40 fuel models are grouped into 6 broad categories: grasslands (GR), grasslands with shrubs (GS), shrublands (SH), timber understory (TU), timber litter (TL) or sparse wood with accumulation of necromass on the ground from residues of forestry uses, slash, or blowdown (SB). Land covered by permanent snow, ice, and open water bodies, land devoid of enough fuel to support wildland fire spread, such as sand dunes and rock outcroppings, and land covered by urban and suburban development and some agricultural land such as irrigated annual crops, mowed or tilled orchards, are classified as non-burnable areas (NB).

Table 5-2 Dynamic fuel models (Scott and Burgan, 2005).

Fuel Model	Fuel loading 1h [lb/ft²]	Fuel loading 10h [lb/ft²]	Fuel loading 100h [lb/ft²]	Fuel loading live herb [lb/ft²]	Fuel loading live wood [lb/ft²]	SAVR 1h [ft²/ft³]	Fuel bed depth [ft]	Dead fuel moisture of extinction [%]	Heat content [Btu/lb]
GR1	0.005	0.000	0.000	0.014	0.000	2200	0.40	15	8000
GR2	0.005	0.000	0.000	0.046	0.000	2000	1.00	15	8000
GR3	0.005	0.018	0.000	0.069	0.000	1500	2.00	30	8000
GR4	0.011	0.000	0.000	0.087	0.000	2000	2.00	15	8000
GR5	0.018	0.000	0.000	0.115	0.000	1800	1.50	40	8000
GR6	0.005	0.000	0.000	0.156	0.000	2200	1.50	40	9000
GR7	0.046	0.000	0.000	0.248	0.000	2000	3.00	15	8000
GR8	0.023	0.046	0.000	0.335	0.000	1500	4.00	30	8000
GR9	0.046	0.046	0.000	0.413	0.000	1800	5.00	40	8000
GS1	0.009	0.000	0.000	0.023	0.030	2000	0.90	15	8000
GS2	0.023	0.023	0.000	0.028	0.046	2000	1.50	15	8000
GS3	0.014	0.011	0.000	0.067	0.057	1800	1.80	40	8000
GS4	0.087	0.014	0.005	0.156	0.326	1800	2.10	40	8000
SH1	0.011	0.011	0.000	0.007	0.060	2000	1.00	15	8000
SH2	0.062	0.110	0.034	0.000	0.177	2000	1.00	15	8000
SH3	0.021	0.138	0.000	0.000	0.285	1600	2.40	40	8000
SH4	0.039	0.053	0.009	0.000	0.117	2000	3.00	30	8000
SH5	0.165	0.096	0.000	0.000	0.133	750	6.00	15	8000
SH6	0.133	0.067	0.000	0.000	0.064	750	2.00	30	8000
SH7	0.161	0.243	0.101	0.000	0.156	750	6.00	15	8000
SH8	0.094	0.156	0.039	0.000	0.200	750	3.00	40	8000
SH9	0.207	0.112	0.000	0.071	0.321	750	4.40	40	8000
TU1	0.009	0.041	0.069	0.009	0.041	2000	0.60	20	8000
TU2	0.044	0.083	0.057	0.000	0.009	2000	1.00	30	8000
TU3	0.051	0.007	0.011	0.030	0.051	1800	1.30	30	8000
TU4	0.207	0.000	0.000	0.000	0.092	2300	0.50	12	8000
TU5	0.184	0.184	0.138	0.000	0.138	1500	1.00	25	8000
TL1	0.046	0.101	0.165	0.000	0.000	2000	0.20	30	8000
TL2	0.064	0.106	0.101	0.000	0.000	2000	0.20	25	8000
TL3	0.023	0.101	0.129	0.000	0.000	2000	0.30	20	8000
TL4	0.023	0.069	0.193	0.000	0.000	2000	0.40	25	8000
TL5	0.053	0.115	0.202	0.000	0.000	2000	0.60	25	8000
TL6	0.110	0.055	0.055	0.000	0.000	2000	0.30	25	8000
TL7	0.014	0.064	0.372	0.000	0.000	2000	0.40	25	8000
TL8	0.266	0.064	0.051	0.000	0.000	1800	0.30	35	8000
TL9	0.305	0.152	0.191	0.000	0.000	1800	0.60	35	8000
SB1	0.069	0.138	0.505	0.000	0.000	2000	1.00	25	8000
SB2	0.207	0.195	0.184	0.000	0.000	2000	1.00	25	8000
SB3	0.253	0.126	0.138	0.000	0.000	2000	1.20	25	8000
SB4	0.241	0.161	0.241	0.000	0.000	2000	2.70	25	8000

5.1.2 Custom fuel models

The set of 13 standard fuel models has been developed to represent a large portion of forests, brush fields, and grasslands found in the temperate climates of **North America** by cataloguing fuel bed and particle properties directly measured in the field (Rothermel, 1972). Conversely, the additional 40 fuel models have been defined by assigning fuel particle and fuel bed properties after subjective interpretation of fuel complex data and visual inspection of the stereo photo series produced by the National Interagency Fire Center of the United States between 1998 and 2003 (Scott and Burgan, 2005). Since fuel models are based on physico-chemical properties of plant communities, each fuel model can theoretically represent various vegetation types with comparable physico-chemical properties regardless of the biome or the phytochorion (phytogeographic region) they belong to or their specific floristic composition. However, due to their empirical nature, it is still unclear to what extent standard and dynamic models are applicable to plant communities different from those they have been assembled and tailored for. Even though the development of the 40 additional fuel models, there is no guarantee that they can match all fuel situations and it is unclear to what extent such an extrapolation might result in biased outcomes (Salis et al., 2016).

All the 53 fuel models are currently integrated into most of the available fire behaviour simulation models and those of them based on the BEHAVE system (Andrews, 1986; Burgan and Rothermel, 1984) enable the use of **custom fuel models** instead of, or together with, standard and dynamic fuel models. The process of developing a custom fuel model, as described by Burgan and Rothermel (1984), is in all respects a modelling process which involves collecting field data, exercising the fire model, and comparing results to observed fire behaviour. It is not simply a matter of using raw data measured in the field.

Several custom fuel models have been designed for the European Mediterranean-type climate regions in order to fulfil the need for fuel models synthesising conditions potentially not satisfied by the standard and dynamic fuel models (Sebastián López et al., 2002) (Table 5-3). Conversely to the approach of Scott and Burgan (2005), who obtained fuel properties data from photointerpretation, the most frequent approach to the design of custom fuel models is to collect fuel bed and particle properties from field sampling and to perform a cluster analysis to aggregate these samples in clusters characterised by significantly different fuel bed and particle properties. Dimitrakopoulos (2002) identified 7 custom fuel models by analysing 181 field samples representative of the dominant Mediterranean vegetation types of **Greece**, ranging from grasslands to closed-timber of Mediterranean pine species, including typical shrublands such as the maquis (evergreen-sclerophyllous shrublands) or the phrygana (a complex of small, xeric shrubs up to 0.5 m height). Fernandes (2009) analysed the classification of 19 forest types of **Portugal** (Godinho-Ferreira et al., 2005) by assigning them specific fuel properties collected in the literature and grouped them into 4 clusters according to their effect on surface fire behaviour spread rate, intensity, and potential crowning. Duce et al. (2012) presented 4 additional custom fuel models representative of a wide range of Mediterranean shrublands in **Sardinia, Italy** and **Corsica, France**, from low and open maquis to high, mature, and close maquis. Elia et al. (2015) summarised forest types and shrublands into 4 site-specific custom fuel models by performing a hierarchical cluster analysis on 72 field sampling sites in **Apulia, Italy**. Rodríguez y Silva and Molina-Martínez (2012) defined a complete set of 40 custom fuel models tailored for **Andalusia, Spain**, but declared to be suitable for the application to other European Mediterranean countries, such

as Portugal, Italy, or Greece. Indeed, they found out that vegetations with different structures or different specific compositions, i.e. different associations, may define the same fuel model based on the potential surface fire behaviour. Similarly to Scott and Burgan (2005), the 40 custom fuel models for European Mediterranean applications are grouped into 6 broad categories according with the prevalent fire carrying fuel type: nearly pure grasslands (P), grasslands with up to 50% of shrub coverage (PM), shrublands (M), forest understory with grass, shrub, and litter from the canopy (HPM), litter beneath the forest canopy (HR) or sparse wood with accumulation of necromass on the ground from residues of forestry uses (R). Rodríguez y Silva and Molina-Martínez (2012) successfully validated their results by comparing field data of the rate of spread with those obtained by applying the 13 standard fuel models by Rothermel (1972) or the newly developed set of 40 custom fuel models.

Table 5-3 Sets of developed fuel models.

Set of fuel models	Case studies	Methods for data collection	Methods for clustering and estimation of significance	Systems of units
Rothermel (1972) and Albini (1976)	North America	Field sampling	---	Imperial
Scott and Burgan (2005)	North America	Stereo photo interpretation	---	Imperial
Dimitrakopoulos (2002)	Greece	Field sampling (181 samples)	K-Means clustering with ANOVA	International
Godinho-Ferreira et al. (2005)	Portugal	Literature	---	International
Rodríguez y Silva and Molina-Martínez (2012)	Andalusia, Spain	Field sampling	---	Imperial
Duce et al. (2012)	Sardinia, Italy	Field sampling (57 samples)	Hierarchical clustering with ANOVA	International
Elia et al. (2015)	Apulia, Italy	Field sampling (72 samples)	Hierarchical clustering with Kruskal–Wallis test	International

5.1.3 Mapping fuel models

The application of wildland fire behaviour simulation models requires the process of mapping fuel models, which consists in both **recognising patterns** of homogeneous vegetation units and **assigning a fuel model** to each identified unit.

Traditionally, homogeneous patterns and related fuel properties are extracted from direct **field sampling** and later extended to similar areas non directly investigated through a phytosociological approach. Over the last decades, **remote sensing techniques** have become a useful source of spatial data for mapping fuel models, offering a wide range of different sensors and algorithms that can support in these efforts. The dichotomy between field sampling and the use of remote sensing techniques for mapping fuel models is also expressed by the contrast between direct and indirect approaches. A **direct approach** considers the direct measurement of fuel properties to be assigned to the results of multitemporal image classification techniques based on seasonal changes in plant phenology. An **indirect approach**, instead, assumes that biophysical properties that can be accurately classified from remotely sensed imagery can be used as proxies of those fuel properties needed for the assignment of a specific fuel model to that class. Whatever the chosen approach, the development of site-specific thematic maps of fuel models is subject to a rigorous validation of its accuracy, that can be carried out through the comparison with ground truth, i.e. field observations.

Passive sensors have been largely exploited to distinguish some fuel properties useful to retrieve information for mapping fuel models with a direct approach. Lanorte and Lasaponara (2008) and, lately, Bajocco et al. (2015) showed the suitability of coarse-resolution satellite time-series from the Terra and Aqua Moderate Resolution Imaging Spectrometer (MODIS) to provide a classification of some fuel properties and to develop a medium-scale fuel maps in Southern Italy and Sardinia, Italy, respectively. Unfortunately, the spatial resolution of these fuel maps does not satisfy that required for the application of fire behaviour simulation models. More recently, Stefanidou et al. (2018) proved the Operational Land Imager (OLI) instrument onboard Landsat-8 to be applicable for the operational mapping of the European Mediterranean fuel types at a regional scale. Moreover, multi-temporal analysis of Sentinel-2 data acquired across distinct phenological seasons confirmed its potential to accurately delineate patterns of forest cover and forest type, as well as distinguishing dominant species at the regional scale (Franke et al., 2018; Hościło and Lewandowska, 2019). Similar results have been previously obtained only by means of high-resolution sensors onboard commercial satellites, such as IKONOS or QuickBrid (Arroyo et al., 2006).

However, optical sensors are unable to penetrate forest canopies and to reconstruct the vertical stratification of the plant communities, which is a critical variable when discriminating amongst fuel types. The increasing availability and usage of **active sensors** has allowed to overcome the limitations of optical sensors in differentiating the specific composition of plant communities and directly evaluating fuel height and distribution in the vertical strata even in the presence of a dense canopy cover (Pettinari and Chuvieco, 2020). Synthetic Aperture Radar (SAR) data have also been used for fuel characteristics retrieval at regional and global scale, and specifically to estimate the upper canopy height and the above-ground biomass, defined as the dry weight of live organic matter above the soil and expressed in Mg/ha. L-band SAR have been proven suitable to investigate above-ground biomass of savannahs as well as sparse woodlands with estimated above-ground biomass up to around 100 Mg/ha before losing sensitivity (Quegan et al., 2019). Bouvet et al. (2018) mapped the above-ground biomass of African savannahs at 25 m resolution by means of the Phased Array L-band SAR 2 (PALSAR-2) sensor onboard the commercial Advanced Land Observing Satellite 2 (ALOS-2) from the Japanese Space Exploration Agency (JAXA), whose data policy, however, makes data acquisition rather expensive, except for annual mosaics that are freely available for scientific purposes. C-band and X-band SARs which are particularly sensitive to grasses and leaves, have been found suitable for above-ground biomass estimation in grasslands. Berger et al. (2019) used Sentinel-1 C-band data to develop a biomass map of herbaceous vegetation in the Kruger National Park, South Africa. However, since most of the backscatter is from leaves and small twigs, the application of C-band for biomass estimation requires long time series (Santoro et al., 2011). Airborne light detection and ranging (LiDAR) sensors have been extensively employed alone or combined with optical data to acquire information on vegetation stratification, fuel bed height and load, directly applicable for operational mapping of fuel types (Alonso-Benito et al., 2016; Domingo et al., 2020; González-Olabarria et al., 2012; Hermosilla et al., 2014; Huesca et al., 2019; Price and Gordon, 2016; Saarela et al., 2020). The NASA's Global Ecosystem Dynamics Investigation (GEDI) mission launched a near infrared light detection and ranging (LiDAR) laser system onboard the International Space Station (ISS) in late 2018 providing new opportunities to observe the 3D structure of the Earth's temperate, Mediterranean, and tropical forests (Dubayah et al., 2014; Dubayah, Blair, et al., 2020; Schneider et al., 2020;

Stysley et al., 2016). The mission is addressed to (i) quantify the amount of carbon stored by vegetation, (ii) clarifying the role of above-ground biomass in mitigating carbon fluxes, (iii) analyse the vertical structure of the vegetation to provide an improved characterisation of habitat quality. GEDI is intended to provide the first massive sampling of forest vertical structure across forests between 51.5° S and 51.5° N, returning measurements of forest canopy height, canopy vertical structure, and surface elevation potentially improving existing canopy height products at a near global scale. GEDI has been collecting data since April 2019 and the first validated dataset has been released in early 2020. Preliminary results show that forest canopy height is overestimated within temperate and subtropical mountain grasslands, highlighting limitations in its applicability for estimations in areas of complex topography and sparse tree cover. Moreover, metrics do not discriminate between the height of trees and anthropic features (Potapov et al., 2020).

Fuel model maps at national or continental scale have been generated through an indirect approach based on coarse-scale optical remotely sensed information. Within the context of the National Fire Danger Rating System (NFDRS) a 1 km resolution fuel model map has been created for the United States through use of previously mapped land cover classes and extensive campaign of field sample data. More recently, the Landscape Fire and Resource Management Planning Tools (LANDFIRE) program promoted the use of Landsat information for the development of an up to date map of fuel models for the United States (Nelson et al., 2016). The European Forest Fire Information System (EFFIS) generated a 250 m resolution European Fuel Map (Figure 5-1) by assigning to each CORINE Land Cover (CLC) class (Bossard et al., 2000) one of the 13 standard fuel models by Rothermel (1972) and Albini (1976), excluding those models representing residues of forestry uses (European Forest Fire Information System, 2017).

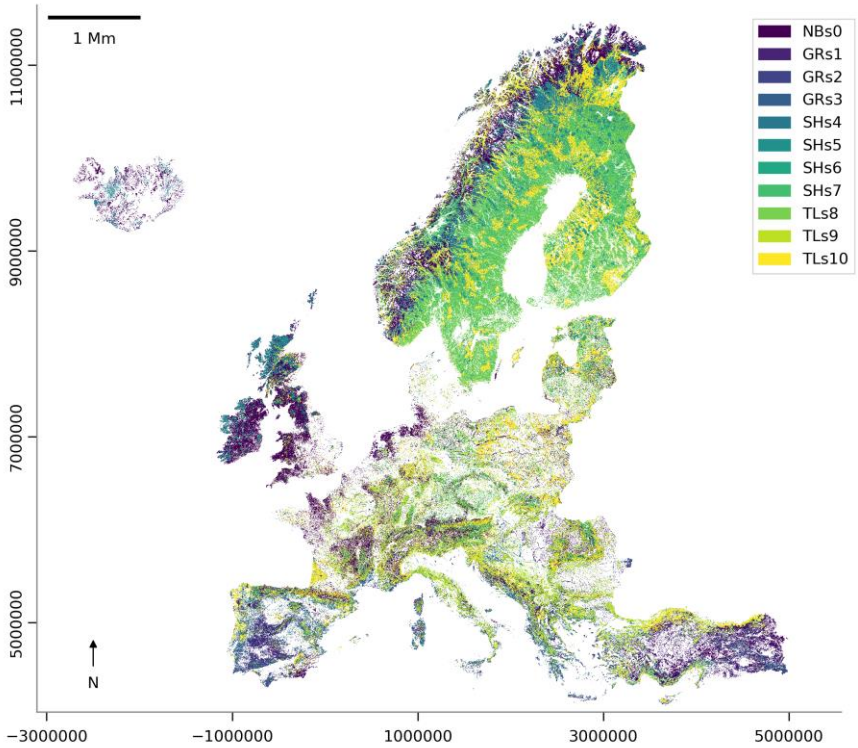

Figure 5-1 European Fuel Map representing the distribution of the 13 standard fuel models by Rothermel (1972) and Albini (1976). Data source: EFFIS.

The European Fuel Map is suitable for coarse-resolution fire danger estimations, but its applicability for fine-resolution surface fire behaviour modelling is limited. Moreover, agricultural and non-vegetated land have been masked out from the thematic map, making it difficult to apply it in European Mediterranean countries, where the vast majority of fires are caused by human activity, whether accidental, negligent or deliberate, and agricultural burning are reported among the most important drivers of wildfires (Ganteaume et al., 2013).
Similarly to the methodology adopted for the development of the European Fuel Map by EFFIS, local thematic maps of fuel models have been generated through the reclassification of previously recognised patters of land use or land cover and the assignment of one of the available fuel models to the defined patches according to the prevalent type of vegetation that would carry the fire (Sebastián López et al., 2000). Crucial questions are the representativeness of the chosen classification system over the actual vegetation community composition as well as the accuracy in distinguishing features of each mapping unit within the classification. Also, the choice of the most appropriate fuel model and the quantification of the canopy abundance and distribution in the horizontal and vertical strata of the vegetation remains a major challenge if the possibility of performing real-time field measurements is precluded.

5.2 Fuel moisture content

The amount of moisture contained in wildland fuels is reported to be a decisive factor in determining wildfire ignition and spread (Albini, 1976b; Rothermel, 1983). The dryer the fuel, the more rapidly it will ignite, and the higher the expected rate of spread of the fire front will be. The Rothermel's mathematical model utilizes fuel moisture content in the determination of both the reaction intensity and the heat of preignition, i.e. the heat required to bring the fuel ahead of a spreading fire up to ignition temperature (Rothermel, 1983). The fuel moisture content is the result of past and present weather conditions and is expressed as the mass of water contained within fuel in relation to the dry mass (Yebra et al., 2013). A distinction is made between dead and live components, that are differently affected by weather conditions.

5.2.1 Live fuel moisture content

Live fuel moisture content (LFMC) is the mass of water contained in live foliage relative to its dry mass. LFMC slightly responds to atmospheric conditions and, more significantly, varies according to morphological and physiological strategies adopted by different species to regulate their water content over different phenological conditions. Pellizzaro et al. (2007) identified two distinct seasonal patterns of LFMC for different species of Mediterranean shrubs: (i) species, such as *Cistus monspeliensis* L., *Rosmarinus officinalis* L., and *Helichrysum italicum* Roth., revealed a stronger sensitivity to seasonal environmental changes, showing LFMC values ranging from as low as 30% in summer up to 302% in spring; contrarily, (ii) species like *Pistacia lentiscus* L., *Phillyrea angustifolia* L., *Juniperus phoenicea* L., and *Chamaerops humilis* L., exhibited a narrower variability of LFMC values throughout the year, with maximum values close to 100% and minimum values of 65-80%, suggesting a little dependence from meteorological conditions. Experimental evidences suggest that those patterns reflect the different physiological and morphological strategies adopted by the various

species to cope with the summer drought season typical of the Mediterranean-type climate: species more sensitive to seasonal variability are swallow-rooted shrubs that avoid water stress by adjusting their growth and reducing the surface they expose in order to limit the evapotranspiration, whereas species exhibiting slighter changes in moisture content are deep-rooted evergreen sclerophyllous species which are far more tolerant to water stress. While LFMC predictive models based solely on meteorological variables are supposed to be inadequate to describe seasonal variations of fuel moisture content of species like *Pistacia lentiscus* L. and *Phillyrea angustifolia* L., for practical purposes, it seems not to be of crucial importance to accurately model their LFMC seasonal variation (Pellizzaro et al., 2007). At a landscape scale, that seasonal variability moisture content of live fuels has shown high accuracy in predicting the number of fires and of the total burned area in Mediterranean-type climate regions, especially in grasslands and shrublands (Chuvieco et al., 2009). However, the immediate influence of LFMC on fire behaviour has not been effectively evaluated so far (Yebra et al., 2013).

LFMC can be directly measured in the field or can be estimated from satellite observations which, in any case, need to be calibrated and validated against field measurements. Field measurements are accurate but prohibitive for monitoring LFMC spatiotemporal variability at regional or national scale. Yebra et al. (2013) provided an extensive review of the diverse methods that have been developed to estimate LFMC from remotely sensed data, distinguishing empirical methods and physical model-based methods. **Empirical methods** for LFMC estimation are based on statistical fitting between field measurements and spectral measures based on reflectance data. The most used spectral information comes from various vegetation indices, mostly the Normalized Difference Vegetation Index (NDVI), Normalized Difference Water Index (NDWI), or the Enhanced Vegetation Index (EVI), that are analysed together with ancillary information such as the surface temperature. This extensive use of vegetation indices is rooted in the sensitivity of the reflectance in the visible bands, especially in the red end of the visible spectrum, to the leaf water content. Senescence or dehydration of the tissues causes a depletion of the chlorophyll content significantly reducing the vegetation reflectance in the near-infrared (NIR) and short-wave-infrared (SWIR) spectral regions (Yebra et al., 2013). **Physical model-based methods**, instead, estimate LFMC based on simulation scenarios derived from physical models, such as the inversion of radiative transfer model (RTM) (Jurdao et al., 2013; Yebra et al., 2008; Yebra and Chuvieco, 2009a, 2009b). The observed reflectances of every pixel are compared to those simulated in a lookup table and the parameters of the most similar simulated spectrum are assigned to each pixel. The concept of similarity is commonly formalised using a merit function, which implies minimising the differences between the observed and modelled reflectance. Physical model-based methods are independent of sensor or site conditions and have been proved more robust when several calibration samples were selected (Yebra et al., 2008). Yebra et al. (2008) compared the effectiveness of LFMC estimations from empirical methods and those based on simulated data for Mediterranean grasslands and shrublands. According to their results simulation methods performed better with respect to empirical methods, but their calibration is far more complex since it requires detailed parametrisation, such as plant physiological and structural variables that are not always available, and, hence, they are considered less suitable for operational purposes. On the other hand, empirical relationships cannot be easily applied to regional or global scales due to spatial differences in leaf and canopy characteristics, soil background, sensor characteristics, and observation conditions

(Yebra et al., 2013). Whatever the method of choice, methodologies tailored to grasslands or shrublands physiology cannot be easily extended to other vegetation types, such as woodlands (Mendiguren et al., 2015).
Coarse-to-medium-resolution optical sensors have been widely used for LFMC estimation in Mediterranean-type climate regions, ranging from the Advanced Very High Resolution Radiometer (AVHRR) onboard the polar-orbiting National Oceanic and Atmospheric Administration (NOAA) (Chuvieco et al., 2004; García et al., 2008) to the Moderate Resolution Imaging Spectroradiometer (MODIS) onboard Terra and Aqua satellites (Caccamo et al., 2012; Mendiguren et al., 2015; Myoung et al., 2018). Higher spatial resolution optical sensors, such as the Landsat or the Sentinel-2 Multi-Spectral Instrument (MSI), have been recently employed as well (Marino et al., 2018; Shu et al., 2019) despite their lower temporal resolution. More recently, Konings et al. (2019) illustrated the potential of both passive and active microwave remote sensing observation to estimate plant water content metrics, including LFMC, and Wang et al. (2019) demonstrated the possibility of developing new operational methodologies for forest LFMC estimation based on the C-band Sentinel-1A.

5.2.2 Dead fuel moisture content

Dead fuel moisture content (DFMC) is the mass of water contained in dead plant tissues (senescent grasses, dry leaves, small twigs, litter, and organic material in the topsoil) relative to its dry mass. DFMC is inversely related to the probability of ignition because part of the energy is consumed in the process of evaporation right before the ignition (Dimitrakopoulos and Papaioannou, 2001). Moreover, DFMC critically affects the rate of spread by reducing fuel flammability (Rothermel, 1983; Viney, 1991). DFMC values are usually less than 30% and can range as low as 1% in extreme drought conditions (Aguado et al., 2007). The moisture content of dead fuels lying on the forest floor, including litter, fallen foliage and branches, is highly dependent on rapid atmospheric changes, especially temperature and relative humidity, and tend to gain or lose moisture until the equilibrium moisture content (EMC), the equilibrium with the surrounding atmosphere, is achieved (Nieto et al., 2010). The moisture content of dead fuels is a function of their size, and respond to both prolonged periods of drought and to hourly changes in the microclimate surrounding the fuel particle (Nolan et al., 2016; Rothermel, 1983). The estimation of DFMC rests on the unique system for classifying dead fuels defined by Rothermel (1972), which is based on the length of time required for a fuel particle to change its moisture content by a specified amount when subjected to a change in its environment. Dead fuels are classified based on 1 h, 10 h, or 100 h classes, or time lags, depending on their size and how slowly they lose or gain moisture; the larger the fuels that dry out, the slower they return to normal conditions and the longer they can sustain a possible combustion. Fuel particles more than 1/4 inch but less than 1 inch in diameter constitute the class of fine dead fuels (10 h time lag), that take 10 h to lose 63% of the difference between their initial moisture content and equilibrium moisture content in an atmosphere of constant temperature and humidity (Sebastián López et al., 2002).
Field sampling provides the most accurate estimations of DFMC, but it is costly and unfeasible over wide areas. In addition, field sampling does not provide instantaneous estimations since the samples must be oven-dried for at least 24 h; hence, this approach has limited applicability when continuous or real-time moisture information is needed or when monitoring needs to be performed remotely (Aguado et al., 2007). Meteorological indices measured at weather stations have been traditionally

used to estimate the degree of dryness of different fuel types. Relying on current and past weather conditions, the estimation of the moisture content of fine dead fuels makes use of the concept of EMC, which is a function of the atmospheric temperature and the relative humidity (Simard, 1968). Another increasingly popular approach is the use of automated fuel moisture sticks, which are designed to emulate 10 h fuels and to collect moisture data, providing a real-time continuous monitoring (Nelson Jr, 2000). Cawson et al. (2020) assessed the ability of automated fuel sticks to predict surface DFMC across a range of forest types from 27 sites, concluding that despite fuel sticks typically underestimates surface DFMC, forest fuel-specific linear calibration functions can provide a reasonable accuracy. Among the difficulties associated with the estimation of DFMC form meteorological indices, or by means of fuel sticks, there is the need for spatial interpolation techniques which may introduce added estimation errors (Aguado et al., 2007). Remotely sensed predictions of fuel moisture have been typically focused on live fuels, while spatially explicit estimates of dead fuel moisture have been less common. Nieto et al. (2010) proposed a methodology to estimate hourly meteorological data (i.e. relative humidity and air temperature) and then assess the EMC of dead fuel with remotely sensed data acquired by the Spinning Enhanced Visible and Infrared Imager (SEVIRI) sensor, onboard the Meteosat Second Generation (MSG) satellite. Their results, however, showed the remotely sensed EMC tends to underestimate the EMC from ground data. More recently, the spatial variation of dead fuel moisture content has been successfully assessed based on the exponential decline of fine fuel moisture with increasing vapour pressure deficit, calculated with observations from the MODIS instrument onboard the Terra satellite (Nolan et al., 2016).

5.3 Wind speed and direction at midflame height

Horizontal wind speed and direction are the most variable drivers required to predict surface fire behaviour (Rothermel, 1983). Besides their inherent temporal variability, the horizontal and vertical components of the wind vector significantly vary across the landscape as a result of the influence of both complex topography and vegetation cover. Indeed, due to the increasing friction, the horizontal wind speed vertically decreases with the proximity to the surface producing a logarithmic vertical profile. According to the World Meteorological Organization (WMO), wind measurements are usually provided by land management agencies at a standard height of 10 m above the ground, except for the National Weather Service of the United States, whose forecasts are provided at a 6.01 m (20 ft) height above the bare ground or above the vegetation. Most fires in surface fuels burn below those heights, specifically at a height above the surface fuel equivalent to the mid-level height of flames, hereafter **midflame height**. The term midflame height was coined by Rothermel (1972) to make a clear distinction between the wind speed measured at 20 ft or 10 m above the vegetation and the reduced wind that is required to calculate the rate of spread of the surface fire. The midflame wind speed calculated at a midflame height is, hence, the average wind velocity that actually affects the surface fire spread. Fine-scale near-surface wind predictions are significantly affected by mechanical channelling and velocity variations induced by complex topographies and sheltering conditions from the overstory layer of forest canopies.

5.3.1 Effects of complex topography

Ideally, simulation of wildland surface fire behaviour should be linked to the atmosphere in a coupled approach taking into consideration fire-atmosphere interactions. However, fully coupled models are not likely to be used in truly operational applications because of their high computational demands and coarse spatial resolution of the outputs. Hence in order to meet operational constraints, near real-time incident support in wildland surface fire management are typically operated in a decoupled mode (Finney, 1998). Variation in the local terrain configuration, such as wind speed-up over ridges, flow channelling in valleys, flow separation around terrain obstacles, and enhanced surface roughness, alter the flow of the wind field over spatial scales finer than those employed by **prognostic models**, such as those used in numerical weather forecasting. Mesoscale numerical weather prediction systems provide accurate real-time weather predictions over a range of spatiotemporal scales but, with horizontal resolutions from 3 km up to 12 km, these models could not resolve winds at sufficient scales to capture detailed and complex topographic effects that can influence surface fire behaviour (Quill et al., 2019). Hence, Wagenbrenner et al. (2016) stressed the need for downscaling results from prognostic models to better predict meteorological variables at fine-scale. Steady-state or **diagnostic models** are mostly preferred to simulate fine-scale near-surface winds for operational fire management (Forthofer, Butler, and Wagenbrenner, 2014). Steady-state models predict the wind field at a single instant in time and can be used to represent winds during a quasi-steady or time-averaged period. Forthofer et al. (2009) developed a diagnostic model specifically intended for operational wildland fire modelling. It produces spatially varying wind fields and is the primary wind model used to dynamically downscale hourly 10 m or 20 ft predictions starting from the numerical weather predictions. Two different steady-state models with different physical assumptions are implemented in the model by Forthofer et al. (2009): a **mass conserving model**, based solely on conservation of mass, and a **mass and momentum conserving model**, capable of solving some form of turbulent conditions. Both solvers exhibited a reduced accuracy when predicting downslope wind flows, although the mass and momentum conserving solver outperformed the solely mass conserving solver (Forthofer, Butler, and Wagenbrenner, 2014; Wagenbrenner et al., 2016). However, a threshold of acceptable accuracy should be determined by the user according to the specific application. Under operational constraints of restricted decision time frames for fire management, the use of the momentum conserving model could be precluded in favour of the near real-time outputs of the mass-conserving model with the trade-off being the loss of some accuracy, especially in the wake region of a terrain feature (Forthofer, Butler, Mchugh, et al., 2014). Recently, Quill et al. (2019) recommended a probabilistic modelling approach to predict multi-modal wind direction distributions and to perform a quantitative assessments of uncertainty in operational fire spread and behaviour predictions. However, quantifying the effects of probabilistic prediction of input variables, including wind speed and direction, remain an open quest and no detailed analysis of the influence of individual input parameters has been conducted (Quill et al., 2019).

5.3.2 Effects of sheltering from forest canopy

Andrews (2012) conceived the concept of **wind adjustment factor** (WAF) to indicate a multiplier intended to reduce the wind speed measured at 10 m or 20 ft above the vegetation to a value at

midflame height as needed by the Rothermel's surface fire behaviour model. The evaluation of the wind adjustment factor is based on the logarithmic vertical profile of the wind, the surface fuel bed depth, and the presence, or absence, of a sheltering from overstory vegetation. Andrews (2012) presented two distinct models for determining the wind speed at a midflame height above a surface fuel that is sheltered or unsheltered from the wind by the overstory layer of a forest canopy.
Given that the midflame height is not consistently defined, the midflame wind speed in unsheltered conditions is evaluated as the average wind speed over a height ranging from the surface fuel bed depth H and the flame extent above the fuel H_F, which is mostly assumed to be equal to the surface fuel bed depth H itself. The **unsheltered** WAF is then evaluated as an average wind speed from the top of the fuel bed to a height of twice the fuel bed depth.

$$WAF = \frac{1.83}{\ln\left(\frac{20 + 0.36\,H}{0.13\,H}\right)} \qquad [5.1]$$

The **sheltered** WAF instead assumes that (i) the wind speed is approximately constant with height below the top of a uniform forest canopy and that (ii) the tree crown can be approximated to a conical shape. The evaluation of the sheltered WAF is based on both the total canopy height H and the crown fill portion f, that is the volume of the canopy layer that is occupied by tree crowns. The crown fill portion f is in turn a function of the horizontal fraction canopy cover c and of the crown ratio r, that is the fraction of the total canopy height occupied by tree crowns.

$$WAF = \frac{0.555}{\sqrt{fH}\;ln\left(\frac{20 + 0.36\,H}{0.13\,H}\right)}, \qquad f = \frac{cr}{3} \qquad [5.2]$$

Given the description of the overstory, different factors contribute to determining whether the fuel is sheltered or unsheltered from the wind. While the ability of the wind to penetrate the canopy also depends on the relative location on the slope and on the presence of adjacent overstory, the adjustment of the 20 ft wind speed to the midflame height provided by Andrews (2012) currently depends only on the overstory sheltering. Different methods and criteria are adopted by existing simulation models implementing the Rothermel's equations. The BehavePlus system directly provides precalculated WAF values in a tabular form indicating WAF values for sheltered and unsheltered conditions for each of the 53 standard fuel models. However, it also allows calculating WAF values for each pixel by making use of a crown fill portion f greater than 5% as a criterion indicating sheltering conditions. Instead, the FARSITE-FlamMap system criterion for sheltered conditions is a canopy cover c greater than 0.

Chapter 6

Proxy model for predicting fire spread

The development of a spatial simulation model capable of predicting the surface fire behaviour in terms of spread and growth across heterogeneous landscapes, firstly requires the implementation of a consistent methodology for the evaluation of fire descriptors. The need for flexibility in handling the equations of the Rothermel's original and associated models (Albini, 1976b, 1976a; H. E. Anderson, 1969; Andrews, 2012; Rothermel, 1972), together with the necessity of integrating recent updates from Andrews (2018), have led to an original implementation of a computer algorithm that evaluates the descriptors of fire behaviour defined within the context of the extended Rothermel's model: (i) the rate and direction of the maximum fire spread, (ii) the eccentricity of the ellipse approximating the fire shape, (iii) the intensity of the fire front, and (iv) the flame length. Then, the Rothermel's model has been approximated by means of a machine learning ensemble method and its behaviour and its ability to detect patterns produced by the Rothermel's model have been evaluated by means of a synthetic dataset specifically designed for this application. Finally, explanations for each model's prediction have been elaborated and a feature importance analysis has been performed on the proxy model to enhance the comprehension of the interdependence of the drivers and to understand their relative importance in predicting fire descriptors.

6.1 Model development

6.1.1 Implementation of the Rothermel's model

Andrews (2018) has recently conducted a detailed analysis of the Rothermel's equations and of the existing relations among input variables in order to provide a comprehensive documentation of the model. Within the context of this study, an authentic implementation of the Rothermel's model has been developed leveraging on NumPy (Harris et al., 2020; Van Der Walt et al., 2011), the primary **array programming** library for the Python language. Python is an open source interpreted programming language that has been recently provided with a solid foundation for array programming thanks to NumPy, together with interactive environment such as IPython (Pérez and Granger, 2007) or Jupyter (Kluyver et al., 2016). The NumPy array is a data structure that efficiently stores and accesses multi-dimensional data, enabling the parallelisation of requested operations. Array operations can be vectorised and executed in parallel over a chosen dimension rather than on individual elements, potentially accelerating the final process by leveraging on more than one processing unit. Numba has been employed as a just-in-time compiler to perform **dynamic translation** and optimise operations (Lam et al., 2015).

6.1.2 Synthetic dataset generation

In order to develop a proxy model of the original implementation of the Rothermel's model based on supervised machine learning regression techniques, it has been chosen to generate an ad hoc synthetic dataset to be used for model's training and testing. The synthetic dataset contains 1.000.000 records each one composed by multiple input features, i.e. drivers of fire spread, plus a target variable. Each record is generated by randomly sampling unique combinations of drivers of fire spread and providing them to the original implementation of the Rothermel's model as input data in order to compute the maximum rate of spread relative to upslope, Equation [4.32], the direction of the maximum rate of spread relative to upslope, Equation [4.31], and the eccentricity of the ellipse approximating the fire perimeter, Equation [4.37], which are alternatively chosen here as target variables (Table 6-1). Combinations of drivers of fire spread have been generated by sampling each parameter from its estimated frequency distribution (Figure 6-1) in Sardinia over the period 2015-2019. The methodology adopted for the estimation of each of the drivers of fire spread will be described in detail in Chapter 9. In a nutshell, (i) **fuel models** have been sampled from an harmonised dataset collecting 123 fuel models from both North American (Albini, 1976b; Rothermel, 1972; Scott and Burgan, 2005) and European Mediterranean sets (Dimitrakopoulos, 2002; Duce et al., 2012; Elia et al., 2015; Godinho-Ferreira et al., 2005; Rodríguez y Silva and Molina-Martínez, 2012), (ii) **live and dead fuel moisture fractions** have been estimated from the MODIS instrument onboard the Terra satellite by applying and adapting relations from García et al. (2008) and Nolan et al. (2016) respectively, and (iii) hourly **horizontal wind speeds and directions** at a 10 m height have been retrieved from ERA5-Land (Muñoz Sabater, 2019) and downscaled to 20 ft. The custom implementation also includes the adjustment of the horizontal wind speed and direction at 20 ft height to the midflame height accounting for the effects of vegetation according to Andrews (2012).

Table 6-1 Subsample of the synthetic dataset. The maximum rate of spread [m/min] represents the target variable. Superscripts beside the fuel model's code refer to (1) Rothermel, 1972 or (2) Rodríguez y Silva and Molina-Martínez, 2012.

Fuel model	Live moisture fraction	Dead moisture fraction (10h)	Wind direction [degree CW from N]	Wind speed 20 ft [m/s]	Canopy cover	Crown ratio	Dip direction [degree CW from N]	Dip angle [degree]	Maximum rate of spread [m/min]
GRs3(1)	1.82	0.10	259	2.13	0.24	0.23	181	6.24	19.87
GRp7(2)	1.20	0.09	18	5.52	0.03	0.87	64	24.06	106.15
SHs4(1)	1.22	0.07	40	0.17	0.63	0.48	359	0.55	1.90
SHm9(2)	1.01	0.08	34	2.40	0.11	0.18	183	8.09	38.56
TUhpm2(2)	0.76	0.07	239	7.24	0.86	0.14	326	1.48	14.11

The large multidimensional dataset strives to fulfil the need for an exhaustive exploration of the space of all possible solutions. When dealing with multi-temporal higher-dimensional spatial data, the number of operations to be executed over all the dimensions of the dataset might become too large to fit into a single processing pipeline or the amount of data required for a single operation might become too large to fit into the available RAM memory of a single workstation. The Dask parallel computing framework (Rocklin, 2015) has been employed to perform **parallel and out-of-core computation** in order to use the available processing resources simultaneously and to efficiently use external memory as extensions of the RAM memory. The Dask framework has been used jointly with other libraries

from the scientific Python ecosystem founded on NumPy, such as SciPy (Virtanen et al., 2020), pandas (McKinney, 2011), xarray (Hoyer and Hamman, 2017), and scikit-learn (Pedregosa et al., 2011).

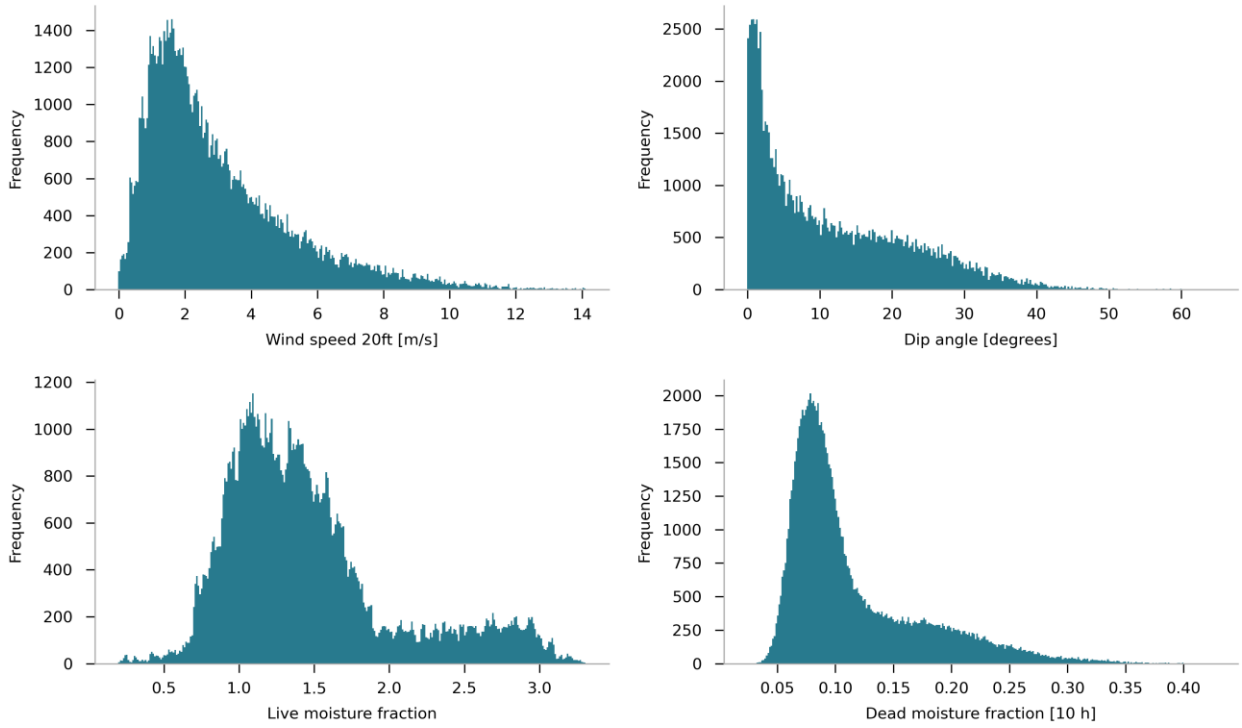

Figure 6-1 Frequency distribution of the drivers of fire spread in Sardinia from 2015 to 2019: horizontal wind speeds at 20 ft height (upper left), dip angle (upper right), live and dead fuel moisture fractions (lower left and right respectively).

6.1.3 Proxy model development

6.1.3.1 Model selection

A tree boosting machine learning method has been chosen to develop a proxy model of the original implementation of the Rothermel's model for predicting fire spread in wildland fuels.

The eXtreme Gradient Boosting (XGBoost), a scalable end-to-end tree boosting system, is currently used in literature to achieve state-of-the-art results for supervised learning regression problems where training data with multiple features x_i are used to predict a target variable y_i (Chen and Guestrin, 2016). Because of its scalability, XGBoost is particularly suitable for large multidimensional datasets, such as the synthetic dataset generated for this implementation.

XGBoost is an efficient implementation of gradient boosted decision trees, an ensemble method which combine the predictions of several base decision tree estimators built with a given learning algorithm in order to improve the robustness and generalisability over a single estimator. A decision tree can be described by a root node, some internal nodes, and leaf nodes, i.e. end nodes. Decision tree algorithms generally use simple rules to start from the root node and branch out, going through internal nodes, to finally end up in the leaves. Ensemble methods combine several weak decision tree models to produce a powerful ensemble. Gradient boosted decision trees, such as XGBoost, belong to the family of boosting methods, where base estimators are built sequentially in order to reduce the bias of the combined estimator, as opposed to the family of averaging methods, such as Random Forests, where several estimators are built independently and their predictions are later averaged.

XGBoost generates high accuracy and fast processing time while being computationally less costly and less complex with respect to other machine learning methods such as deep learning methods (Chen and Guestrin, 2016). As an added benefit, XGBoost is scarcely impacted by **multi-collinearity**. Decision trees are inherently robust to multi-collinearity (Kotsiantis, 2013). When deciding upon a split the decision tree randomly chooses only one of two highly correlated features, whereas other models such as logistic regression would use both the features. However, correlated features can have significant impacts in feature importance analysis of ensemble methods. In averaging methods, such as Random Forests (Breiman, 2001), the random choice of one of two correlated features is performed independently for each tree, potentially leading to an importance equally distributed among the two correlated features. Boosting methods, such as XGBoost, are reported to be less affected by multi-collinearity than averaging methods because the candidate splitting is not performed independently for each tree but sequentially (Chen and Guestrin, 2016). Indeed, gradient boosted decision trees use a sequence of estimators, where each decision tree learns from the previous tree and affects the next tree to improve the model and build a strong learner (Friedman, 2001). Therefore, even if two variables capture the same phenomenon in a system, both can be kept, and their collinearity can be detected by performing a significant feature analysis.

Another major advantage in using gradient boosted decision trees is their interpretability. Even though complex machine learning approaches such as deep learning can easily provide satisfying prediction accuracy, their application to real world regression problems is often limited by the scarce interpretability of their results. Lundberg, Nair, et al. (2018) proved the capability of gradient boosted decision trees, and more specifically of XGBoost to combine high-accuracy complex models with **interpretable explanations** for each prediction.

6.1.3.2 Hyper-parameters tuning

Overfitting frequently affects the performance of several machine learning non-linear algorithm like gradient boosting trees. Overfitting happens when a model starts to learn noises and random fluctuations and finally considers them as meaningful facts or concepts. In order to prevent overfitting, the hyper-parameters space has been explored by means of a ***k*-fold cross-validation**, that is, the training set is randomly divided into k subsamples, and k models are trained so that each time $k - 1$ subsamples are used to train a model and 1 subsample is used to test a model. Moreover, the cross-validation process allowed for hyper-parameters' tuning. Hyper-parameters are parameters that are not directly learnt within estimators but passed as arguments to the constructor of the estimator classes. Hyper-parameters which might cause overfitting includes: (i) the overall number of estimators or the number of gradient boosted trees that are fitted in the model, (ii) the maximum depth of each single tree, which represents the maximum number of splits, (iii) the learning rate, (iv) the parameters lambda and alpha, which are regularization terms on weights, and (v) the subsample, which represents the fraction of observations that are randomly selected as training instances prior to growing trees in every boosting iteration. Specifically, increasing both the number of estimators and the maximum depth will generate a complex model more likely to overfit. Similarly, higher learning rates tends to cause the model to overfit and an increment of both lambda and alpha parameters makes the model more conservative. At each step, the learning rate is used to shrink the weights and change the impact of each individual tree and make the model more robust (Chen and Guestrin, 2016). Subsampling the training instances might also effectively prevent overfitting.

An **early stopping** approach has been jointly adopted for monitoring training performance on the test set in order to prevent the model to overfit. Early stopping avoids overfitting by automatically interrupting the training procedure once the performance on the test dataset has not improved after a fixed number of training iterations. For the purpose of this study, the mean absolute error (MAE) has been optimised as performance measure to train the model.
In order to evaluate the proxy model **predictive capacity**, its predictions of the maximum rate of spread have been compared with the maximum rate of spread computed by means of the custom implementation of the Rothermel's model. The model's evaluation based on linear regressions has been performed according to Piñeiro et al. (2008) by plotting computed values on the y-axis and predicted values on the x-axis.

6.1.4 Model explanation

Interpretability is referred to the possibility of understanding how models based on gradient boosted trees uses input features to make predictions. Scarce attention is generally paid to **local explanations** which reveal the impact of input features on individual predictions and can be combined across an entire dataset to enhance traditional global representations of feature importance.
The SHapley Additive exPlanations (SHAP) framework (Lundberg, Erion, et al., 2018; Lundberg and Lee, 2017) has been employed in this study to explain the output of the implemented proxy model and to consistently interpret its predictions. The SHAP framework has been developed by Lundberg and Lee (2017) to assign an importance value or **SHAP value** to each prediction of each feature. Given a specific prediction, Lundberg and Lee (2017) computed the SHAP values by approximating the Shapley values that represents the contribution of each feature to the model output. Shapley values, initially proposed by Shapley (1953), are a concept from the game theory literature borrowed to explain the output of gradient boosting model and to provide a consistent individualised feature importance attribution method for individual trees that can be extended to tree ensembles. Shapely values have been shown to be the only way to assign feature importance while maintaining consistency, meaning that if a feature is more important in one model than another, no matter what other features are also present, then the importance attributed to that feature should also be higher (Lundberg, Nair, et al., 2018).
More recently, local explanations have been computed within the SHAP framework based on exact Shapley values rather than on their approximations (Lundberg et al., 2020). Hence, within the SHAP framework, Shapely values are computed as defined in Equation [6.1] by introducing each feature, one at a time, into a conditional expectation function $f_x(S)$ of the model's output and attributing the change produced at each step to the feature that was introduced; then averaging this process over all possible feature orderings (Lundberg et al., 2020):

$$f_x(S) = E[f(x)|do(X_S = x_S)] \qquad [6.1]$$

where S is the set of features, X is a random variable representing the model's input features, and x is the model's input vector for the current prediction. The do-notation formulation has been adopted following Janzing et al. (2020).

The application of Shapley values for explaining prediction models and individual predictions with feature contributions is not new (Štrumbelj and Kononenko, 2014), but SHAP is increasingly being used for varied applications (Lundberg et al., 2020; Lundberg, Nair, et al., 2018; Parsa et al., 2020). For the purpose of this study, SHAP values have been computed as a consistent measure of the importance of individual features, i.e. drivers of fire spread, in driving the model's predictions in terms of the maximum rate of spread, expressed as ft/min. By means of the SHAP framework, local explanations have been then combined in concise representations of the magnitude, prevalence, and direction of each feature's effect on the overall SHAP value. Moreover, the SHAP values of all features can be summed up to explain why a specific prediction is different from the **base value** or expected value, that is the average model output value over the training dataset. Hence, the SHAP values allow to decompose a prediction to show the contribution of each feature to push the model output towards higher or lower values.

6.2 Results

6.2.1 Implementation of the Rothermel's model

The implementation of the equations of the Rothermel's extended model as described in Chapter 4, Section 4.1.1 has resulted in a computer algorithm designed to perform **pixel-based evaluations** of the descriptors of fire behaviour: (i) maximum rate of spread relative to upslope, (ii) direction of the maximum rate of spread relative to upslope, (iii) flame length, and (iv) eccentricity. The custom implementation takes as inputs the drivers of fire spread defined in Chapter 5: (i) fuel bed properties and fuel particle properties, which can be summarised in a fuel model, (ii) canopy cover and crown ratio, (iii) live and dead moisture fractions, (iv) dip angle and direction, and (iv) horizontal wind speed and direction at 20 ft height. Horizontal wind speed and direction data are pre-processed according to Andrews (2012) as described in Chapter 5, Section 5.3, to obtain values of the horizontal wind speed and direction at a midflame height, as required by the Rothermel's model.

6.2.2 Proxy model for predicting the maximum rate of spread

The proxy model based on a XGBoost regressor has been trained on 60% of the records in the original synthetic dataset, whereas the remaining 40% have been used to test the model and to evaluate its predictive capacity on previously unseen records.

When the space of all possible solutions is too vast to be exhaustively explored, a search algorithm can only propose a local minimum instead of an absolute global minimum of the objective function. The local minimum detected by the 5-fold cross-validation identified a maximum depth of 5 nodes for each tree and a learning rate of 0.3. The complete set of hyper-parameters is reported in Table 6-2. The local minimum of the error function identified by means of the early stopping suggested that 931 estimators are sufficient to limit the mean absolute error on the test set while containing the overfitting, being the mean absolute error on the training and test set of 1.05 m/min (3.45 ft/min) and 1.21 m/min (3.97 ft/min) respectively, as shown in Figure 6-2. Figure 6-3 illustrates the regression equations of computed vs. predicted values of the maximum rate of spread for both the training and test sets. The coefficient of determination r^2, indicating a measure of the proportion of the variance in

computed values that is explained by the variance in predicted values, is reported for both the training and test sets. Both the training and test sets returned intercept values close to 0 whereas slope values did not differ significantly from 1. Moreover, the r^2 values approximate to 1 for both the training and test sets, 0.98 and 0.97 respectively, suggesting a good agreement between the maximum rate of spread relative to upslope computed by means of the custom implementation of the Rothermel's model and that predicted by the proxy model.

Table 6-2 Hyper-parameters tuned by means of a 5-fold cross-validation and an early stopping strategy.

Hyper-parameters	Tuned values
Early stopping rounds	10
Number of estimators	931
Maximum depth of a tree	5
Learning rate	0.3
Minimum sum of instance weight	1
Regularisation lambda	1
Regularisation alpha	0
Tree method	exact
Subsample	1

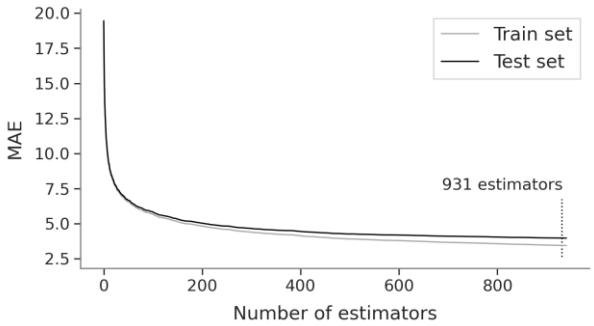

Figure 6-2 Mean absolute error (MAE) for the training set (grey line) and for the test set (black line) as a function of the number of estimators included in the XGBoost regressor. After 10 rounds with no improvements in the MAE on the test set, the model's training is stopped. The local minimum is identified at 931 estimators, with an error of 1.05 m/min (3.45 ft/min) for the training set and 1.21 m/min (3.97 ft/min) for the test set.

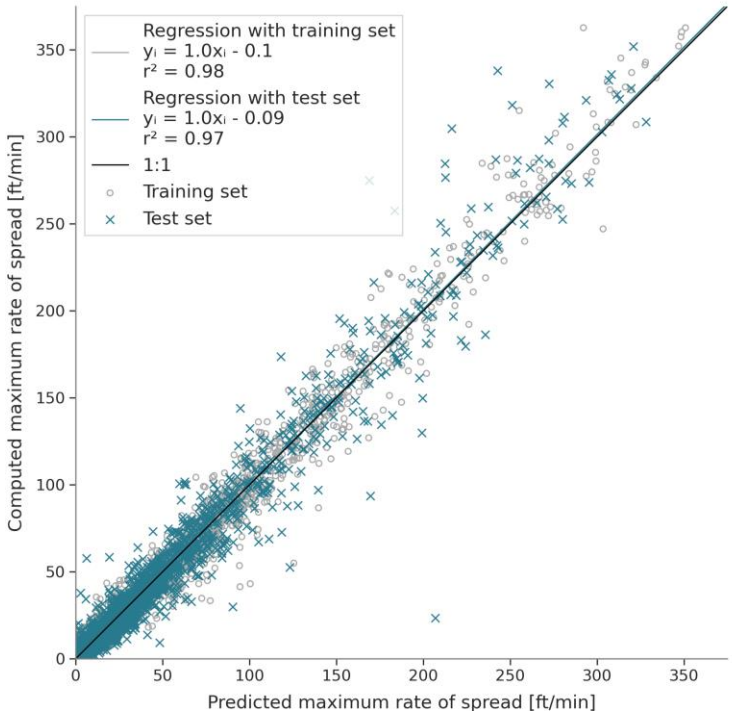

Figure 6-3 Computed vs. predicted values of maximum rate of spread. Computed and predicted values have been plotted on the y-axis and x-axis respectively, according to Piñeiro et al. (2008). Hence, the regression of computed vs. predicted values of maximum rate of spread are expected to have no bias from the $1:1$ line (black line) and the slope and intercept of the regression are expected to be equal to 1 and 0 respectively. In order to improve the readability of the figure, only small fractions (1%) of both the training and test sets have been represented in the scatter plot, whereas the regression equations and parameters have been computed from the complete training (grey) and test (petrol green) sets.

Figure 6-4 shows a single estimator, a decision tree, with a maximum depth of 5 nodes randomly sampled from those generated by the XGBoost regressor.

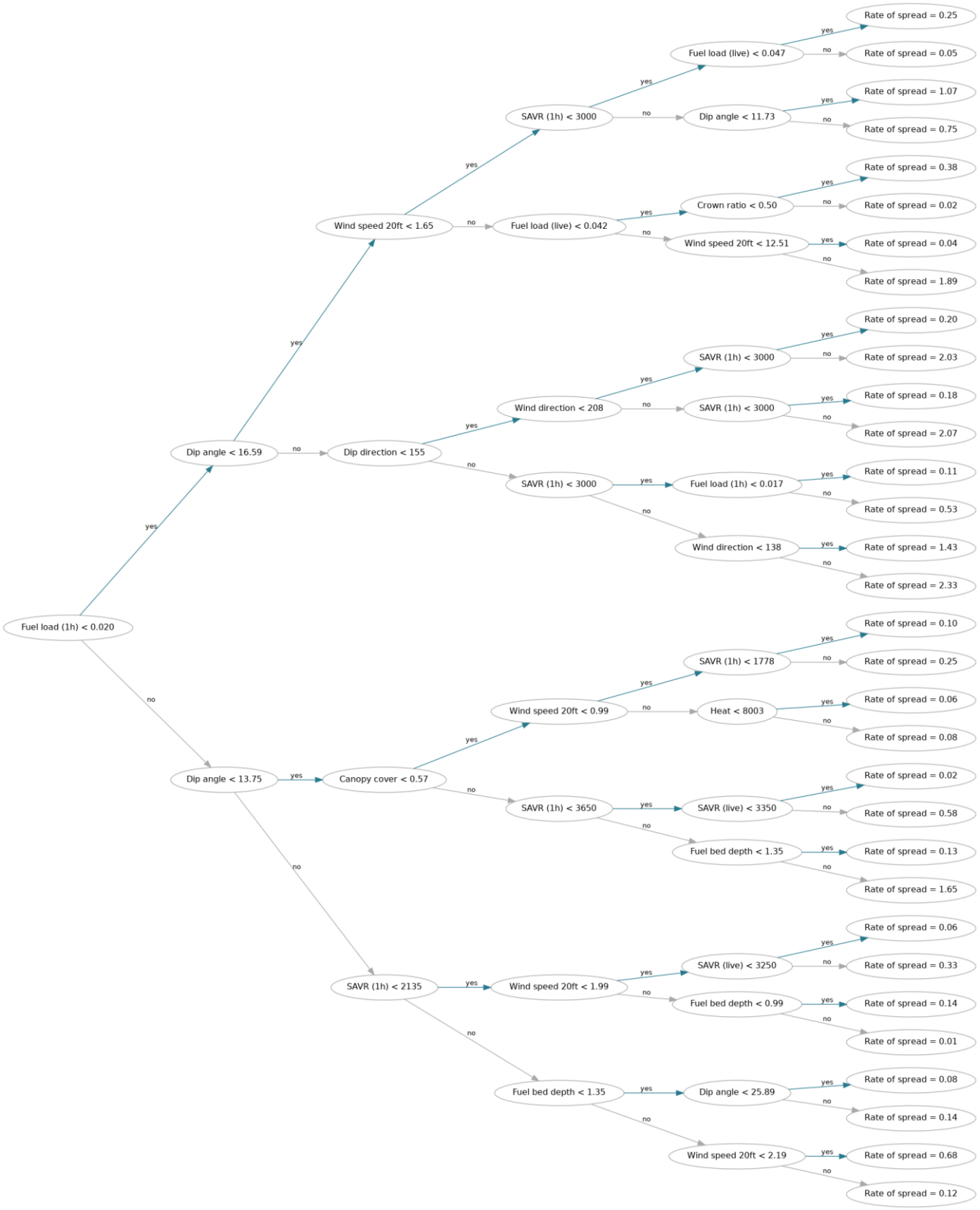

Figure 6-4 Decision tree randomly sampled from those generated by the XGBoost regressor. The root node (leftmost node) represents the feature that best splits the data, whereas each leaf node (rightmost node) evaluates the predicted value of the maximum rate of spread. Each internal node represents a single variable with a threshold value used to determine the model's output.

6.2.2.1 Feature importance analysis

While the Rothermel's model takes as input fuel bed properties and fuel particle properties as distinct features, they can be treated as a single entity and summarised by means of the concept of fuel model. Hence, two distinct feature importance analyses performed on the proxy model for the Rothermel's extended model are presented: the one by considering all fuel bed properties and fuel particle properties as independent features, the other by summarising their importance into a single feature representing the fuel model. Results of the feature importance analyses are presented in Figure 6-5, Figure 6-6, and Figure 6-7, where features are sorted according to their importance in determining the model's output. Their ordering suggests that the trained XGBoost regressor has been able to detect highly correlated features, such as dead moisture fractions at different time lags (1h, 10h, and 100h), assigning a high relative importance to only one of those correlated features, while the remaining are given a limited or null importance.

As detailed in Chapter 5, Section 5.1, fuel bed properties include the thickness of the fuel bed depth, the moisture of extinction of the dead fuel, and parameters specific for each live and dead size class, such as the oven-dry fuel load and the surface-area-to-volume ratio, whereas fuel particle properties include the fuel heat content, its oven-dry particle density, and its total and effective mineral content. The feature importance analysis performed by considering fuel bed properties and fuel particle properties as independent features shows horizontal wind speed at 20 ft height as the most important feature in determining the maximum rate of spread (Figure 6-5), with an average absolute impact on the model output of 4.45 m/min (14.6 ft/min). Similarly, fuel bed depth and dip angle exhibit an average impact of 3.99 m/min (13.1 ft/min) and 1.89 m/min (6.2 ft/min) respectively, whereas remaining features display an average impact lower than 1.65 m/min (5.4 ft/min). Figure 6-6 provides a concise representation of the magnitude, prevalence, and direction of a feature's effect on the overall model output by representing each feature's global importance as an ensemble of local explanations. This representation enables a better comprehension of the model's output by indicating which values of a single feature has the major impact on each single prediction. It emerges that higher values of horizontal wind speed at 20 ft height, fuel bed depth, dip angle, and surface-area-to-volume ratio (1h time lag) are predictive of higher values of maximum rate of spread. The distribution of individual predictions for these features reveal strong positive impacts of maximum rate of spread, adding up to 64.77 m/min (212.5 ft/min) and 80.71 m/min (264.8 ft/min), for wind speed and dip angle respectively, to the mean expected output value of 8.25 m/min (27.06 ft/min). Other features show long left and right tails indicating that even features with a low global importance can be extremely incisive for some individual predictions.

However, by adding up the local explanations for fuel bed properties and fuel particle properties in a summarised importance value of the fuel model, the feature importance analysis reveals that the fuel model has the highest average impact of 6.19 m/min (20.3 ft/min) on the maximum rate of spread (Figure 6-7). The importance values of horizontal wind speed at 20ft height and dip angle remain stable (at 4.45 m/min (14.6 ft/min) and 1.89 m/min (6.2 ft/min) respectively) and so the average impact of the remaining features. Local explanations of the effect of encoded fuel models on the model's output indicate a decreasing impact when passing from grasslands mixed with shrublands (lower values) to timberlands with grassy and shrubby understories (higher values).

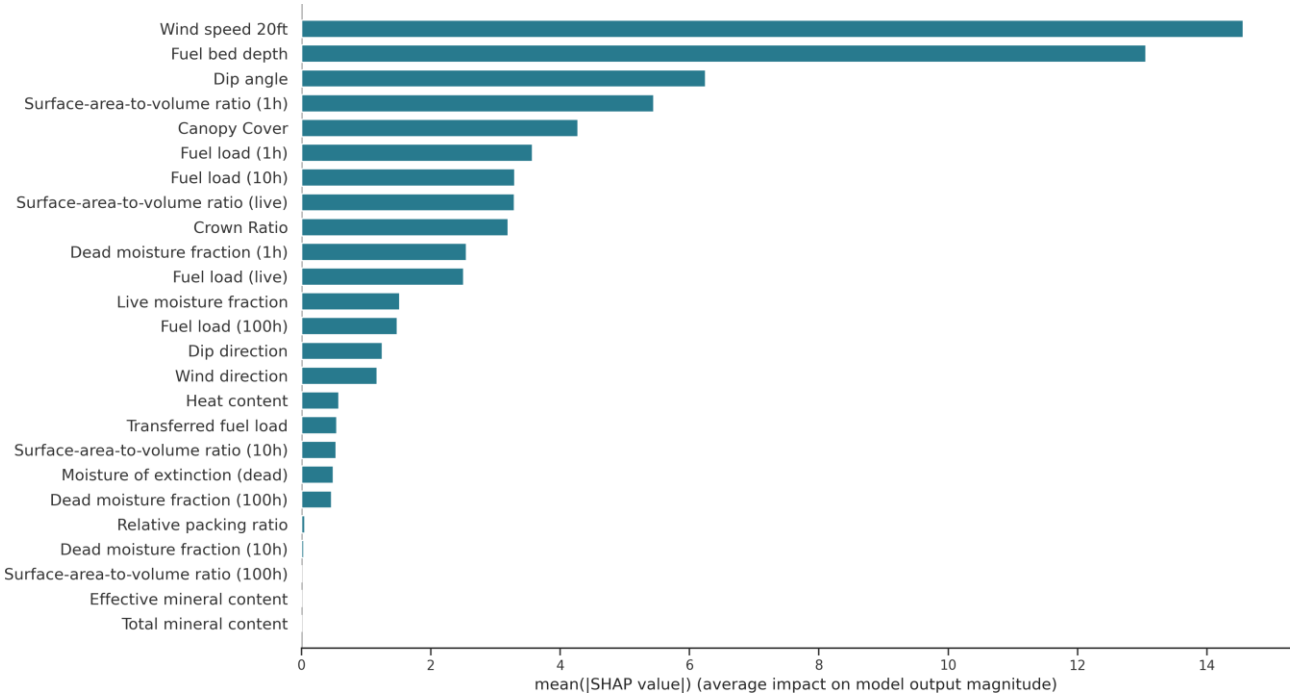

Figure 6-5 Global feature importance. Bar chart representing on the x-axis the impact of each feature on the model's predictions computed by averaging the absolute SHAP values of that feature across the dataset. Features are sorted on the y-axis according to their importance in determining the model's output.

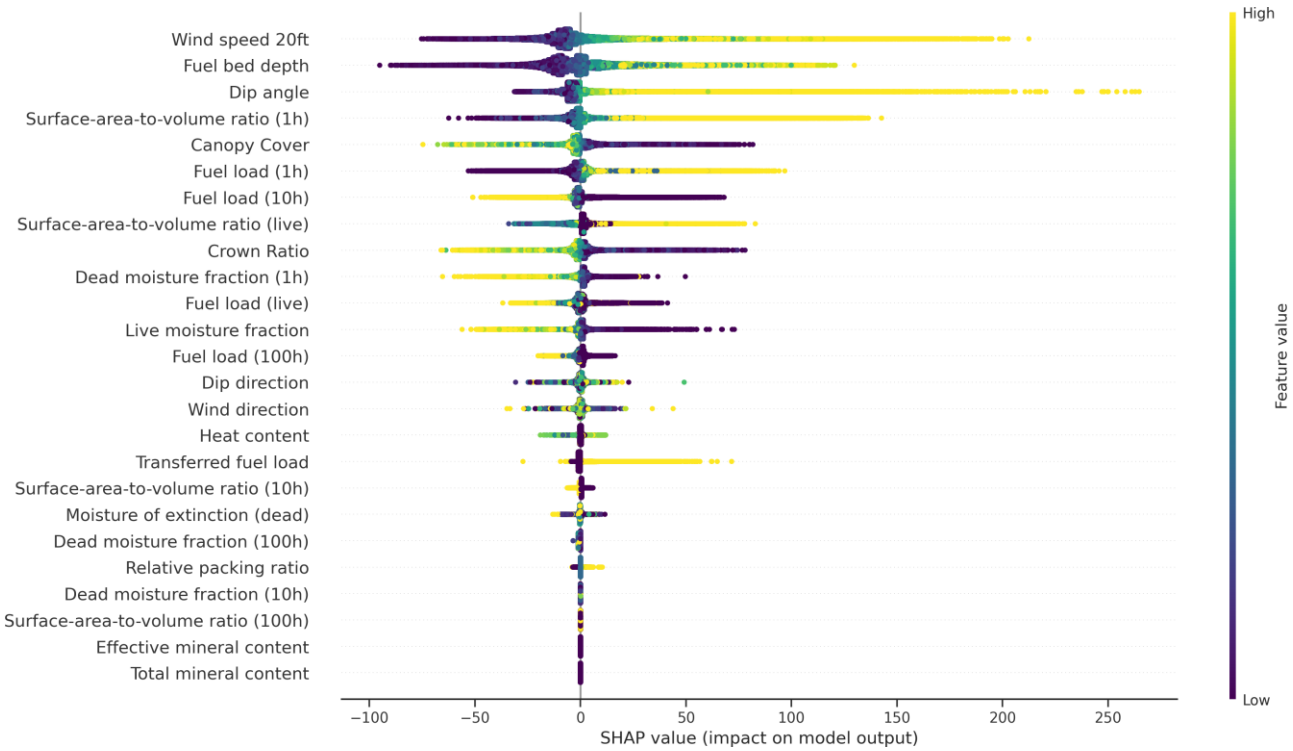

Figure 6-6 Local explanation summary plots. Each dot in each beeswarm plot corresponds to an individual prediction (row) from the synthetic dataset. The dot's position on the x-axis shows the SHAP value for that feature, that is its impact on the model's prediction for that record. When multiple dots land at the same x position, they are jittered in y-axis direction to show the density of the SHAP values per that feature. The colour represents the value of the feature from low to high. Features are sorted on the y-axis according to their importance in determining the model's output.

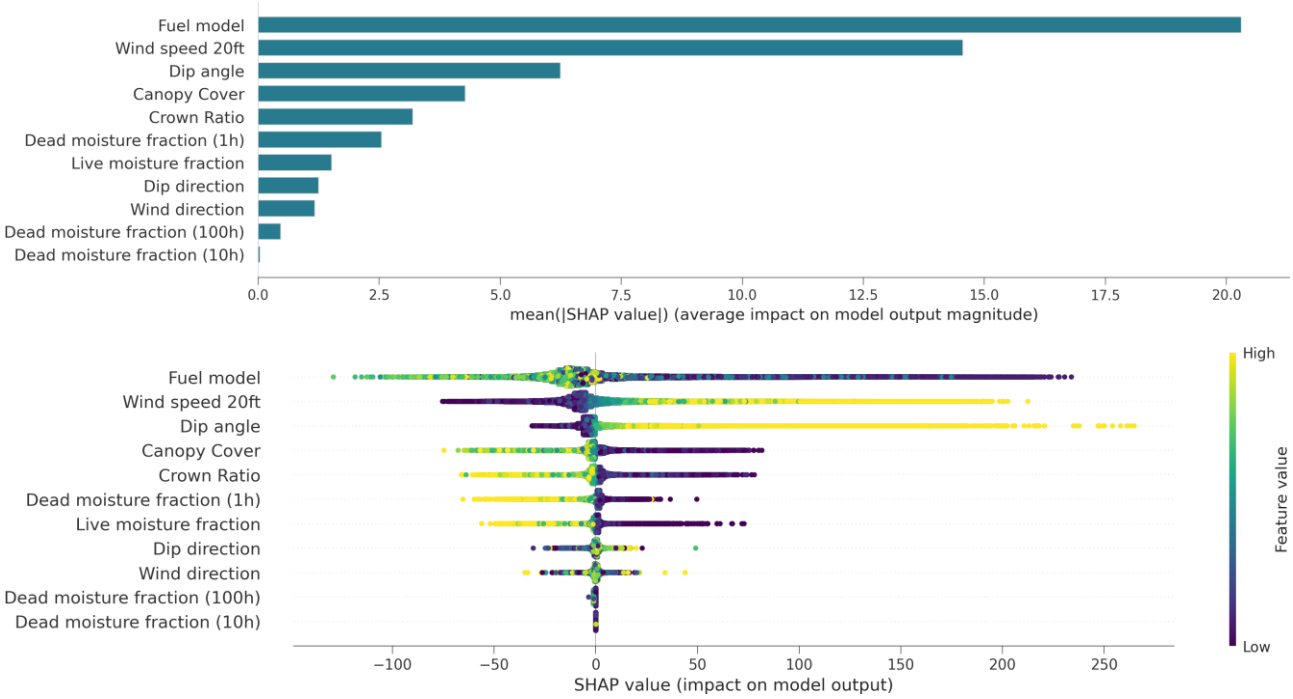

Figure 6-7 Global feature importance (upper) and local explanation summary plots (lower). The impact on the model output of the selected fuel model is computed by adding up the impacts of fuel bed properties and fuel particle properties. Feature values of the fuel model indicate encoded values referring to (from lower to higher values): nearly pure grasslands; grasslands with shrubs; shrublands; timberlands with litter; timberlands with grassy or shrubby understories.

6.2.2.2 Explained model's predictions

The decision plots shown in Figure 6-8 and Figure 6-9 illustrate how the proxy model arrives at individual predictions starting from a base value of 8.25 m/min (27.06 ft/min) and successively adding positive or negative effects of different features until the model's output value for each individual prediction is reached. An individual prediction has been randomly sampled from the synthetic dataset and taken as an example to explain the inner operating mode of the proxy model (Figure 6-8). The sampled prediction describes a surface fire spreading onto an almost flat topography covered by nearly pure grasslands, represented by the standard fuel model GRs3 (Rothermel, 1972), and sustained by a light horizontal wind (0.5 m/s). The decision plot indicates that live fuel moisture fraction as well as wind and dip directions have limited effects in determining the model's output value, whereas low values of dead fuel moisture fraction, canopy cover, and crown ratio slightly shifts the models' prediction toward higher values of maximum rate of spread. The strongest positive effect (+ 11.6 m/min or 38 ft/min) is provided by the selected fuel model, while the strongest negative effect (- 13.1 m/min or 43 ft/min) is offered by the weak wind speed, followed by the flat topography, leading to a model's output value of 7.11 m/min (23.33 ft/min). Typical prediction paths can be identified by cumulating multiple individual predictions. Figure 6-9 reports cumulative decision plots for different standard fuel models (Rothermel, 1972) representing: nearly pure grasslands (GRs3), shrublands of Mediterranean type climate regions in North America (SHs4), and timberlands with understoreys (TLs10). Recurrent patterns emerge across the different cumulative decision plots: (i) fuel model and wind speed at 20 ft return the highest impacts on the overall model's predictions, whereas other input features show a lesser effect; (ii) wind speed has a little negative impact on many individual predictions and a strong positive impact on others. Each fuel model, instead, generates a peculiar pattern of positive (GRs3 and SHs4) or negative (TLs10) effects on the model's output value.

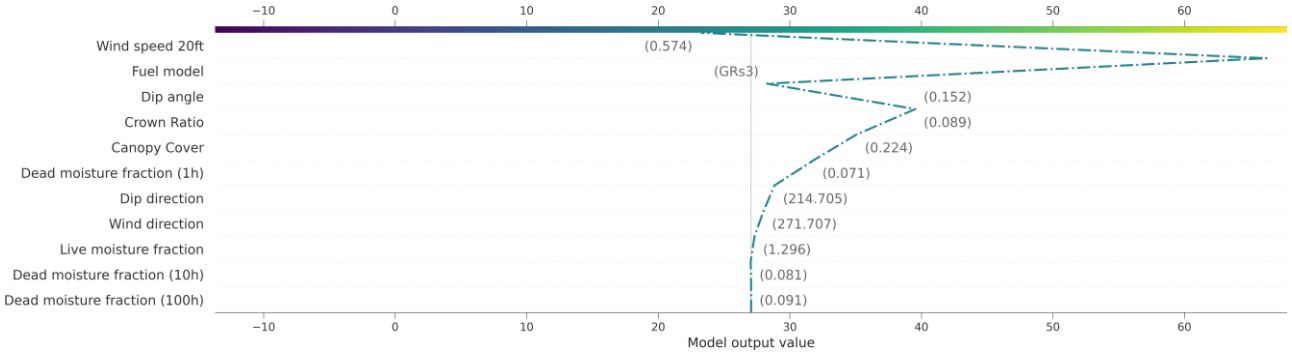

Figure 6-8 Decision plot for a single model's prediction for the standard fuel model GRs3 (Rothermel, 1972), representing tall grasslands with a fuel bed depth of 0.76 m or 2.5 ft. Starting at the lower limit of the plot, the prediction line (green dash-dotted line) indicates how the SHAP values accumulate from the model's base value, 8.25 m/min or 27.06 ft/min (grey vertical line), to arrive at the model's final score at the top of the plot, 7.11 m/min or 23.22 ft/min for that specific prediction. True values of each feature are reported next to the prediction line for reference. Features are sorted according to their importance in determining the model's output for that specific prediction.

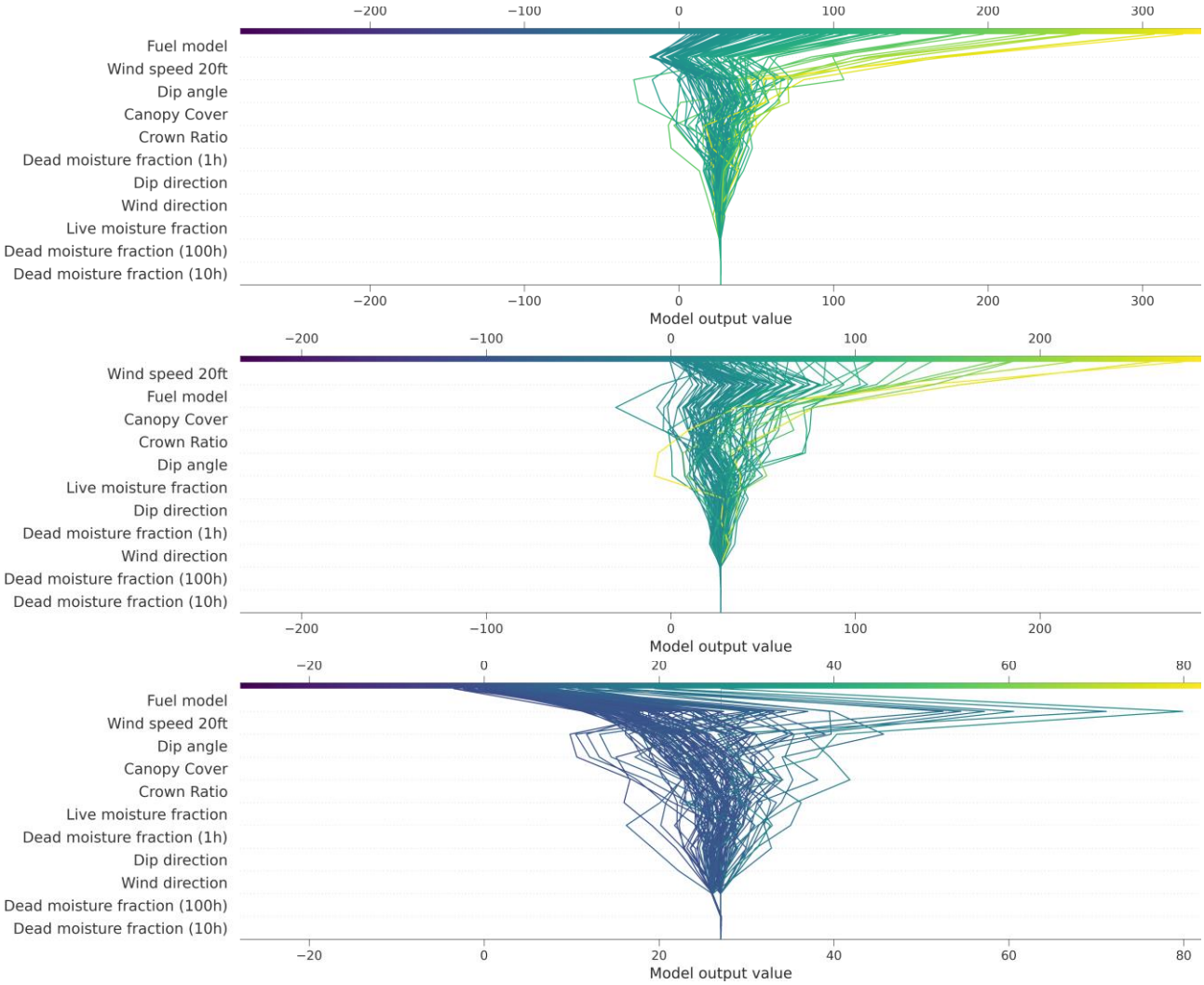

Figure 6-9 Cumulative decision plots for some of the standard fuel models (Rothermel, 1972): GRs3 (upper), SHs4 (centre), TLs10 (lower). Note that features are sorted differently amongst the different plots and according to their relative importance in determining the model's outputs. Prediction lines are coloured according to their correspondent model's output values (represented with different scales across the different plots).

6.2.2.3 Feature dependences

Local feature dependence reveals both global patterns and individual variability in the maximum rate of spread. Feature dependences have been investigated posing major attention to features with the highest importance in determining the model's output according to the feature importance analysis, i.e. fuel model, wind speed at 20 ft, and dip angle.

Figure 6-10 further investigates the impacts of different fuel models on the maximum rate of spread. Most of the fuel models describing timberlands (TU and TL) shows a negative impact on the maximum rate of spread, while fuel models representing grasslands and shrublands (GR, GS and SH) provide both negative and positive impacts on the model's output values, with the positive impacts being more significant than the negative ones. It becomes evident that fuel models describing grasslands and shrublands typical of the European Mediterranean regions (Dimitrakopoulos, 2002; Duce et al., 2012; Elia et al., 2015; Godinho-Ferreira et al., 2005; Rodríguez y Silva and Molina-Martínez, 2012) show an overall major impact on the maximum rate of spread with respect to those developed for North America (Albini, 1976b; Rothermel, 1972; Scott and Burgan, 2005), which generally show negative impacts on the model's output values. The interaction effect between fuel models and wind speed is confirmed by the large dispersion in the impacts of diverse fuel models on the maximum rate of spread, which is partially driven by differences in values of wind speed at 20 ft height. The vertical dispersion of the effects of fuel models with extremely high positive impacts, such as GRp6 or SHm9 (Rodríguez y Silva and Molina-Martínez, 2012) seems to be not fully explained by the variability in wind speeds. Contrarily, the vertical dispersion of fuel models with lesser impacts seems to be mostly explained by variation in wind speeds, so that, the lower the wind speed, the more the impacts, both positive or negative, of fuel models on the maximum rate of spread get close to 0. The greater the wind speed, the more significant is the impact, both positive or negative, of the fuel model on the maximum rate of spread: for fuel models with positive impacts on the maximum rate of spread, the occurrence of higher values of wind speed raises the expected model's output value, whereas for fuel models with negative impacts on the model's output value, the occurrence of higher values of wind speed reduces the predicted maximum rate of spread. Figure 6-11 illustrates the effects of the horizontal wind speed at 20 ft above ground and of the dip angle on the model's predictions, while also highlighting the presence of interaction effects between these features and the fuel model. The functions describing the relation between both wind speed or dip angle and their relative impacts on the maximum rate of spread are monotonically non-decreasing. Wind speeds of 3 m/s and dip angles of 16 degrees represent the thresholds between negative and positive impacts on the model's output, but these thresholds are strictly dependent on the initial distribution of the input features. The vertical dispersion in the impacts on the maximum rate of spread of both wind speed and dip angle, which is higher for higher values of both wind speed and dip angle, appears to be mostly explained by differences in fuel models. More specifically, wind speeds have less significant impacts on the maximum rate of spread when fuels, such as timber litter, are involved in the fire spread rather than shrubs and grasses. Similarly, reduced dip angles have limited impacts on the maximum rate of spread in the presence of fuels with little effects on the model's output values, such as those referring to timber litter understories. However, the vertical dispersion in the impacts on the maximum rate of spread of both wind speed and dip angle seems to be better explained by fuel bed depth (Figure 6-12 upper left and upper right).

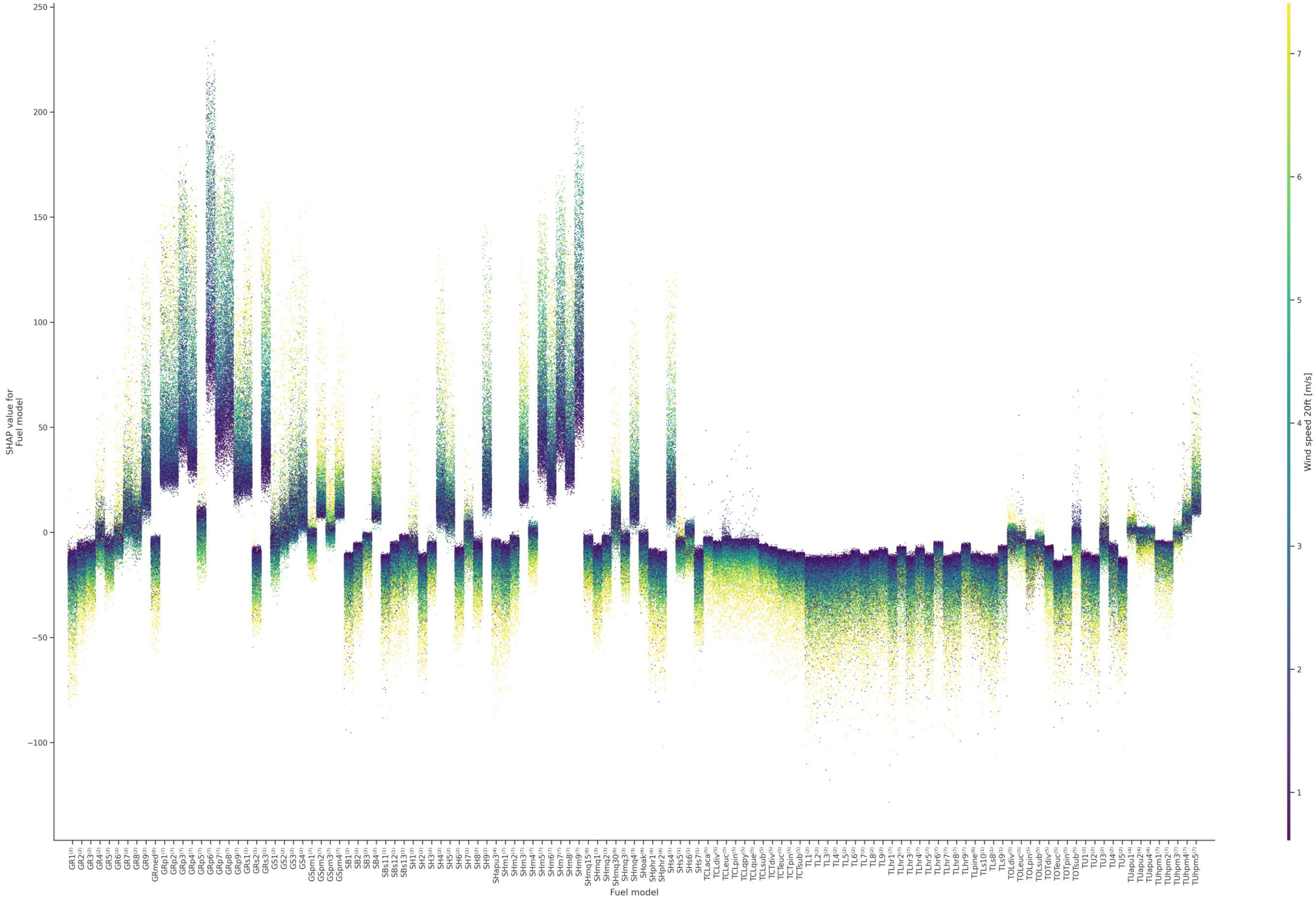

Figure 6-10 Local feature dependence illustrating the effects that different fuel models have on the model's predictions, expressed in terms of maximum rate of spread. Each dot corresponds to an individual prediction, i.e. a single row from the synthetic dataset. The y-axis indicates the encoded values for each fuel model, whereas the x-axis represents the SHAP value of the fuel model, i.e. the entity of the variation in the model's output induced by a specific fuel model. The colour bar refers to a second feature, i.e. the wind speed at 20 ft [m/s]. Superscripts beside the fuel model's code refer to (1) Rothermel, 1972, (2) Scott and Burgan, 2005, (3) Duce et al., 2012, (4) Elia et al., 2015; (5) Godinho-Ferreira et al., 2005, (6) Dimitrakopoulos, 2002, (7) Rodríguez y Silva and Molina-Martínez, 2012.

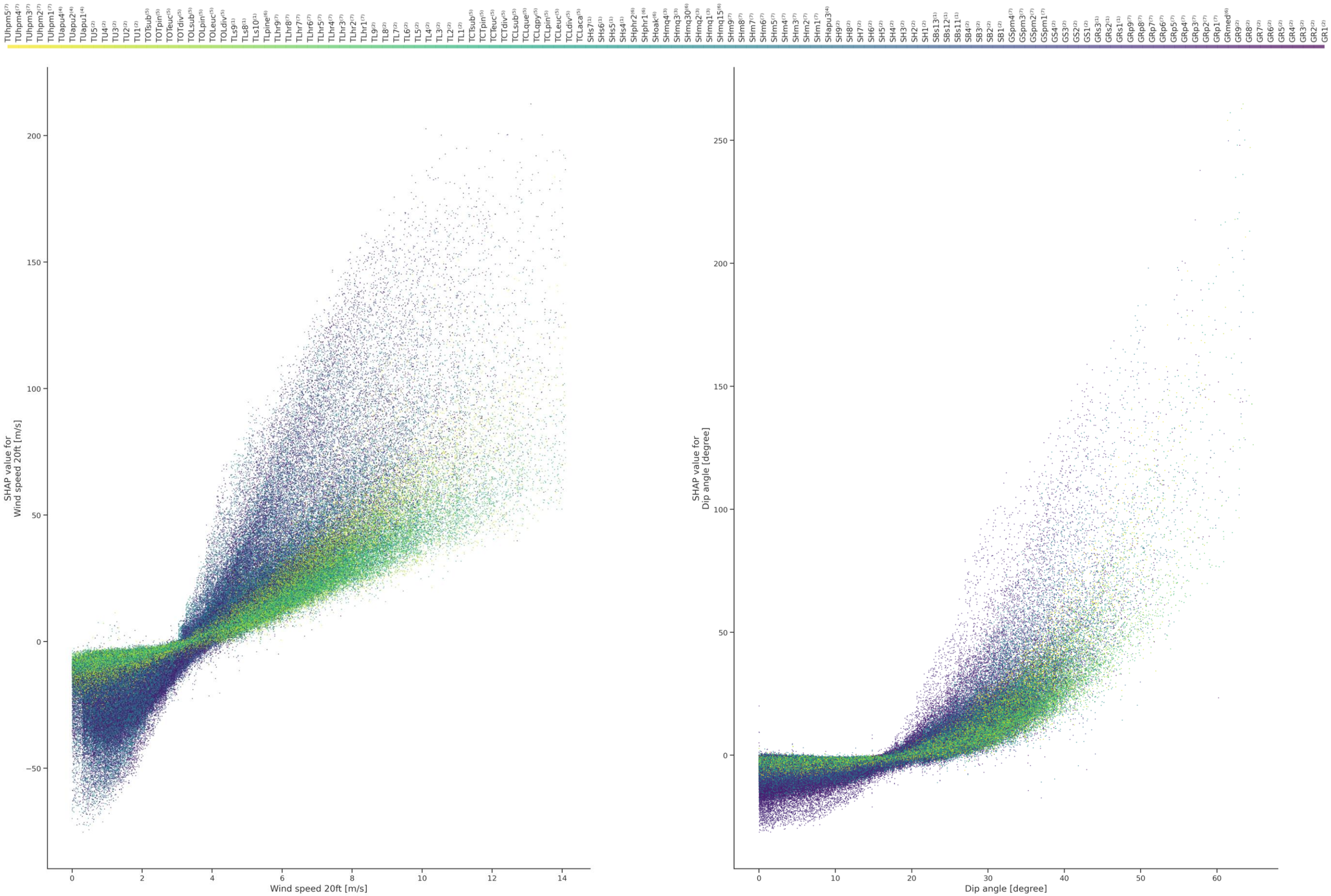

Figure 6-11 Local feature dependence illustrating the effects the wind speed at 20 ft (upper) and the dip angle (lower) have on the model's predictions, expressed in terms of maximum rate of spread. Each dot corresponds to an individual prediction, i.e. a single row from the synthetic dataset. The x-axis indicates the value for the wind speed at 20 ft or for the dip angle, whereas the y-axis represents their relative SHAP value, i.e. the entity of the variation in the model's output induced by a specific value of wind speed or dip angle. The colour bar refers to a third feature, i.e. the encoded values for fuel models. Superscripts beside the fuel model's code refer to [(1)] Rothermel, 1972, [(2)] Scott and Burgan, 2005, [(3)] Duce et al., 2012, [(4)] Elia et al., 2015; [(5)] Godinho-Ferreira et al., 2005, [(6)] Dimitrakopoulos, 2002, [(7)] Rodríguez y Silva and Molina-Martínez, 2012.

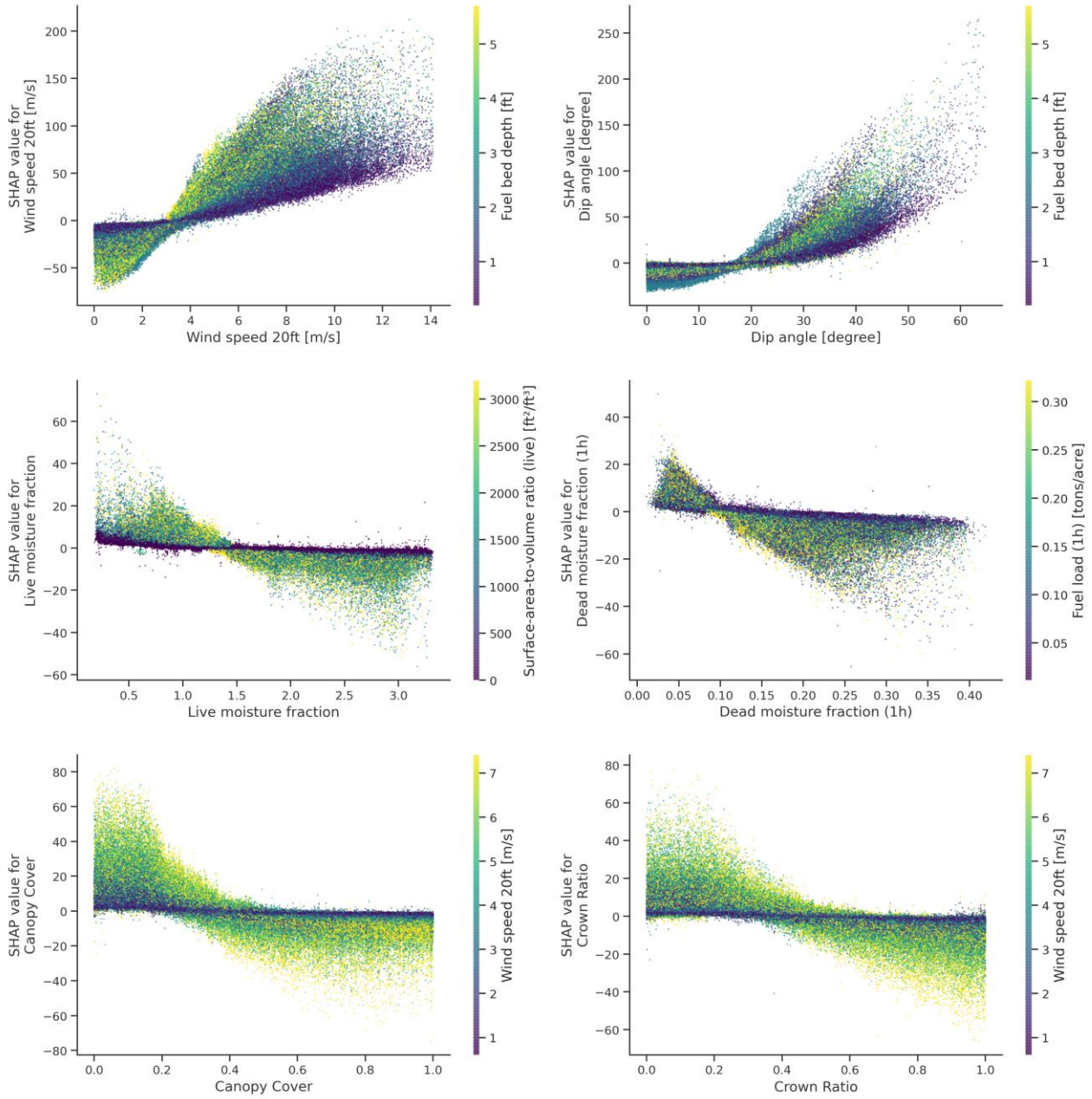

Figure 6-12 Local feature dependences illustrating the impacts of single features on the model's output value. Each dot in each scatter plot corresponds to an individual prediction, i.e. a single row from the synthetic dataset. The value of the feature is reported on the x-axis, whereas the y-axis represents the SHAP value of that feature, i.e. the entity of the variation in the model's output induced by a specific feature's value. The colour bar refers to a second feature from the dataset showing the most significant interaction effect with the analysed feature.

Figure 6-12 also illustrates partial interaction effects between fuel moisture fractions and fuel bed and particle properties, which together constitute and describe the fuel model. The impacts of live fuel moisture fraction on the maximum rate of spread are positive for live fuel moisture values lower than 1.5 (Figure 6-12 centre left), while the impacts of dead fuel moisture fraction on the maximum rate of spread are positive only for dead fuel moisture values lower than 0.1 (Figure 6-12 centre right). The vertical dispersion of impacts values of live and dead fuel moisture fractions is partially explained by variations in surface-area-to-volume ratio (live class) and fuel load (1h time lag) respectively. Finally, relations between both canopy cover (Figure 6-12 lower left) and crown ratio (Figure 6-12

lower right) and their relative impacts on the model's output values describe monotonically decreasing functions. The vertical dispersion is mostly explained by variations in wind speed values and the interaction effects might reflect the softening effect of the overstory layer of the forest canopy on the horizontal wind speed. Accordingly, positive impacts on the model's output are produced by reduced values of both canopy cover and crown ratio indicating vegetation dominated by grass and shrubs with sparse trees, whereas negative impacts originate from more dense forest canopies with minor crown ratios.

6.2.3 Proxy model for predicting other fire descriptors

The implementation of the proxy models for predicting the direction of the maximum rate of spread and the eccentricity of the ellipse follows the same procedure defined for the implementation of the proxy model for predicting the maximum rate of spread relative to upslope. Two different XGBoost regressors have been trained on 60% of the records in the original synthetic dataset, whereas the remaining 40% have been used to test the model and to evaluate its predictive capacity on previously unseen records. Both the models required a significatively lower number of estimators to limit the mean absolute error on the test set while containing the overfitting: 446 estimators for the eccentricity and 236 estimators for the direction of the maximum rate of spread. The r^2 values approximate to 1 for both the models and for both training and test sets, with better results for the model estimating eccentricity with respect to that for the direction of the maximum rate of spread. Results suggest a good agreement between the values computed by means of the custom implementation of the Rothermel's model and that predicted by the proxy models (Figure 6-13).

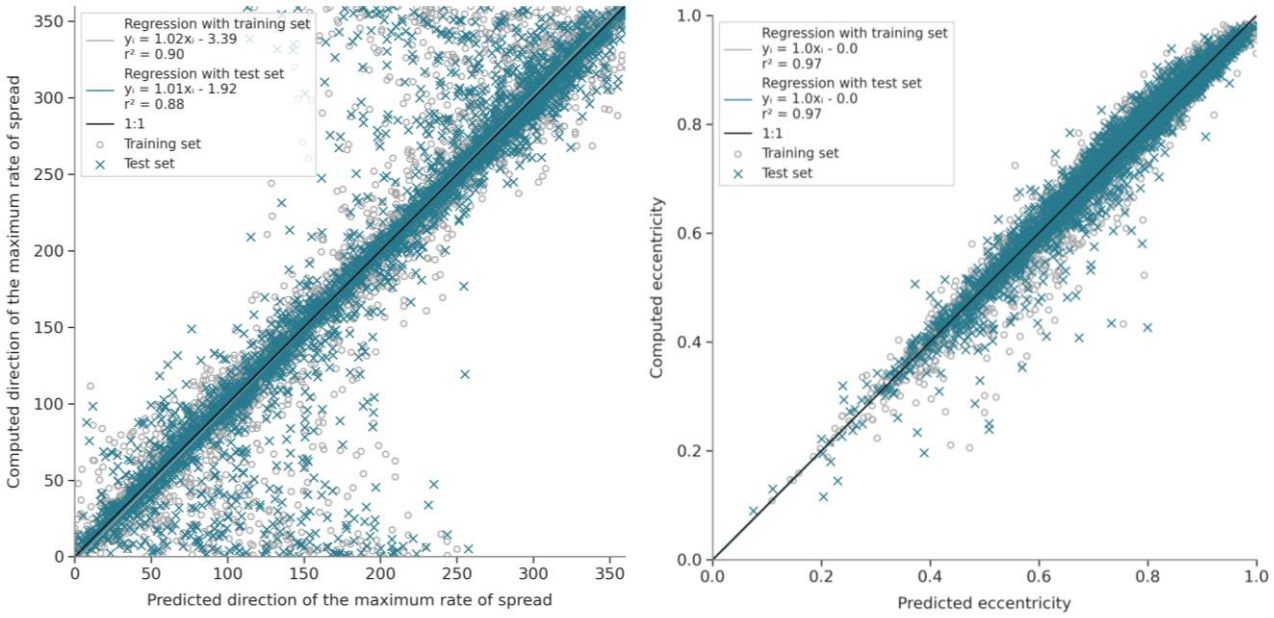

Figure 6-13 Computed vs. predicted values of direction of the maximum rate of spread (left) and eccentricity (right). The regression of computed vs. predicted values of maximum rate of spread are expected to have no bias from the $1:1$ line (black line) and the slope and intercept of the regression are expected to be equal to 1 and 0 respectively. In order to improve the readability of the figure, only small fractions (1%) of both the training and test sets have been represented in the scatter plot, whereas the regression equations and parameters have been computed from the complete training (grey) and test (petrol green) sets.

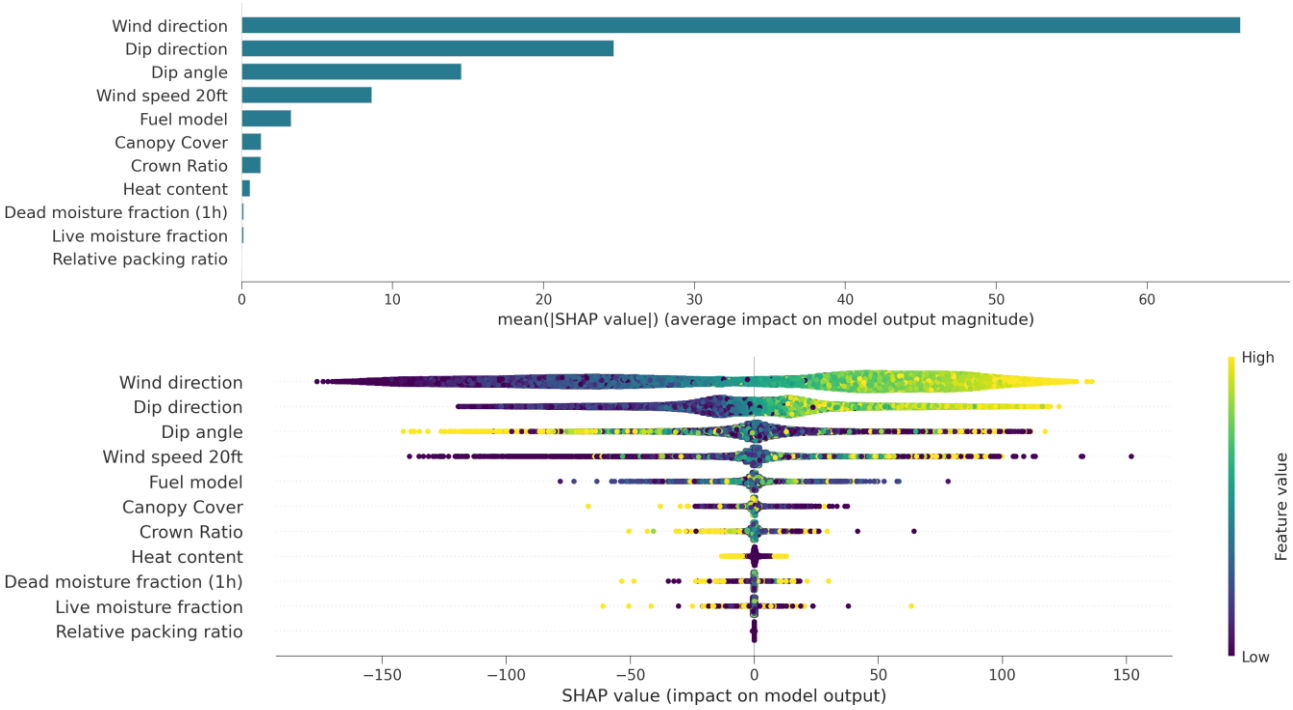

Figure 6-14 Global feature importance (upper) and local explanation summary plots (lower) evaluating the impact of the model's input features on the model's output, i.e. the direction of the maximum rate of spread.

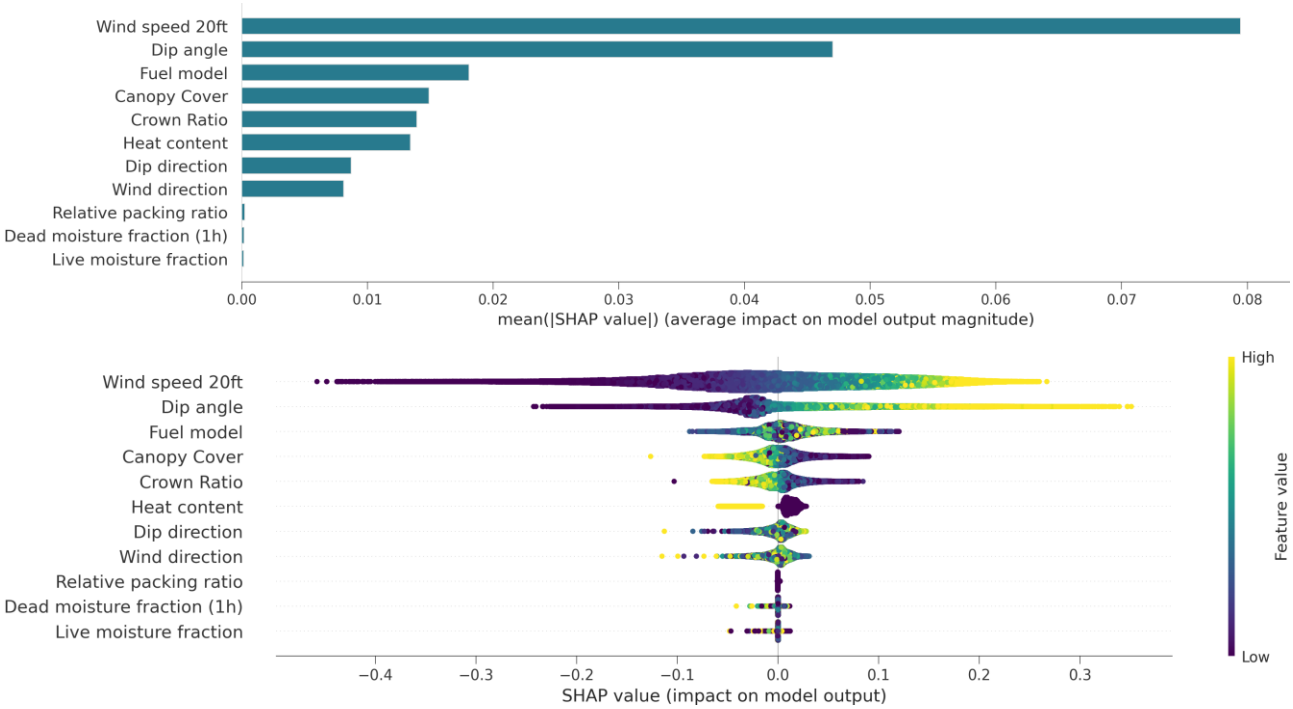

Figure 6-15 Global feature importance (upper) and local explanation summary plots (lower) evaluating the impact of the model's input features on the model's output, i.e. the eccentricity.

6.2.3.1 Feature importance analysis

The feature importance analyses performed by considering fuel bed properties and fuel particle properties as a single input feature, suggested that horizontal wind at 20 ft height and geomorphometrical characteristics are the most important feature in determining the direction of the maximum rate of spread and the eccentricity. Figure 6-14 shows horizontal wind direction has a more than twice average absolute impact on the direction of maximum rate of spread with respect to the dip direction. Other features show a relatively low global feature importance, but long left and right tails indicate that they are indeed extremely incisive for some individual predictions. Figure 6-15 indicates horizontal wind speed and dip angle as the most incisive features in determining the eccentricity of the ellipse that describes the fire perimeter and, specifically, higher values of both horizontal wind speed and dip angle have a positive impact on the model's output. Left and right tails are less pronounced with respect to those observed for the estimation of the direction of the maximum rate of spread.

6.2.4 Computing time

To allow a direct comparison, the same drivers of fire spread have been chosen as input data for both the implementation of the Rothermel's model and the developed proxy model based on gradient boosted trees. Both the models also include implicit or explicit procedures for the horizontal wind data adjustment. By comparing the computing time required to execute both the custom implementation of the Rothermel's model and the proxy model, it emerges that in both cases the processing time increases linearly with the number of samples, which is a function of the total surface of the study area, the temporal extent of the event, and the desired output resolution. However, the growth of the computing time is sharper for the implementation of the Rothermel's model with respect to the proxy model. Figure 6-16 shows that for 100,000 samples, the computing time of the proxy model is 10% of that required to run the Rothermel's implementation.

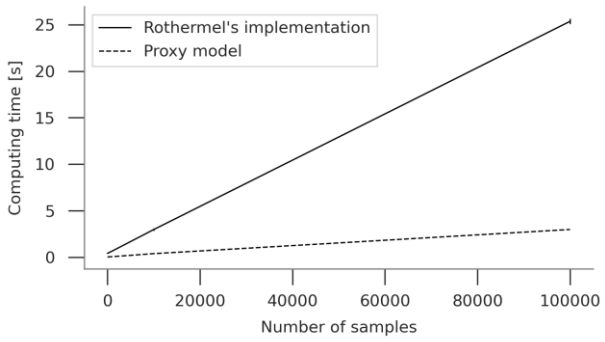

Figure 6-16 Comparison of the computing time required to run the implementation of the Rothermel's model (black line) and the proxy model (dashed black line).

6.3 Discussion

Two different tools have been presented within the context of this Chapter: a custom implementation of the extended Rothermel's model for Python and its proxy model based on gradient boosted trees. The custom implementation of the extended Rothermel's model poses itself as a useful tool to further investigate on the Rothermel's equations and to continue improving the scientific understanding of the dynamics regulating wildland surface fire behaviour.

The proxy model comprehensively integrates easily accessible input data to predict the maximum rate of surface fire spread in wildland fuels. Achieved results show that the proxy model based on gradient boosted trees operates analogously to the Rothermel's model as described by Andrews (2018) and including the adjustment of the horizontal wind at 20 ft at midflame height which accounts for the effect of the forest canopy cover according to Andrews (2012). This suggests that the proxy model could effectively replace the Rothermel's implementation as an operational tool for decision support system in wildland surface fire management. The proxy model combines high-accuracy complex models based on ensemble machine learning methods with interpretable explanation. This combination of accuracy and interpretability provides fire managers with near real-time reliable predictions while also suppling insight into the operating mode of the model.

The explanations of the proxy model provided by SHAP offered the opportunity to perform an in-depth exploration of the relations existing among the drivers of fire spread, i.e. the inputs of the model, with the aim of understanding their relative importance in determining the descriptors of fire spread and growth, i.e. the outputs of the model.

The **horizontal wind speed** at 20 ft height has been identified as the feature with the most significant impacts on the maximum rate of spread when considering fuel bed properties and fuel particle properties as independent features. This relevance may be higher with respect to that expected for the original implementation of the Rothermel's model and this might be partially due to the integration of the adjustments factor accounting for the interactions with fuel bed characteristics and heat transfer mechanisms, which together have allowed to reproduce the complex effect of the horizontal wind speed on the rate of spread of the flame front. However, the data of the horizontal wind speed provided as input to the proxy model does not account for wind gusts which might further increase the importance of the wind speed in determining the maximum rate of spread. The availability of accurate near real-time information on the spatiotemporal variability of weather conditions and more specifically of the horizontal wind speed assume a primary significance for reliable estimation of the maximum rate of spread.

The feature importance analyses highlighted the relevance of the **fuel model** in determining the descriptors of fire spread and growth. More specifically, the thickness of the fuel bed depth, the surface-area-to-volume ratio and the oven-dry fuel load of the 1h dead size class have revealed the highest impacts on the model's output value with respect to the other fuel bed properties and fuel particle properties when considered as independent features. An overall tendency emerges for fuel models developed for the European Mediterranean regions to produce higher impacts on the maximum rate of spread with respect to those developed for North America by Scott and Burgan (2005). These diverse behaviours might be due to inherent discrepancies in sampling techniques or might reflect tangible differences amongst the various fuel types in terms of their physico-chemical properties. The

more fuel models are developed in literature, the more accurate might be the characterisation of the existing fuel types and the representation of their spatial variability across diverse ecosystems. On the other hand, the growing number of fuel models poses major challenges in the assignment of fuel models to existing patterns of vegetation. Hence, a clear understanding of the impacts of each single fuel model in terms of its effects on the maximum rate of spread, could serve as a guideline to identify those fuel models with similar behaviour and thus simplifying the process of fuel model assignment (Figure 6-10). That is to say that assigning an incorrect fuel model does not always have the same impact: fuel models describing timber understories show quite similar behaviours with limited impacts on the maximum rate of spread, whereas fuel models representing grasslands and shrublands, which are mostly unsheltered fuel types, show a greater variability but also a greater impact in terms of values of maximum rate of spread they are potentially able to sustain.

Presented outcomes strengthen the idea that accurate estimations of the horizontal wind fluxes as well as fuel types characterisation and mapping should assume a central role in wildland surface fire behaviour modelling when simulators based on the Rothermel's model are chosen. Results from this research agree with findings from other studies according to which both fuel models and wind flows are frequently addressed as major sources of errors and uncertainties in surface fire spread and growth simulation modelling (Arca et al., 2007; Ricotta and Di Vito, 2014; Salis et al., 2016). Furthermore, extreme weather conditions, the accumulation of heavy fuel loads and the lack of appropriate thinning fuel treatments are increasingly identified as prevailing factors in the upsurge of extreme wildfire events across Mediterranean type climate regions which can be distinguished in fuel-dominated and wind-dominated fires (Keeley and Syphard, 2019; Salis et al., 2018; San-Miguel-Ayánz et al., 2013). The proxy model trained for those purposes accurately reproduces the Rothermel's model with the advantage of providing truthful results in a lesser amount of time, thus making it more suitable for operational purposes. However, some input features that have been proven extremely relevant in determining the model output are difficult, if not impossible, to estimate in near real-time by means of field sampling. The growing availability of remotely sensed data and their increasingly higher spatiotemporal resolution might help in the extensive detection and continuous monitoring of some relevant fuel bed properties. Challenges in the procedure of fuel models' mapping from remotely sensed data mainly concern the estimation of fuel particle properties, such as the surface-area-to-volume ratio of the 1h dead size class which showed a significant relevance in determining the model's output values. Hence, future activities will be addressed to retrain the developed proxy model providing it solely with input features that could be directly and accurately retrieved from remotely sensed data. Preliminary tests showed r^2 values of 0.94 and 0.93 for the training and test sets respectively, suggesting a good agreement between the maximum rate of spread computed by means of the custom implementation of the Rothermel's model and that predicted by the proxy model while conserving the feature importance.

More interestingly, the availability of a consistent dataset of field observations of the maximum rate of spread together with associated information on input features, e.g. fuel bed properties and horizontal wind speed and direction at the time of ignition, would provide the opportunity to train a machine learning model untied from assumptions and constraints of the Rothermel's model and enriched by interpretable explanation.

Chapter 7

Agent-based model for simulating fire growth

The structure of an agent-based spatial simulation model for predicting patterns of fire growth and its performance under simplified test conditions will be described in the following Sections. The agent-based model incorporates the proxy model built on top the Rothermel's equations (Chapter 6, Section 6.1.3), which provides the input for a hybrid vector-raster propagation technique for fire perimeter expansion that controls for both spatial and temporal resolution of fire growth over the landscape. The model is intended for operational purposes so that its design and implementation are aimed at providing near real-time multi-temporal maps of fire growth capable of accurately and dynamically capture the intrinsic spatiotemporal variability of the drivers of fire spread. Fire growth simulations have been then performed under synthetic conditions to test for the conceptual validity of the developed model, whereas the model's validation on case studies from the real world will be presented in Chapter 9.

7.1 Agent-based models

Agent-based models (ABMs) are a class of computational models for simulating behaviours, actions, and interactions of autonomous individual or collective entities, with the aim of emulating the overall system behaviour and predicting the spatial patterns of complex phenomena (Clarke, 2014). ABMs share their origins with Cellular Automata (Wolfram, 2002) whereas one of the earliest ABMs in concept was the Schelling's segregation model (Schelling, 1971).

ABMs' concepts and theories are rooted in the complexity theory and aims to model and comprehend system-level patterns and properties emerging from interactions amongst individual agents. **Agents** are discrete and autonomous entities capable of processing information and interacting with the environment or with other agents to make independent decisions and even to learn and adapt to the surrounding conditions. Agents' interactions with other agents and with their surrounding environment are basically expressed by rules which are derived from theory or empirical data and provides the foundation of an agent's behaviour. Rules and relationships may be specified in a variety of ways, with agents being simply reactive, i.e. performing actions only then triggered by external stimulus such as other agents, or proactive, i.e. intrinsically oriented to the achievement of specific goals. The same set of rules can be applied to all agents or each agent or category of agents can have its own unique set of custom rules. The **environment** provides the spatial context in which agents operate and is typically represented by a grid of raster cells with specific attributes that change in space and time. Agents within an environment may be spatially explicit, meaning they have a precise location in geometrical space although the agent itself may be static, or spatially implicit, meaning that their location within the environment is irrelevant. Agents are also characterised by a specific location in

time which is conceptualised in **discrete time steps** regardless of whether the analysed phenomenon is continuous or discrete. Agents' actions can be scheduled to take place synchronously or asynchronously at each discrete time step, with a specific order or randomly.

7.2 Model development

7.2.1 Conceptualisation

An agent-based spatial simulation model has been developed with the specific purpose of predicting complex patterns of fire growth starting from the spatiotemporal variability in both intensity and direction of the maximum rate of spread. The agent-based approach has been chosen for the purpose of this research because of its flexibility, particularly in relation to the geospatial component, and its ability to design heterogeneous populations of agents. Whereas ABMs are typically used to capture emergent patterns by means of stochasticity, this study implements a deterministic approach, where the surface fire growth is regulated by the values of the fire descriptors estimated by means of the proxy model based on the Rothermel's equations and introduced in Chapter 6.
The designed ABM is grounded on a hybrid raster-vector implementation, where the space is discretised into a grid of hexagonal cells within which a vectorial simulation is executed to compute the fire growth.

7.2.1.1 Entities

Hexagonal grid cells represent the model's discrete spatial units within which the space is treated as continuous by the vectorial simulation. A hexagonal grid have been preferred over square grid because hexagons closely approximate the circular radiation pattern that is proper of the process of fire growth in hypothetical isotropic environmental conditions (Chapter 3). The advantage of a hexagonal mesh in simulating fire growth with ABM is the isotropy of the hexagonal neighbourhood: each pair of adjacent hexagonal grid cells shares an edge and all their centroids are equidistant. Each hexagonal cell stores multitemporal sets of dynamic variables whose characteristics have been extensively discussed in the previous Chapters. At any discrete time step each hexagonal grid cell is characterized by both time independent and dependent state variables. Time independent state variables include the location of the grid cell's centroid and an indicator of the presence of an outbreak in that grid cell. Time dependent variables are (i) the maximum rate of spread relative to upslope, (ii) the direction of the maximum rate of spread, and (iii) the eccentricity of the ellipse approximating the fire perimeter. The sequence of discrete time step allows the model to reproduce the intrinsic spatiotemporal variability of time dependent variables according to data availability.
Each hexagonal cell can accommodate a single agent which may assume any static spatially explicit position inside the hosting cell: the position of each agent remains unchanged throughout the model's time steps. **Agents** might represent both primary fire outbreaks as well as secondary sources of ignition which are identified over the course of the vectorial simulation. The agents' behaviour is conceptually inspired by the Huygens' wavelet principle, which states that each point on a fire perimeter can be considered a new source of ignition for the vectorial simulation. Starting from an ignition source, i.e. an agent, the fire spreads in any direction with a rate that is computed from the maximum rate of spread assuming the fire perimeter to be elliptically shaped.

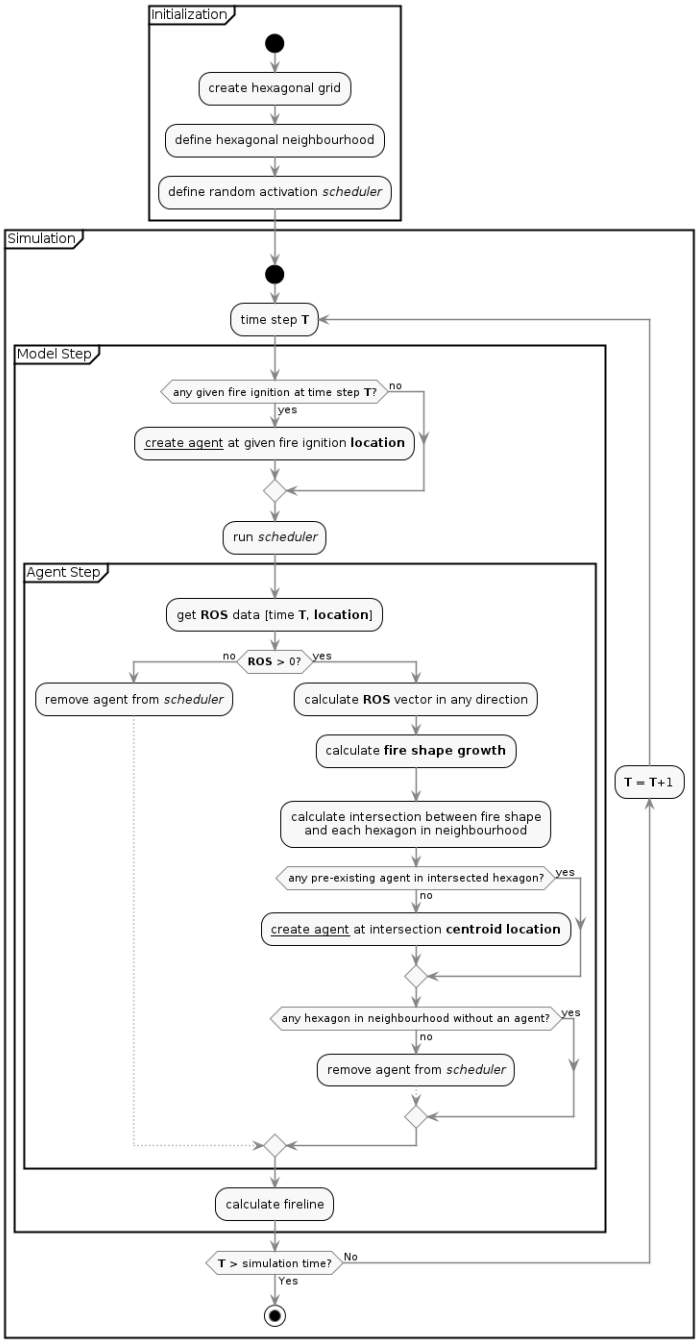

Figure 7-1 UML activity diagram to describe the logical flow of agents' behaviour and interactions with the hexagonal grid cells.

7.2.1.2 Spatial and temporal scales

The model includes explicit spatial and temporal dimension and is intended to be applied to multiple sites and scenarios that can vary in spatial and temporal scales and extent. The selection of spatial and temporal scales and extent also strictly depends on the available computational resources. However, to test the fire growth conformity to idealised patterns, simulations have been performed under simplified test conditions with synthetic spatial and temporal extents. The **spatial resolution**, which is the area of a single hexagonal grid cell, has been set to 1 ha, whereas the **temporal resolution**, which is conceptualised by discrete time steps, has been set to 1 minute.

7.2.1.3 Process overview

The fire growth process is modelled as a diffusion process between adjacent cells of the considered domain, where the status of each hexagonal cell at the time step t_n is defined by the status of the same cell at the time step t_{n-1} and the status of its six neighbouring cells at the time step t_{n-1}. The simulation starts at the time step t_0 with a single agent being instantiated in the centroid of the hexagonal cell for each given fire outbreak. It can be said the state of that cell is changed from **unburnt** to **burning**. Then a continuous vector process makes the fire starts propagating from the centroid of the burning cell towards its edges in any possible direction. The rate of spread in each direction and hence the elliptical shape of the fire growth within each burning cell are computed from the maximum rate of spread, the direction of the maximum rate of spread, and the eccentricity defined for that cell according to the Equation [4.38]. Once the vector process overreaches the edge of the burning cell, a new agent is instantiated in the centroid of the intersection between each neighbouring unburnt hexagonal cell and the elliptical shape of the fire growth. New vector simulations start from those agents and unburnt cells change their status to burning. A cell persists into the burning status until the vector simulation within it has reached all its edges; then, the agent is removed, and the state of the cell is turned into **exhaust**.

Depending on the time step length and on the maximum rate of spread, each cell might need one or more steps to complete the transition from unburnt, to burning, and then exhaust states, so that the vector simulation continue to spread over multiple time steps with different rates according to updated information on the maximum rate of spread, direction of the maximum rate of spread, and eccentricity.

7.2.1.4 Initialisation

The model's initialisation is intended to be generic since the model itself is designed to be applicable to multiple sites. The initialisation varies amongst diverse scenarios, which differ from each other in terms of location and characterisation of both hexagonal grid cells and agents.

The initialisation of the model at time t_0 starts with the definition of global conditions that are experienced by all the model's entities: (i) the time step length is set and (ii) constants describing the geometry of the hexagonal grid cells are initialised, defining the cells' side length and their orientation as well as their neighbourhood, which includes the six adjacent cells which surround each cell. Then, time- and site-specific information for the initial time step t_0 are imported: (i) the list of initial agents representing the real fire outbreaks is retrieved together with information on their timing and location and (iii) maps of maximum rate of spread, its direction, and eccentricity for the initial time step t_0. Finally, (i) the hexagonal grid cell is instantiated together with (ii) the agents and (iii) the scheduler, which handles the time component by defining when agents are called upon to act.

7.2.1.5 Scheduling

At each step of the model and all the agents are activated and take their own actions, changing their state variables and interacting with one another or the environment.

An overview of the whole initialisation and scheduling process is provided by the activity diagram in Figure 7-1, whereas Figure 7-2 provides a schematic representation of the vector simulation that occurs within a single hexagonal cell and how it propagates to its neighbouring cells over multiple time steps.

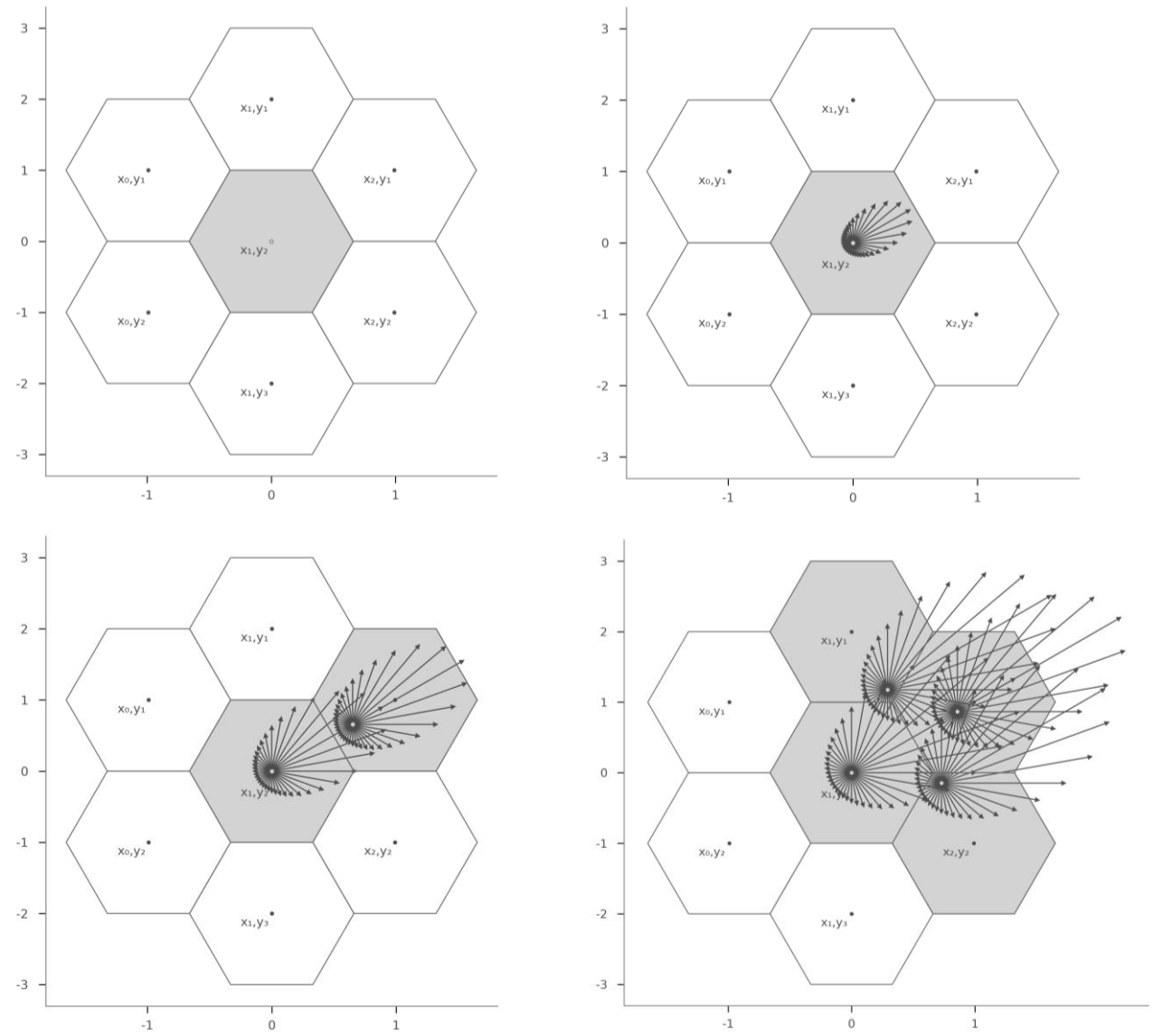

Figure 7-2 Agents behaviour from the model's time step t_0 to t_3. Unburnt hexagonal cells are represented in white, burning hexagonal cells, i.e. containing an active agent, are highlighted in grey, and cell's centroid are identified by black dots. Agents' location is pinpointed by light grey dots. At the time step t_0, the first agent is initialised in the centroid x_1, y_2 of the hexagonal cell containing the fire outbreak (upper left); at the end of the time step t_1, the vector simulation started from that agent has produced an elliptical shape (upper right); at the end of the time step t_2, a new agent has been instantiated with an offset from the centroid x_2, y_1 of the neighbouring cell whose edges have been overreached by the vector simulation (lower left); at the end of the time step t_3, two more agents have been instantiated starting new vector simulations (lower right). Simulation parameters: maximum rate of spread of 50 ft/min, direction of the maximum rate of spread of 60 degrees clockwise from north and eccentricity equal to 0.8.

At the beginning of each time step, the model (i) calculates the current epoch t_{n+1} to keep track of the simulation time, (ii) updates the list of agents and initialises new agents for any ignition point that exists before the current epoch t_{n+1}, (iii) updates the maps of maximum rate of spread, direction of the maximum rate of spread, and eccentricity for the current epoch, and (iii) executes the agent's process by activating all agents once per step in random order according to the scheduler. While each process is performed by agents in random order, state variables are updated synchronously, meaning that the new values are not stored until all agents have executed their process and then they are updated all at once.

During each time step, each agent (i) collects updated time dependent variables, i.e. maximum rate of spread, direction of the maximum rate of spread, and eccentricity, for the hexagonal cell in which it is accommodated, (ii) calculates vectors of the rate of spread in any radial direction from its own location inside the hexagonal cell if the maximum rate of spread is greater than 0, (iii) calculates the elliptical shape defined by the vectors of the rate of spread at the end of the current epoch t_{n+1}, (iv) calculates the intersection between the elliptical shape and each hexagonal cell in neighbourhood, (v) computes the offset location of each centroid's intersection with respect to the location of the hexagonal cell's centroid, (vi) instantiates a new agent in the offset location and add it to the scheduler if the cell does not contain any other agent, and, then, (vii) deactivates itself if all the cells in the neighbourhood have been ignited, i.e. contains an agent yet.
Finally, at the end of each time step the model computes the modelled fire growth at time t_{n+1}.

7.2.2 Formalisation

The Hex-utils tool-kit has been employed to handle the hexagonal meshes (de Sousa and Leitão, 2017). To the purpose of the present study, a flat-topped orientation for the hexagonal cells has been chosen and hexagonal grids are built by offsetting odd columns producing an odd-q vertical layout.
The conceptualised fire growth model has been implemented in a Python environment by means of the Mesa agent-based modelling framework (Masad and Kazil, 2015) and rendered with Matplotlib (Hunter, 2007) and Shapely (Gillies, 2013). The model is basically made up of two core classes: one for the overall model, the other for the agents. Both the model and agent classes are child classes of Mesa's generic Model and Agent classes. The model class holds the model-level attributes, manages the agents, and handles the global level of the model. Each instantiation of the model class constitutes a specific model run, whereas each model contains multiple agents, all of which are instantiations of the agent class.

7.2.3 Verification

To test the fire growth conformity to idealised patterns, simulations have been performed under simplified test conditions with synthetic spatial and temporal extents. Model verification is intended as the process of determining whether an implemented model corresponds to the target conceptual model (Wilensky and Rand, 2007). Model verification is equivalent to making sure that the implemented model is correct and executes properly. By contrast, the model validation is intended as the process of determining whether the implemented model corresponds to and explains some phenomenon in the real world.
To iteratively verify the model's outputs, raster maps of homogenous sets of combinations of drivers of fire spread, i.e. horizontal wind speed and direction, dip angle and direction, fuel models and fuel moisture fractions, have been provided as inputs to the developed proxy model (Chapter 6). Resulting raster maps of maximum rate of spread, direction of the maximum rate of spread, and eccentricity have been turned into hexagonal meshes to be provided as inputs to the developed ABM. Resulting simulations of fire growth in synthetic homogeneous environments have been arranged in multiple matrices. Each matrix aims at analysing the combined effects of couples of drivers of fire spread by representing their variations along the x and y axis while maintaining constant all the other variables.

7.3 Results

In this Section, fire growth simulations performed under synthetic homogenous conditions are presented. Spatial and temporal scales are kept constants across all the executed fire growth simulations. Each simulation is the result of one single run of the model for 60 discrete time steps, each one of a length of 1 minute.

Figure 7-3 and Figure 7-4 illustrate the joint effect on simulated fire growth produced by varying dip angles and varying horizontal wind speed at 20 ft height above ground, while all other drivers of fire spread remaining unchanged within each matrix. Dip angle and wind speed varies along x and y axis respectively producing similar effects on simulated fire growth. Specifically, fires propagating on topographies with increasing dip angles in the absence of wind generate patterns similar to that produced by fires propagating on flat topographies with increasing wind speeds. Sustained by winds blowing upslope, the fire front spreads upslope with maximum rates in conditions of higher wind speeds (15 m/s) and higher dip angles (60 degrees). Figure 7-3 and Figure 7-4 only differ from each other for the fuel model: SHs4 and GRs2 respectively (Rothermel, 1972), which are representative of Mediterranean shrublands and tall grasslands. Differences in terms of patterns of fire growth are emphasised for both higher wind speeds and higher dip angles.

Figure 7-5 and Figure 7-6 represent the joint effect on simulated fire growth produced by varying wind direction and increasing dip angles; all other drivers of fire spread remain unchanged within each matrix, while the two matrices only differ from each other only for the wind speed, which is equal to 3 m/s and 10 m/s respectively. Figure 7-5 shows that at relatively low wind speeds (3 m/s) and low dip angles (less than 30 degrees), the wind direction determines the direction of maximum rate of spread of the fire front, with the borderline case of a dip angle of 30 degrees with wind blowing downslope impeding the fire to spread in any direction. However, higher dip angles generate higher rates of spread and causes the dip direction (240 degrees clockwise from north) to become dominant on the wind direction in determining the direction of the maximum rate of spread. For example, with a dip angle of 60 degrees and a wind blowing exactly downslope (240 degrees clockwise from north), the fire front continues to spread upslope with rates similar to that of simulations with wind blowing upslope (60 degrees clockwise from north). Different patterns emerge from Figure 7-6, where relatively high wind speeds (10 m/s) makes the wind direction always dominant on the dip direction, even at high dip angles (60 degree). Here, a wind blowing exactly downslope (240 degrees clockwise from north) causes the fire front to spread more rapidly downslope rather than upslope, but with a rate of spread significantly reduced.

Figure 7-7 and Figure 7-8 show the joint effect on simulated fire growth produced by varying wind directions and dip directions; all other drivers of fire spread remain unchanged within each matrix, while the two matrices differ from each other only for the dip angle, which is equal to 15 and 60 degrees respectively. Figure 7-7 sharply underlines that, with low dip angles (15 degrees), wind direction plays a dominant role in determining the direction of the maximum rate of spread with respect to the dip direction. Higher dip angles (60 degrees) alter this pattern so that the dip direction assumes a growing influence on the direction of the maximum rate of spread, but without overcoming the dominant effect of the wind direction (Figure 7-8).

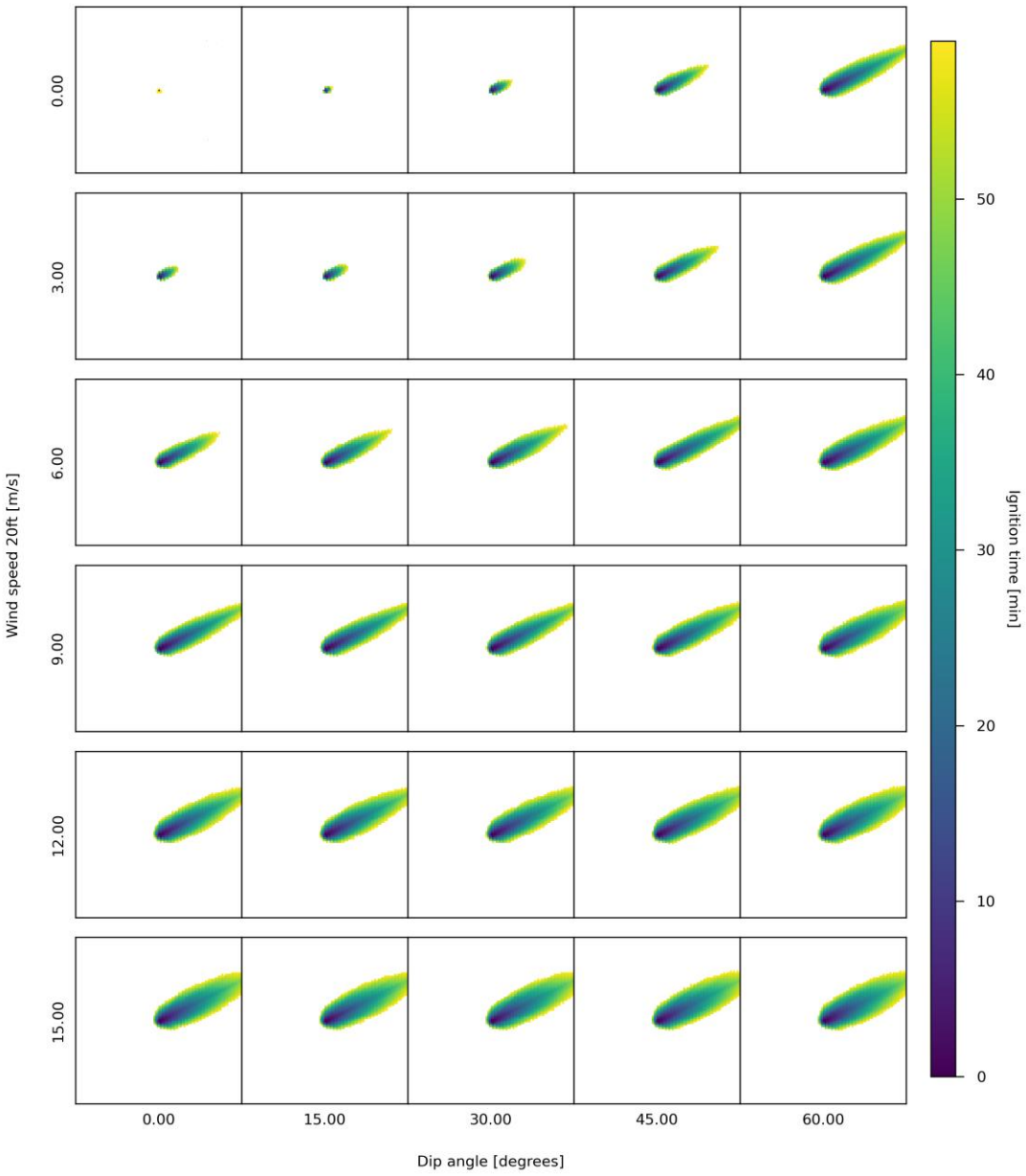

Figure 7-3 Joint effect of wind speed at 20 ft height and dip angle for fuel model SHs4 (Rothermel, 1972). Simulation parameters: wind speed varying between 0 and 15 m/s; wind direction equal to 60 degrees clockwise from north; dip angle varying between 0 and 60 degrees; dip direction equal to 240 degrees clockwise from north; live and dead moisture fraction equal to 1.0 and 0.07 respectively.

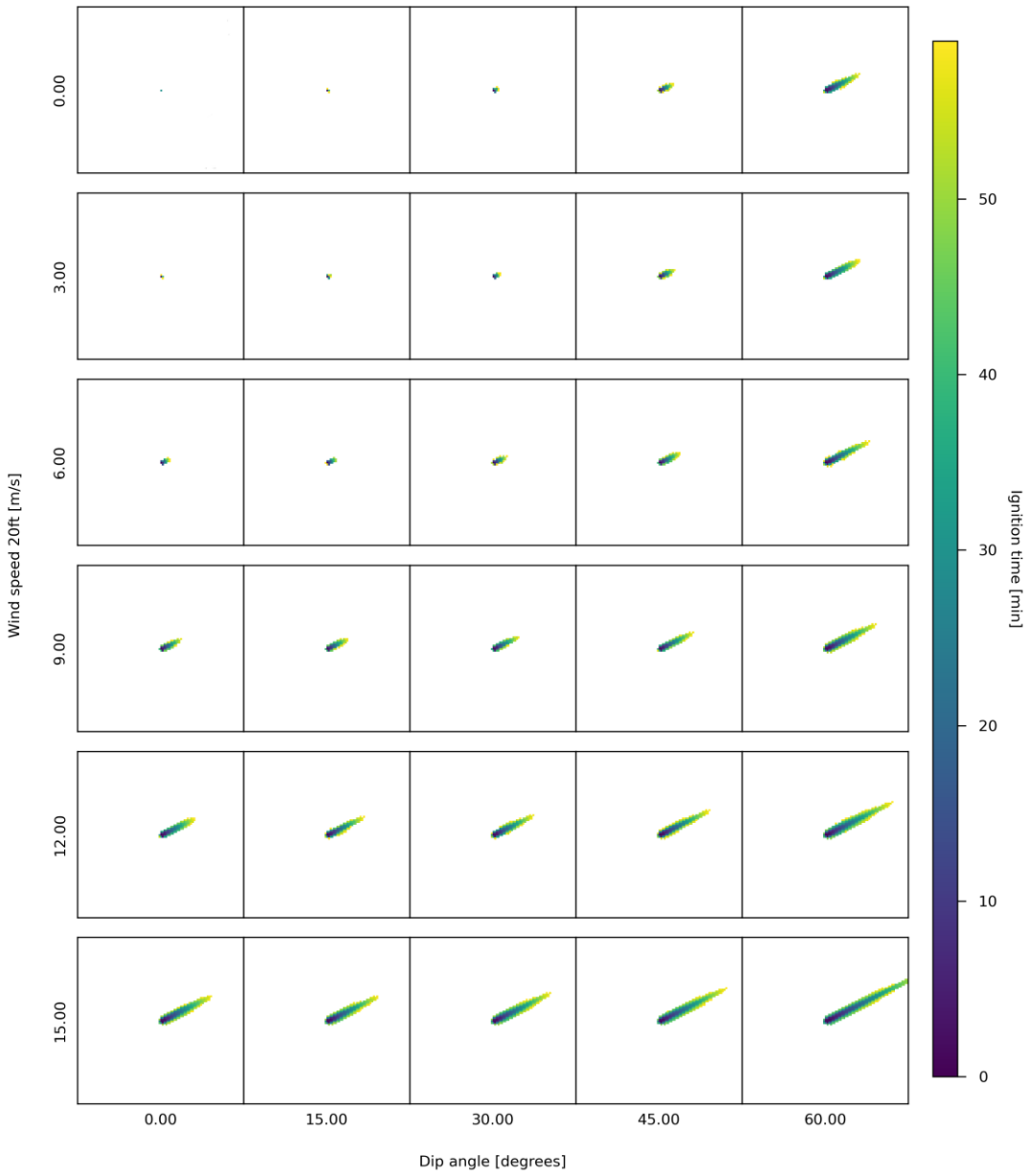

Figure 7-4 Joint effect of wind speed at 20 ft height and dip angle for fuel model GRs2 (Rothermel, 1972). Simulation parameters: wind speed varying between 0 and 15 m/s; wind direction equal to 60 degrees clockwise from north; dip angle varying between 0 and 60 degrees; dip direction equal to 240 degrees clockwise from north; live and dead moisture fraction equal to 1.0 and 0.07 respectively.

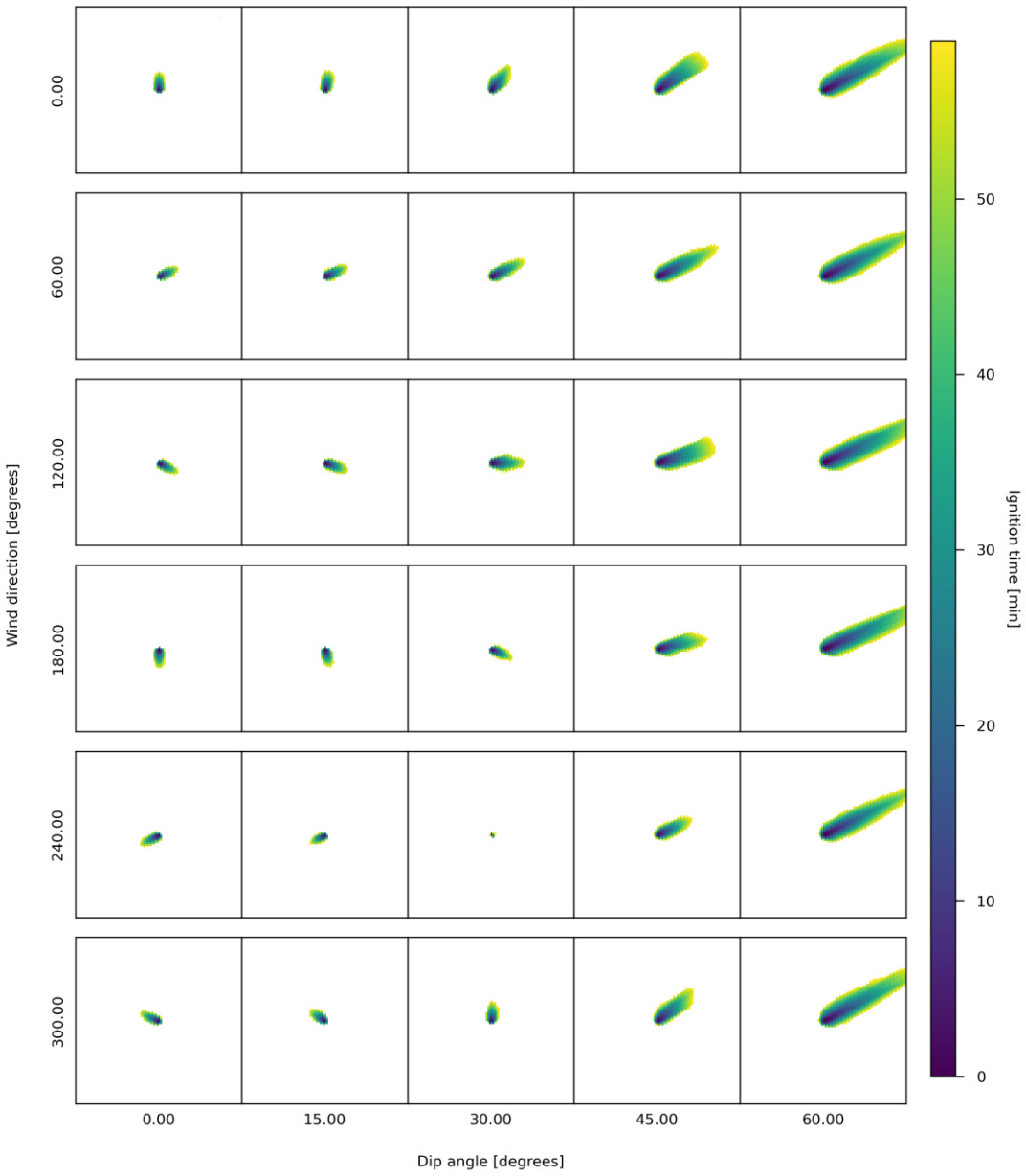

Figure 7-5 Joint effect of wind direction and dip angle for fuel model SHs4 (Rothermel, 1972). Simulation parameters: wind direction varying between 0 and 300 degrees clockwise from north; wind speed equal to 3 m/s; dip direction equal to 240 degrees clockwise from north; dip angle varying between 0 and 60 degrees; live and dead moisture fraction equal to 1.0 and 0.07 respectively.

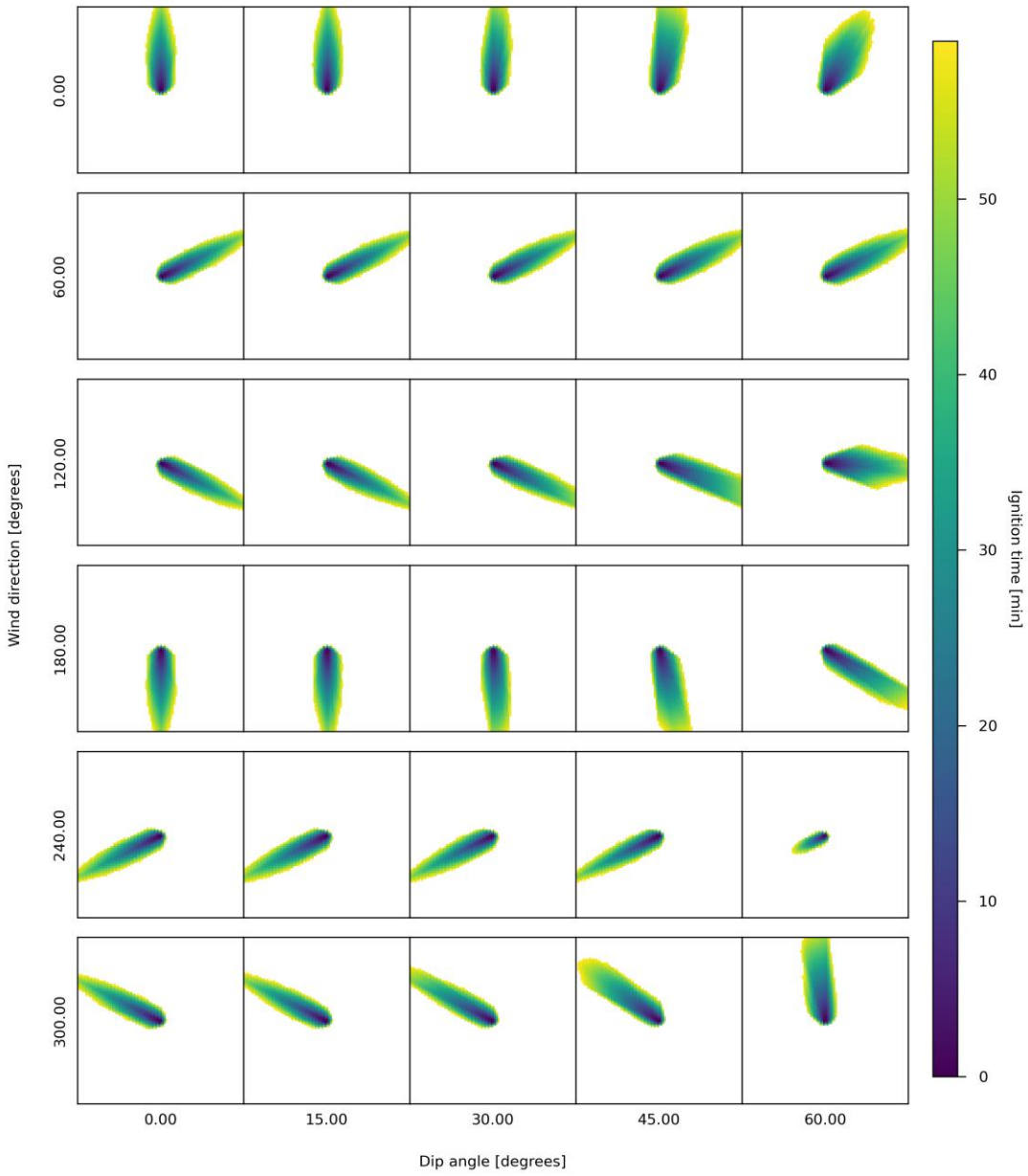

Figure 7-6 Joint effect of wind direction and dip angle for fuel model SHs4 (Rothermel, 1972). Simulation parameters: wind direction varying between 0 and 300 degrees clockwise from north; wind speed equal to 10 m/s; dip direction equal to 240 degrees clockwise from north; dip angle varying between 0 and 60 degrees; live and dead moisture fraction equal to 1.0 and 0.07 respectively.

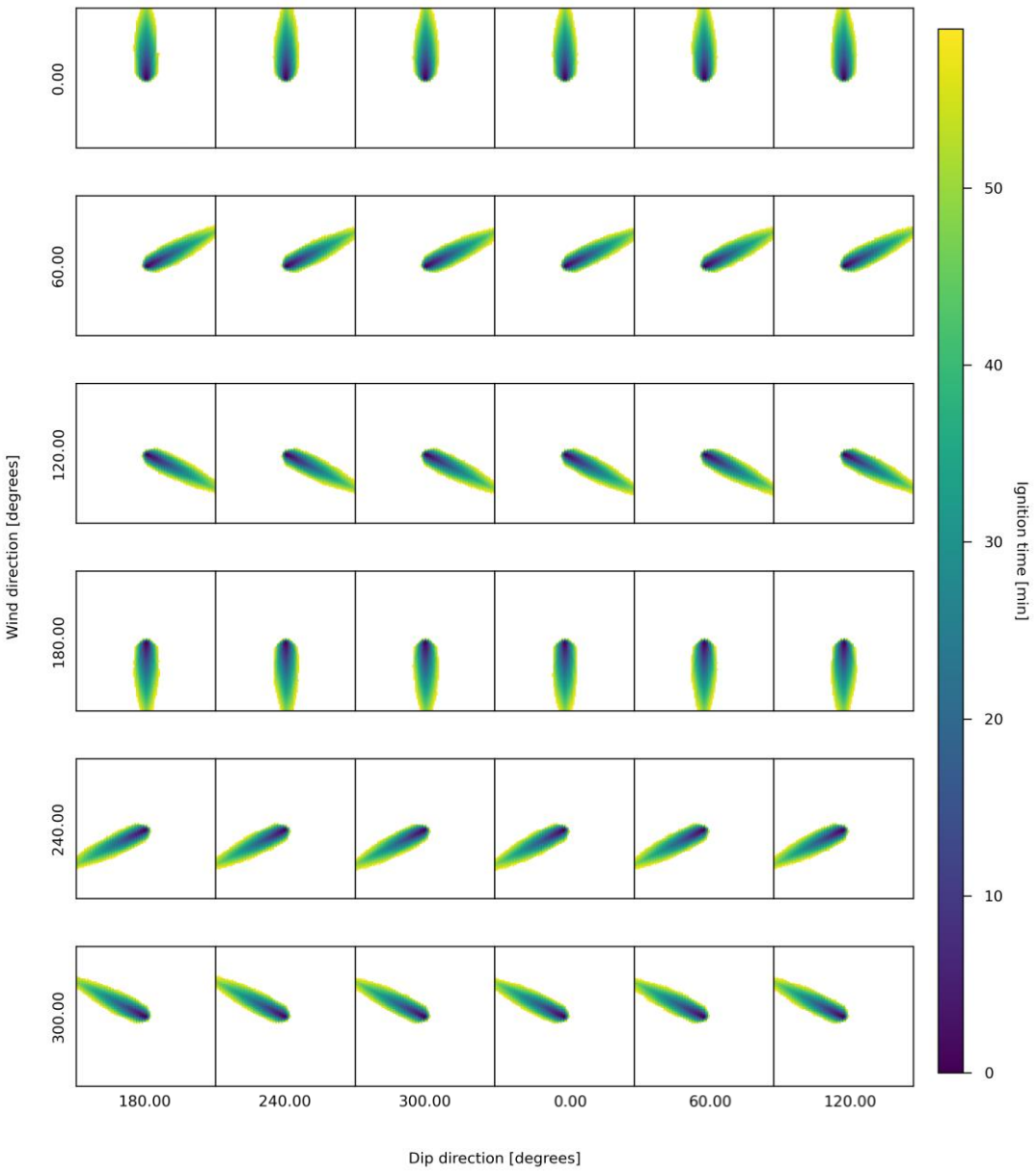

Figure 7-7 Joint effect of wind direction and dip direction for fuel model SHs4 (Rothermel, 1972). Simulation parameters: wind direction varying between 0 and 300 degrees clockwise from north; wind speed equal to 10 m/s; dip direction varying between 0 and 300 degrees clockwise from north; dip angle equal to 15 degrees; live and dead moisture fraction equal to 1.0 and 0.07 respectively.

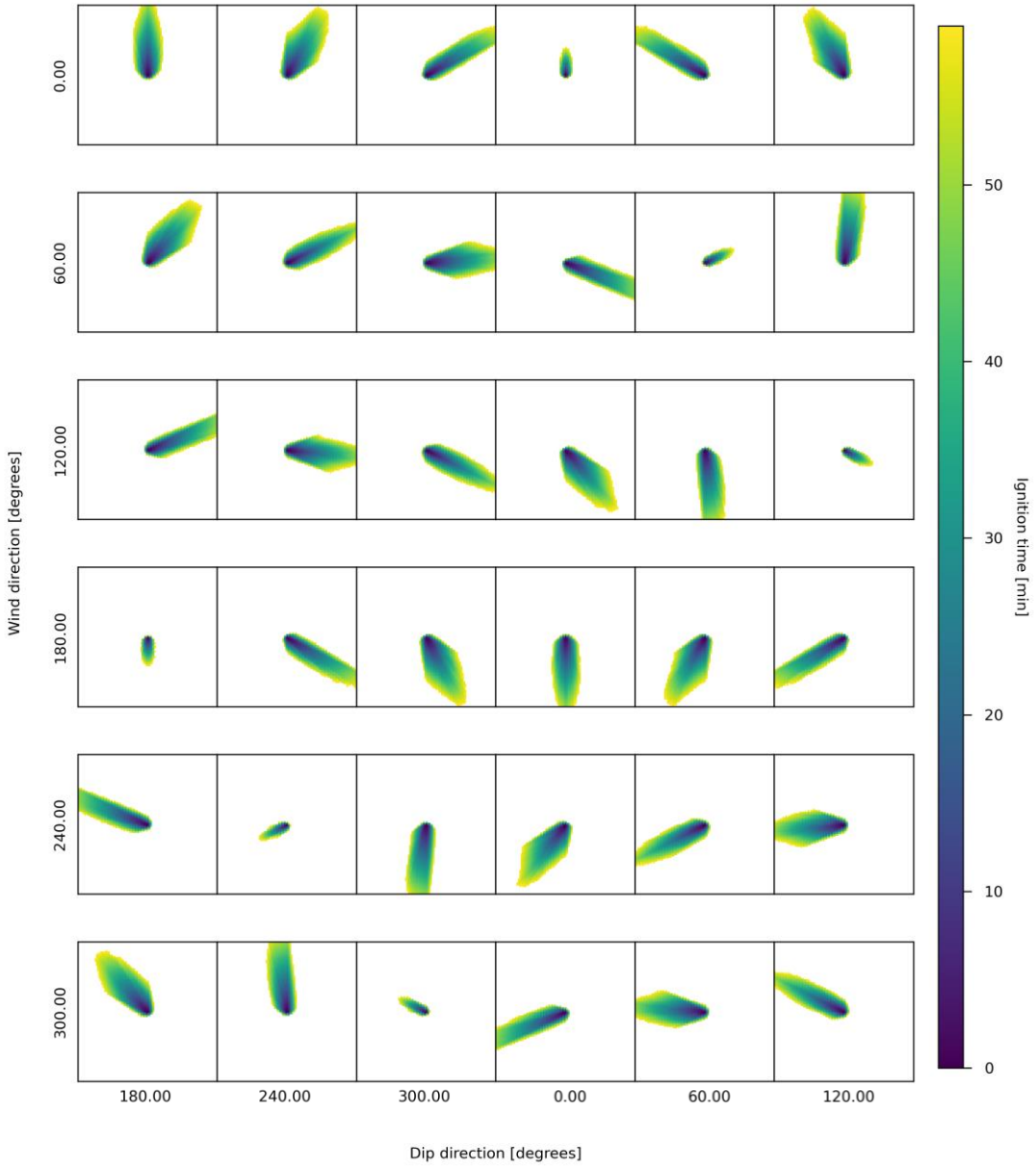

Figure 7-8 Joint effect of wind direction and dip direction for fuel model SHs4 (Rothermel, 1972). Simulation parameters: wind direction varying between 0 and 300 degrees clockwise from north; wind speed equal to 10 m/s; dip direction varying between 0 and 300 degrees clockwise from north; dip angle equal to 60 degrees; live and dead moisture fraction equal to 1.0 and 0.07 respectively.

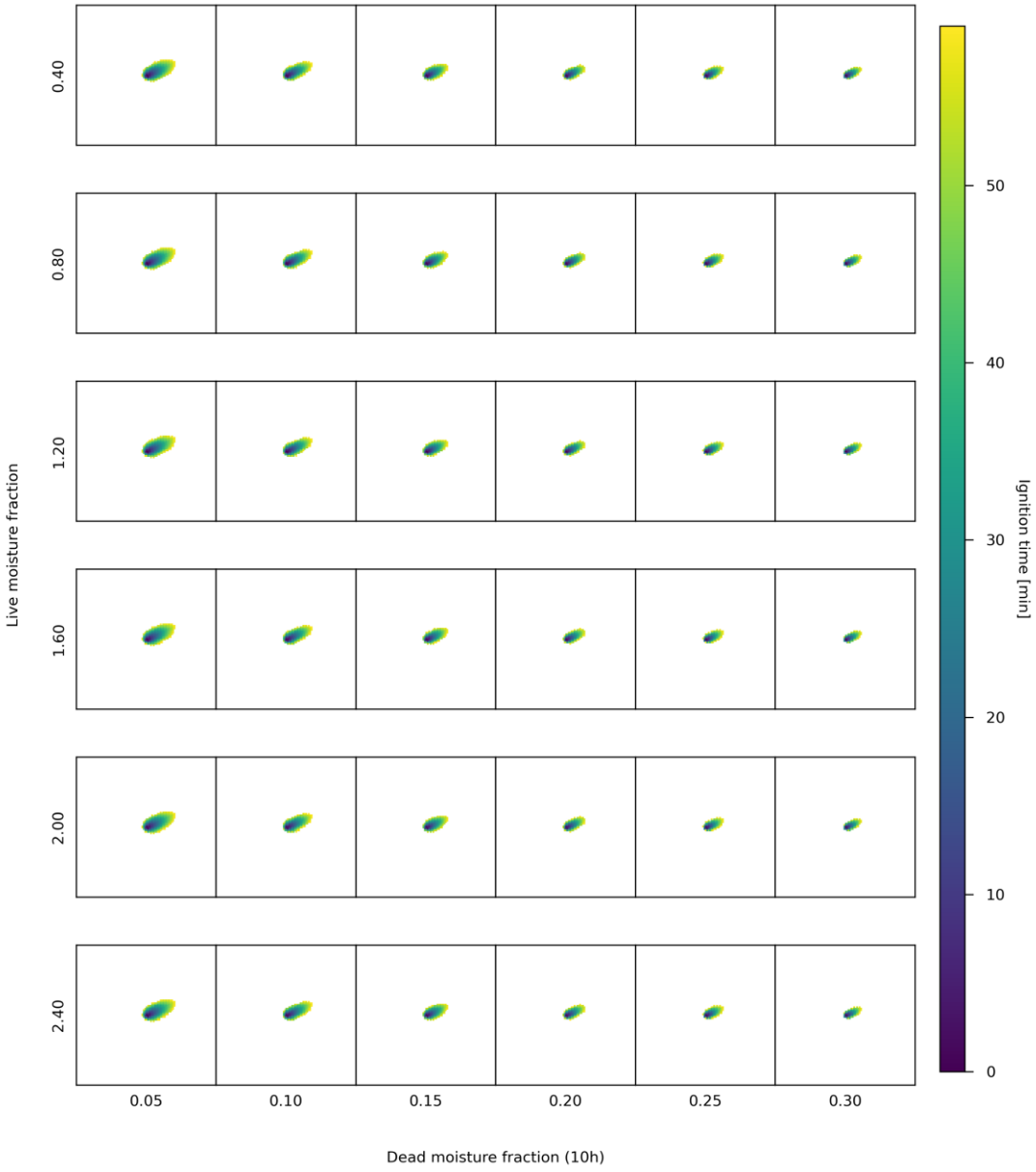

Figure 7-9 Joint effect of live and dead moisture fractions for fuel model GRs3 (Rothermel, 1972). Simulation parameters: wind speed equal to 3 m/s; wind direction equal to 60 degrees clockwise from north; dip angle equal to 15 degrees; dip direction equal to 240 degrees clockwise from north; live moisture fraction varying between 0.40 and 2.40; dead moisture fraction varying between 0.05 and 0.30.

Figure 7-9 illustrates the joint effect of live and dead fuel moisture fractions on the simulated fire growth, which is more clearly perceptible for low values of wind speed (3 m/s). Both live and dead fuel moisture fractions show a limited influence on the maximum rate of spread, with a slightly more significant impact of the dead moisture fraction with respect to the live moisture fraction.

7.4 Discussion

Patterns resulting from the simulations of fire growth exhibited a satisfying level of agreement with theoretical knowledge on fire behaviour modelling. Horizontal wind speed and direction have played a pivotal role in determining both direction and intensity of the maximum rate of spread across most of the performed simulations. Analogous effects have been observed for the dip angle. Indeed, increasing dip angles as well as increasing upslope winds generated higher rates of upslope spread with respect to downslope, reflecting the fire behaviour observed in the real world, where fuel ahead of a fire front is subject to an increasing convection that is greater the more the dip angle and the upslope wind speed upslope increase. Conversely, higher downslope wind speeds resulted in higher rates of downslope spread with respect to upslope, thus demonstrating the dominant role of wind speed and direction in determining both the intensity and direction of the maximum rate of spread.
Furthermore, obtained results essentially confirmed the explanations of the proxy model presented in Chapter 6. Wind speed and dip angle resulted in the most significant variations in terms of fire growth, reflecting their high feature importance in determining both maximum rate of spread (Figure 6-7) and eccentricity (Figure 6-15). However, significant variations in the resultant simulations of fire growth need to be attributed to the selected fuel model. For instance, differences in terms of patterns of fire growth can be observed when comparing Figure 7-3 and Figure 7-4 which only differ from one another for the selected fuel model, SHs4 and GRs2 respectively (Rothermel, 1972), which have been proven to sustain different rates of spread (Figure 6-10). Finally, wind direction and dip direction have been correctly identified as the most important features in determining the direction of the maximum rate of spread (Figure 6-14).
Obtained outcomes suggest that the developed ABM for simulating fire growth produces patterns showing an adequate accordance with the target conceptual model. However, in most of the simulated fire growth, the fire front exhibits an angular rather than rounded pattern suggesting that the model slightly suffers from the distortion that is typical of the raster implementations, especially in synthetic conditions and potentially in real-world applications. Major improvements to the developed agent-based spatial simulation model could be granted by addressing these distortions.
To determine whether the implemented model corresponds to and explains phenomena in the real world, it has been validated against historical events occurred in Sardinia, Italy (Chapters 8 and 9).

Chapter 8

Historical wildfire events in Sardinia

8.1 Wildfires in Italy

According to the results of the most recent National Inventory of Forests and forest Carbon pools (INFC), forest areas in Italy occupy 35% of the national territory, covering an overall surface of 10,982,013 ha, with 9,165,505 ha of forests and 1,816,508 ha of wooded land, mainly shrublands, maquis, and garrigues (INFC 2015). Forest areas have steadily increased over the last century across the whole nation, thanks to the spontaneous recolonization of marginal agricultural areas that followed the abandonment of croplands and the resulting changes in land use. The overall annual increase in forest areas (forests and woodlands) for the periods 1985-2005 and 2005-2015 is 0.3% and 0.2% of the national territory respectively, with correspondent annual increases of 77,960 ha and 52,856 ha (Gasparini and Marchetti, 2019). However, forest areas are increasingly exposed to forest fires. In the period 1980-2017, forest fires in Italy affected an overall surface of 4,061,988 ha with an annual average of 106,894 ha of burnt areas (Corona and Gismondi, 2019). According to the annual report on environmental data produced by the Italian Institute for Environmental Protection and Research (ISPRA, 2019), the annual burnt area and the total number of fires showed fluctuating trends in the period 1970-2018 (Figure 8-1), with peaks in 2007, 2012, and 2017 in the last couple of decades and softening in fire activity in 2013, 2014, and 2018. More specifically, the 2007 fire season was one of the heaviest ever recorded, with 10,639 forest fires that affected an area of 227,729 ha, of which 116,602 were wooded (Camia et al., 2008).

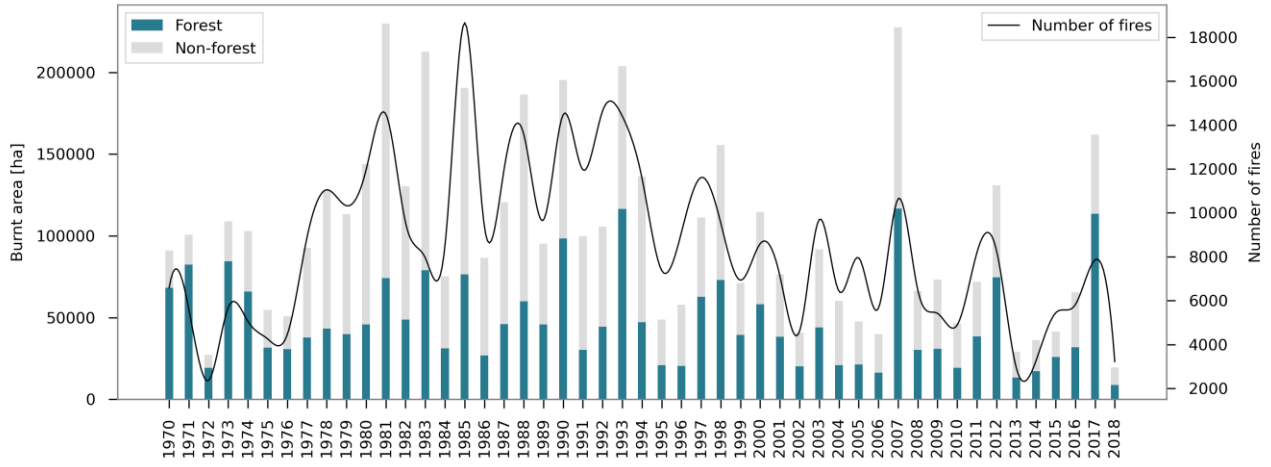

Figure 8-1 Total surface burnt area (forest and non-forest) and overall number of fires in Italy from 1970 to 2018. Data sources: ISPRA, 2019.

Data published in the JRC Technical Reports highlight that 58,593 wildland fires occurred in Italy in the years 2009-2019 burning an overall surface of 694,860 ha, of which 381,553 wooded. When analysing the spatial distribution of wildland fires on the national territory, Figure 8-2 show a clear difference in terms of fire activity amongst Italian Regions and thus reflecting the diversity between fire-prone Mediterranean ecosystems and non-fire-prone ecosystems. Indeed, 56.2% of the total number of events occurred in Sicily (16.6%), Calabria (15.2%), Campania (14.0%), and Sardinia (10.4%), whereas 60.1% of the overall burnt area were located in Sicily (29%), Calabria (15.9%) and Sardinia (15.2%) alone (Figure 8-2). Wildfires in Sardinia are larger on average (20.63 ha per event) if compared with other Regions severely affected by wildfires, such as Campania (6.2 ha per event). According to these estimates, 8,252 wildfires have ignited during the 2012 fire season, the greatest number of events in Italy for the period 2009-2019, burning an overall surface of 130,814 ha. However, the 2017 fire season is responsible for the largest annual burnt area, affecting 161,987 ha, which account for 23.3% of the overall area burnt in the period 2009-2019, consumed by 7,855 events (San-Miguel-Ayánz et al., 2018).

Estimates provided by the JRC Technical Reports point out that while the 2017 fire season have fuelled exceptionally large events across most of the Italian Regions, this seems not true for Sardinia, where the largest annual burnt area has been recorded in 2009, with 37,104 ha compared to 7,843 ha burnt in 2017 and an average annual burnt area of 6,841 ha for the period 2010-2019. Moreover, only 684 wildfire events are reported for the 2009 fire season, implying an average burnt area of 54.25 ha per event, while the reported average brunt area per each single event for the period 2010-2019 is 17.27 ha. However, more accurate sources of data, such as the Sardinia Forest Service, suggest an underestimation of both the number of fire events and the total burnt areas for the period 2009-2019.

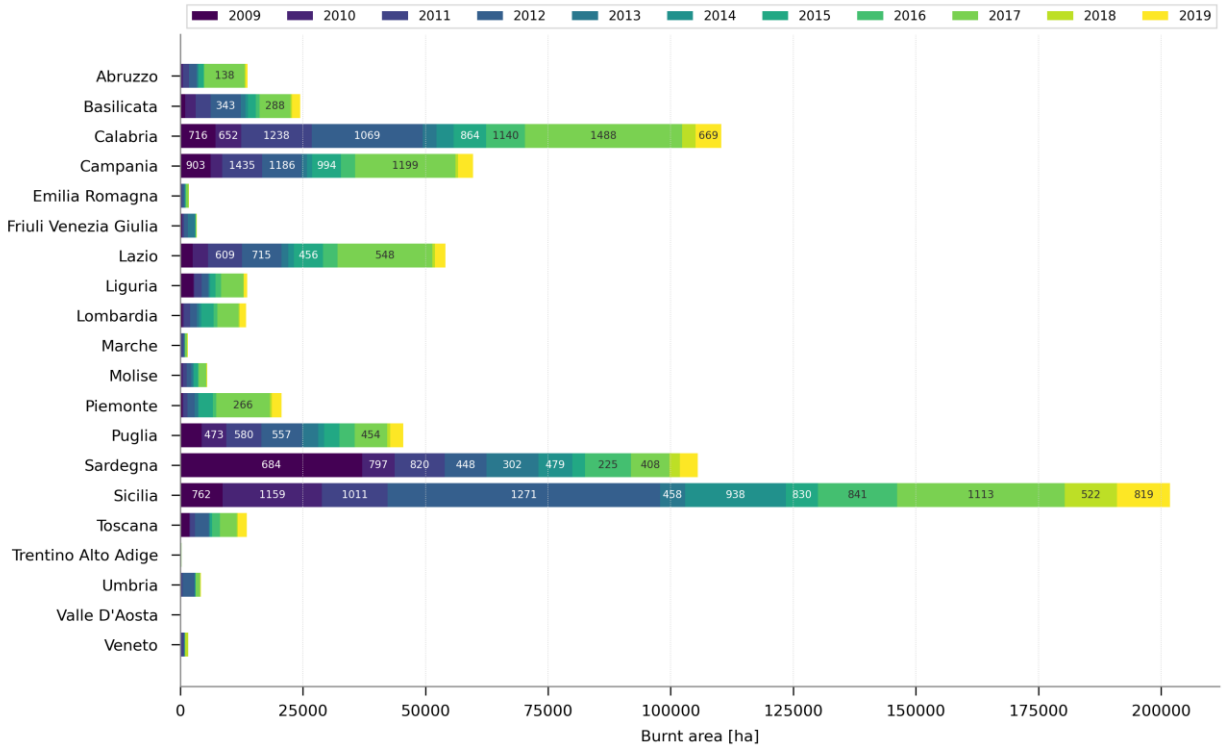

Figure 8-2 Wildfire events in the diverse Regions of Italy from 2009 to 2019. Bar width represents the total burnt area [ha] in different years. The number of wildland fires per year is also reported on respective bars for reference. Data sources: JRC Technical Reports for the years 2009-2019.

8.2 Wildfires in Sardinia

This section is aimed at characterising the study area in general terms of fire activity by performing an exploratory data analysis on available institutional information on historical wildfire events. The chosen study area is Sardinia, Italy, the second largest island of the Mediterranean Basin. According to the latest JRC Technical Reports, Sardinia has been of the most affected regions in Italy in the period 2009-2019 in terms of total number of fires (6,097 events), overall burnt area (105,518 ha), and average fire size (20.6 ha).
An in-depth analysis of the historical events occurred between 1974-2003 has been derived from the Proceedings of the Conference "*Incendi boschivi e rurali in Sardegna. Dall'analisi delle cause alle proposte d'intervento*" (Section 8.2.1). Data of wildfire events occurred between 2005 and 2019 have been specifically investigated for the purpose of the present study (Section 8.2.2).

8.2.1 Period 1974-2003

In the period 1974-2003, 3,436 fires have been recorded annually in Sardinia, with an average burnt area of 34,394 ha, of which 8,440 ha wooded (Boni, 2004). In 1983, a critical year for wildland fires, 1,600 events corresponded to an overall forest area burnt of 37,500 ha. Although an extremely irregular trend, the number of events has remained almost stable with about 3,000 events per year from 1983 to 2003, but the average burned area has decreased, with 92% of burnt areas under 10 ha and 67% under 1 ha. This drop is traditionally ascribed to an increased efficiency and effectiveness of fire suppression activities as well as to the introduction and enforcement of the general policy on wildfires, L. November 21st, 2000 n. 353 (*Legge Quadro in materia di incendi boschivi*). However, Boni (2004) has raised concerns about the increase in ignition locations' proximity to the roadsides: while in the period 1983-1989 wildfires ignited along the roadside represented just 16% of the total, in the period 1995-2003 reached 42% of the total (46% for the 3-year period 2001-2003). Moreover, while from 1974 to 2003 the greater number of fires that caused larger burnt areas occurred between 10:00 in the morning and 19:00 in the evening, with peaks at around 13:00, wildfires rage more and more frequently after the sunset.
Burnt areas are surveyed in Sardinia by the local Forestry Corps of the Autonomous Region of Sardinia (*Corpo forestale e di vigilanza ambientale della Regione Autonoma della Sardegna*, CFVA) which is also in charge of the control and repression of criminal offenses related to wildfires as well as of the investigation on their causes. Indeed, in compliance with the general policy on wildfires, L. November 21st, 2000 n. 353, kindling wildland fuels constitutes a criminal offense which can be punished with 4-10 years of detention. However, the vast majority (99%) of fires in Sardinia in the period 1974-2004 (Saba, 2004) have been attributed to anthropogenic causes, both arson and unintentional. At a national level, complete surveys on wildfire crimes carried out by the former State Forestry Corps (*Corpo forestale dello Stato*) confirmed that only 1.23% of recorded wildland fires in Italy in the period 1997-2007 were a result of natural causes (Lovreglio et al., 2010). These results reflect the general tendency observed in European Mediterranean regions where 97.1% of wildland fires are directly or indirectly caused by human agents (Ganteaume et al., 2013).
From the investigations carried out by the CFVA relatively to the period 1996-2016, it emerges that 70.0% of human-caused wildfires in Sardinia were due to intentional causes (arson), 14.2% were due

to unintentional causes (negligence), and 15.8% were due to undefined human-causes (Autonomous Region of Sardinia, 2017b). According to Saba (2004), most frequent intentional causes of wildfire events occurred in Sardinia between 1974 and 2004 included: pasture renewal or creation; agricultural use of fire; ownership conflicts and personal revenge; conflicts with Authorities; protest of seasonal firefighters; acts of intimidation, vandalism, and pyromaniacs. Building speculation, i.e. the use of fire as a tool to convert rural or natural lands into urban lands, is also enumerated among intentional causes. Instead, motives connected to negligent fires occurred in Sardinia between 1974 and 2004 included: careless use of agricultural fires; stubble burning; unsafety use of mechanical, electrical or fuel-burning tools; lack of maintenance of power lines, pipelines, railroad lines; and careless discard of cigarettes. Those results are in line with main findings at a national level (Lovreglio et al., 2010).

8.2.2 Period 2005-2019

According to the official Sardinia Forest Service database, the average annual number of fire ignitions for the period 2005-2019 is about 3,000 per year. Institutional information about historical wildfire events in Sardinia between 2005 and 2019 have been specifically collected and analysed for the purpose of the present study. Data are provided on a vector basis by the official website of the Autonomous Region of Sardinia (Autonomous Region of Sardinia, 2020b). The database currently consists of institutional delimitation of a selection of burned scars with a final area greater than 0.1 ha, which is the size threshold set by the Forest Service to map an event, produced by wildland fires occurred between 2005 and 2019, each supplied with information on the date of the ignition. The maps of burned scars have been delineated directly with GPS ground surveys and cross-validated through photointerpretation by the local Forestry Corps of the Autonomous Region of Sardinia (*Corpo forestale e di vigilanza ambientale della Regione Autonoma della Sardegna*, CFVA) in compliance with the local and national general policy on wildfires, L. November 21st, 2000 n. 353 (Autonomous Region of Sardinia, 2017b).

8.2.2.1 Exploratory data analysis

An exploratory data analysis has been performed on the available dataset. It emerges that 21,020 historical events greater than 0.1 ha occurred between 2005 and 2019 in Sardinia, with an average of 1,401 events per year, burning an overall surface of 223,543 ha (a mean of 15,967 ha per year).

The 2007 fire season has fuelled the highest number of events greater than 0.1 ha, with 2,211 fire outbreaks, an overall burnt area of 34,404 ha, and an average fire size of 15.6 ha (Figure 8-3). Both the largest annual burnt area and the largest average fire size were recorded in 2009, when 1,442 events with an average fire size of 31.1 ha have burnt an overall surface of 44,875 ha. However, this anomaly can be attributed to 8 concurrent extreme wildfire events occurred on July 23rd and a relight on July 24th, which together accounted for 30,347 ha, i.e. 67.6% of the annual burnt area, of which 21,622 ha burnt by 3 events alone. At the opposite, the 2018 fire season sustained 461 fire outbreaks that burnt an average of 4.5 ha per year and an overall annual surface of 2,094 ha.

Figure 8-4 describes the seasonality of fire events greater than 0.1 ha occurred between 2005 and 2019. Wildfire outbreaks are quite evenly distributed in the months from June to October, when 93.15% of the events occurred, 28.3% of which in July. Similarly, months from June to October account for 97.49% of the overall burnt area, of which July represents 55.25% and August 18.72%.

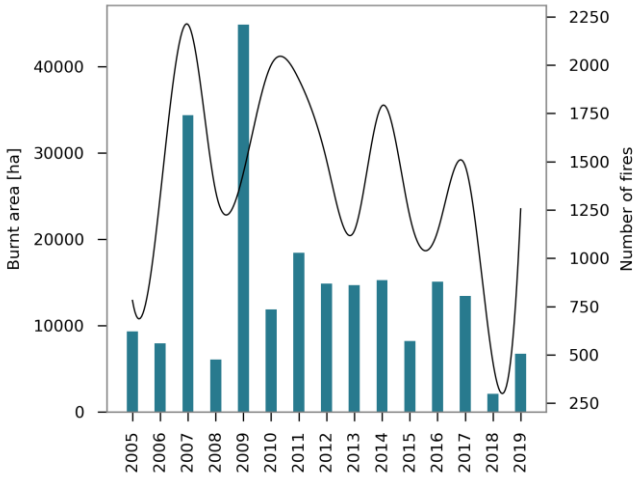

Figure 8-3 Total surface burnt area and overall number of fires in Sardinia from 2005 to 2019. Data sources: Autonomous Region of Sardinia, 2019

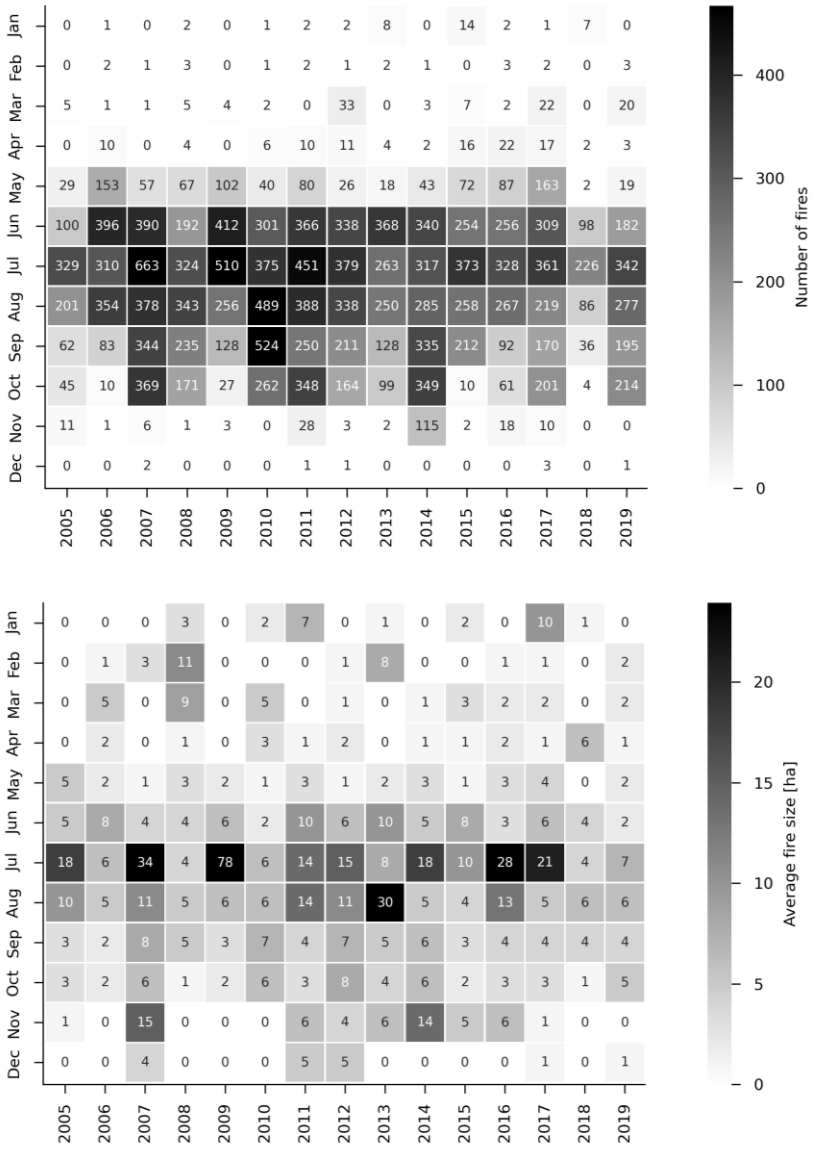

Figure 8-4 Heatmap representing the distribution by month and years of both the number of wildfire events (upper) and the average fire size [ha] (lower) in Sardinia between 2005 and 2019.

These findings seem to confirm the observed decreasing trend in both number of fire events and overall annual burnt area as well as the 15 days advance in the fire season peak identified in Sardinia between 1980-1994 and 1995-2009 by Salis, Ager, Finney, Arca, et al. (2014).
Figure 8-5 show the distribution of fire events into different size classes, highlighting the presence of a higher number of fire events with an area smaller than 100 ha, mostly located in the rural plain of Campidano, in southern Sardinia. Events with a size between 100 ha and 5,000 ha are evenly distributed across the whole region. Events larger than 5,000 ha are rarer and mainly found in the north-western uplands of Marghine and Meilogu subregions.
Only 4.41% of the wildfires greater than 0.1 ha recorded in Sardinia between 2005 and 2019 have an area burnt greater than 30 ha, but they contribute to 71.03% of the total burnt area (223,543 ha). Moreover, 1.23% of the fires exceed 100 ha, and less than 0.22% are greater than 500 ha, respectively contributing to 55.71% and 36.47% of the overall burnt area.

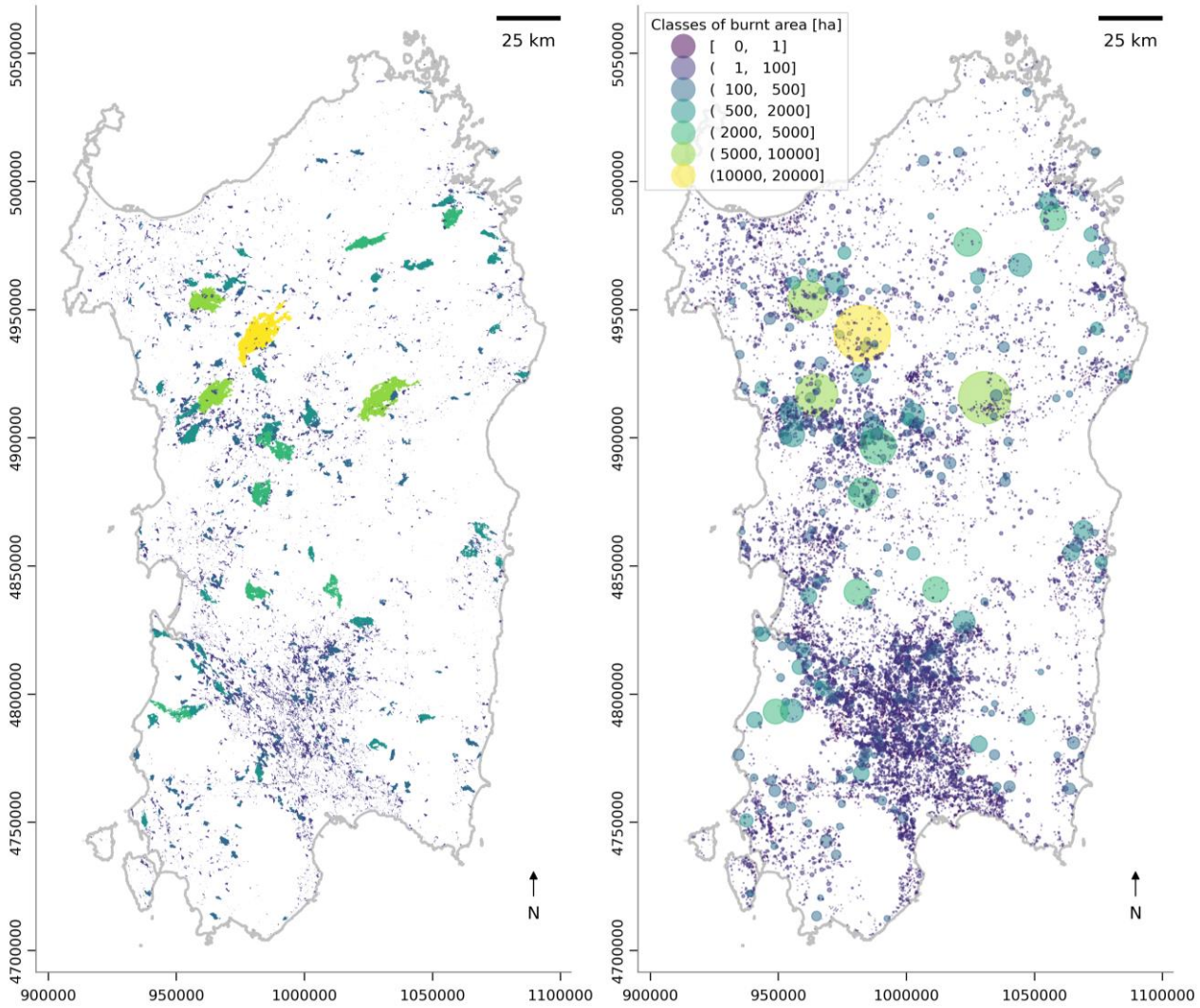

Figure 8-5 Wildfire events in Sardinia. Each event is represented as a point with a size proportional to the surface it has burnt, Different colours represent different classes of burned area [ha]: events with an area less than 1 ha are represented in dark purple, whereas events bigger that 10.000 ha are represented in yellow.

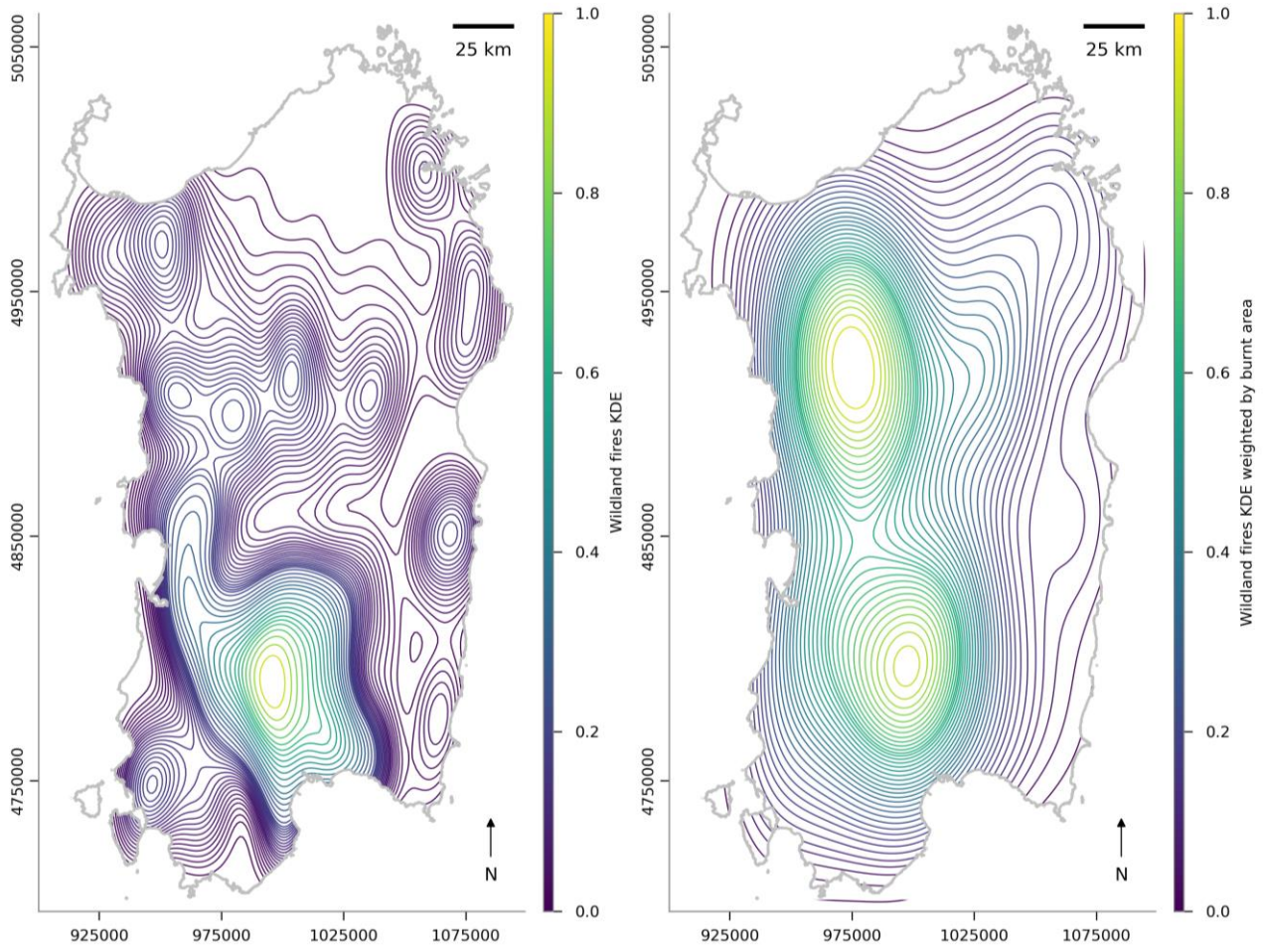

Figure 8-6 Kernel density estimation of the spatial distribution of wildfire events (left) and kernel density estimation of the spatial distribution of wildfire events weighted by burnt area (right).

Only less than 0.10% of the wildfires greater than 0.1 ha spread for over 1,000 ha, but alone these fires are responsible for 29.32% of the damaged area in Sardinia. Events greater that 10,000 ha represent 0.005% of the total and represent 4.72% of the overall burnt area. These findings are in agreement with the general trends identified across Europe (Costa et al., 2020).

Figure 8-6 shows the greater density of fire outbreaks is found in the rural plain of Campidano, where events with a burnt area less than 1 ha are gathered. However, if weighted by their burnt area, the density of occurred events is greater in north-western uplands of Marghine and Meilogu, where events with an area greater than 5,000 ha are accumulated (Autonomous Region of Sardinia, 2017b). Those findings are in satisfying agreement with results from Ager et al. (2014).

According to the land use map of Sardinia developed at a regional scale (Autonomous Region of Sardinia, 2008), land use classes with greatest incidence on the overall areas burnt by wildfires larger than 1 ha (194,245 ha) include (Figure 8-7): permanent and non-irrigated arable lands (31.4%), artificial meadows (12.8%), natural pastures (9.4%), maquis and garrigue (15.6%), broad-leaved forests (5.1%), forests with prevalence of cork oaks (3.6%), non-permanent crops associated with permanent crops, including fruit trees or olive trees or vines (3.6%), olive groves and vineyards (1.7%).

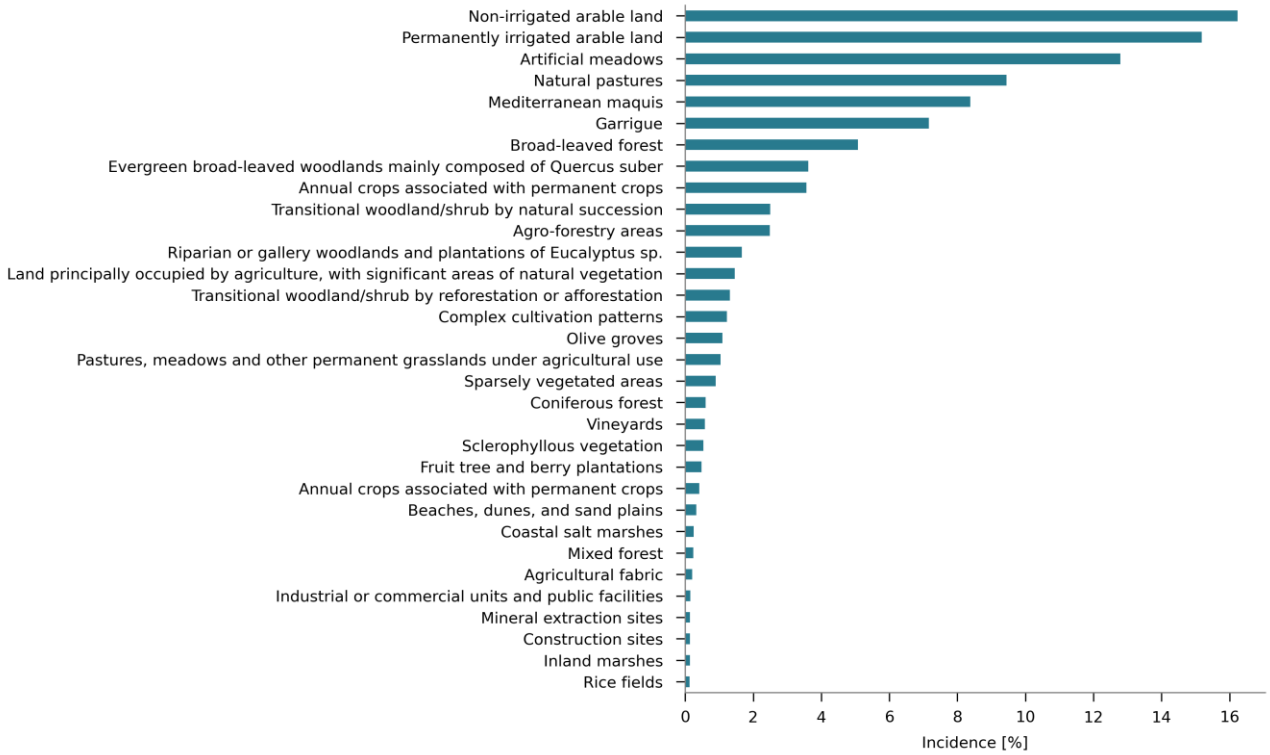

Figure 8-7 Incidence [%] of land use classes on the overall burnt areas in Sardinia from 2005 to 2019.

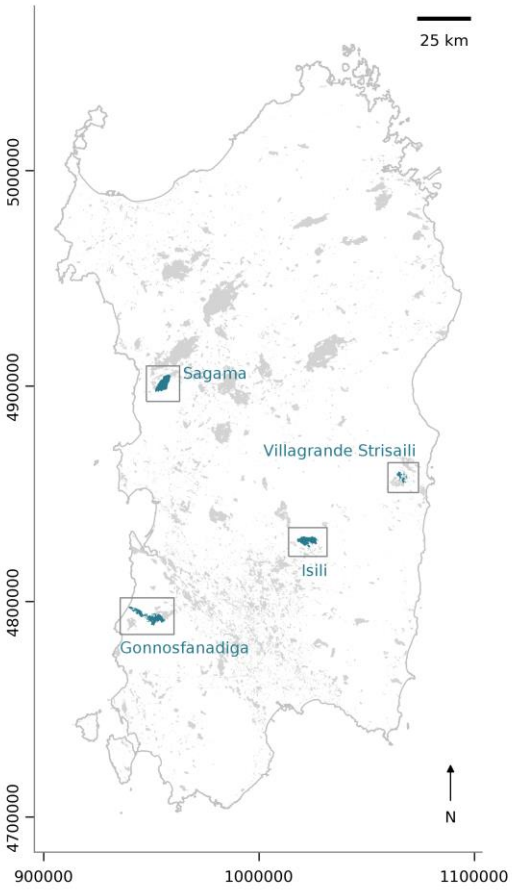

Figure 8-8 Case studies' location in Sardinia, Italy.

8.3 Selection of case studies

In addition to institutional delimitation of burned areas, simulation modelling of wildland surface fire behaviour requires information on both the overall burning time and the exact timing and location of fire occurrence. Moreover, detailed information on the timing and location of any fire suppression activity are needed to correctly evaluate the accuracy of a simulation. Hence, the selection of the case studies for the validation of the developed wildland surface fire behaviour simulation model has been guided by the availability of ancillary sources of information, including official daily or annual reports provided by the Autonomous Region of Sardinia (2017b, 2020a) for events occurred in 2016, but also local newspapers and chronicles for events occurred in 2017.
The selected case studies (Figure 8-8) occurred between July and August 2016 and in July 2017 in Sardinia, Italy, under a varied range of geo-environmental conditions, with direct and indirect consequences on human lives, properties, and activities as well as on the environmental heritage. Authoritative reports describe in detail ignition date, time, and location of two events occurred in 2016 as well as the fire suppression activities carried out to extinguish the flames. Contrarily, information on wildfires occurred in 2017 have been retrieved from local newspapers and chronicles.
In the 2016 fire season, Isili and Sagama events burned a total area of 3,444 ha, equal to almost 22.8% of the overall burnt area in the whole fire season. The events of Gonnosfanadiga and Villagrande Strisaili burned a total area of 2,525 ha, 16.7% of the overall burnt area in the 2017 fire season.
All fire outbreaks occurred between 10:00 and 12:00 UTC (Table 8-1), mainly in conjunction with meteorological conditions that can be defined as severe or extreme. The active propagation lasted less than 24 hours for each of the selected case studies excluding secondary outbreaks and mop-up operations which continued for a further 24-72 hours. Fire duration time is intended as the time interval between the fire ignition and the conclusion of active fire suppression operations, so that the fire size reflects the perimeter burned in this interval. Information on the timing and location on both ground and aerial fire suppression intervention, involving either direct, indirect, or parallel attack, have been collected for each case study.

Table 8-1 Selected case studies with information provided by authoritative reports by the Autonomous Region of Sardinia (*) or by local chronicles (°).

	Ignition date	Ignition time UTC	Burnt area [ha]	Suppression
Sagama*	24-08-2016	11:20	1,841	Terrestrial and aerial
Isili*	20-07-2016	10:10	1,603	Terrestrial and aerial
Villagrande Strisaili°	25-07-2017	11:00	489	Mostly terrestrial
Gonnosfanadiga°	31-07-2017	12:00	2,036	Mostly terrestrial

8.3.1 Sagama

The case study of Sagama occurred on August 24th, 2016 and burned an overall surface of 1,841 ha. According to the authoritative report provided by the Autonomous Region of Sardinia (2017b), it has originated from two simultaneous ignition points 2 km apart from each other and located in agricultural lands outside the urban circuit of the municipality of Sagama (OR) in the sub-region of Planargia, north-western Sardinia. Contextually, an accurate description of the evolution of the observed wildfire event is also provided starting from the outbreaks signalled at 11:20 UTC (13:20 local time).

The synoptic framework depicted by the authoritative report suggests that the Sagama event occurred with a maximum temperature of 30° C and a relative humidity varying between 15 and 30%. Sustained by north-east winds with intensities up to 8 m/s, the flaming front rapidly consumed the cured grassy fuels threatening the residential area of Sagama for the defence of which the first ground suppression activities have been organised. These interventions secured exposed anthropogenic elements but did not prevent the fire to further propagate toward south-west. The flaming front spread on a nearly flat surface (1.4% slope) and covered 8 km along the maximum direction of fire spread (Figure 8-9). The fire spread has been characterised by high flame length and frequent spotting events due to the moderate wind speeds, contributing to low visibility for the aerial interventions that, however, have focused on the fire flanks rather than on the proper fire front until 18:00 UTC. In order to consume the fuel in the path of the fire flanks and front, multiple backfires have been set along the edges of fuel-free firelines: (i) on the east side of the provincial road SP21 at about 14:00 UTC for the defence of the residential area of Scano di Montiferro; (ii) on the east side of the dual carriageway SS292 at around 16:00 UTC for the defence of the residential area of Sennariolo; (iii) on the east side of the provincial road from Sagama to Sennariolo after 18:00 UTC. Secondary outbreaks along the fire perimeter, especially in forest areas, engaged ground crews and aircrafts until 18:00 UTC, on August 25th. Mop-up operations, on the other hand, continued until August 28th.

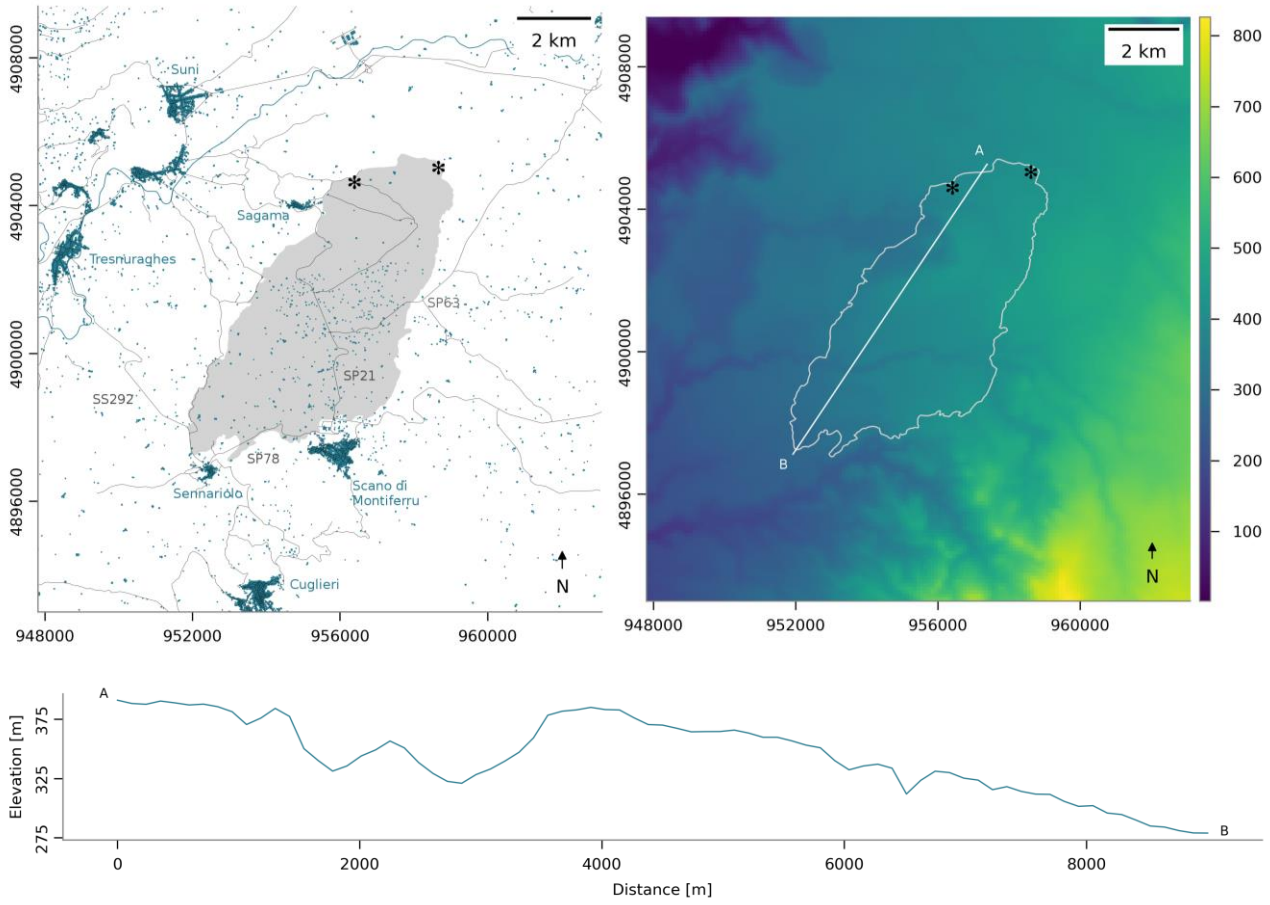

Figure 8-9 Sagama case study: buildings, roads, and railway lines from the topography database provided by the Autonomous Region of Sardinia (upper left) and DTM (upper right). Fire burnt scars (light grey) and fire outbreaks (✻) are reported. The topographical profile (lower) is computed along the section AB suggesting a slightly downslope fire spread.

In terms of land use classes (Autonomous Region of Sardinia, 2008), the event mainly consumed artificial and stable meadows (41.5%), non-irrigated arable lands (27.5%), pastures (8.5%), broad-leaved forests (5.7%), olive groves and vineyards (3.7%), broad-leaved forests with cork oak (*Quercus suber* L.) (1.4%), and Mediterranean maquis (0.9%) (Figure 8-10). According to the habitat map developed as part of the national project *Carta della Natura* (Camarda et al., 2015), Mediterranean meadows represent 80.7% of the burnt area and include abandoned agricultural areas interspersed with areas of significant natural or semi-natural vegetation, such as *dehesas* with evergreen *Quercus* spp., mainly cork oaks (*Quercus suber* L.).

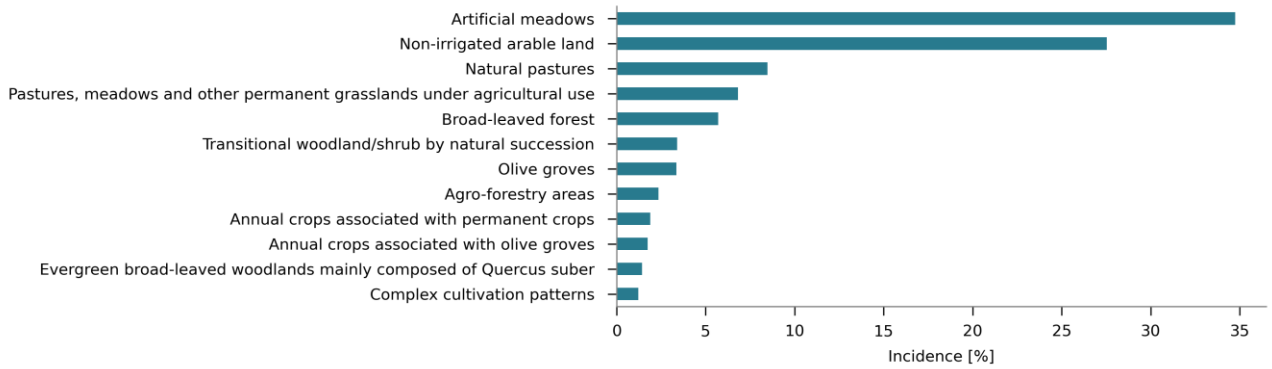

Figure 8-10 Incidence [%] of land use classes on the burnt scar of Sagama fire event.

8.3.2 Isili

The Isili wildfire event occurred on July 20th, 2016 and burned an overall surface of 1,603 ha. As for the previous case study, an accurate description of the evolution of the fire spread has been provided by the Autonomous Region of Sardinia (2017b). According to the authoritative report, the outbreak has been firstly signalled at 10:10 UTC (12:10 local time), in agricultural lands, north-west from the residential area of the municipality of Isili (SU) in the sub-region of Sarcidano. Ground suppression activities started a few minutes later, namely at 10:18 UTC, and focused on both fire flanks but successfully extinguishing flames on the left flank solely. Indeed, the right flank and the fire front continued to spread sustained by increasing wind intensities from south-west, up to 6.9 m/s. The depicted synoptic framework reports a maximum temperature of 35° C and a relative humidity varying between 13 and 25%. The complexity of the topography, together with high fuel load accumulations and frequent spotting events, led to the request for aerial suppression intervention at 10:50 UTC (Figure 8-11). Indeed, the area is characterised by the presence of geomorphological landforms recognisable as *mesas* such as Taccu de Nurri (694 m), i.e. a tabular plateaux of Middle-Upper Jurassic dolomitic limestones of the Dorgali Formation, and Monte Guzzini (734 m), i.e. a tabular plateaux of Middle-Upper Pliocene sub-alkaline basalts, generally constituting tabular expansions locally known as Giare. Ground fire suppression activities continued until July 22nd and 23rd to rapidly contain and control secondary outbreaks.

Most affected land use classes (Autonomous Region of Sardinia, 2008) were: non-irrigated arable lands (40.1%), followed by broad-leaved forests (15.1%), pastures (11.6%), artificial meadows (8.3%), agro-forestry areas (4.6%), Mediterranean maquis (4.3%) and garrigue (7.9%) (Figure 8-12). According to the habitat map developed as part of the national project *Carta della Natura* (Camarda et al., 2015), the Isili event consumed complex agricultural systems (51.6%), Mediterranean maquis

(25.3%), Mediterranean meadows (11.3%), and *Olea* and *Ceratonia* forests dominated by sclerophyllous vegetation including *Olea europaea* ssp. *sylvestris* L., *Ceratonia siliqua* L., *Pistacia lentiscus* L., *Myrtus communis* L. (11.1%).

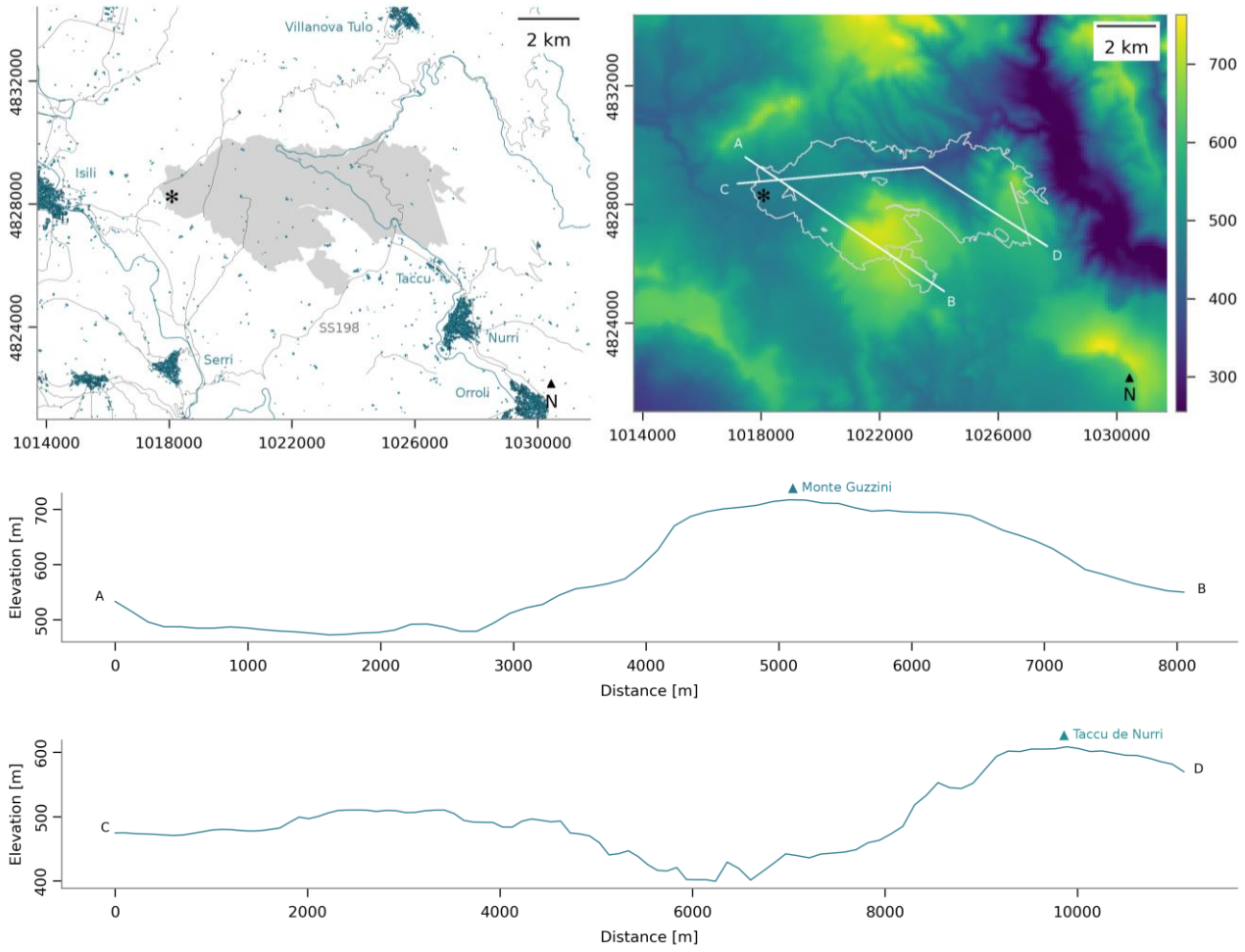

Figure 8-11 Isili case study: buildings, roads, and railway lines from the topography database provided by the Autonomous Region of Sardinia (left) and DTM (right). Fire burnt scars (light grey) and fire outbreaks (✻) are reported. The topographical profiles (centre and lower) are computed along the sections AB and CD suggesting an overall upslope fire spread.

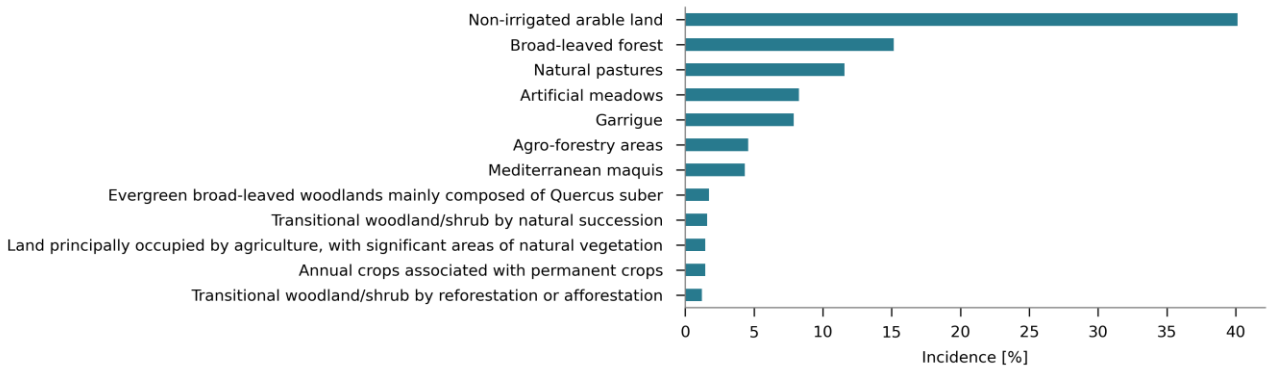

Figure 8-12 Incidence [%] of land use classes on the burnt scar of Isili fire event.

8.3.3 Gonnosfanadiga

The case study of Gonnosfanadiga refers to a wildland fire occurred on July 31st, 2017 in the agricultural lands of the municipality of Gonnosfanadiga (SU) in the sub-region of Medio Campidano. According to a press release of the Autonomous Region of Sardinia (2017a), the investigations by the local Forestry Corps (*Corpo forestale e di vigilanza ambientale della Regione Autonoma della Sardegna*, CFVA) have ascertained the anthropic origin of the event as a result of an act of negligence and the violation of the local regulations prohibiting the disposal of waste through the use of fire. Reconstructions identified an outbreak in the early hours of July 31st in Sibiri, in the countryside of Gonnosfanadiga, as the source of the secondary outbreak, which, in the afternoon of the same day at around 12:00 UTC (14:00 local time), sustained by strong south-east winds, burned an overall surface of 2,036 ha south-west of the residential area of the municipality of Arbus (SU) (Figure 8-13). Aerial fire suppression activities have been diffusely carried out, along with ground interventions, by 9 aircrafts of both the local Forestry Corps and the State air fleet. Notwithstanding fire suppression activities, the event has damaged properties, touristic infrastructure, and farms, with grave consequences for crops and livestock. The dual carriageway SS126 "Sud Occidentale Sarda" was temporarily closed, from kilometre 73 to kilometre 80. Then, the fire front climbed over the ridge between Punta Tintillonis (609 m) and Passo Bidderdi (492 m) threatening residential areas of Ingurtosu, Pitzinurri, and Gennamari, and compelling the evacuation of the prison "Is Arenas", in Bau. Finally, the fire front has reached the aeolian dune field of Piscinas, a Site of Community Importance (SCI ITB040071, "Da Piscinas a Riu Scivu") according to the European Commission Habitats Directive (92/43/EEC), burning 355 ha of Mediterranean maquis and garrigue of the dune field, including patches of costal dunes with *Juniperus* spp. (Priority Habitat 2250*).

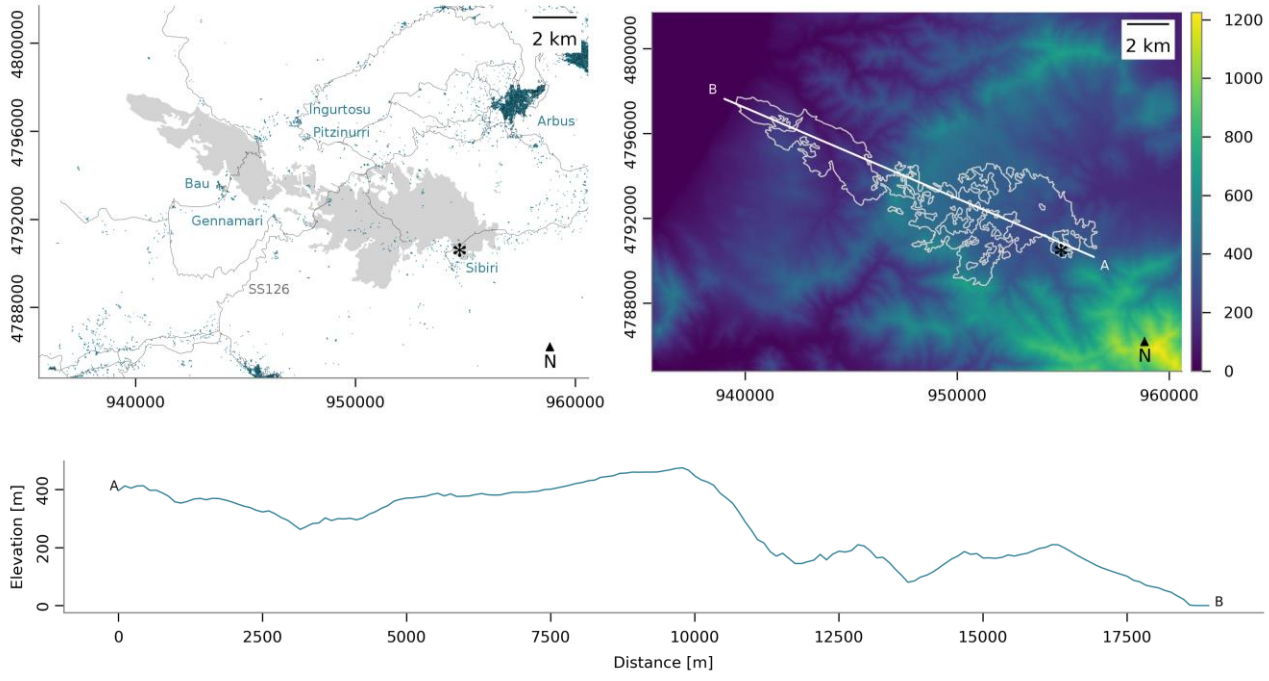

Figure 8-13 Gonnosfanadiga case study: buildings and roads from the topography database provided by the Autonomous Region of Sardinia (upper left) and DTM (upper right). Fire burnt scars (light grey) and fire outbreaks (✻) are reported. The topographical profile (lower) is computed along the section AB suggesting a downslope fire spread.

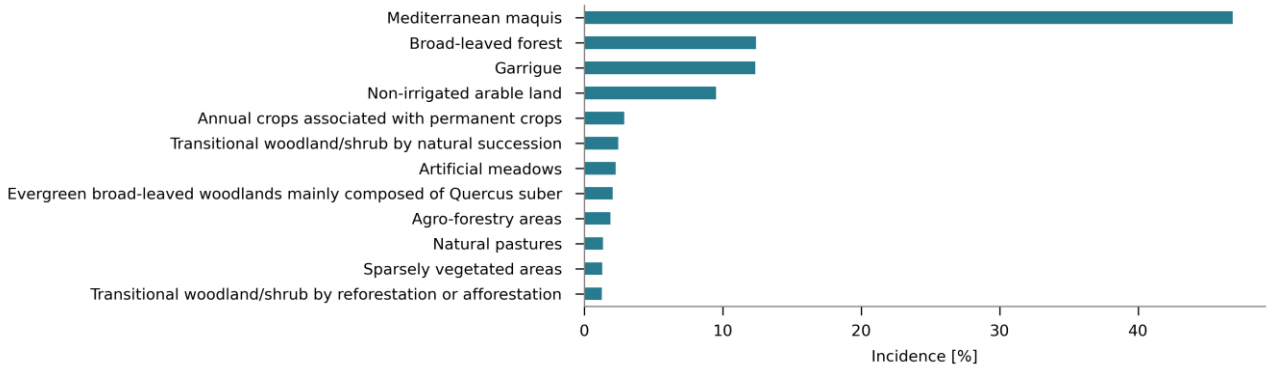

Figure 8-14 Incidence [%] of land use classes on the burnt scar of Gonnosfanadiga fire event.

In terms of land use classes (Autonomous Region of Sardinia, 2008), the event mainly consumed Mediterranean maquis (46.8%) and garrigue (12.4%), broad-leaved forests (12.4%), non-irrigated arable lands (9.5%), non-permanent crops associated with permanent crops, including fruit trees or olive trees or vines (2.9%), arable lands with significant areas of natural vegetation (2.5%), artificial meadows (2.3%), and broad-leaved forests with cork oak (2%) (Figure 8-14). According to the habitat map developed as part of the national project *Carta della Natura* (Camarda et al., 2015), burnt areas included Mediterranean maquis and garrigue (58.5%), complex cultivation patterns (14.3%), costal dunes with *Juniperus* spp. (10.5%), Mediterranean meadows (7.9%), and broad-leaved forests with evergreen oak (*Quercus ilex* L.) (4.9%) and cork oak (*Quercus suber* L.) (2.1%).

8.3.4 Villagrande Strisaili

Villagrande Strisaili wildfire event occurred on July 25th, 2017, burning an overall surface of 489 ha. The event is poorly documented except for some information that have been retrieved from local newspapers and chronicles. The primary outbreak is supposed to have been taken place at around 10:00 UTC (12:00 local time) along the provincial road SP27 at the level crossing in Tricarai, in the countryside of Villagrande Strisaili (NU), in the sub-region of Ogliastra. Sustained by strong north-west winds, the fire damaged at least 3,600 sleepers of the tourist railway line Arbatax-Gairo causing an estimated economical losses 300,000 euros. Aerial fire suppression interventions have been suspended due to the turbulence caused by the convection column.
The fire spread across complex topographies (Figure 8-15), essentially consuming Mediterranean maquis (63.1%) according to the land use classes (Autonomous Region of Sardinia, 2008). The remaining portions of the burnt area is represented essentially by olive groves, and vineyards, and complex cultivation patterns (Figure 8-16).

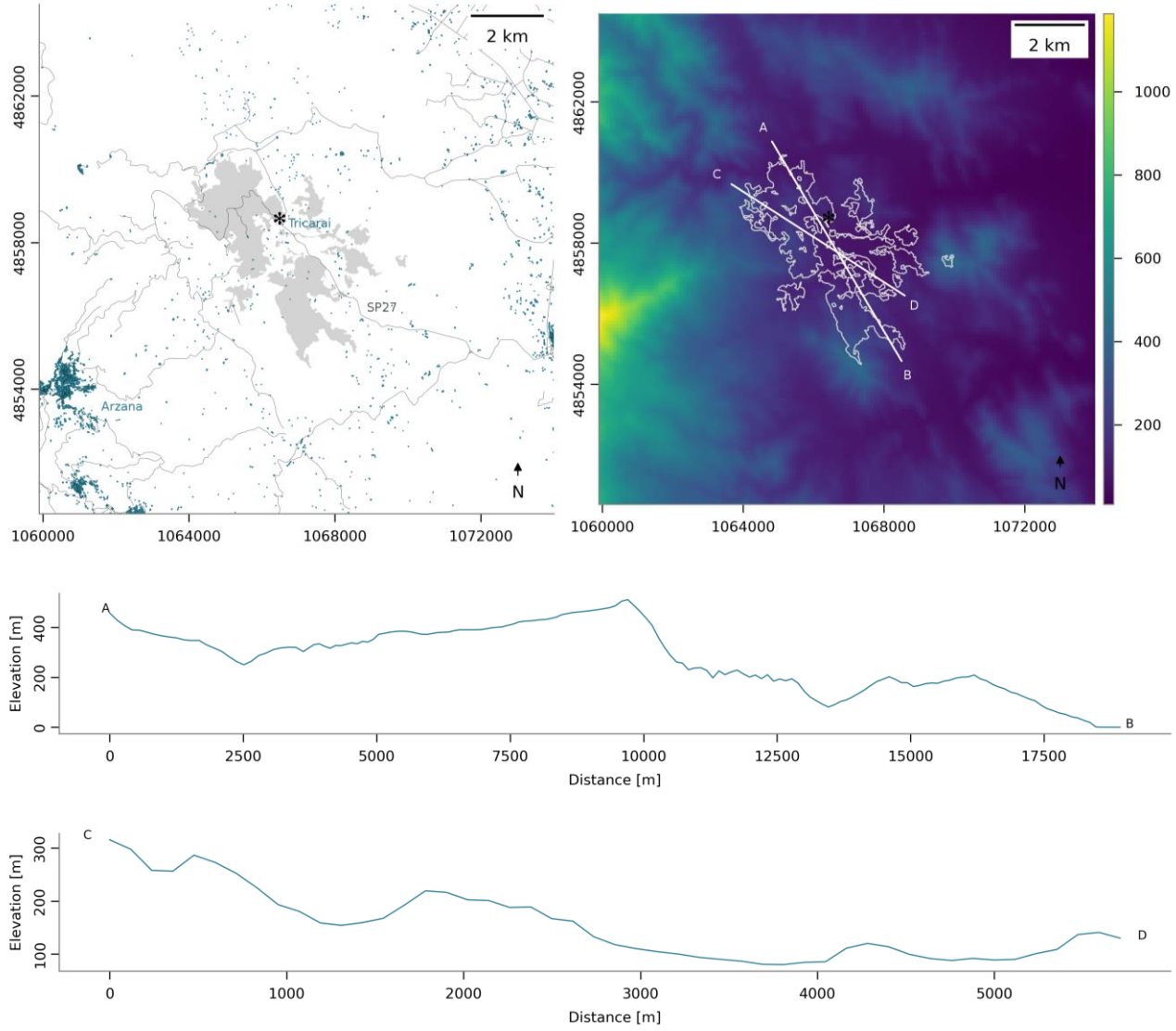

Figure 8-15 Villagrande Strisaili case study: buildings, roads, and railway lines from the topography database provided by the Autonomous Region of Sardinia (left) and DTM (right). Fire burnt scars (light grey) and fire outbreaks (✻) are reported. The topographical profiles (centre and lower) are computed along the sections AB and CD suggesting a mixed upslope-downslope fire spread.

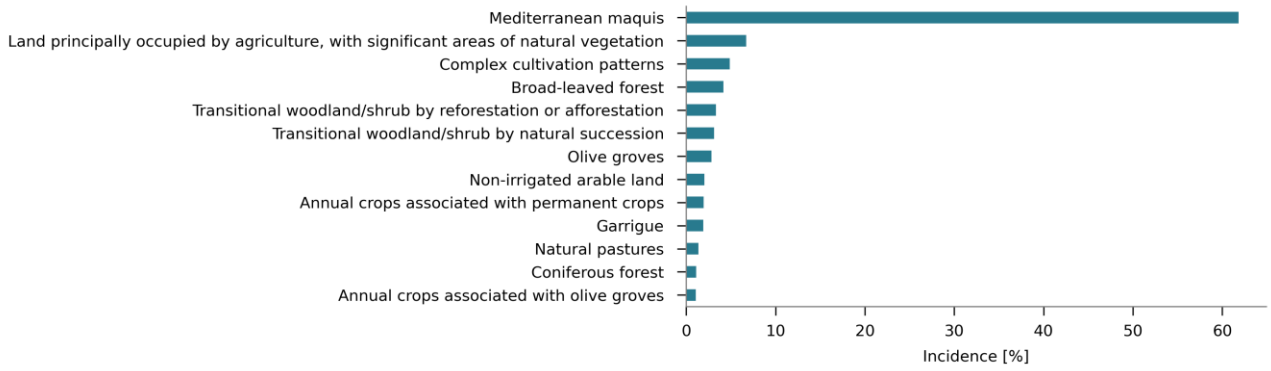

Figure 8-16 Incidence [%] of land use classes on the burnt scar of Villagrande Strisaili fire event.

Chapter 9

Model application

The extensive review of the state of the art for the estimation of the drivers of surface fire behaviour (Chapter 5) suggests that parameters characterising fuel models and fuel moisture content have been traditionally collected in the field following standard protocols. Nevertheless, field measurements have revealed to be inadequate to elaborate operative response plans due to the effort needed to obtain a sufficient number of samples over a realistically wide spatial extent in a brief period of time (San-Miguel-Ayánz et al., 2011). Whereas field samplings still remain crucial in models' calibration and validation, the general tendency is to shift the attention on remote sensing methods for spatial mapping of fuel models and fuel moisture content (Mutlu, Popescu, Stripling, et al., 2008).
An in-depth investigation of freely available products from optical sensors onboard non-commercial satellites have been conducted in order to define a comprehensive methodology for a near real-time estimation of the drivers of surface fire behaviour in the pre-fire environment.
Data collection and processing for the estimation of the drivers of surface fire behaviour has been mainly performed by means of **Google Earth Engine** (EE), a cloud-based platform for planetary-scale geospatial analysis (Gorelick et al., 2017). The EE data catalogue holds a large repository of publicly available geospatial datasets, including observations from a variety of satellite and aerial imaging systems in both optical and non-optical wavelengths, environmental variables, weather and climate forecasts and hindcasts, land cover, and topographic and socioeconomic datasets. Datasets not yet included in the EE data catalogue, have been retrieved from other data sources and loaded as external assets. The major advantage offered by EE is an intrinsic **parallel computing** service that can be accessed and controlled through an Internet-accessible application programming interface (API), the EE JavaScript API, and an associated web-based interactive development environment (IDE), the EE Code Editor. Indeed, EE uses a **lazy evaluation** which is a computer science language theory strategy that delays the evaluation of an expression as late as possible or until the value is needed, e.g. only the portions of output that are necessary to fulfil the current request are computed. EE programs track a chain of function calls before their execution and assemble them into a directed acyclic graph expressing the complete computation. This dependency graph is then sent to the EE service for evaluation. This structure potentially allows to maximize the geographical extent for computations, i.e. to simultaneously evaluate the model outputs at a global scale.
The EE programs developed for the purpose of the present research project cover the whole procedure, ranging from data collection to data pre-processing, and have been initially implemented within the Code Editor, which enables rapid visualisation of results and exploration and analysis of spatial data. However, to easily integrate the EE programs within the working environment chosen for the present study, the code has been converted by means of the Earth Engine **Python API** that have been accessed through Jupyter Notebook.

9.1 Data sources

Within the context of this project, information on the spatiotemporal variability of fuel models, horizontal wind speed and direction and of live and dead fuel moisture content have been gathered mainly from Earth Observation (EO). Diverse products have been retrieved from online archives made available by United States Government agencies (NASA, 2020; USGS, 2020) as well as from the Copernicus Open Access Hub of the European Space Agency (ESA, 2020). However, most of the collected data products have been lately made available also in the EE data catalogue, as summarised in Table 9-1. The selection of specific products and granules will be further detailed in the current Section.

9.1.1 Static assets: topography and fuel models

Topography and fuel models are considered as static in time because their variability is limited at the temporal scale of interest for wildfire events' spatial simulation modelling.

Dip angle and direction have been computed from the regional Digital Terrain Model (DTM) with a spatial resolution of 5 m (Autonomous Region of Sardinia, 2010). The DTM represents the bare ground surface excluding vegetation, anthropic structure and infrastructure, or other geomorphological objects that are not mappable at a 5 m resolution but might have a significative influence on the surface fire spread and growth.

An indirect approach has been chosen to generate maps of **fuel models**. Hence, different maps designed for different purposes have been jointly examined in order to elicit the information required for defining homogeneous vegetation units: (i) the land cover map from the CORINE Land Cover (CLC) programme (European Union, Copernicus Land Monitoring Service, European Environment Agency (EEA), 2012); (ii) the land use map of Sardinia developed at a regional scale (Autonomous Region of Sardinia, 2008); (iii) the habitat map developed as part of a national project *Carta della Natura* coordinated by the Italian Institute for Environmental Protection and Research (ISPRA) (Camarda et al., 2015). The CLC 2012 map consists of an inventory of land cover across Europe in 44 unique classes with a minimum mapping unit of 25 ha, and a minimum mapping width of 100 m. Whereas the land cover indicates the physical land type and can help in distinguishing amongst forest, wetlands, or grasslands, the land use documents how people are using those lands. However, the land use map provided by the Autonomous Region of Sardinia, has been realised according to the same standard classification methodology of the CORINE Land Cover programme, and units have been adjusted through photointerpretation and field sampling (Autonomous Region of Sardinia, 2008). The land use map has a minimum mapping unit of 0.5 ha in urban areas and 0.75 ha in rural and natural areas (reference scale 1:25.000). The habitat map, instead, provides detailed information on regional plant communities, on their phytosociology, on their specific composition, and on forest stratification and canopy cover. The habitat map by ISPRA has a minimum mapping unit of 1 ha and has been developed by applying supervised machine learning classification techniques on Landsat products that have been trained and validated with 10.000 field measurements (Camarda et al., 2015).

Data sources employed for fuel model assignment have included: (i) the Global Aboveground and Belowground Biomass Carbon Density Maps (Spawn and Gibbs, 2020), provided by the NASA's Oak Ridge National Laboratory (ORNL) Distributed Active Archive Center (DAAC), and (ii) the GEDI Level 2B dataset Canopy Cover and Vertical Profile Metrics, provided by NASA (Dubayah,

Tang, et al., 2020). Specifically, the Global Aboveground and Belowground Biomass Carbon Density Maps integrate multiple local and global data sources, including a combination of L-band SAR imagery and ancillary maps of percent tree cover and landcover, in order to provide temporally consistent and harmonized global maps of above-ground and below-ground biomass carbon density estimates (Mg C ha^{-1}) across different vegetation types for the year 2010 at a 300 m spatial resolution (Spawn et al., 2020). The GEDI Level 2B dataset provides, instead, canopy cover metrics, canopy height above ground metrics as well as vertical structure metrics. The GEDI lidar instrument consists of 3 lasers producing a total of 8 beam ground transects of structural information separated by about 600 m across the flight track direction within a ~4.2 km swath. The GEDI waveforms are intended to quantify the vertical distribution of vegetation at different heights above the ground at a footprint resolution of 25 m (Dubayah, Blair, et al., 2020). Data collected from the GEDI Level 2B dataset include the first year of observations (April 2019 - June 2020) and have been investigated in an attempt to reconstruct the stratification of forested areas.

9.1.2 Dynamic assets: fuel moisture content and horizontal wind speed and direction

Information on the spatiotemporal variability of live and dead fuel moisture have been gathered from the adaptation of empirical relationships defined in literature for plant communities in Mediterranean-type climate regions.
In the search for a trade-off between spatial and temporal resolution, major attention has been focused on the MODIS instrument onboard the Terra satellite. LFMC and DFMC have been retrieved by combining MOD09GA MODIS Terra Surface Reflectance Daily Level 2 (Vermote and Wolfe, 2015)

Table 9-1 Data sources used for the estimation of the drivers of fire spread.

Source	Description	EE data catalogue
Copernicus Land Monitoring Service, 2012	CORINE Land Cover 2012 (1:250.000)	COPERNICUS/CORINE/V20/100m
Autonomous Region of Sardinia, 2008	Land use map for the year 2008 (1:25.000)	(external asset)
Camarda et al., 2015	Habitat map for the year 2013 (1:50.000)	(external asset)
Spawn and Gibbs, 2020	Global Aboveground and Belowground Biomass Carbon Density Maps for the year 2010	NASA/ORNL/biomass_carbon_density/v1
Dubayah, Tang, et al., 2020	GEDI L2B Canopy Cover and Vertical Profile Metrics Data Global Footprint Level V001	(external asset)
Abatzoglou, Dobrowski, et al., 2018	TerraClimate, a high-resolution (1/24°, ~4 km) global dataset of monthly climate and climatic water balance from 1958-2015	IDAHO_EPSCOR/TERRACLIMATE
Vermote and NOAA CDR Program, 2019	NOAA CDR of AVHRR Normalized Difference Vegetation Index (NDVI), Version 5	NOAA/CDR/AVHRR/NDVI/V5
Vermote and Wolfe, 2015	MODIS MOD09GA.006 Terra Surface Reflectance Daily Global 1km and 500m	MODIS/006/MOD09GA
Wan et al., 2015	MODIS MOD11A1.006 Terra Land Surface Temperature and Emissivity Daily Global 1km	MODIS/006/MOD11A1
Autonomous Region of Sardinia, 2010	Digital Terrain Model (DTM), pace 5 m	(external asset)
Muñoz Sabater, 2019	ERA5-Land hourly data from 1981 (~9 km)	ECMWF/ERA5_LAND/HOURLY

and MOD11A1 MODIS Terra Land Surface Temperature Daily Level 3 (Wan et al., 2015) products. Additional data sources included: (i) the NOAA AVHRR NDVI (Vermote and NOAA CDR Program, 2019) and (ii) the TerraClimate dataset of high-resolution (1/24°, ~4 km) monthly climate and climatic water balance for global terrestrial surfaces from 1958–2019 (Abatzoglou, Dobrowski, et al., 2018).
Horizontal wind speed and direction data have been retrieved from the climate reanalysis ERA5-Land, which has been produced by replaying the land component of the European Centre for Medium-Range Weather Forecasts (ECMWF) ERA5 climate reanalysis (European Union, Copernicus Climate Change Service, European Environment Agency (EEA), 2020; Muñoz Sabater, 2019). Speed and direction of the horizontal wind are provided every 3 hours as eastward and northward component of the 10 m wind above ground with a spatial resolution of 9 km.

9.2 Data pre-processing

9.2.1 Harmonised dataset of fuel models

The procedure of assigning fuel models to homogenous patterns of vegetation requires a profound knowledge of the local plant communities as well as a deep comprehension of the distinctive characteristics of each fuel model including fuel bed properties and fuel particle properties (described in Section 5.1). The differential effects produced by diverse fuel models on surface fire behaviour have been investigated in literature with various levels of detail, mainly by comparing fuel models within each developed set rather than across different sets. That is to say, the effects of each of the 53 standard and dynamic fuel models on surface fire behaviour have been exhaustively described in terms of the fire descriptors defined by Rothermel (H. E. Anderson, 1982; Andrews, 2018; Rothermel, 1983; Scott and Burgan, 2005). Accordingly, authors that developed single sets of custom models specific for the European Mediterranean fuel types evaluated the differential effects of their fuel models in terms of fire descriptors. However, only few comparative studies have been conducted in recent years with the specific aim of analysing differential effects on fire descriptors of standard and custom fuel models that have been developed for the European Mediterranean vegetation types (Arca et al., 2007, 2009; Rodríguez y Silva and Molina-Martínez, 2012; Salis et al., 2016).
Available sets of standard and custom fuel models have been collected from literature and harmonised to populate a standardised database of 123 fuel models (Appendix) divided into 2 subsets: a set of **53 fuel models for North America** (Albini, 1976b; Rothermel, 1972; Scott and Burgan, 2005) and a set of **70 fuel models for European Mediterranean regions** (Dimitrakopoulos, 2002; Duce et al., 2012; Elia et al., 2015; Godinho-Ferreira et al., 2005; Rodríguez y Silva and Molina-Martínez, 2012). Firstly, the whole dataset has been harmonised to the Imperial system to maintain measure units consistent with the original implementation of the Rothermel's model. Secondly, some fuel models required additional processing. Specifically, fuel models developed by Dimitrakopoulos (2002) were characterised only by fuel bed properties, while fuel particle properties have been obtained from Dimitrakopoulos and Panov (2001) by mediating the values measured for the dominant plant species compatible with described fuel model. Finally, each fuel model has been given a unique identifier with a two-character prefix reflecting the prevalent fire carrying fuel type following the nomenclature

by Scott and Burgan (2005) and Rodríguez y Silva and Molina-Martínez (2012): GR for nearly pure grass fuels; GS for mixed grass and shrub fuels; SH for dominant shrub; TU for timber understory with grass and shrub; TL for timber litter; SB for slashed or blowdown timber. An exception to these classification is represented by the fuel models developed for 19 different forest types in Portugal and reported by Fernandes (2009). Those fuel models describe timber understory with grass and shrub (TU) but are further classified as TOT for open and tall timber stands, TOL for open and low timber stands, TCT for closed and tall timber stands, and TCL for closed and low timber stands.

9.2.2 Assignment of fuel models

The CORINE Land Cover is the most used map in literature for the development of maps of fuel models in Sardinia and in the European Mediterranean regions (Arca et al., 2007; Bajocco et al., 2015; Rodriguez-Aseretto et al., 2013; Salis et al., 2013, 2016). According to the feature importance analysis of the developed proxy model of surface fire spread (Chapter 6, Section 6.2.2.1) fuel models seem to represent the most important driver. Hence, the land use map of Sardinia (1:25.000) for the year 2008 (Autonomous Region of Sardinia, 2008) integrated with information from the habitat map (Camarda et al., 2015) has been preferred as reference map for the present study for the **definition of homogenous patterns** of vegetation.

Study areas have not been directly investigated in the field. Fuel models have been assigned to each homogeneous pattern of vegetation by combining different data sources. A distinct map has been generated for each of the 2 subsets of fuel models, one for North American fuel models (Rothermel, 1972; Scott and Burgan, 2005) and one for European Mediterranean fuel models (Dimitrakopoulos, 2002; Duce et al., 2012; Elia et al., 2015; Godinho-Ferreira et al., 2005; Rodríguez y Silva and Molina-Martínez, 2012). In both cases, the process of **fuel model assignment** followed distinct patterns: one for grasslands and shrublands (GR, GS, and SH fuel models) and the other for timber litter and understories (TU and TL fuel models).

In order to distinguish amongst GR, GS, and SH fuel models, their total live and dead ultrafine (1 h time lag) fuel loadings have been compared with the amount of above-ground biomass carbon which have been estimated for grasslands and shrublands by Spawn et al. (2020) and distributed as an harmonised global map of above-ground and below-ground biomass carbon density for the year 2010. The unavailability of locally specific products lead to the utilisation of these maps even though they are more explicitly intended for global applications and not fully suitable for areas where shrublands biomass is of primary importance (Spawn and Gibbs, 2020). Because of these assumptions, credence should be given to the pixel-level uncertainty estimates; however, for the purpose of this study the accuracy of the estimates has not yet been evaluated. Furthermore, while fuel loadings can be accurately estimated from above-ground biomass in grasslands and savannas (Eames et al., 2021; Garcia et al., 2017), in shrublands and timberlands the fuel load, which is the combustible portion of the biomass, should be distinguished from the total above-ground biomass (Pearce et al., 2010). The total above-ground biomass includes all live and dead matter from the overstorey and understorey layers as well as surface litter, whereas the above-ground available fuel comprises fine dead material and a fraction of the fine live material, because fires rarely consume the entire live material of shrublands and timberlands (Ivanova et al., 2020). Nonetheless, for the aim of the present study, the fuel loadings of both grasslands and shrublands have been approximated to the total above-ground biomass.

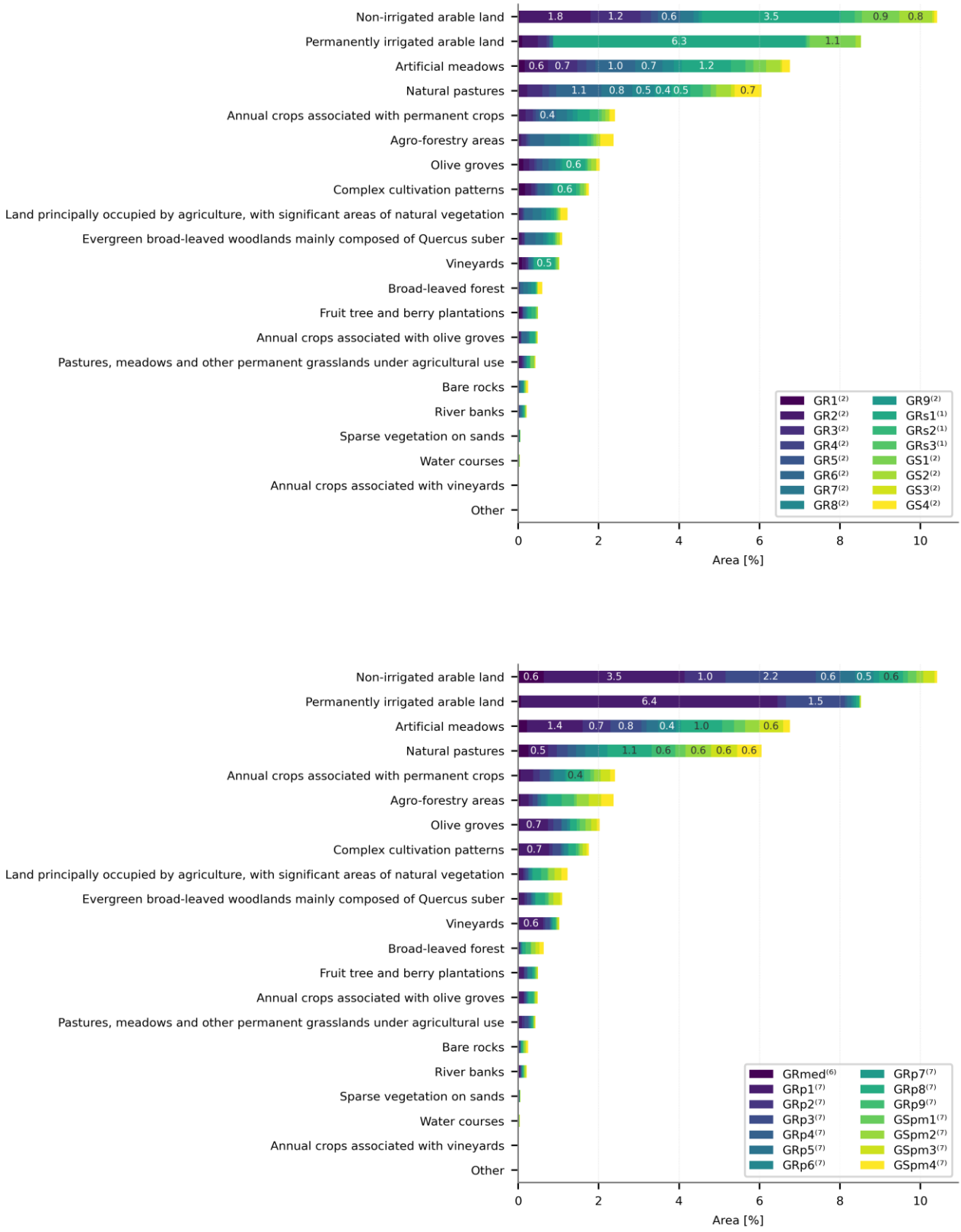

Figure 9-1 Percent distribution of North American (upper) or Mediterranean (lower) fuel models assigned to each land use geometries dominated by herbaceous material and ranked according to their representativeness in the study area. Superscripts beside the fuel model's code refer to (1) Rothermel, 1972, (2) Scott and Burgan, 2005, (3) Duce et al., 2012, (4) Elia et al., 2015; (5) Godinho-Ferreira et al., 2005, (6) Dimitrakopoulos, 2002, (7) Rodríguez y Silva and Molina-Martínez, 2012.

Firstly, zonal statistic methods have been employed to aggregate information on the above-ground biomass and to assign a mean value to each land use geometry. Secondly, this mean value has been then compared with the total live and dead fine fuel load of each fuel model of the harmonised dataset. Finally, the fuel model with a total fine fuel load closest to the average above-ground biomass has been assigned to each land use geometry. The same procedure has been applied on land use geometries dominated by both grassy (Figure 9-1) and shrubby fuels (Figure 9-2).

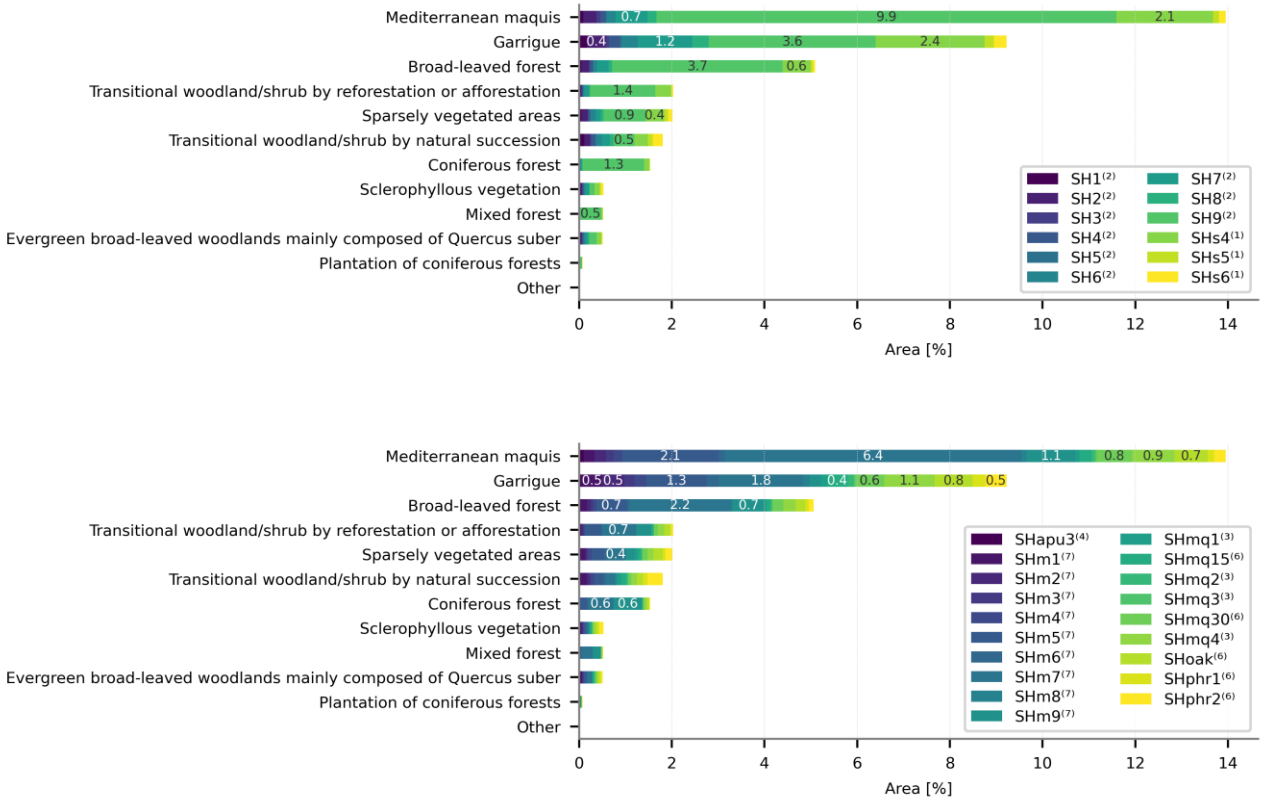

Figure 9-2 Percent distribution of North American (upper) or Mediterranean (lower) fuel models assigned to each land use geometries dominated by shrubs and ranked according to their representativeness in the study area. Superscripts beside the fuel model's code refer to (1) Rothermel, 1972, (2) Scott and Burgan, 2005, (3) Duce et al., 2012, (4) Elia et al., 2015; (5) Godinho-Ferreira et al., 2005, (6) Dimitrakopoulos, 2002, (7) Rodríguez y Silva and Molina-Martínez, 2012.

A different approach has been applied for the assignment of TU and TL fuel models. The fuel loading of fuel models for woodlands and timberlands only account for forest litter and understory. Contrarily, the global above-ground biomass carbon also includes the forest overstory, which is not easily separable from the forest understory. Hence, the assignment of TU and TL fuel models to each homogeneous vegetation patch is based on its prevalent fire-carrying fuel type as well as on the specific descriptions for these models provided by the different authors. Therefore, the GEDI relative height (RH100) metrics have been investigated with the aim of reproducing the vertical stratification of vegetation with a height of 3 m or above in each homogeneous patch within the study areas. Low-to-medium quality shots have been masked out in order to filter only highest quality data, i.e. shots with a quality flag equal to 1, indicating they meet criteria based on energy, sensitivity, amplitude, and real-time surface tracking quality. The filtered GEDI dataset resulted in 193,662 shots and only 860 shots reported a height of 3 m or above. As observed by Potapov et al. (2020) GEDI do not

discriminate trees from building, confounding vegetation height mapping in urban areas: GEDI shots reporting a RH100 of 3 m or above show a good agreement with the distribution of broad-leaved and coniferous woodlands, but groups of points are clustered together close to the urban centres of Sassari and Cagliari (Figure 9-3). Moreover, vegetation height is overestimated in areas of complex topography, especially on steep slopes.

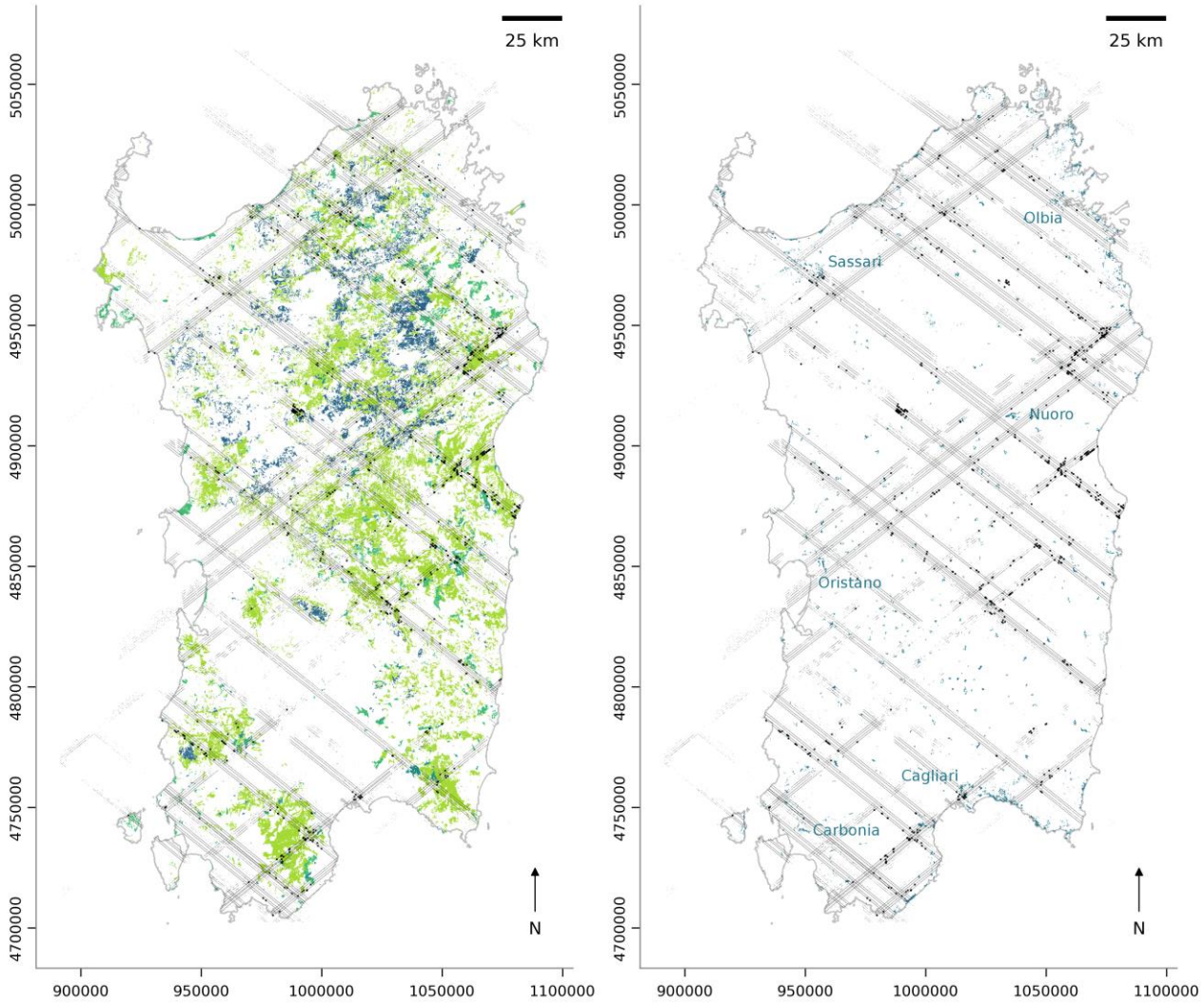

Figure 9-3 GEDI high quality dataset (grey dots) with highlighted 3 m height shots (black dots). Shots' location is compared with the location of broad-leaved (light green), coniferous (dark green), and mixed woodlands (blue) (left) and urban areas (right).

9.2.3 Estimation of fuel moisture fractions

9.2.3.1 Live fuel moisture fraction

Obtaining spatially comprehensive and temporally frequent estimates for LFMC, less dependent on meteorological variables than DFMC, is far more problematic. Remotely sensed data provided the opportunity to estimate LFMC over large areas at fine spatial and temporal resolutions (Yebra et al., 2013). According to the need for a methodology applicable for operational purposes, the empirical approach proposed by Chuvieco et al. (2004) and updated by García et al. (2008) has been preferred over simulated approaches. Those empirical relations, calibrated and validated in different homogeneous areas of grasslands and shrublands across Spain, has been applied for the LFMC estimation in the selected study areas. The original relations from García et al. (2008) assess the LFMC from the NOAA AVHRR as a function of the day of the year, the Normalized Difference Vegetation Index (NDVI) and the Land Surface Temperature (LST). The NOAA AVHRR capability to estimate both NDVI and LST has been compared in literature to those of MODIS Terra and those empirical relations have been employed to numerically adjust MODIS Terra estimates to AVHRR in order to improve the spatial resolution of the analysis.

Even if MODIS Terra LST was expected to produce higher quality LST estimates with respect to AVHRR, Frey et al. (2012) showed a good agreement (r^2 = 0.99) between AVHRR LST and MODIS Terra LST, which accuracy is claimed to be better than 1 K. Hence, for the purposes of the present research, estimates from MODIS MOD11A1.006 Terra Land Surface Temperature (Wan et al., 2015) have been assumed as a good proxy for AVHRR LST estimates and directly employed for LFMC evaluation.

Contrarily, Fensholt and Sandholt (2005) demonstrated that in situ NDVI was more accurately emulated by estimates from the MODIS Terra rather than from AVHRR. The AVHRR sensors were not originally intended for vegetation study and their spectral configuration does not permit an accurate atmospheric correction introducing errors in AVHRR estimates of surface NDVI (Fensholt and Proud, 2012). Fensholt and Proud (2012) derived NDVI AVHRR to MODIS conversion coefficients specific for land cover types on a global scale, but Europe were not directly included in the analysis. Hence, a similar approach has been adopted in this study to develop NDVI AVHRR to MODIS conversion coefficients specifically tailored to Sardinia. Daily AVHRR NDVI (Vermote and NOAA CDR Program, 2019) and MODIS MOD09GA.006 Terra Surface Reflectance (Vermote and Wolfe, 2015) have been collected from the EE data catalogue for the period 2016-2018. NDVI composites have been created from daily cloud-masked 250 m MODIS Terra surface reflectance images. Punctual NDVI values have been sampled from each couple of AVHRR NDVI and MODIS Terra NDVI daily water and cloud-masked images. Pixel wise linear regression analyses have been performed to compare AVHRR NDVI and MODIS Terra NDVI monthly estimates as a function of different CORINE Land Cover classes (Figure 9-4). The agreement between AVHRR and MODIS NDVI estimates varies according to the CORINE Land Cover class, showing the best accuracy for permanently irrigated arable lands (r^2 = 0.73), non-irrigated arable lands (r^2 = 0.62), and pastures (r^2 = 0.7), whereas the worst accuracy is observed for coniferous woodlands (r^2 = 0.21), broad-leaved woodlands (r^2 = 0.24), and sclerophyllous vegetation (r^2 = 0.28).

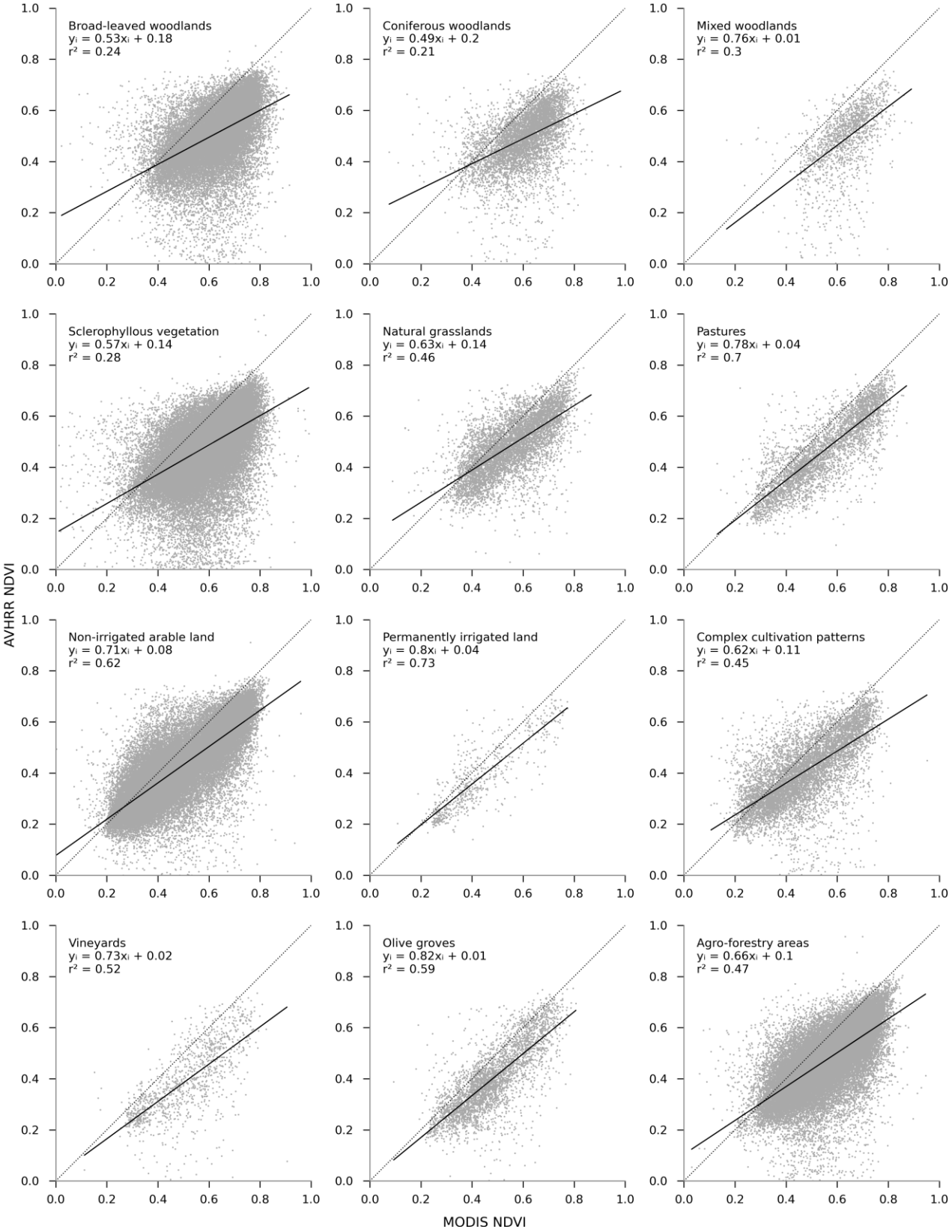

Figure 9-4 Scatterplots including regression line (black line) with slope, intercept, and coefficient of determination for the comparison between AVHRR NDVI monthly estimates and MODIS NDVI monthly estimates over the period 2016-2018 in Sardinia for different CORINE Land Cover classes. Pixels containing clouds or cloud shadows and pixels over water have been masked.

In order to avoid altering the empirical relations defined by Chuvieco et al. (2004) and García et al. (2008), MODIS Terra NDVI estimates have been numerically calibrated to AVHRR NDVI measures by means of the previously derived conversion coefficients specific for each land cover class (Fensholt and Proud, 2012).
Then, MODIS Terra LST and adjusted MODIS Terra NDVI have been employed to estimate LFMC according to García et al. (2008), who derived different empirical estimation models for grasslands, Equation [9.1], and shrublands, Equation [9.2]:

$$LFMC_{grass} = 27.745 - 1.1 \times LST + 293.197 \times NDVI + 0.676 \times f_d \quad [9.1]$$

$$LFMC_{shrub} = 31.773 - 0.476 \times LST + 45.81 \times NDVI + 0.761 \times f_d \quad [9.2]$$

where f_d is the function of the day of the year, derived by an adjustment based on a nonlinear regression analysis, and expressed by the Equation [9.3]:

$$f_d = A \times \sin\left(\pi \times \frac{DOY + \varphi}{365}\right)^x + t \quad [9.3]$$

where A is the amplitude of the range of LFMC values, DOY is the day of the year (from 1 to 365), φ is the initial phase, i.e. the DOY at which the actual maximum LFMC value is reached, x represents the flatness of the function, which will depend on the water stress, and t is the offset over the y axis, which is related to the minimum LFMC value. García et al. (2008) developed different set of parameters for grasslands and shrublands, for dry and wet years, which are presented in Table 9-2. Accordingly, dry and wet years have been discerned by evaluating the regional drought stress by means of the Cumulative Water Balance Index (CWBI) (Dennison et al., 2003). The CWBI cumulatively sums precipitation and reference evapotranspiration over time so that the CWBI at time T is defined by the Equation [9.4]:

$$CWBI_T = \sum_{t=0}^{T} (P_t - ET_{0t}) \quad [9.4]$$

where t is the time interval, P_t is the precipitation over each interval, and ET_{0t} is the reference evapotranspiration over each interval. Monthly cumulative precipitation and reference evapotranspiration, calculated using the Penman Montieth approach, have been estimated from the TerraClimate dataset (Abatzoglou, Dobrowski, et al., 2018), which provides monthly climate and climatic water balance for global terrestrial surfaces at a resolution of ~4 km. Only years with a negative CWBI, calculated monthly for each hydrological year from September to April, have been classified as dry.

Table 9-2 Parameters for f_d developed by García et al. (2008) for grasslands and shrublands, for dry and wet years.

	$CWBI$	A	φ	x	t
Dry grasslands	< 0	99.08	55.15	25.97	3.93
Wet grasslands	> 0	280.35	67.73	15.82	1.28
Dry shrublands	< 0	57.57	61.78	11.72	50.97
Wet shrublands	> 0	61.66	63.44	8.8	76.21

9.2.3.2 Dead fuel moisture fraction

Since DFMC is more closely related to meteorological conditions, it is traditionally estimated in literature as a function of air temperature and relative humidity from ground weather stations (Aguado et al., 2007). To reduce potential errors arising from spatial interpolation, in this study, DFMC has been indirectly predicted from remotely sensed data according to Nolan et al. (2016), who showed the moisture content of suspended dead fine fuels can be monitored and forecast across large spatial areas using a model based on vapour pressure deficit D as expressed by the Equation [9.5] from Resco de Dios et al. (2015). Nolan et al. (2016) suggested this model can be effectively applied across forest and woodlands without the need for site-specific calibration, but warned the tendency of remotely sensed LST to be under-predicted in arid and semi-arid areas.

$$DFMC = 7.86 + 140.94 \times e^{-3.73D} \quad [9.5]$$

The vapour pressure deficit D has been estimated by applying Equation [9.6], an empirical relationship between the saturation vapour pression e_s and ground-based observations of D defined by Hashimoto et al. (2008) and further validated by Nolan et al. (2016):

$$D = 0.353 \times e_s + 0.154 \quad [9.6]$$

where e_s is the saturation vapour pression, calculated using Equation [9.7]:

$$e_s = 0.6108 \times e^{17.27 \times \frac{LST}{LST \times 237.3}} \quad [9.7]$$

where LST has been estimated from MODIS MOD11A1.006 Terra Land Surface Temperature (Wan et al., 2015), as originally suggested by Nolan et al. (2016).

9.2.4 Downscaling the horizontal wind at midflame height

Speed and direction of the horizontal wind have been retrieved from ERA5-Land (Muñoz Sabater, 2019) as eastward and northward component of the 10 m wind above ground with a spatial resolution of 9 km and a 3 hour forecast interval.

The mass conserving model implemented by Forthofer et al. (2009) has been employed to downscale the horizontal wind predictions from ERA5-Land to a 100 m spatial resolution. Horizontal winds at 10 m height above ground have been extrapolated at 20 ft above ground by means of the mass conserving model and then reduced to the midflame height by computing unsheltered or sheltered wind adjustment factors (WAF) according to Equations [5.1] and [5.2] as defined by Andrews (2012). The horizontal fraction canopy cover c and the crown ratio r for the evaluation of the sheltered conditions have been deduced form the land cover map and the habitat map.

9.3 Model performance

The data pre-processing methodologies described in Section 9.2 have been applied to extrapolate multitemporal maps of drivers of fire spread describing the geo-environmental conditions at the ignition time and their spatiotemporal evolution throughout the duration of the fire event of the selected case studies (Figure 8-8). Obtained maps of horizontal wind speed and direction, dip angle and direction, fuel models and fuel moisture fractions, have been provided as input to the developed proxy model for predicting fire spread (Chapter 6). Resulting sets of raster maps of maximum rate of spread, direction of the maximum rate of spread, and eccentricity have been turned into **hexagonal meshes** preserving the cells' area by means of the Hex-utils tool-kit (de Sousa and Leitão, 2017) to be provided as inputs to the developed ABM for simulating the fire growth (Chapter 7). The whole modelling procedure (Figure 9-5) has been run twice in order to test the performance of each of the two subsets of fuel models, the one designed for North America and the one specifically developed for European Mediterranean regions.

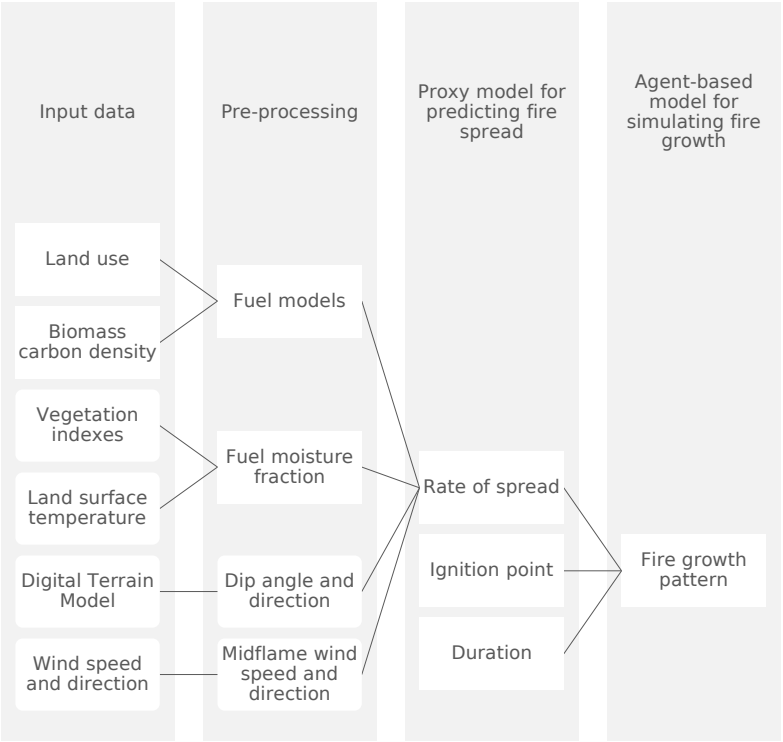

Figure 9-5 Processing pipeline.

The Web Mercator or WGS84/Pseudo-Mercator projected coordinate system (EPSG:3857) has been adopted as reference coordinate system. It is a variant of the Mercator projection that, despite significant distortion in high latitude areas, has become the standard for sharing data on the web (Lumley and Sieber, 2019). Spatial and temporal extents vary with the selected case study according to data availability. The spatial extent of the model's computational region varies according to the simulated scenario but typically includes a hexagonal grid with an extent between 100 x 100 and 500 x 500 cells. The **spatial resolution** has been set to 1 ha, which is the Cartesian area of a single hexagonal grid cell, while the **temporal resolution** has been set to 1 minute. The temporal extent varies according to the applications time window and depends on data availability.

9.3.1 Fire suppression activities

The selected wildfire case studies are characterised by large impact of fire suppression activities undertaken in order to contain and control the event. Hence, to properly compare observed and modelled burnt areas, fire suppression operations have been simulated as well. Different fire suppression tactics have been adopted according to the incident reports provided by the Autonomous Region of Sardinia. **Offensive** suppression tactics have been carried out by both ground and aerial crews to contain fires using control lines, including both direct and indirect attacks: direct attacks essentially involved the application of water, or water with suppressant additives, onto burning fuels, whereas indirect attacks involved the manipulation of unburned fuels ahead of the moving fire, either by consuming it in a backfire or by chemically altering it through the application of retardants designed to reduce the flammability of unburnt fuels. **Defensive** tactics have been adopted as well to protect points of value along the fire's path, mainly residential buildings, by means of firebreaks or reducing the ignitability of exposed surfaces or suppressing spot fires. Most controlled firelines also required **mop-up** operations to maintain control of the fire, preventing fuels to re-ignite and flames to spread into unburnt areas.
However, only fire suppression operations that, according to the incident reports, successfully contributed to the fire containment have been simulated by means of impermeable barriers, independently form the adopted tactics. Those barriers are designed to stop the fire spread by nullifying the maximum rate or fire spread of the hexagonal grid cells they intersect. Where accurate information on both timing and location of interventions were not made available, fire suppression activities have been located exclusively along roads where major ground suppression activities are supposed to have been deployed.
Simulations with and without the fire suppression actions have been both performed to illustrate the differential effects of the fire suppression actions on the modelled burnt area.

9.3.2 Quantitative analysis

Standard quantitative indexes have been computed to estimate the performance of the obtained spatial simulation model in terms of spatiotemporal agreement between observed and modelled burnt areas. The Sørensen similarity coefficient, together with sensitivity and specificity measures, have been computed for each time step of the implemented fire growth model for each simulated scenario for each wildfire case study.
The Sørensen similarity coefficient is a statistical index which computes the value of similarity between two samples. Perry et al. (1999) firstly adopted this index to assess the agreement between fire simulation models and observation according to the Equation [9.8]:

$$Sørensen = \frac{2a}{2a + b + c} \qquad [9.8]$$

where a is the number of hexagonal cells coded as burnt into both observed and modelled fire scars, b is the number of hexagonal cells predicted as burnt by the model but unburnt in the actual fire, and c is the number of cells burnt in the actual fire but predicted as unburnt by the model. The result is a value between 0 and 1, with 0 indicating no agreement between observed and modelled fire scar and 1 indicating a perfect agreement.

Sensitivity and specificity are statistical measures of the performance of binary classification problems computed according to Equation [9.9] and Equation [9.10] respectively. Sensitivity is intended as the proportion of burnt areas that are correctly identified by the model, i.e. the ratio of the number of cells correctly classified as burnt by the model (a) to the total number of burnt cells in the actual fire perimeter ($a + c$). Its complementary measure, 1-sensitivity, stands for the probability of committing an error of omission (false negative). Specificity measures the proportion of unburnt areas that are correctly identified by the model, i.e. the ratio of the number of cells correctly classified as unburnt by the model (d) and the total number of cells effectively unburnt ($d + b$). Its complementary measure, 1-specificity, corresponds to the probability of committing an error of commission (false positive).

$$Sensitivity = \frac{a}{a + c} \quad [9.9]$$

$$Specificity = \frac{d}{d + b} \quad [9.10]$$

9.4 Results

9.4.1 Sagama

The case study of Sagama, August 24th, 2016, has been simulated starting from the two simultaneous ignition points indicated by the authoritative incident report. The model's runs have been stopped once the simulation time reached the declared time of fire containment, even when no fire suppression operation had been implemented. An improved performance in terms of the Sørensen similarity coefficient (Table 9-3) has been obtained by implementing the set of European Mediterranean fuel models rather than the set of North American fuel models. By comparing the model's outputs at the time of fire containment, the set of North American fuel models (Figure 9-6) seems to underpredict the maximum rate of spread, generating fire growth patterns with limited sensitivity. Conversely, the set of European Mediterranean fuel models (Figure 9-7) have produced higher sensitivity and, hence, lower error of omission, while maintaining a high specificity, even if lower with respect to the set of North American fuel models. However, large portions of unburnt areas, both east and west of the observed burnt area, are identified as burnt by the model. The performance of the model has been further enhanced thanks to the implementation of barriers simulating the fire suppression activities (Figure 9-8) that have been dispatched to protect the residential areas of Sagama, Scano di Montiferro, and Sennariolo. The barriers effectively prevented the fire from enveloping points of value, slightly improving the model's specificity, but they are rapidly bypassed south of Sagama. Similarly, the false positives east of the actually burnt areas are not mitigated by fire suppression activities.

Table 9-3 Quantitative model performance for the Sagama case study. USA indicates the set of fuel models for North America, whereas MED indicates the set of fuel models developed for European Mediterranean regions. Measures of performance are referred to the declared time of fire containment.

	Suppression	*Sørensen*	*Sensitivity*	*Specificity*	*Time* [min]
Sagama USA	0	0.42	0.30	0.98	420
Sagama MED	0	0.57	1.00	0.80	420
Sagama MED	1	0.64	0.96	0.86	420

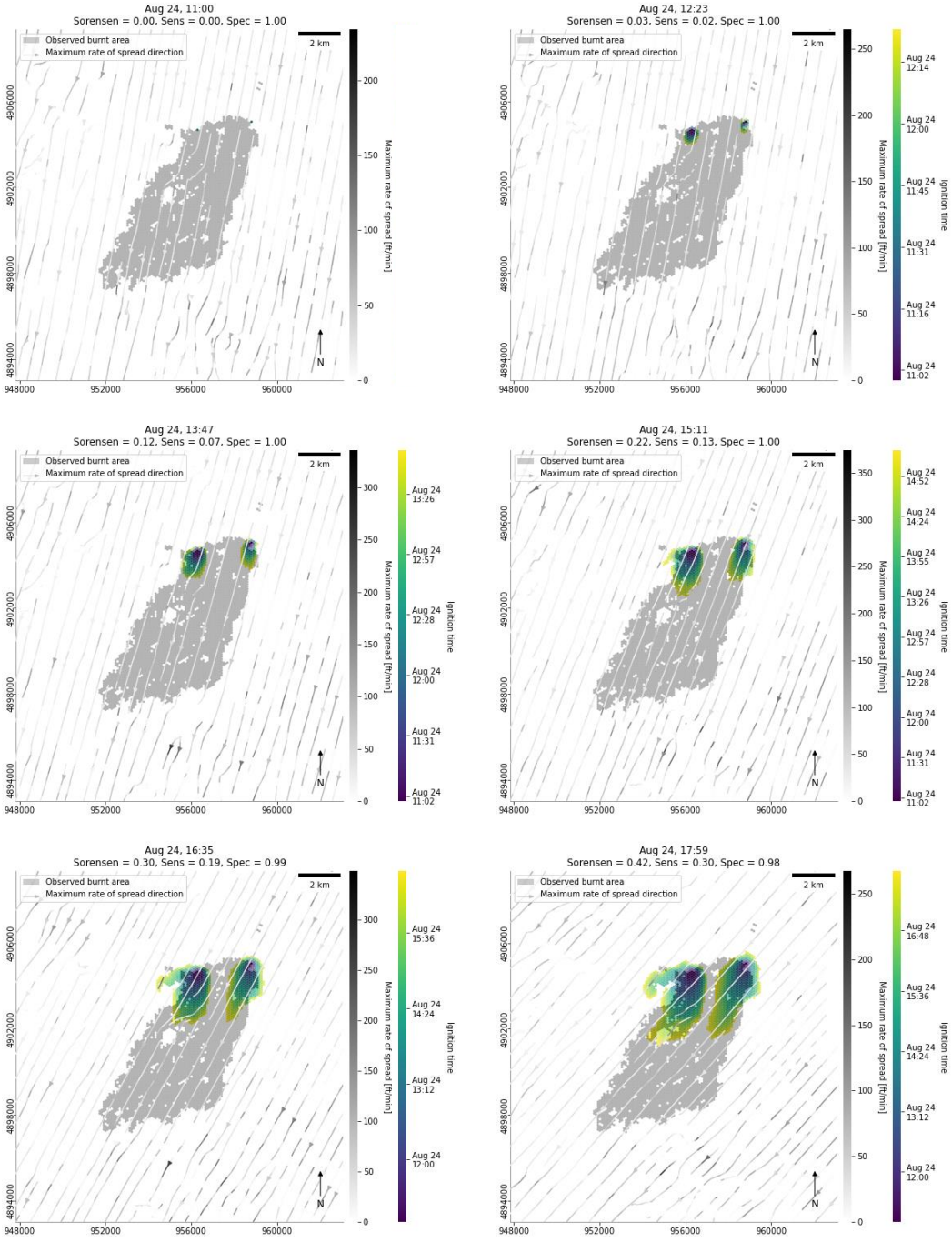

Figure 9-6 Sagama wildfire event, August 24th, 2016, with the fuel model set for North America and without fire suppression activities.

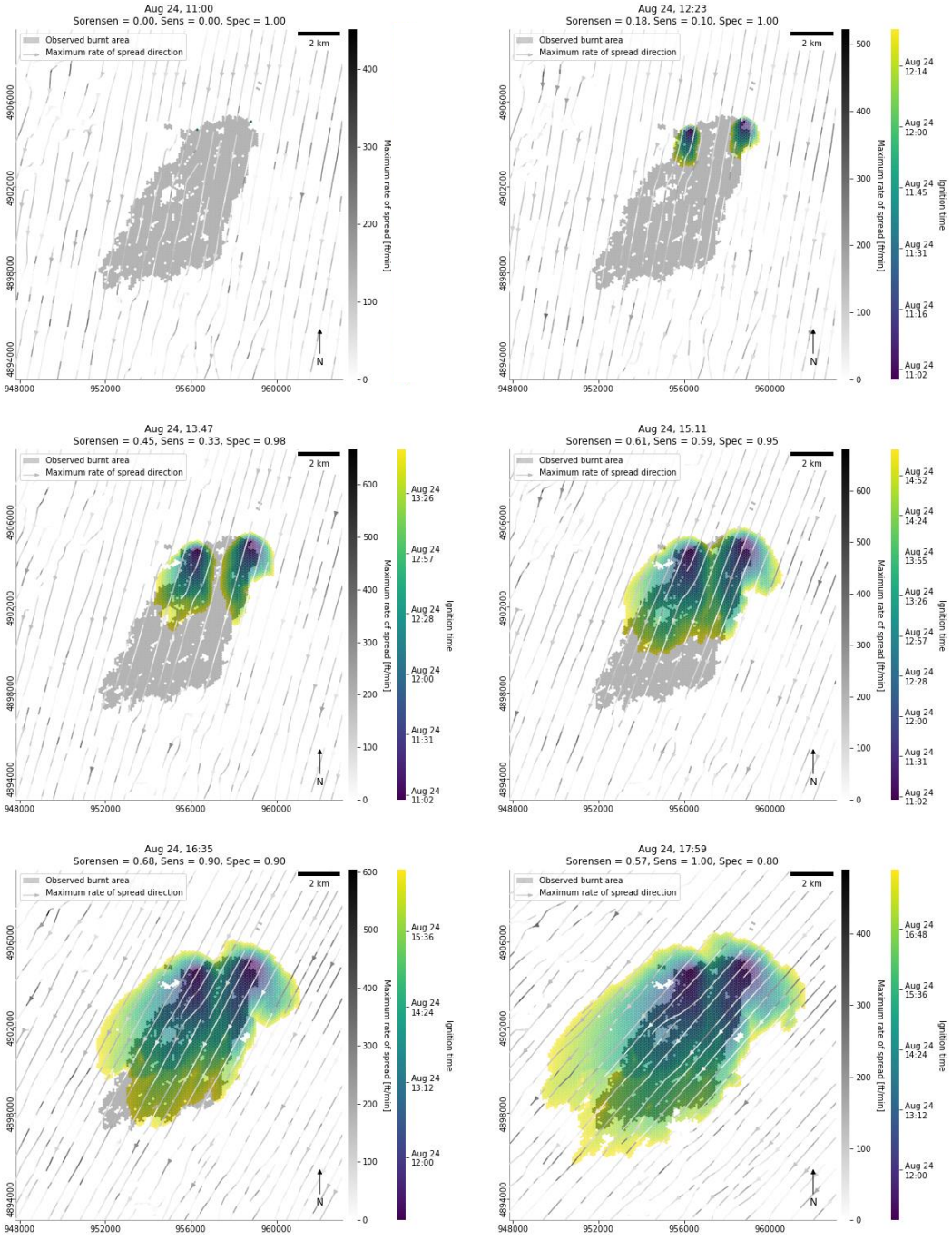

Figure 9-7 Sagama wildfire event, August 24th, 2016, with the fuel model set for European Mediterranean regions and without fire suppression activities.

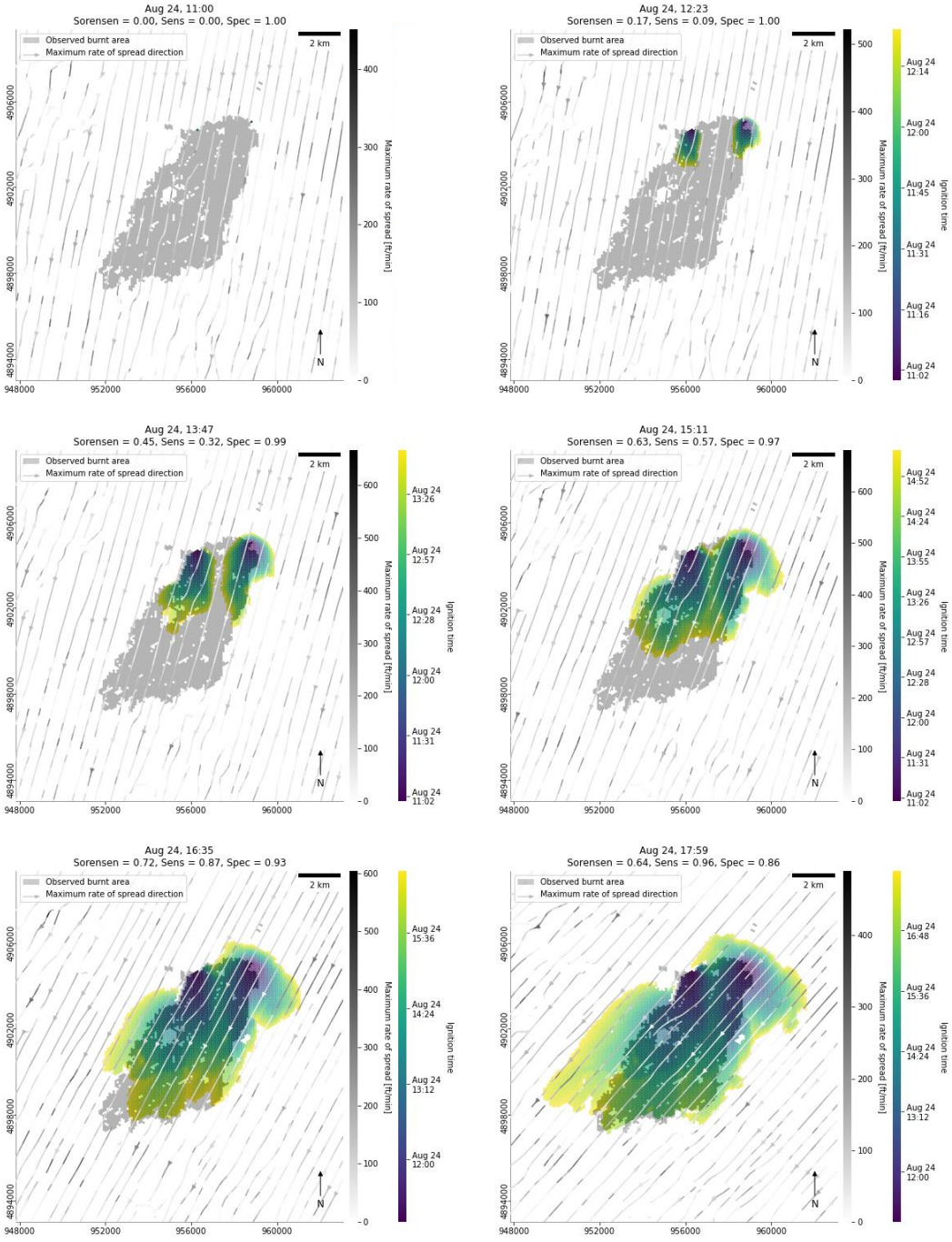

Figure 9-8 Sagama wildfire event, August 24th, 2016, with the fuel model set for European Mediterranean regions and with implemented fire suppression activities.

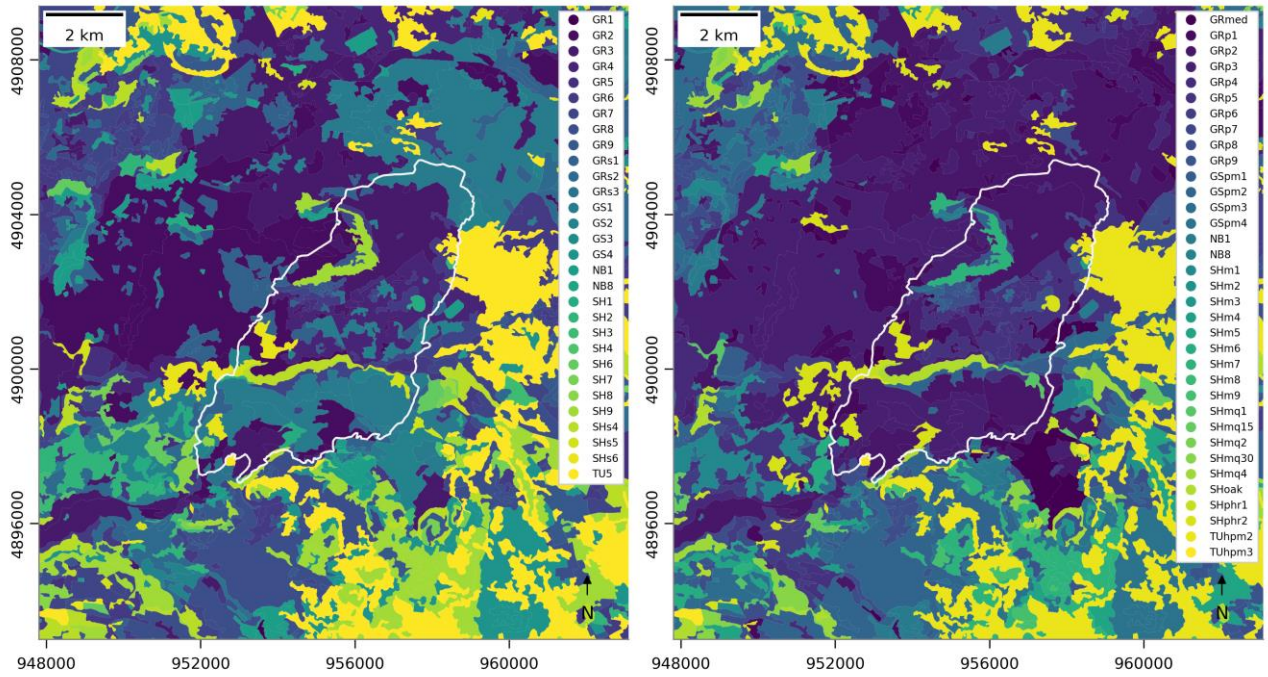

Figure 9-9 Maps of North American (left) and European Mediterranean (right) fuel models for the Sagama wildfire case study.

The portion of unburnt area, which is predicted to burn by the model and is located northeast from the fire outbreaks, is dominated by broad-leaved forests with cork oak (*Quercus suber* L.) according to the land use map. Both the North American and the European Mediterranean fuel maps classified those patches using fuel models compatible with the understory of broad-leaved forests (Figure 9-9). Such an overprediction in the obtained patterns of fire growth might be due to both overestimated rates of fire spread or underestimated fire suppression interventions.

9.4.2 Isili

The case study of Isili, July 20th, 2016, has been simulated starting from the ignition point signalled by the authoritative incident report. Analogously to the case study of Sagama, the model's runs have been stopped once the simulation time reached the declared time of fire containment, even when no fire suppression operation had been implemented. The model's performances in terms of spatiotemporal agreement between observed and modelled burnt areas are significatively better with the set of European Mediterranean fuel models with respect to the North American one, which, instead, resulted in a particularly low sensitivity (Table 9-4). The set of North American fuel models has generated sharply underpredicted patterns of fire growth (Figure 9-10). Similarly, the patterns of fire growth produced with the set of European Mediterranean fuel models were not able to completely cover the southeast portion of the burnt area, which is characterised by the presence of the *mesa* known as Taccu de Nurri (694 m) (Figure 9-11). This discrepancy might be due to either an inaccurate modelling of wind fields in the presence of complex morphology or underpredicted values of the maximum rate of spread. The implementation of fire suppression operations on the right and left fire flanks slightly improved the model's performances, especially in terms of specificity (Figure 9-12).

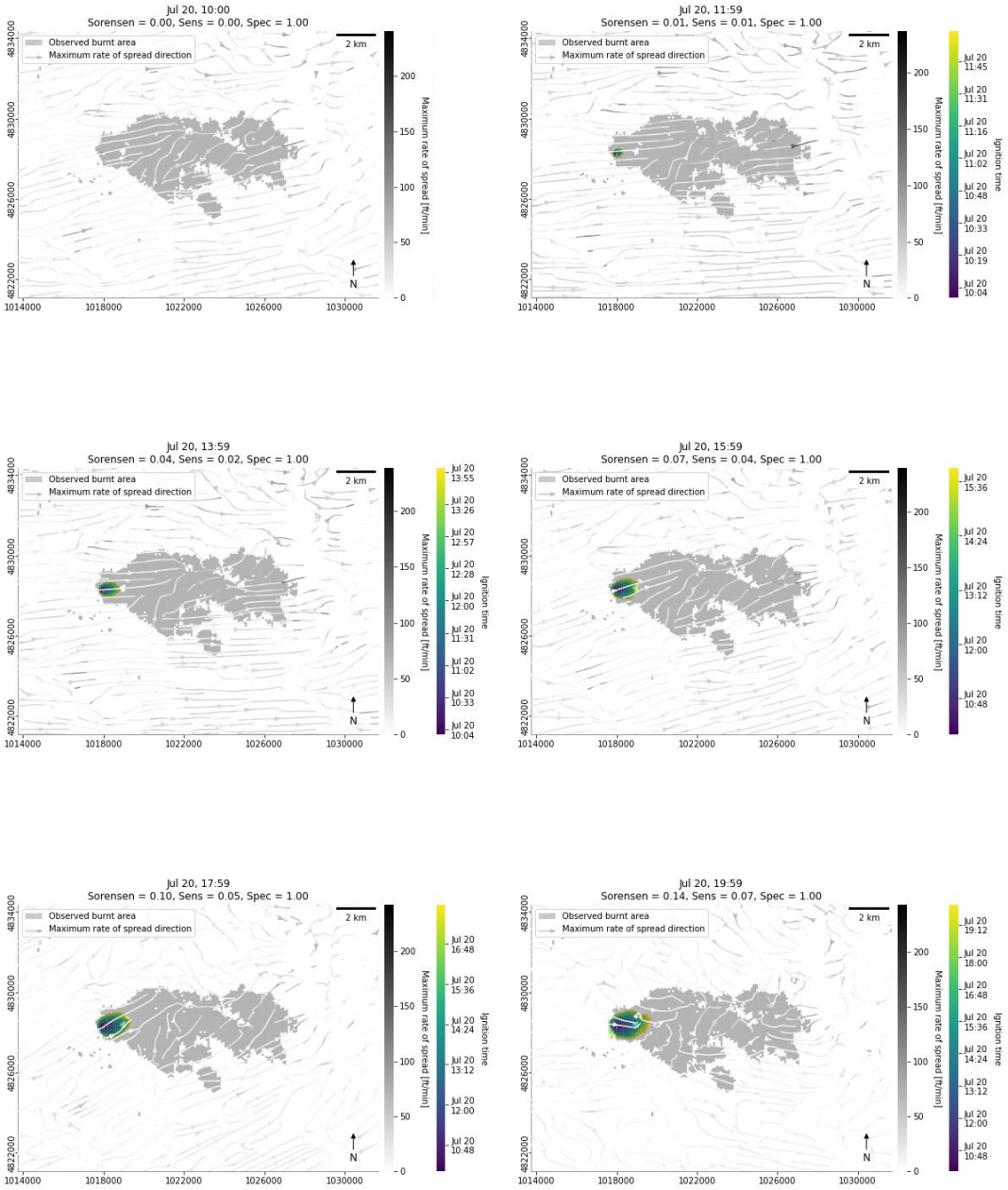

Figure 9-10 Isili wildfire event, July 20th, 2016, with the fuel model set for North America and without fire suppression activities.

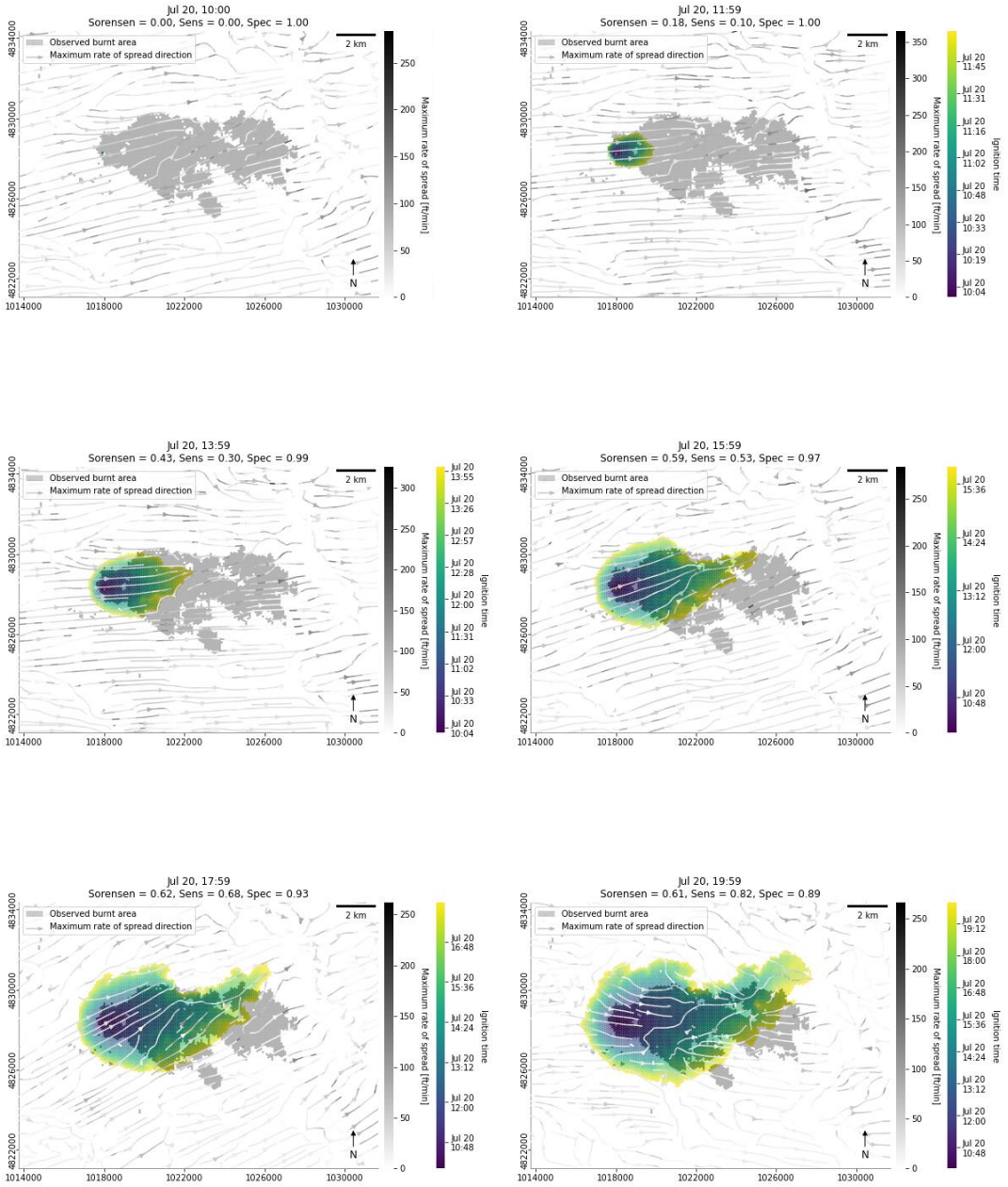

Figure 9-11 Isili wildfire event, July 20th, 2016, with the fuel model set for European Mediterranean regions and without fire suppression activities.

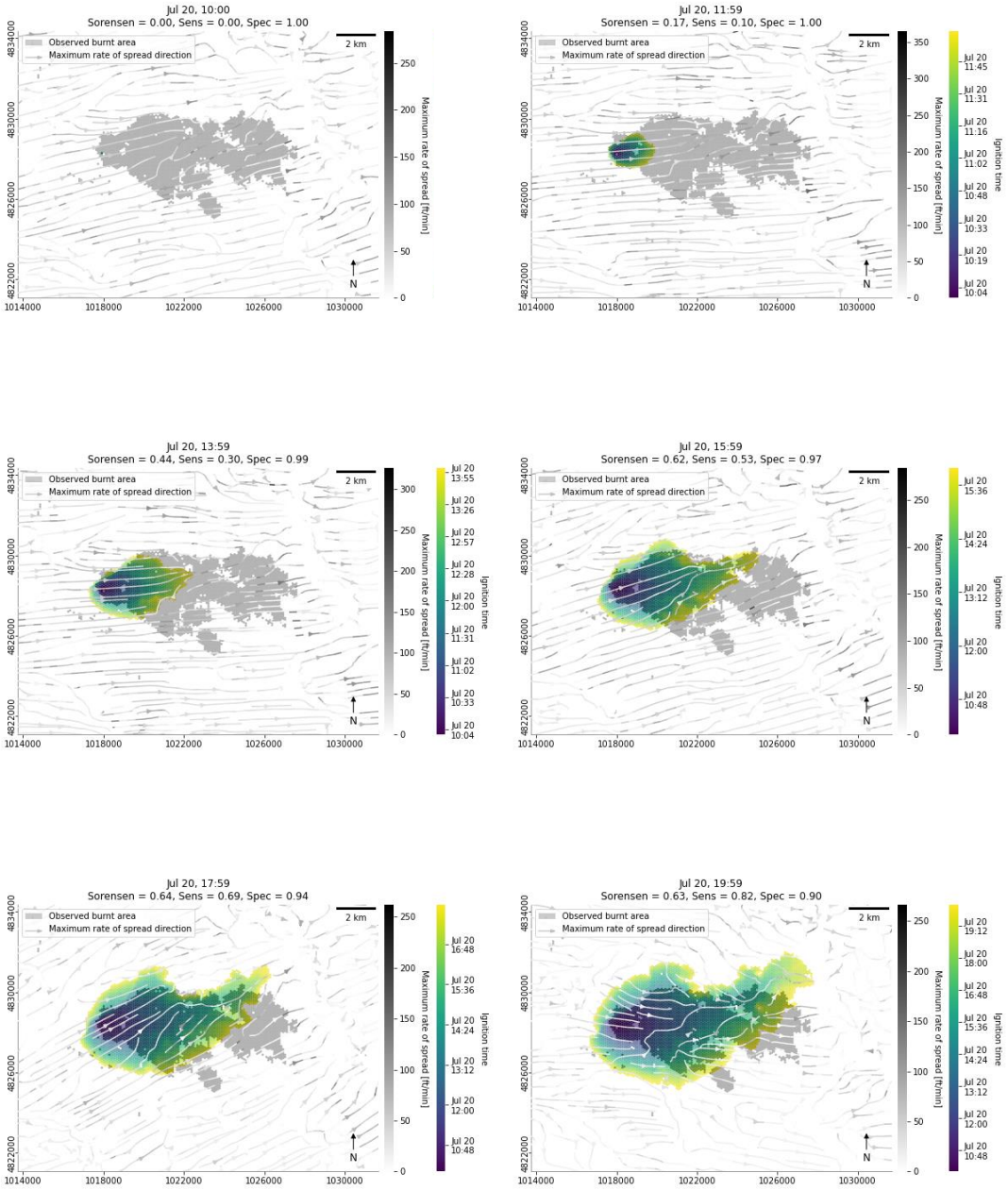

Figure 9-12 Isili wildfire event, July 20th, 2016, with the fuel model set for European Mediterranean regions and with implemented fire suppression activities.

Table 9-4 Quantitative model performance for the Isili case study. USA indicates the set of fuel models for North America, whereas MED indicates the set of fuel models developed for European Mediterranean regions. Measures of performance are referred to the declared time of fire containment.

	Suppression	*Sørensen*	*Sensitivity*	*Specificity*	*Time* [min]
Isili USA	0	0.14	0.07	1.00	600
Isili MED	0	0.61	0.82	0.89	600
Isili MED	1	0.63	0.82	0.90	600

9.4.3 Gonnosfanadiga

The case study of Gonnosfanadiga, July 31st, 2017, has been simulated starting from a single ignition point and the model's runs have been stopped once the simulation time had reached the estimated time of fire containment. The sets of North American (Figure 9-13) and European Mediterranean fuel models (Figure 9-14) produced similar patterns of fire growth, both resulting in large portion of unburnt areas that are incorrectly identified as burnt by the model, especially in the portion northwest of the fire outbreak. However, these areas are significatively reduced and correctly classified as unburnt when simulating the implementation of fire suppression activities along the dual carriageway SS126 "Sud Occidentale Sarda" (Figure 9-15 and Figure 9-16). A narrow opening has been left in the implemented barrier where the fire front is supposed to have eluded the suppression operations. That allowed to successfully reproduce the fire plume which, headed towards northwest, climbed over the ridge with a southwest-northeast orientation. Nevertheless, a minor portion of actually burnt area, located at the north-western tip of the recorded event, has resulted not to burn neither with the North American set nor with the European Mediterranean set. According to the land use map, that area is populated by sclerophyllous shrubs representative of the Mediterranean garrigue on sandy soils. North American and European Mediterranean fuel models with a low fuel load, SH2 and SHm1 respectively, have been assigned to that area reflecting the low aboveground biomass carbon density predicted by the global map (Spawn et al., 2020). Discrepancies in the observed and predicted patterns in that area might be attributed to either inaccuracies in the fuel mapping procedure or the complexity of the topography.

The sets of North American and European Mediterranean fuel models resulted in overall similar model's performances both with and without the implementation of fire suppression activities (Table 9-5). Specifically, European Mediterranean fuel models provided slightly better results in terms of Sørensen similarity coefficient if compared with the North American fuel models when fire suppression activities were introduced.

Table 9-5 Quantitative model performance for the Gonnosfanadiga case study. USA indicates the set of fuel models for North America, whereas MED indicates the set of fuel models developed for European Mediterranean regions.

	Suppression	*Sørensen*	*Sensitivity*	*Specificity*	*Time* [min]
Gonnosfanadiga USA	0	0.40	0.91	0.76	420
Gonnosfanadiga MED	0	0.38	0.90	0.75	420
Gonnosfanadiga USA	1	0.49	0.90	0.84	420
Gonnosfanadiga MED	1	0.52	0.88	0.86	420

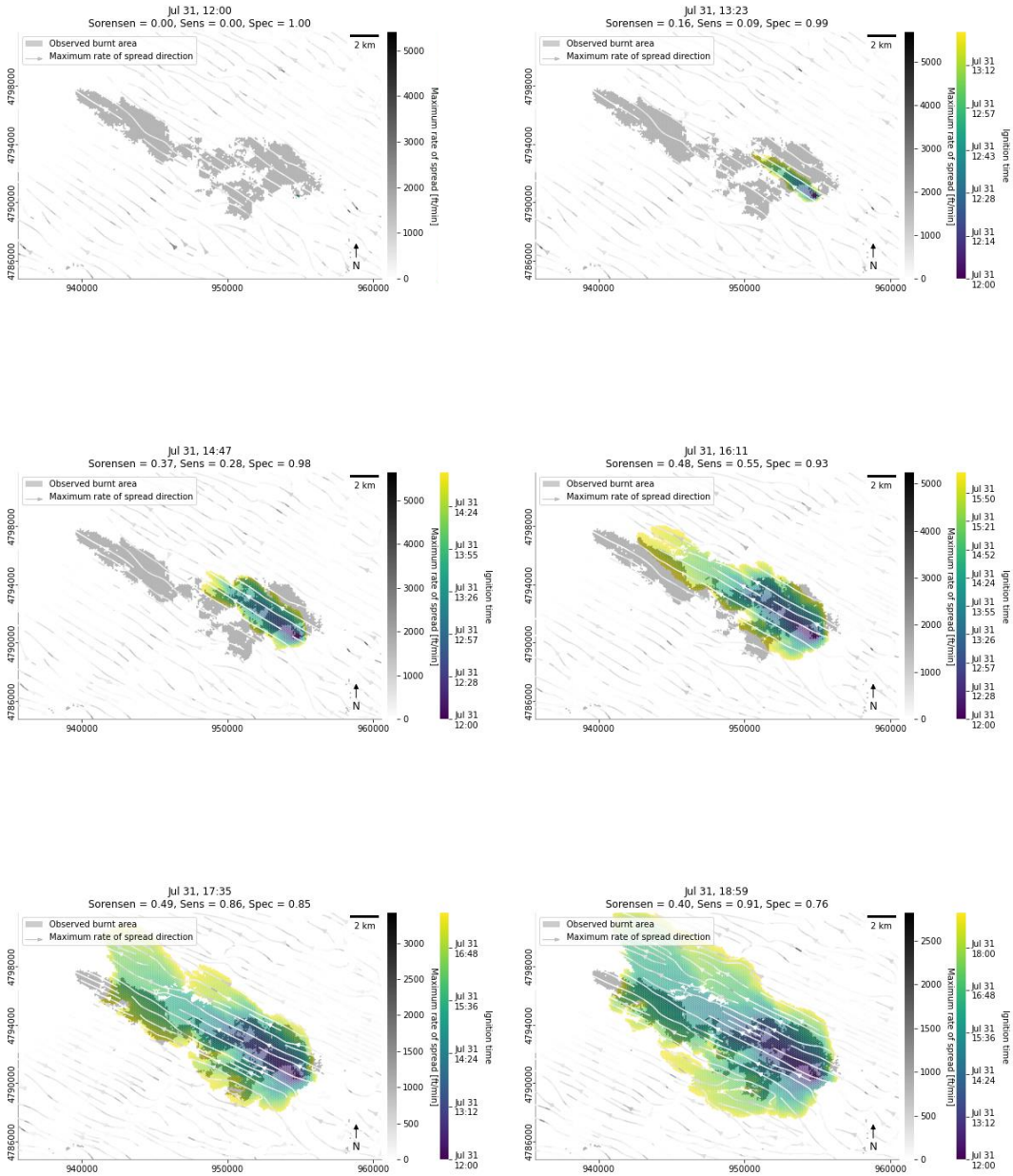

Figure 9-13 Gonnosfanadiga wildfire event, July 31st, 2017, with the fuel model set for North America and without fire suppression activities.

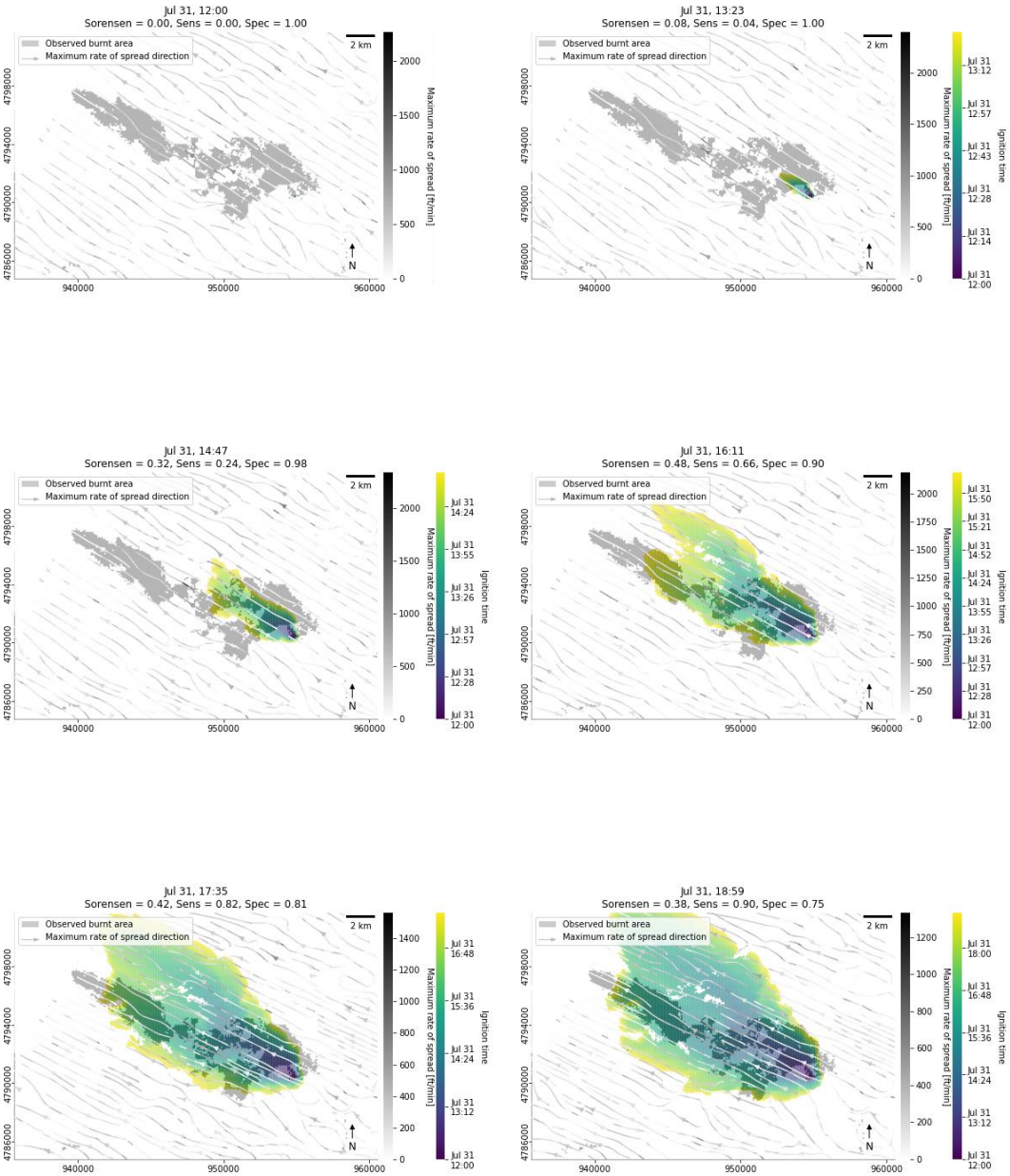

Figure 9-14 Gonnosfanadiga wildfire event, July 31st, 2017, with the fuel model set for European Mediterranean regions and without fire suppression activities.

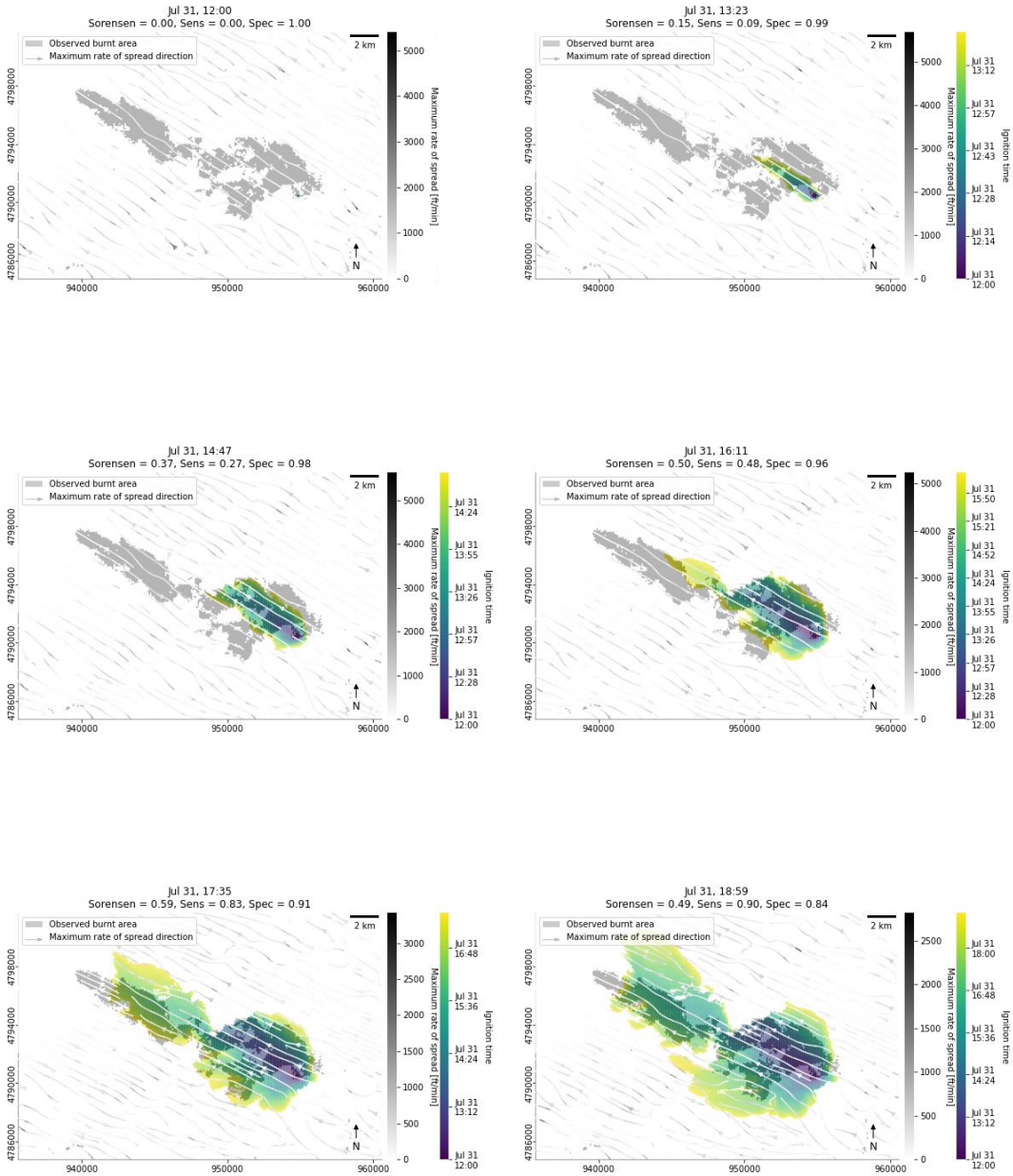

Figure 9-15 Gonnosfanadiga wildfire event, July 31st, 2017, with the fuel model set for North America and with implemented fire suppression activities.

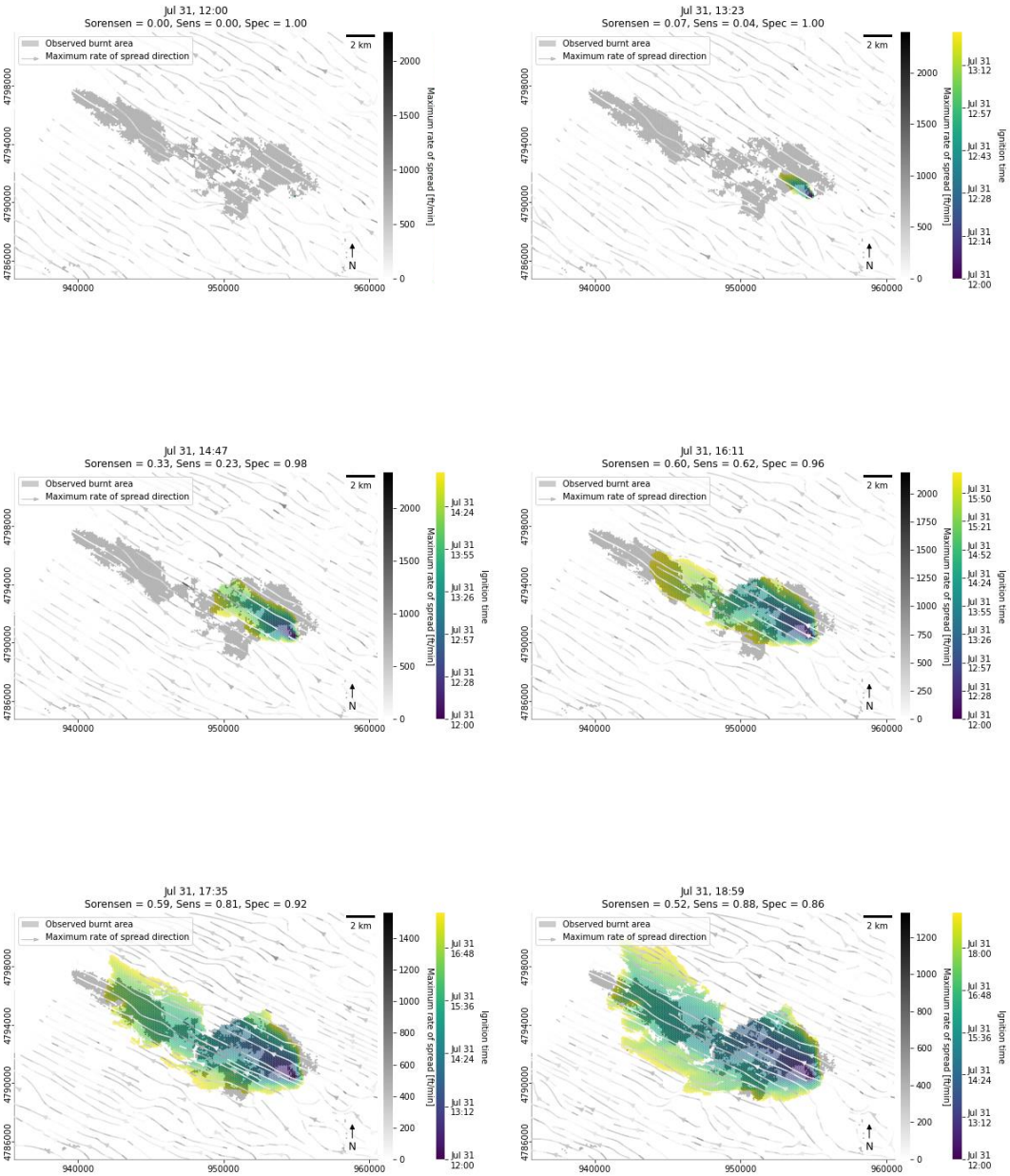

Figure 9-16 Gonnosfanadiga wildfire event, July 31st, 2017, with the fuel model set for European Mediterranean regions and with implemented fire suppression activities.

9.4.4 Villagrande Strisaili

The case study of Villagrande Strisaili, July 25th, 2017, has been simulated starting from a single ignition point and the model's runs have been stopped once the simulation time had reached the estimated time of fire containment. The sets of North American and European Mediterranean fuel models resulted in overall similar model's performances if compared without the implementation of fire suppression activities (Table 9-6). Specifically, the sets of North American (Figure 9-17) and European Mediterranean fuel models (Figure 9-18) produced similar patterns of fire growth, introducing large portions of unburnt areas that are incorrectly modelled as burnt areas because of the strong northwest winds. Those same winds prevent the model from simulating the fire growth upslope in areas located east from the ignition points.
The model's performance has been improved, in terms of both the Sørensen similarity coefficient and the specificity, with the implementation of fire suppression activities along the provincial road SP27 (Figure 9-19). As expected, the model's sensitivity has decreased because of a large portion of the actually burnt surface which has remained unburnt according to the simulation. This area is characterised by the presence of a quite complex topographies which might have generated the turbulences that forced the interruption of the aerial intervention.

Table 9-6 Quantitative model performance for the Villagrande Strisaili case study. USA indicates the set of fuel models for North America, whereas MED indicates the set of fuel models developed for European Mediterranean regions.

	Suppression	*Sørensen*	*Sensitivity*	*Specificity*	*Time* [min]
Villagrande USA	0	0.34	0.79	0.81	210
Villagrande MED	0	0.26	0.56	0.82	210
Villagrande USA	1	0.53	0.57	0.96	210
Villagrande MED	1	0.40	0.34	0.98	210

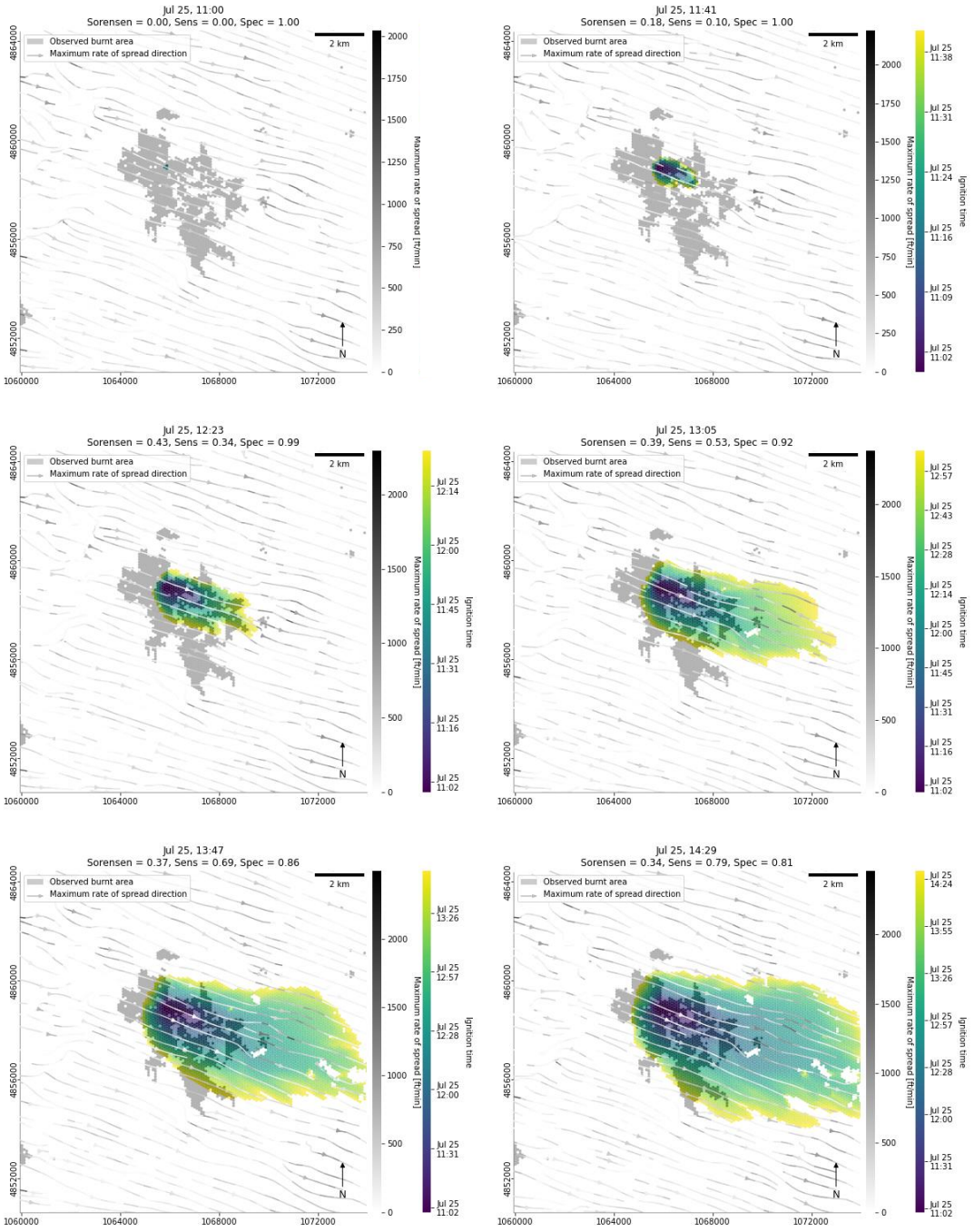

Figure 9-17 Villagrande Strisaili wildfire event, July 25th, 2017, with the fuel model set for North America and without fire suppression activities.

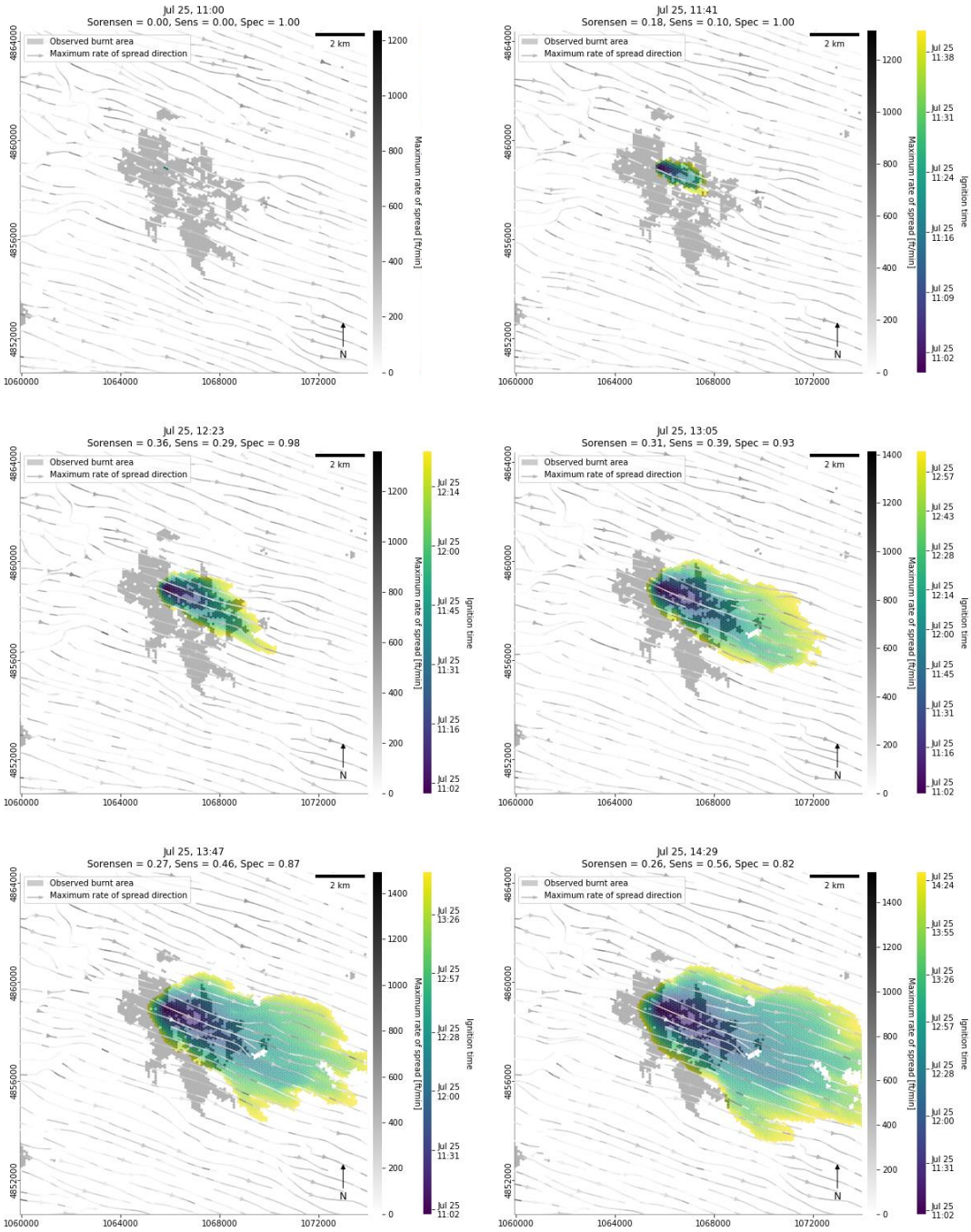

Figure 9-18 Villagrande Strisaili wildfire event, July 25th, 2017, with the fuel model set for European Mediterranean regions and without fire suppression activities.

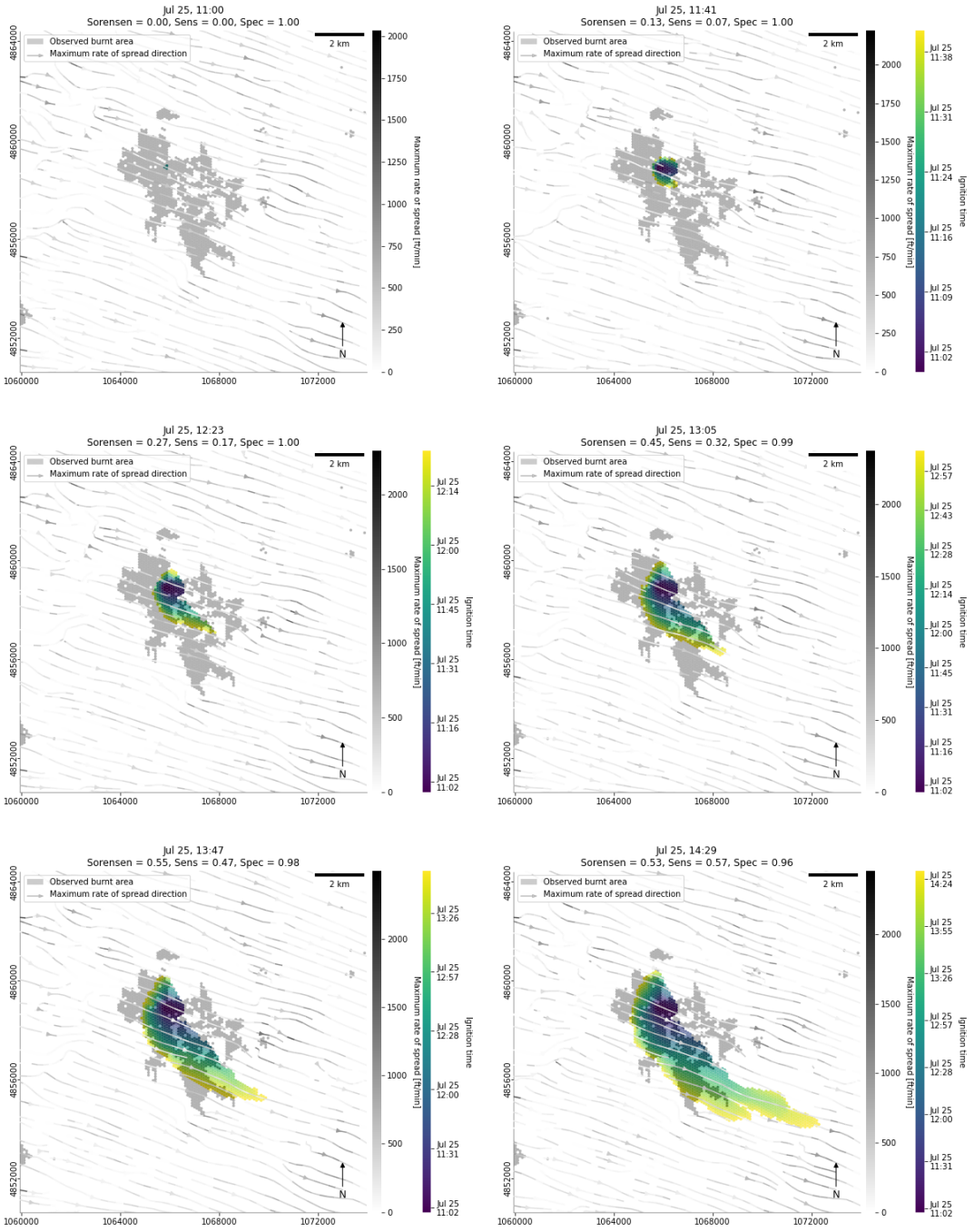

Figure 9-19 Villagrande Strisaili wildfire event, July 25th, 2017, with the fuel model set for North America and with implemented fire suppression activities.

9.5 Discussion

Modelling fire spread and growth is a complex task due to multiple factors including the spatiotemporal heterogeneity of geo-environmental conditions as well as the effect of fire suppression interventions (Alexander and Cruz, 2013; Mutlu, Popescu, and Zhao, 2008).
The selection of case studies is certainly not representative of the complexity and diversity of geo-environmental conditions in the study area. Nevertheless, they strived to capture different conditions ranging from grasslands to Mediterranean maquis and garrigue, and from flat to complex topographies. Both the case studies dominated by herbaceous fuels (Sagama and Isili) showed a significatively improved model's performance by implementing the set of European Mediterranean fuel models rather than the North American ones, which produced underestimated patterns of fire growth. Conversely, the case studies dominated by sclerophyllous shrubby fuels of the Mediterranean maquis and garrigue (Gonnosfanadiga and Villagrande Strisaili) showed similar model's performances by implementing North American or European Mediterranean fuel models. However, case studies with prevalent herbaceous fuels resulted in better model's performances with respect to case studies with prevalent shrubby fuels, suggesting the procedure of fuel model mapping might result in greater accuracy when dealing with grasslands rather than shrublands. Indeed, discrepancies between above-ground biomass and fuel load, that is the combustible portion of the biomass, are more pronounced for shrublands with respect to grasslands. Moreover, the maps of above-ground and below-ground biomass carbon density which have been employed to approximate the fuel load are overtly not fully suitable for areas where shrublands biomass is of primary importance (Spawn et al., 2020).
According to the obtained results on its performance, the model is more suitable in the absence of complex topographies. This could be due to either the Rothermel's model inheritance or the intrinsic difficulties in simulating and downscaling the wind fields with the mass conserving model by Forthofer (2007). Horizontal wind speed and direction deserve major attention since, while data seem to accurately reproduce the wind fields, wind speed and direction have resulted of dominant importance in predicting both the rate and direction of maximum fire spread (Chapter 6). For instance, it could be valuable to evaluate the level of agreement between wind data obtained from the downscaling of the ERA5-Land climate reanalysis and ground measurements. Moreover, the spatiotemporal resolution of the ERA5-Land estimates makes the model blind to wind gusts, which instead might have a significative influence on the maximum rates and directions of fire spread. Finally, uncoupled models could be used to further improve the surface fire behaviour modelling outputs by simulating winds and turbulences generated by the fire events themselves.
As expected, the case studies simulated with a proper implementation of fire suppression activities provided an improved performance on their counterpart simulations without fire suppression activities. However, since the simulation without fire suppression actions covered a much wider area, it exhibits better indices for what concerns sensitivity. This motivates the inclusion of a complete set of performance indicators, capable of accounting for both errors of omission and commission. Nevertheless, this suggests that further attention should be paid in simulating fire suppression activities when modelling historical case studies. Impermeable barriers implemented to simulate fire suppression activities tend to be easily bypassed by the fire front. It could be because of barriers are not suitable for simulating every fire suppression tactic, especially backfires, i.e. fires set along the inner

edge of a fuel-free fireline to consume the fuel in the fire's path. The simulation of fire suppression activities conducted by aerial crews might be also improved, integrating the use of both suppressants and retardants.

Future research activities will be addressed to the validation of the proposed methodology for data pre-processing, especially for the estimation and mapping of fuel models and fuel moisture content. Indeed, part of the procedure is derived from empirical relationships whose applicability to the study area should be further investigated.

The process of mapping fuel models could be significatively improved by integrating results from GEDI with those from the upcoming NASA-ISRO SAR (NISAR) mission (Kellogg et al., 2020; Rosen et al., 2015). The NISAR mission (to be launched in 2022) will observe Earth's surface through two fully polarimetric SARs, one at L-band and one at S-band, in exact repeating orbits every 12 days. NISAR will measure the above-ground biomass and its disturbance in low biomass forests (above-ground biomass < 100 t/ha) at 1 ha resolution, focusing on boreal and temperate forests and savanna woodlands. At a global scale, unique relevance will be assumed by the complementarity of GEDI and NISAR missions with the ESA's BIOMASS mission (Quegan et al., 2019). The BIOMASS mission (to be launched in 2022) will investigate upper canopy height and above-ground biomass in dense forests (above-ground biomass > 50 t/ha) at 4 ha resolution by means of a polarimetric P-band SAR, but focusing its attention on tropical and sub-tropical woodlands. Hence, GEDI, NISAR, and BIOMASS missions will retrieve measurements of different components of the above-ground biomass at different spatial and temporal scales, providing unprecedent opportunities to develop more consistent fuel type classifications at a global scale. Furthermore, recently developed and defined fuel models for different Italian Alpine, temperate, and Mediterranean conditions (Ascoli et al., 2020) will be also integrated into the harmonised dataset of fuel models.

Estimated fuel moisture contents should be then validated against direct ground measures. For example, live fuel moisture content estimates could be validated against field measurements from local datasets specific for the European Mediterranean area (Fan et al., 2018; Martin-StPaul et al., 2018) as well as from the global plant water status database, Globe-LFMC (Yebra et al., 2019), which provides in situ live fuel moisture content measurements from Argentina, Australia, China, France, Italy, Senegal, Spain, South Africa, Tunisia, United Kingdom and the United States of America.

Finally, major attention will be focused on the improvement of the model's ability to explain phenomena from the real world. Indeed, results suggest that fire growth's patterns suffered from overestimated rates of fire spread in the rear portions of the fire and underestimated rates of fire spread in all the other portions of the fire front and flanks.

Chapter 10

Geospatial decision support system

The reduction of disaster risk is a common concern for all governments at different institutional levels (UNISDR, 2015). According to the Sendai Framework 2015-2030, policies and practices for disaster risk prevention and management should be firmly grounded in the comprehension of risk in its complexity, ranging from susceptibility and hazard characterization to vulnerability and exposure assessment. Leveraging on such knowledge, appropriate preparedness and effective response can be efficiently developed. Progress in disaster risk reduction research has also placed emphasis on the insufficient advancement in converting new findings into concrete applications in practical disaster risk reduction actions (Weichselgartner and Pigeon, 2015).

Hence the need to identify strategies aimed at strengthening communities' resilience and risk awareness as well as reducing expected impacts and potential damage. Collecting, analysing, processing data, and organizing information are fundamental in eliciting and constructing knowledge that has to be inevitably transferred and applied in disaster risk management to make individual and common risk awareness arise. Further actions should be hence directed towards sharing and disseminating results, both among public administrations and citizens (Haworth, 2018). The strengthening of disaster risk governance requires promoting informed decision making and coordinated action across relevant institutions and stakeholders at appropriate levels (UNISDR, 2015). Potential hindrances in the science-policy interface threatening the effective use of existing knowledge have to be minimized and decision makers need to have most appropriate scientific information available in decision making processes. At the same time, citizens should be given the opportunity to actively participate and contribute to institutional risk management activities. The enhancement of both personal and societal aware and conscious involvement is indeed the way to trigger communities' ability to anticipate, respond to, and recover from disaster effects (UNISDR, 2015).

To accomplish its tasks, the Sendai Framework promotes «a real time access to reliable data, the use of space and in situ information, including geographic information systems (GIS), and use information and communications technology (ICT) innovations to enhance measurement tools and the collection, analysis and dissemination of data» (UNISDR, 2015).

At global and regional scales, innovative early warning systems for natural disaster are increasingly being developed (Alfieri et al., 2013; Canli et al., 2018; Glade and Nadim, 2014), providing useful entry points for disaster risk management (W. Liu et al., 2018). Nonetheless, gaps still exist between offered models and local managers' needs and there is a significant lack of appropriate local information on disaster impacts, as well as on exposure and vulnerability. Here the urgency of promoting science-based risk management policies and participatory activities among citizens comes to light.

In line with that needs, the objective of the present study is to strengthen communities' resilience to disaster-related emergencies by both improving and optimizing decision-making processes as well as promoting individual and societal conscious involvement in risk preparedness and management.
Within the context of the PhD project, three modules of a geospatial decision support system have been designed and implemented with the aim of improving the efficiency of risk management strategies and reducing expected impacts and potential damage. The first module is a dynamic workflow of actions and represents the core of the decision support system. This module aims to guide decision makers in carrying out the procedures of the intervention model compliant with the legislative framework. The workflow is then supported by a second module, a customised version of a geographic information system with dynamic forms designed to support users with limited expertise in geodatabase management. This module will incorporate a structured relational geodatabase storing (i) existing institutional susceptibility, hazard, and risk maps, (ii) newly developed event scenarios, (iii) available resources and socioeconomic exposed values, and (iv) real-time data from field surveys. Finally, the decision support system will provide authorities, technicians, and volunteers with a third module composed by web applications for mobile field data collection and sharing.
The architecture of the geospatial decision support system is inherently applicable to diverse natural hazards, ranging from seismic, hydraulic, and hydrogeologic events to chemical accident or sanitary emergencies. The following sections will focus on the specific application to wildland fire management.

10.1 Decision support system for wildland fire management

The geospatial decision support system is meant to cover the whole risk management cycle and to endorse interventions in diverse stages, ranging from prevention and preparedness to response and post-event recovery. The system is meant to help in: (i) planning mitigation strategies and disaster relief operations, (ii) enhancing disaster managers' knowledge of intervention procedures and state-of-the-art strategies and tools for geospatial data analysis, (iii) organising and managing resources and responsibilities, and (iv) promoting data collection and sharing during ongoing hazardous events and in their aftermath.

10.1.1 Procedural workflow

The procedural workflow is the core of the decision support system and has been designed to guide risk managers through the intervention model by providing them a procedural workflow fully compliant with the regulatory framework in force at national and regional level. As part of a decision support system, the procedural workflow does not possess any decision-making ability and does not substitute decision makers. Instead, it is supposed to support them by providing at any emergency stage a selection of possible, recommended or compulsory actions together with (i) instructions of execution, (ii) contacts of actors in charge of performing each operation, (iii) legal documents or modules to be issued at each emergency stage, and (iv) real-time reports of resources and structures availability will be implemented in the near future.
The flow of procedures is the result of an accurate and in-depth analysis of the regulatory framework at different institutional level. The intervention model can be customized based on specific policies

and needs. Once defined, the workflow has been formalised by means of the graphical and mathematical formal notation of Generalized Stochastic Petri Nets for mutually exclusive, interactive or concurrent stepwise processes modelling, capable of representing the rules that control the evolution of distributed systems (Murata, 1989). Such formalization allows a preliminary validation of the whole intervention model even before the emergency outbreak by testing the coherence of the workflow, synthesizing redundant operations, and suppressing those preventing the whole system to fail or to precociously conclude the procedure. Figure 10-1 provides an example of a Petri Net representing the procedural workflow for the wildfire emergency management in the wildland urban interface. Petri Nets have been modelled and validated with the open source software package GreatSPN (GRaphical Editor and Analyzer for Timed and Stochastic Petri Nets) (Amparore et al., 2016).

10.1.2 Geographic information system

The geographic information system (GIS) module consists of a customized version of QGIS 3 provided with simplified editing tools and dynamic forms to support users with small expertise in geographic information systems and database management systems. The GIS module is deputed to integrate the developed model for predicting and simulating wildland surface fire spread and growth (Chapter 6, Chapter 7, and Chapter 9).

The GIS module incorporates a repository to store, manage, and retrieve heterogeneous spatially distributed data including susceptibility/hazard and risk maps, either authoritative and research-based, newly generated event scenarios, volunteered geographic information provided by citizens, and every other information useful to cope with disasters. The GIS module is conceived to ease and validate the data entry and the database updating procedure in order to improve emergency preparedness and response. The relational database stores data related to (i) contacts of institutional roles and entities involved in Civil Protection activities, (ii) locations and auxiliary information on surfaces, structures and infrastructures susceptible to assume strategic or significant importance for Civil Protection aims, such as coordination centres and emergency areas establishment, as well as (iii) additional sources of information, e.g. topographic maps and other thematic maps. Crucial is also the (iv) characterization of event scenarios which might be conducted in near real-time by collecting remotely sensed information and running multiple simulations. In the near future, databases will also include information concerning (v) real-time availability of resources and structures. Users can easily interact with collected information through a GIS installation which provides simplified forms with validation and visibility rules to facilitate data insertion in order to preserve the database structure in compliance with national and regional guidelines and needs. The local databases are periodically synchronized with the central server, to make information available even at supra-municipal level.

The GeoPackage format has been chosen for the relational database structure so that the SQLite database could be populated in compliance with the GeoPackage Encoding Standard. Custom forms have been developed from scratch using QGIS form design functionalities and validation and visibility rules are inspired to the RDForms Javascript library.

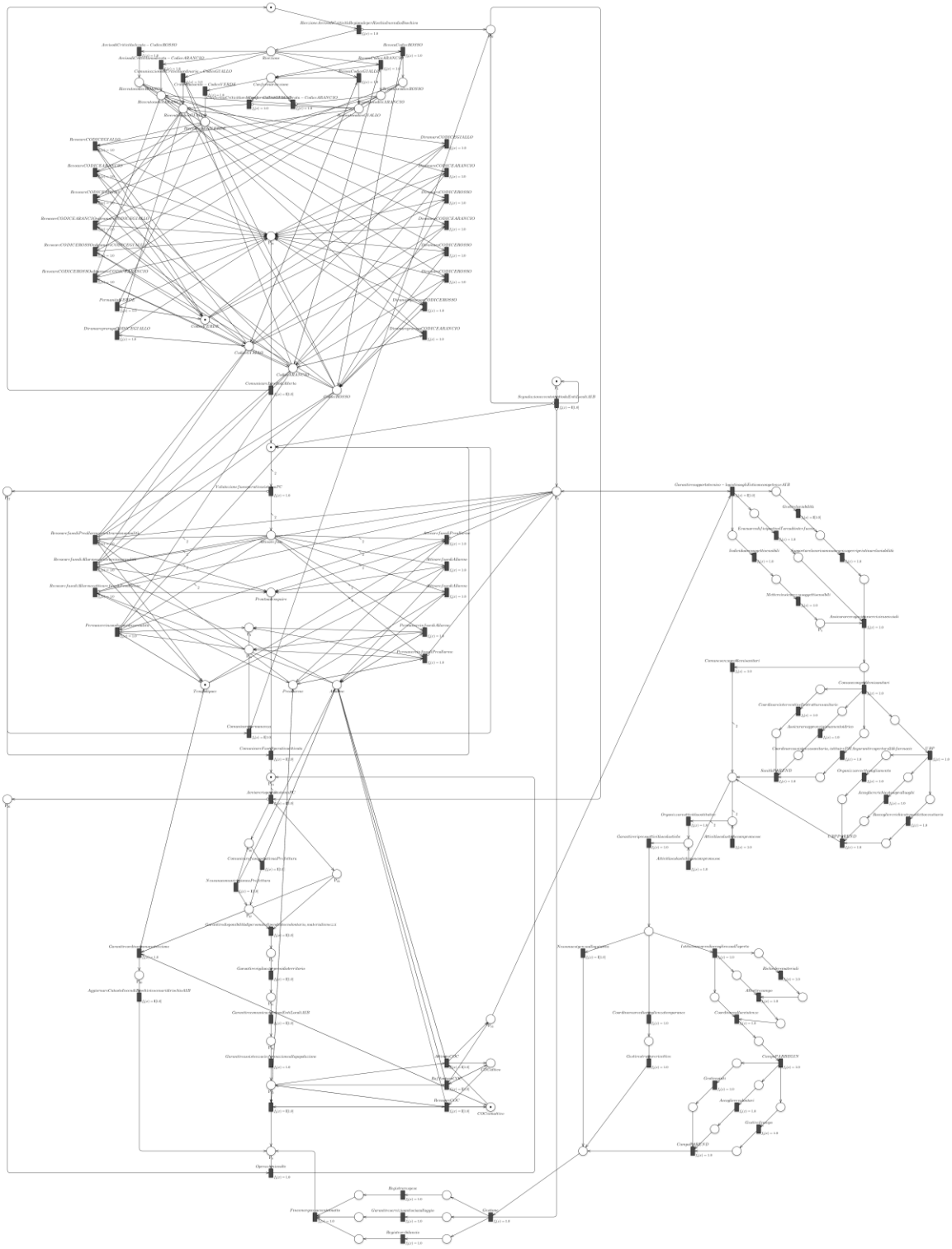

Figure 10-1 Formalisation by means of the formal notation of Generalized Stochastic Petri Nets of a procedural workflow for wildfire risk management in the wildland urban interface.

10.1.3 Web applications for field data collection

The last module is constituted by a pool of web applications which have been designed and implemented by means of KoBoToolbox, a suite of tools for field data collection for use in challenging environments. Web applications are intended for field data collection, analyses, and share, and ask for signallers to contribute with georeferenced, qualified, and updated information on where, when, and what kind of evidence they are reporting.

The module allows to create, collect, share and analyse Volunteered Geographic Information (VGI) freely provided in the earliest stages of the emergency or in the aftermath by newly enrolled signallers, i.e. properly trained citizens and technicians or volunteers with an adequate technical background. Because of legal issues, only technicians and volunteers will be allowed to submit their signals in the midst of the emergency. However, the module is even conceived as a strategy to increase citizens' understanding of the multiple risk dimensions in order to lead them to a proactive participation in risk management activities. The goal is indeed to leverage on citizens' newly acquired risk awareness to make them act like human sensors and to further improve their consciousness of the spatial distribution of both local resources and critical circumstances.

Interactive dynamic forms with validation rules and skip logic defined for every question permit the users to quickly report data on expected, ongoing or completed hydrogeological events, forwarding standardized and structured information. The forms include many multiple-choice questions and only a few free text responses, collect detailed temporal and spatial information and support various media files inputs, e.g. images, audio, and video. The developed forms rest on the XLSForm standard, compatible with the subset of XForm functionalities supported by Javarosa project, an open-source platform for data collection on mobile devices.

Data collection is allowed either online or offline thanks to the strong safeguards against data loss provided by KoBoToolbox: answers are automatically saved and stored for future submission. A back-end system gathers submitted reports from users that will be progressively profiled and categorized according to their role, e.g, volunteers or technicians, as well as to the accuracy and reliability of their submissions, in order to discard inappropriate warnings. The central crawler implemented in the geospatial decision support system periodically checks local independent databases looking for new reports. Advisories will be imported in the database in order to be checked and validated. Thanks to a flexible query system, newly provided observations can be consulted separately or jointly to recover, analyse, process, and display on maps only those reports that satisfy query constraints. Moreover, reliable information can be exploited to validate and update available institutional or non-institutional susceptibility, hazard, and risk scenarios, raising those reports to a dynamic support for disaster risk management.

Chapter 11

Conclusions and future research

Simulating wildland surface fire spread and growth assumes a crucial role in planning and optimising wildfire risk management strategies and emergency response activities. Nevertheless, modelling fire behaviour is a remarkably challenging task due to the complex combination of interdependent multi-scale physical and chemical phenomena involved.

An operational predictive wildland surface fire simulation model has been designed and developed within the context of the present research. As a whole, the model is composed of three distinct modules corresponding to as many independent sets of algorithms: (i) the first module promotes a dynamic, consistent, and fully reproducible pre-processing methodology for the remotely sensed near real-time estimation of the drivers of fire spread, i.e. fuel models, live and dead fuel moisture content, dip angle and direction, horizontal wind speed and direction; (ii) the second module implements a proxy model for predicting wildland surface fire spread based on an explainable ensemble learning method; and (iii) the third module consists of an agent-based model for simulating fire growth across heterogeneous geo-environmental conditions. Given the spatiotemporal location of the primary outbreaks as input, the model sequentially applies the three modules in order to (i) automatically and dynamically retrieve near real-time estimations of the drivers of fire spread, (ii) compute the direction and intensity of the maximum rate of spread as well as the eccentricity of the elliptical fire shape, and (iii) simulate the fire growth returning a spatiotemporal map representing the predicted fire behaviour.

The use of remote sensing methodologies for the estimation of the drivers of fire spread provided exceptional advantages over traditional methods in terms of near real-time data collection and dynamic updating with unprecedent regularity. The adoption of a machine learning based proxy model for predicting the fire spread has guaranteed a significative reduction of the computing time in the face of a limited loss in accuracy, at the scale required for the model's application, if compared with the original implementation of the Rothermel's equations. The choice of an agent-based model for simulating fire growth is rooted in its intrinsic ability to handle heterogeneous geo-environmental conditions and their spatiotemporal variability with limited computational requirements. Moreover, agent-based models allow for exceptional modelling flexibility which is still far from being fully exploited in wildland fire management sciences. The implementation of simple fire suppression activities has allowed to effectively compare the modelled and observed fire growths, which otherwise would have led to biased comparisons. Comprehensively, the developed modular wildland surface fire simulation model has resulted in a satisfying predictive capacity, which has been quantitatively evaluated in terms of spatial and temporal agreement between modelled and observed burnt areas. Despite the intrinsic uncertainties in input data as well as in models' assumptions and limitations the outcomes open to the possibility of an effective operational use of the developed simulation model for predicting surface fire spread and growth in wildland fuels.

Future research could be addressed at improving each single module of the developed wildland surface fire simulation model. Simulations making use of mathematical models are subject to parametric uncertainty, which includes uncertainty in the input data for initial conditions that may vary temporally or spatially, affecting the model outputs, as well as error in the model parameters due to either measurement error or intrinsic variability in the parameters. In the Rothermel's mathematical model, abrupt changes in input parameters have immediate impact on fire spread rate and direction, so that parametric uncertainty is directly propagated to the model outputs. The developed proxy model based on the Rothermel's equations suffers from the same parametric uncertainty. It emerges the need for further improvements in managing uncertainties in the drivers of fire spread stemming from multiple sources including their inherent spatiotemporal variability, the accuracy and precision of the satellite products employed for their estimation, and the propagation of those uncertainties throughout the whole modelling process. Major attention should be given to those drivers of fire spread that resulted to have the greatest influence on the direction and intensity of the maximum rate of spread, i.e. fuel models and horizontal wind speed and directions. Indeed, recent research into extreme wildfire events suggests that both horizontal wind speed and direction can have significant impacts on surface fire spread and growth. Finally, while a single run of the model for predicting fire spread might result in a poor accuracy because of the propagation of uncertainty, estimated distribution of the direction and intensity of the maximum rate of spread with an associated measure of uncertainty can be more useful than a single prediction.

The developed wildland surface fire spread model, together with the use of easily accessible remotely sensed data, might assume specific relevance for risk and emergency management. Within the context of the PhD project, three modules of a geospatial decision support system have been designed and implemented with the aim of improving the efficiency of risk management strategies and reducing expected impacts and potential damage: (i) the first module is a dynamic workflow of actions, designed by means of the formal mathematical approach of the Petri Nets, which aims to guide decision makers in carrying out the procedures of the intervention model compliant with the legislative framework; (ii) the second module is a customised version of a geographic information system with dynamic forms designed to ease the handling of the underlying relational geodatabase which stores the required information for risk and emergency management, among which scenarios of wildfire events, produced by means of the developed predictive wildland surface fire behaviour simulation model; (iii) the third module is composed by web applications for mobile field data collection and sharing. Amongst the major advantages in the developed geospatial decision support system, there is the opportunity to methodically check the stakeholders' intervention models for coherence, effectiveness, and legal compliance.

The PhD project strived to investigate principles and accepted theories on the complex dynamics of wildland surface fire behaviour and to shed light on the need for a better understanding of the difference between real and simulated fire behaviour in terms of the importance of the drivers of fire spread in predicting fire spread and growth. The project also tried proposing solutions integrating remote sensing and machine learning techniques with the aim of improving the applicability of near real-time simulation models as well as the effectiveness of decision-making strategies.

Acknowledgments

I would like to express my sincere gratitude to my tutor, Professor Tiziana Apuani, and co-tutors, Dr. Simone Sterlacchini and Dr. Giacomo Cappellini, for their patient support, unbounded trust, and experienced supervision. I would like to acknowledge them as well as the Coordinator of the PhD programme, Professor Fernando Camara Artigas, for the opportunity I was given to achieve this personally meaningful accomplishment.
I am also grateful to the external referees, Professor Cristina Vega Garcia and Dr. Michele Salis, for their precious comments.
Finally, I would like to thank researchers at the Laboratory for Risk Analysis and Emergency Management of the CNR's Institute of Environmental Geology and Geoengineering, who have professionally accompanied me throughout these years.

Appendix

Table 12-1 Standard fuel models (Albini, 1976a; Rothermel, 1972).

Fuel Model	Fuel loading 1h [lb/ft²]	Fuel loading 10h [lb/ft²]	Fuel loading 100h [lb/ft²]	Fuel loading live herb [lb/ft²]	Fuel loading live wood [lb/ft²]	SAVR 1h [ft²/ft³]	Fuel bed depth [ft]	Dead fuel moisture of extinction [%]	Heat content [Btu/lb]
GRs1	0.034	0.000	0.000	0.000	0.000	3500	1.00	12	8000
GRs2	0.092	0.046	0.023	0.023	0.000	3000	1.00	15	8000
GRs3	0.138	0.000	0.000	0.000	0.000	1500	2.50	25	8000
SHs4	0.230	0.184	0.092	0.000	0.230	2000	6.00	20	8000
SHs5	0.046	0.023	0.000	0.000	0.092	2000	2.00	20	8000
SHs6	0.069	0.115	0.092	0.000	0.000	1750	2.50	25	8000
SHs7	0.052	0.086	0.069	0.000	0.017	1750	2.50	40	8000
TLs8	0.069	0.046	0.115	0.000	0.000	2000	0.20	30	8000
TLs9	0.134	0.019	0.007	0.000	0.000	2500	0.20	25	8000
TLs10	0.138	0.092	0.230	0.000	0.092	2000	1.00	25	8000
SBs11	0.069	0.207	0.253	0.000	0.000	1500	1.00	15	8000
SBs12	0.184	0.644	0.759	0.000	0.000	1500	2.30	20	8000
SBs13	0.322	1.058	1.288	0.000	0.000	1500	3.00	25	8000

Table 12-2 Dynamic fuel models (Scott and Burgan, 2005).

Fuel Model	Fuel loading 1h [lb/ft²]	Fuel loading 10h [lb/ft²]	Fuel loading 100h [lb/ft²]	Fuel loading live herb [lb/ft²]	Fuel loading live wood [lb/ft²]	SAVR 1h [ft²/ft³]	Fuel bed depth [ft]	Dead fuel moisture of extinction [%]	Heat content [Btu/lb]
GR1	0.005	0.000	0.000	0.014	0.000	2200	0.40	15	8000
GR2	0.005	0.000	0.000	0.046	0.000	2000	1.00	15	8000
GR3	0.005	0.018	0.000	0.069	0.000	1500	2.00	30	8000
GR4	0.011	0.000	0.000	0.087	0.000	2000	2.00	15	8000
GR5	0.018	0.000	0.000	0.115	0.000	1800	1.50	40	8000
GR6	0.005	0.000	0.000	0.156	0.000	2200	1.50	40	9000
GR7	0.046	0.000	0.000	0.248	0.000	2000	3.00	15	8000
GR8	0.023	0.046	0.000	0.335	0.000	1500	4.00	30	8000
GR9	0.046	0.046	0.000	0.413	0.000	1800	5.00	40	8000
GS1	0.009	0.000	0.000	0.023	0.030	2000	0.90	15	8000
GS2	0.023	0.023	0.000	0.028	0.046	2000	1.50	15	8000
GS3	0.014	0.011	0.000	0.067	0.057	1800	1.80	40	8000
GS4	0.087	0.014	0.005	0.156	0.326	1800	2.10	40	8000
SH1	0.011	0.011	0.000	0.007	0.060	2000	1.00	15	8000
SH2	0.062	0.110	0.034	0.000	0.177	2000	1.00	15	8000

SH3	0.021	0.138	0.000	0.000	0.285	1600	2.40	40	8000
SH4	0.039	0.053	0.009	0.000	0.117	2000	3.00	30	8000
SH5	0.165	0.096	0.000	0.000	0.133	750	6.00	15	8000
SH6	0.133	0.067	0.000	0.000	0.064	750	2.00	30	8000
SH7	0.161	0.243	0.101	0.000	0.156	750	6.00	15	8000
SH8	0.094	0.156	0.039	0.000	0.200	750	3.00	40	8000
SH9	0.207	0.112	0.000	0.071	0.321	750	4.40	40	8000
TU1	0.009	0.041	0.069	0.009	0.041	2000	0.60	20	8000
TU2	0.044	0.083	0.057	0.000	0.009	2000	1.00	30	8000
TU3	0.051	0.007	0.011	0.030	0.051	1800	1.30	30	8000
TU4	0.207	0.000	0.000	0.000	0.092	2300	0.50	12	8000
TU5	0.184	0.184	0.138	0.000	0.138	1500	1.00	25	8000
TL1	0.046	0.101	0.165	0.000	0.000	2000	0.20	30	8000
TL2	0.064	0.106	0.101	0.000	0.000	2000	0.20	25	8000
TL3	0.023	0.101	0.129	0.000	0.000	2000	0.30	20	8000
TL4	0.023	0.069	0.193	0.000	0.000	2000	0.40	25	8000
TL5	0.053	0.115	0.202	0.000	0.000	2000	0.60	25	8000
TL6	0.110	0.055	0.055	0.000	0.000	2000	0.30	25	8000
TL7	0.014	0.064	0.372	0.000	0.000	2000	0.40	25	8000
TL8	0.266	0.064	0.051	0.000	0.000	1800	0.30	35	8000
TL9	0.305	0.152	0.191	0.000	0.000	1800	0.60	35	8000
SB1	0.069	0.138	0.505	0.000	0.000	2000	1.00	25	8000
SB2	0.207	0.195	0.184	0.000	0.000	2000	1.00	25	8000
SB3	0.253	0.126	0.138	0.000	0.000	2000	1.20	25	8000
SB4	0.241	0.161	0.241	0.000	0.000	2000	2.70	25	8000

Table 12-3 Fuel models for Northern Sardinia, Italy (Duce et al., 2012).

Fuel Model	Fuel loading 1h [lb/ft²]	Fuel loading 10h [lb/ft²]	Fuel loading 100h [lb/ft²]	Fuel loading live herb [lb/ft²]	Fuel loading live wood [lb/ft²]	SAVR 1h [ft²/ft³]	Fuel bed depth [ft]	Dead fuel moisture of extinction [%]	Heat content [Btu/lb]
SHmq1	0.067	0.067	0.003	0.007	0.054	750	2.30	25	8006
SHmq2	0.131	0.051	0.000	0.001	0.138	750	2.99	25	8006
SHmq3	0.177	0.111	0.013	0.008	0.200	750	3.35	25	8006
SHmq4	0.236	0.091	0.001	0.001	0.267	750	5.74	25	8006

Table 12-4 Fuel models for Apulia, Italy (Elia et al., 2015).

Fuel Model	Fuel loading 1h [lb/ft²]	Fuel loading 10h [lb/ft²]	Fuel loading 100h [lb/ft²]	Fuel loading live herb [lb/ft²]	Fuel loading live wood [lb/ft²]	SAVR 1h [ft²/ft³]	Fuel bed depth [ft]	Dead fuel moisture of extinction [%]	Heat content [Btu/lb]
TUapu1	0.321	0.045	0.015	0.015	0.075	1609	1.35	25	8000
TUapu2	0.236	0.034	0.006	0.016	0.185	1270	1.77	25	8000
SHapu3	0.173	0.010	0.002	0.130	0.084	689	1.67	25	8000
TUapu4	0.293	0.102	0.124	0.009	0.113	1358	1.94	25	8000

Table 12-5 Fuel models for Portugal (Godinho-Ferreira et al., 2005).

Fuel Model	Fuel loading 1h [lb/ft²]	Fuel loading 10h [lb/ft²]	Fuel loading 100h [lb/ft²]	Fuel loading live herb [lb/ft²]	Fuel loading live wood [lb/ft²]	SAVR 1h [ft²/ft³]	Fuel bed depth [ft]	Dead fuel moisture of extinction [%]	Heat content [Btu/lb]
TCLaca	0.106	0.031	0.000	0.071	0.000	1589	1.41	32	8713
TOTeuc	0.023	0.041	0.021	0.010	0.000	1111	0.52	27	9042
TOLeuc	0.027	0.008	0.000	0.024	0.000	1757	1.67	30	8987
TCTeuc	0.106	0.058	0.026	0.044	0.000	1753	0.92	28	9019
TCLeuc	0.076	0.010	0.000	0.082	0.000	1700	1.87	30	8984
TCLqpy	0.033	0.012	0.003	0.051	0.000	1675	2.26	26	8514
TCLque	0.130	0.012	0.003	0.100	0.000	1536	1.41	25	8428
TOTdiv	0.042	0.008	0.000	0.009	0.000	2170	0.56	26	8827
TOLdiv	0.035	0.005	0.000	0.024	0.000	1439	1.28	28	8810
TCTdiv	0.052	0.040	0.006	0.029	0.000	1455	1.28	28	8799
TCLdiv	0.039	0.021	0.000	0.073	0.000	1621	1.90	32	8793
TOTpin	0.109	0.061	0.024	0.018	0.000	1387	0.39	38	9195
TOLpin	0.038	0.021	0.000	0.048	0.000	1312	1.18	36	9219
TCTpin	0.151	0.058	0.018	0.062	0.000	1520	0.79	37	9130
TCLpin	0.136	0.018	0.004	0.130	0.000	1509	1.51	36	9146
TOTsub	0.028	0.004	0.000	0.011	0.000	1827	1.35	28	8776
TOLsub	0.026	0.052	0.000	0.020	0.000	1617	1.64	32	8766
TCTsub	0.067	0.039	0.000	0.024	0.000	1702	0.56	22	8795
TCLsub	0.097	0.032	0.000	0.090	0.000	1422	1.28	25	8762

Table 12-6 Fuel models for Greece (Dimitrakopoulos, 2002). Heat content and surface area-to-volume ratio values were obtained from Dimitrakopoulos and Panov (2001).

Fuel Model	Fuel loading 1h [lb/ft²]	Fuel loading 10h [lb/ft²]	Fuel loading 100h [lb/ft²]	Fuel loading live herb [lb/ft²]	Fuel loading live wood [lb/ft²]	SAVR 1h [ft²/ft³]	Fuel bed depth [ft]	Dead fuel moisture of extinction [%]	Heat content [Btu/lb]
SHmq15	0.152	0.139	0.074	0.158	0.000	1300	3.67	16	8678
SHmq30	0.297	0.272	0.299	0.217	0.000	1400	7.15	16	8867
SHque	0.260	0.215	0.096	0.138	0.000	1200	4.07	16	8277
SHphr1	0.090	0.045	0.014	0.053	0.000	700	1.80	16	8276
SHphr2	0.072	0.020	0.006	0.018	0.000	700	1.31	16	8191
GRmed	0.089	0.010	0.000	0.000	0.000	700	0.98	16	8070
TLpin	0.034	0.010	0.005	0.000	0.000	1700	0.20	16	8867

Table 12-7 Fuel models for Spain and Mediterranean Europe (Rodríguez y Silva and Molina-Martínez, 2012)

Fuel Model	Fuel loading 1h [lb/ft²]	Fuel loading 10h [lb/ft²]	Fuel loading 100h [lb/ft²]	Fuel loading live herb [lb/ft²]	Fuel loading live wood [lb/ft²]	SAVR 1h [ft²/ft³]	Fuel bed depth [ft]	Dead fuel moisture of extinction [%]	Heat content [Btu/lb]
GRp1	0.036	0.000	0.000	0.000	0.000	3800	1.00	12	8000
GRp2	0.078	0.000	0.000	0.000	0.000	3800	1.00	12	8000
GRp3	0.049	0.000	0.000	0.000	0.000	3800	1.50	12	8000
GRp4	0.079	0.000	0.000	0.000	0.000	3800	1.20	12	8000
GRp5	0.013	0.000	0.000	0.080	0.000	3800	2.60	12	8000
GRp6	0.111	0.000	0.000	0.000	0.000	3800	2.50	12	8000
GRp7	0.138	0.000	0.000	0.000	0.000	1800	2.80	25	8000
GRp8	0.114	0.000	0.000	0.038	0.000	1800	4.00	25	8000
GRp9	0.189	0.000	0.000	0.283	0.000	1800	4.00	25	8000
GSpm1	0.091	0.042	0.000	0.000	0.044	2500	1.00	15	8000
GSpm2	0.206	0.103	0.051	0.000	0.099	2500	2.00	15	8000
GSpm3	0.190	0.111	0.023	0.010	0.091	3000	1.20	20	8000
GSpm4	0.402	0.201	0.100	0.022	0.169	2600	2.00	20	8000
SHm1	0.056	0.000	0.000	0.000	0.151	2100	1.00	20	8000
SHm2	0.197	0.000	0.068	0.000	0.152	2100	1.00	20	8000
SHm3	0.235	0.059	0.069	0.000	0.125	2200	2.70	40	8000
SHm4	0.143	0.325	0.091	0.000	0.104	1600	3.30	40	8000
SHm5	0.363	0.125	0.062	0.000	0.216	1500	5.30	20	8000
SHm6	0.128	0.088	0.000	0.023	0.122	2200	4.00	25	8000
SHm7	0.457	0.246	0.122	0.000	0.272	2000	5.70	20	8000
SHm8	0.230	0.125	0.071	0.000	0.149	2300	4.00	25	8000
SHm9	0.711	0.202	0.101	0.000	0.387	2000	6.00	20	8000
TUhpm1	0.091	0.060	0.000	0.000	0.061	2000	1.00	15	8000
TUhpm2	0.164	0.108	0.000	0.000	0.109	2000	1.00	15	8000
TUhpm3	0.181	0.139	0.022	0.000	0.147	1750	2.00	40	8000
TUhpm4	0.361	0.271	0.024	0.000	0.228	1750	2.50	40	8000
TUhpm5	0.420	0.330	0.028	0.000	0.220	2000	2.80	25	8000
TLhr1	0.050	0.015	0.084	0.000	0.000	2000	0.10	30	8000
TLhr2	0.093	0.029	0.004	0.000	0.000	2500	0.20	25	8000
TLhr3	0.025	0.007	0.042	0.000	0.000	2000	0.10	30	8000
TLhr4	0.025	0.006	0.045	0.000	0.000	2500	0.40	25	8000
TLhr5	0.058	0.018	0.097	0.000	0.000	2000	0.20	30	8000
TLhr6	0.144	0.068	0.007	0.000	0.000	2500	0.40	25	8000
TLhr7	0.015	0.077	0.071	0.000	0.000	2000	0.60	25	8000
TLhr8	0.146	0.025	0.114	0.000	0.000	2000	0.20	25	8000
TLhr9	0.291	0.192	0.120	0.000	0.000	2500	0.60	25	8000

Bibliography

Abatzoglou, J. T., Dobrowski, S. Z., Parks, S. A., Hegewisch, K. C. (2018). TerraClimate, a high-resolution global dataset of monthly climate and climatic water balance from 1958-2015. *Scientific Data*, *5*, 1–12. https://doi.org/10.1038/sdata.2017.191

Abatzoglou, J. T., Williams, A. P., Barbero, R. (2019). Global Emergence of Anthropogenic Climate Change in Fire Weather Indices. *Geophysical Research Letters*, *46*(1), 326–336. https://doi.org/10.1029/2018GL080959

Abatzoglou, J. T., Williams, A. P., Boschetti, L., Zubkova, M., Kolden, C. A. (2018). Global patterns of interannual climate – fire relationships. *Global Change Biology*, *24*, 5164–5175. https://doi.org/10.1111/gcb.14405

Ager, A. A., Preisler, H. K., Arca, B., Spano, D., Salis, M. (2014). Wildfire risk estimation in the Mediterranean area. *Environmetrics*, *25*(6), 384–396. https://doi.org/10.1002/env.2269

Aguado, I., Chuvieco, E., Borén, R., Nieto, H. (2007). Estimation of dead fuel moisture content from meteorological data in Mediterranean areas. Applications in fire danger assessment. *International Journal of Wildland Fire*, *16*, 390–397.

Albini, F. A. (1976a). Computer-based models of wildland fire behavior: a users' manual. *U.S. Department of Agriculture, Forest Service, Intermountain Forest and Range Experiment Station. General Technical Report*, 68 pp.

Albini, F. A. (1976b). *Estimating Wildfire Behaviour and Effects*. *U.S. Department of Agriculture, Forest Service, Intermountain Forest and Range Experiment Station. General Technical Report* (Vol. INT-30).

Albini, F. A. (1984). Wildland Fires: Predicting the behavior of wildland fires—among nature's most potent forces—can save lives, money, and natural resources. *American Scientist*, *72*(6), 590–597. https://doi.org/10.1007/978-1-4939-2565-0_87

Alexander, M. E., Cruz, M. G. (2013). Limitations on the accuracy of model predictions of wildland fire behaviour: A state-of-the-knowledge overview. *The Forestry Chronicle*, *89*(3), 370–381.

Alexandridis, A., Vakalis, D., Siettos, C. I., Bafas, G. V. (2008). A cellular automata model for forest fire spread prediction : The case of the wildfire that swept through Spetses Island in 1990. *Applied Mathematics and Computation*, *204*, 191–201. https://doi.org/10.1016/j.amc.2008.06.046

Alfieri, L., Burek, P., Dutra, E., Krzeminski, B., Muraro, D., Thielen, J., Pappenberger, F. (2013). GloFAS-global ensemble streamflow forecasting and flood early warning. *Hydrology and Earth System Sciences*, *17*(3), 1161–1175. https://doi.org/10.5194/hess-17-1161-2013

Alkhatib, A. A. A. (2014). A review on forest fire detection techniques. *International Journal of Distributed Sensor Networks*, 1–12. https://doi.org/10.1155/2014/597368

Almasi, G. S., Gottlieb, A. (1989). *Highly Parallel Computing*. (Benjamin-Cummings Publishing Co., Ed.).

Alonso-Benito, A., Arroyo, L. A., Arbelo, M., Hernández-Leal, P. (2016). Fusion of WorldView-2 and LiDAR Data to Map Fuel Types in the Canary Islands. *Remote Sensing*, *8*, 669–687. https://doi.org/10.3390/rs8080669

Amparore, E. G., Balbo, G., Beccuti, M., Donatelli, S., Franceschinis, G. (2016). 30 Years of GreatSPN. In L. Fiondella & A. Puliafito (Eds.), *Principles of Performance and Reliability Modeling and Evaluation* (pp. 227–254). Springer Series in Reliability Engineering. https://doi.org/10.1007/978-3-319-30599-8

Andela, N., Morton, D. C., Giglio, L., Chen, Y., Van Der Werf, G. R., Kasibhatla, P. S., … Randerson, J. T. (2017). A human-driven decline in global burned area. *Science*, *356*(6345), 1356–1362. https://doi.org/10.1126/science.aal4108.A

Anderson, D. H., Catchpole, E. A., De Mestre, N. J., Parkes, T. (1982). Modelling the spread of grass fires. *The Journal of the Australian Mathematical Society. Series B. Applied Mathematics*, *23*(4), 451–466. https://doi.org/10.1017/s0334270000000394

Anderson, H. E. (1969). Heat transfer and fire spread. *U.S. Department of Agriculture, Forest Service, Intermountain Forest and Range Experiment Station. Research Paper, INT-69*. https://doi.org/10.5962/bhl.title.69024

Anderson, H. E. (1982). *Aids to Determining Fuel Models for Estimating Fire Behavior*. *U.S. Department of Agriculture, Forest Service, Intermountain Forest and Range Experiment Station. General Technical Report* (Vol. INT-122).

Andrews, P. L. (1986). *BEHAVE : Fire Behavior Prediction and Fuel Modeling System - BURN Subsystem. U.S. Department of Agriculture, Forest Service, Intermountain Forest and Range Experiment Station. General Technical Report* (Vol. INT-194).

Andrews, P. L. (2012). *Modeling Wind Adjustment Factor and Midflame Wind Speed for Rothermel's Surface Fire Spread Model*. *U.S. Department of Agriculture, Forest Service, Rocky Mountain Research Station. General Technical Report* (Vol. RMRS-GTR-2).

Andrews, P. L. (2018). *The Rothermel Surface Fire Spread Model and Associated Developments: A Comprehensive Explanation*. *U.S. Department of Agriculture, Forest Service, Rocky Mountain Research Station. General Technical Report* (Vol. RMRS-GTR-3).

Arca, B., Bacciu, V. M., Pellizzaro, G., Salis, M., Ventura, A., Duce, P., Brundu, G. (2009). Fuel model mapping by IKONOS imagery to support spatially explicit fire simulators. In *7th International Workshop on Advances in Remote Sensing and GIS Applications in Forest Fire Management towards an Operational Use of Remote Sensing in Forest Fire Management*.

Arca, B., Duce, P., Laconi, M., Pellizzaro, G., Salis, M., Spano, D. (2007). Evaluation of FARSITE simulator in Mediterranean maquis. *International Journal of Wildland Fire*, *16*(5), 563–572. https://doi.org/10.1071/WF06070

Arroyo, L. A., Healey, S. P., Cohen, W. B., Cocero, D., Manzanera, J. A. (2006). Using object-oriented classification and high-resolution imagery to map fuel types in a Mediterranean region. *Journal of Geophysical Research: Biogeosciences*, *111*(4), 1–10. https://doi.org/10.1029/2005JG000120

Ascoli, D., Vacchiano, G., Scarpa, C., Arca, B., Barbati, A., Battipaglia, G., … Bacciu, V. M. (2020). Harmonized dataset of surface fuels under Alpine, temperate and Mediterranean conditions in Italy. A synthesis supporting fire management. *I Forest, 13*, 513–522. https://doi.org/10.3832/ifor3587-013

Autonomous Region of Sardinia. (2008). Carta dell'Uso del Suolo in scala 1:25.000. Retrieved from http://webgis2.regione.sardegna.it/catalogodati/card.jsp?uuid=R_SARDEG:TVWIX

Autonomous Region of Sardinia. (2010). Modello Digitale del Terreno (DTM), passo 5 m. Retrieved from http://webgis2.regione.sardegna.it/geonetwork/srv/ita/

Autonomous Region of Sardinia. (2017a). Corpo Forestale, un indagato per l'incendio di Gonnosfanadiga e Arbus: evento colposo secondo investigatori. Retrieved from https://www.regione.sardegna.it/

Autonomous Region of Sardinia. (2017b). *Piano regionale di previsione, prevenzione e lotta attiva contro gli incendi boschivi 2017-2019.*

Autonomous Region of Sardinia. (2017c). *Rapporto sugli incendi boschivi e rurali in Sardegna - Anno 2016*. (Regione Autonoma della Sardegna - Assessorato alla Difesa dell'Ambiente, Ed.).

Autonomous Region of Sardinia. (2020a). Notiziari giornalieri incendi boschivi. Retrieved from http://www.sardegnaambiente.it/

Autonomous Region of Sardinia. (2020b). Sardegna Geoportale - Perimetrazioni aree percorse dal fuoco. Retrieved from http://www.sardegnageoportale.it/webgis2/sardegnamappe/?map=aree_tutelate

Bajocco, S., Dragoz, E., Gitas, I., Smiraglia, D., Salvati, L., Ricotta, C. (2015). Mapping Forest Fuels through Vegetation Phenology: The Role of Coarse-Resolution Satellite Time-Series. *PLoS ONE*, *10*(3), 1–14. https://doi.org/10.1371/journal.pone.0119811

Barmpoutis, P., Papaioannou, P., Dimitropoulos, K., Grammalidis, N. (2020). A review on early forest fire detection systems using optical remote sensing. *Sensors*, *20*(22), 1–26. https://doi.org/10.3390/s20226442

Belcher, C. M., Mills, B. J. W., Vitali, R., Baker, S. J., Lenton, T. M., Watson, A. J. (2021). The rise of angiosperms strengthened fire feedbacks and improved the regulation of atmospheric oxygen. *Nature Communications*, *12*(1), 1–9. https://doi.org/10.1038/s41467-020-20772-2

Bennie, J., Huntley, B., Wiltshire, A., Hill, M. O., Baxter, R. (2008). Slope, aspect and climate: Spatially explicit and implicit models of topographic microclimate in chalk grassland. *Ecological Modelling*, *216*(1), 47–59. https://doi.org/10.1016/j.ecolmodel.2008.04.010

Berger, C., Werner, S., Wigley-Coetsee, C., Smit, I., Schmullius, C. (2019). Multi-temporal Sentinel-1 data for wall-to-wall herbaceous biomass mapping in Kruger National Park, South Africa - First results. *IGARSS 2019 - 2019 IEEE International Geoscience and Remote Sensing Symposium*, (1), 7358–7360.

Boni, C. (2004). Il fenomeno degli incendi in Sardegna. In *Atti del Convegno Incendi boschivi e rurali in Sardegna. Dall'analisi delle cause alle proposte d'intervento* (pp. 9–17).

Bossard, M., Feranec, J., Otahel, J. (2000). *CORINE land cover technical guide - Addendum 2000*.

Bouvet, A., Mermoz, S., Le Toan, T., Villard, L., Mathieu, R., Naidoo, L., Asner, G. P. (2018). An above-ground biomass map of African savannahs and woodlands at 25 m resolution derived from ALOS PALSAR. *Remote Sensing of Environment*, *206*(December 2016), 156–173. https://doi.org/10.1016/j.rse.2017.12.030

Bowman, D. M. J. S. (2018). Wildfire science is at a loss for comprehensive data. *Nature*, *560*(7716), 7. https://doi.org/10.1038/d41586-018-05840-4

Bowman, D. M. J. S., Balch, J., Artaxo, P., Bond, W. J., Cochrane, M. A., D'Antonio, C. M., … Swetnam, T. W. (2011). The human dimension of fire regimes on Earth. *Journal of Biogeography*, *38*(12), 2223–2236. https://doi.org/10.1111/j.1365-2699.2011.02595.x

Bowman, D. M. J. S., Kolden, C. A., Abatzoglou, J. T., Johnston, F. H., van der Werf, G. R., Flannigan, M. (2020). Vegetation fires in the Anthropocene. *Nature Reviews Earth & Environment*, *1*(10), 500–515. https://doi.org/10.1038/s43017-020-0085-3

Bowman, D. M. J. S., Williamson, G. J., Abatzoglou, J. T., Kolden, C. A., Cochrane, M. A., Smith, A. M. S. (2017). Human exposure and sensitivity to globally extreme wildfire events. *Nature Ecology & Evolution*, *1*(February), 1–6. https://doi.org/10.1038/s41559-016-0058

Breiman, L. (2001). Random Forests. *Machine Learning*, *45*, 5–32. https://doi.org/10.1201/9780367816377-11

Brewer, M. J., Clements, C. B. (2020). The 2018 Camp Fire: Meteorological Analysis Using In Situ Observations and Numerical Simulations. *Atmosphere*, *11*(47), 2–19. https://doi.org/10.3390/ATMOS11010047

Burgan, R. E., Rothermel, R. C. (1984). *BEHAVE : Fire Behavior Prediction and Fuel Modeling System - FUEL Subsystem. U.S. Department of Agriculture, Forest Service, Intermountain Forest and Range Experiment Station. General Technical Report* (Vol. INT-167).

Byram, G. M. (1959). Combustion of forest fuels. In K. P. Davis, G. M. Byram, & W. R. Krumm (Eds.), *Forest Fire: Control and Use* (pp. 61–89). New York, NY: McGraw-Hill Book Company.

Caccamo, G., Chisholm, L. A., Bradstock, R. A., Puotinen, M. L., Pippen, B. G. (2012). Monitoring live fuel moisture content of heathland, shrubland and sclerophyll forest in south-eastern Australia using MODIS data. *International Journal of Wildland Fire*, *21*(3), 257–269. https://doi.org/10.1071/WF11024

CAL FIRE. (2020). Daily Wildfire Report. Retrieved from https://www.fire.ca.gov/daily-wildfire-report/

Calviño-Cancela, M., Chas-Amil, M. L., García-Martínez, E. D., Touza, J. (2017). Interacting effects of topography, vegetation, human activities and wildland-urban interfaces on wildfire ignition risk. *Forest Ecology and Management*, *397*, 10–17. https://doi.org/10.1016/j.foreco.2017.04.033

Camarda, I., Laureti, L., Angelini, P., Capogrossi, R., Carta, L., Brunu, A. (2015). *Il sistema Carta della Natura della Sardegna*.

Camia, A., San-Miguel-Ayánz, J., Kucera, J., Amatulli, G., Boca, R., Libertà, G., … Bucki, M. (2008). *Forest Fires in Europe 2007*.

Canli, E., Loigge, B., Glade, T. (2018). Spatially distributed rainfall information and its potential for regional landslide early warning systems. *Natural Hazards*, *91*(s1), 103–127. https://doi.org/10.1007/s11069-017-2953-9

Catchpole, E. A., Alexander, M. E., Gill, A. M. (1992). Elliptical-fire perimeter- and area-intensity distributions. *Canadian Journal of Forest Research*, *22*, 968–972.

Caton, S. E., Hakes, R. S. P., Gollner, M. J., Gorham, D. J., Zhou, A. (2017). Review of Pathways for Building Fire Spread in the Wildland Urban Interface Part I: Exposure Conditions. *Fire Technology*, *53*(2), 429–473. https://doi.org/10.1007/s10694-016-0589-z

Cawson, J. G., Nyman, P., Schunk, C., Sheridan, G. J., Duff, T. J., Gibos, K., … Menzel, A. (2020). Estimation of surface dead fine fuel moisture using automated fuel moisture sticks across a range of forests worldwide. *International Journal of Wildland Fire*, *29*(6), 548–559. https://doi.org/10.1071/WF19061

Certini, G. (2005). Effects of fire on properties of forest soils: a review. *Oecologia*, *143*(1), 1–10. https://doi.org/10.1007/s00442-004-1788-8

Chambers, J. C., Brooks, M. L., Germino, M. J., Maestas, J. D., Board, D. I., Jones, M. O., Allred, B. W. (2019). Operationalizing Resilience and Resistance Concepts to Address Invasive Grass-Fire Cycles. *Frontiers in Ecology and Evolution*, *7*(185), 1–25. https://doi.org/10.3389/fevo.2019.00185

Chen, T., Guestrin, C. (2016). XGBoost: A scalable Tree Boosting System. *Proceedings of the ACM SIGKDD International Conference on Knowledge Discovery and Data Mining*, 785–794. https://doi.org/10.1145/2939672.2939785

Chowdhury, E. H., Hassan, Q. K. (2013). Use of remote sensing-derived variables in developing a forest fire danger forecasting system. *Natural Hazards*, *67*(2), 321–334. https://doi.org/10.1007/s11069-013-0564-7

Chuvieco, E., Cocero, D., Riaño, D., Martin, P., Martínez-Vega, J., de la Riva, J., Pérez, F. (2004). Combining NDVI and surface temperature for the estimation of live fuel moisture content in forest fire danger rating. *Remote Sensing of Environment*, *92*, 322–331. https://doi.org/10.1016/j.rse.2004.01.019

Chuvieco, E., Giglio, L., Justice, C. (2008). Global characterization of fire activity: toward defining fire regimes from Earth observation data. *Global Change Biology*, *14*, 1488–1502. https://doi.org/10.1111/j.1365-2486.2008.01585.x

Chuvieco, E., González, I., Verdú, F., Aguado, I., Yebra, M. (2009). Prediction of fire occurrence from live fuel moisture content measurements in a Mediterranean ecosystem. *International Journal of Wildland Fire*, (18), 430–441.

Chuvieco, E., Lizundia-Loiola, J., Pettinari, M. L., Ramo, R., Padilla, M., Tansey, K., … Heil, A. (2018). Generation and analysis of a new global burned area product based on MODIS 250 m reflectance bands and thermal anomalies. *Earth System Science Data*, *10*, 2015–2031.

Clarke, K. C. (2014). Cellular Automata and Agent-Based Models. In M. M. Fischer & P. Nijkamp (Eds.), *Handbook of Regional Science* (pp. 1217–1233). https://doi.org/10.1007/978-3-642-23430-9

Collins, K. M., Price, O. F., Penman, T. D. (2015). Spatial patterns of wildfire ignitions in south-eastern Australia. *International Journal of Wildland Fire*, *24*(8), 1098–1108. https://doi.org/10.1071/WF15054

Coogan, S. C. P., Cai, X., Jain, P., Flannigan, M. D. (2020). Seasonality and trends in human- A nd lightning-caused wildfires ≥ 2 ha in Canada, 1959-2018. *International Journal of Wildland Fire*, *29*(6), 473–485. https://doi.org/10.1071/WF19129

Corona, P., Gismondi, R. (2019). Gestione e tutela delle foreste. In *RaF 2017-2018 - Rapporto sullo stato delle foreste e del settore forestale in Italia* (pp. 98–119).

Costa, H., de Rigo, D., Libertà, G., Houston Durrant, T., San-Miguel-Ayánz, J. (2020). *European wildfire danger and vulnerability in a changing climate: towards integrating risk dimensions*. Luxembourg: Publications Office of the European Union. https://doi.org/10.2760/46951

Couto, F. T., Iakunin, M., Salgado, R., Pinto, P., Viegas, T., Pinty, J. P. (2020). Lightning modelling for the research of forest fire ignition in Portugal. *Atmospheric Research*, *242*(March), 104993. https://doi.org/10.1016/j.atmosres.2020.104993

Curry, J. R., Fons, W. L. (1940). Forest-fire behavior studies. *Mechanical Engineering, New York*, 219–225.

de Rigo, D., Libertà, G., Houston Durrant, T., Artés Vivancos, T., San-Miguel-Ayánz, J. (2017). *Forest fire danger extremes in Europe under climate change: variability and uncertainty*. Luxembourg: Publications Office of the European Union. https://doi.org/10.2760/13180

de Sousa, L. M., Leitão, J. P. (2017). Hex-utils: A tool set supporting HexASCII hexagonal rasters. *Proceedings of the 3rd International Conference on Geographical Information Systems Theory, Applications and Management (GISTAM)*, 177–183. https://doi.org/10.5220/0006275801770183

Dennison, P. E., Roberts, D. A., Thorgusen, S. R., Regelbrugge, J. C., Weise, D., Lee, C. (2003). Modeling seasonal changes in live fuel moisture and equivalent water thickness using a cumulative water balance index. *Remote Sensing of Environment*, *88*(4), 442–452. https://doi.org/10.1016/j.rse.2003.08.015

Dimitrakopoulos, A. P. (2002). Mediterranean fuel models and potential fire behaviour in Greece. *International Journal of Wildland Fire*, *11*(2), 127–130. https://doi.org/10.1071/WF02018

Dimitrakopoulos, A. P., Panov, P. I. (2001). Pyric properties of some dominant Mediterranean vegetation species. *International Journal of Wildland Fire*, *10*, 23–27.

Dimitrakopoulos, A. P., Papaioannou, K. K. (2001). Flammability assessment of Mediterranean forest fuels. *Fire Technology*, *37*(2), 143–152. https://doi.org/10.1023/A:1011641601076

Doerr, S. H., Santín, C. (2016). Global trends in wildfire and its impacts: perceptions versus realities in a changing world. *Philosophical Transactions of the Royal Society B: Biological Sciences*, *371*(1696). https://doi.org/10.1098/rstb.2015.0345

Domingo, D., de la Riva, J., Lamelas, M. T., García-Martin, A., Ibarra, P., Echeverría, M., Hoffrén, R. (2020). Fuel Type Classification Using Airborne Laser Scanning and Sentinel 2 Data in Mediterranean Forest Affected by Wildfires. *Remote Sensing*, *12*, 3660.

Dubayah, R. O., Blair, J. B., Goetz, S. J., Fatoyinbo, L., Hansen, M., Healey, S. P., … Silva, C. (2020). The Global Ecosystem Dynamics Investigation: High-resolution laser ranging of the Earth's forests and topography. *Science of Remote Sensing*, *1*(January), 100002. https://doi.org/10.1016/j.srs.2020.100002

Dubayah, R. O., Goetz, S. J., Blair, J. B., Fatoyinbo, L., Hansen, M., Healey, S. P., … Swatantran, A. (2014). The Global Ecosystem Dynamics Investigation. In *American Geophysical Union*.

Dubayah, R. O., Tang, H., Armston, J., Luthcke, S. B., Hofton, M. A., Blair, J. B. (2020). GEDI L2B Canopy Cover and Vertical Profile Metrics Data Global Footprint Level V001 [data set]. https://doi.org/10.5067/GEDI/GEDI02_B.001

Duce, P., Pellizzaro, G., Arca, B., Ventura, A., Bacciu, V. M., Salis, M., … Perez, Y. (2012). Fuel types and potential fire behaviour in Sardinia and Corsica islands: a pilot study. In *Modelling fire behaviour and risk* (pp. 2–8). Retrieved from http://www.cmcc.it/wp-content/uploads/2013/04/P_Book_Modelling-Fire-Behaviour-and-Risk.pdf

Dupuy, J.-L., Fargeon, H., Martin-StPaul, N., Pimont, F., Ruffault, J., Guijarro, M., … Fernandes, P. (2020). Climate change impact on future wildfire danger and activity in southern Europe: a review. *Annals of Forest Science*, *77*(2). https://doi.org/10.1007/s13595-020-00933-5

Eames, T., Russell-Smith, J., Yates, C., Edwards, A., Vernooij, R., Ribeiro, N., … van der Werf, G. R. (2021). Instantaneous pre-fire biomass and fuel load measurements from multi-spectral UAS mapping in southern African Savannas. *Fire*, *4*(1), 1–19. https://doi.org/10.3390/fire4010002

Earl, N., Simmonds, I. (2018). Spatial and Temporal Variability and Trends in 2001–2016 Global Fire Activity. *Journal of Geophysical Research: Atmospheres*, *123*, 2524–2536. https://doi.org/10.1002/2017JD027749

Efthimiou, N., Psomiadis, E., Panagos, P. (2020). Fire severity and soil erosion susceptibility mapping using multi-temporal Earth Observation data: The case of Mati fatal wildfire in Eastern Attica, Greece. *Catena*, *187*(July 2019), 104320. https://doi.org/10.1016/j.catena.2019.104320

Elia, M., Giannico, V., Lafortezza, R., Sanesi, G. (2019). Modeling fire ignition patterns in Mediterranean urban interfaces. *Stochastic Environmental Research and Risk Assessment*, *33*(1), 169–181. https://doi.org/10.1007/s00477-018-1558-5

Elia, M., Lafortezza, R., Lovreglio, R., Sanesi, G. (2015). Developing Custom Fire Behavior Fuel Models for Mediterranean Wildland–Urban Interfaces in Southern Italy. *Environmental Management*, *56*(3), 754–764. https://doi.org/10.1007/s00267-015-0531-z

Encinas, L. H., White, S. H., del Rey, A. M., Sánchez, G. R. (2007). Modelling forest fire spread using hexagonal cellular automata. *Applied Mathematical Modelling*, *31*(6), 1213–1227. https://doi.org/10.1016/j.apm.2006.04.001

ESA. (2020). Copernicus Open Access Hub. Retrieved from https://scihub.copernicus.eu/

European Forest Fire Information System. (2017). European Fuel Map, 2017, based on JRC Contract Number 384347 on the "Development of a European Fuel Map". Retrieved from https://effis.jrc.ec.europa.eu/about-effis/technical-background/fuels/

European Union - Copernicus Climate Change Service - European Environment Agency (EEA). (2020). Climate Data Store. Retrieved from https://cds.climate.copernicus.eu/#!/home

European Union - Copernicus Land Monitoring Service - European Environment Agency (EEA). (2012). CORINE Land Cover 2012. Retrieved from https://land.copernicus.eu/pan-european/corine-land-cover

Fan, L., Wigneron, J.-P., Xiao, Q., Al-Yaari, A., Wen, J., Martin-StPaul, N., … Kerr, Y. H. (2018). Evaluation of microwave remote sensing for monitoring live fuel moisture content in the Mediterranean region. *Remote Sensing of Environment*, *205*, 210–223. https://doi.org/10.1016/j.rse.2017.11.020

Fensholt, R., Proud, S. R. (2012). Evaluation of Earth Observation based global long term vegetation trends - Comparing GIMMS and MODIS global NDVI time series. *Remote Sensing of Environment*, *119*, 131–147. https://doi.org/10.1016/j.rse.2011.12.015

Fensholt, R., Sandholt, I. (2005). Evaluation of MODIS and NOAA AVHRR vegetation indices with in situ measurements in a semi-arid environment. *International Journal of Remote Sensing*, *26*(12), 2561–2594. https://doi.org/10.1080/01431160500033724

Fernandes, P. M. (2009). Combining forest structure data and fuel modelling to classify fire hazard in Portugal. *Annals of Forest Science*, *66*(4), 415–423. https://doi.org/10.1051/forest/2009013

Fernandez-Pello, A. C. (2017). Wildland fire spot ignition by sparks and firebrands. *Fire Safety Journal*, *91*(May), 2–10. https://doi.org/10.1016/j.firesaf.2017.04.040

Finney, M. A. (1998). FARSITE: Fire Area Simulator - Model development and evaluation. *U.S. Department of Agriculture, Forest Service, Intermountain Forest and Range Experiment Station. Research Paper, RMRS-RP-4*, 1–47.

Finney, M. A. (2002). Fire growth using minimum travel time methods. *Canadian Journal of Forest Research*, *32*(8), 1420–1424. https://doi.org/10.1139/x02-068

Finney, M. A., Cohen, J. D., McAllister, S. S., Jolly, W. M. (2013). On the need for a theory of wildland fire spread. *International Journal of Wildland Fire*, *22*(1), 25–36. https://doi.org/10.1071/WF11117

Flannigan, M. D., Cantin, A. S., de Groot, W. J., Wotton, B. M., Newbery, A., Gowman, L. M. (2013). Global wildland fire season severity in the 21st century. *Forest Ecology and Management*, *294*, 54–61. https://doi.org/10.1016/j.foreco.2012.10.022

Flannigan, M. D., Krawchuk, M. A., de Groot, W. J., Wotton, B. M., Gowman, L. M. (2009). Implications of changing climate for global wildland fire. *International Journal of Wildland Fire*, *18*(5), 483–507. https://doi.org/10.1071/WF08187

Flannigan, M. D., Wotton, B. M., Marshall, G. A., de Groot, W. J., Johnston, J., Jurko, N., Cantin, A. S. (2016). Fuel moisture sensitivity to temperature and precipitation : climate change implications. *Climatic Change*, *134*, 59–71. https://doi.org/10.1007/s10584-015-1521-0

Forkel, M., Dorigo, W., Lasslop, G., Chuvieco, E., Hantson, S., Heil, A., … Harrison, S. P. (2019). Recent global and regional trends in burned area and their compensating environmental controls. *Environmental Research Communications*, 051005.

Forthofer, J. M. (2007). *Modeling wind in complex terrain for use in fire spread prediction*.

Forthofer, J. M., Butler, B. W., Mchugh, C. W., Finney, M. A., Bradshaw, L. S., Stratton, R. D., … Wagenbrenner, N. S. (2014). A comparison of three approaches for simulating fine-scale surface winds in support of wildland fire management. Part II. An exploratory study of the effect of simulated winds on fire growth simulations. *International Journal of Wildland Fire*, *23*(7), 982–994. https://doi.org/10.1071/WF12090

Forthofer, J. M., Butler, B. W., Wagenbrenner, N. S. (2014). A comparison of three approaches for simulating fine-scale surface winds in support of wildland fire management. Part I. Model formulation and comparison against measurements. *International Journal of Wildland Fire*, *23*(7), 969–981. https://doi.org/10.1071/WF12089

Forthofer, J. M., Shannon, K. S., Butler, B. W. (2009). Simulating Diurnally Driven Slope Winds with WindNinja. In *Proceedings of 8th Symposium on Fire and Forest Meteorological Society* (p. 13).

Frandsen, W. H. (1971). Fire spread through porous fuels from the conservation of energy. *Combustion and Flame*, *16*(1), 9–16. https://doi.org/10.1016/S0010-2180(71)80005-6

Franke, J., Barradas, A. C. S., Borges, M. A., Menezes Costa, M., Dias, P. A., Hoffmann, A. A., … Siegert, F. (2018). Fuel load mapping in the Brazilian Cerrado in support of integrated fire management. *Remote Sensing of Environment*, *217*(January), 221–232. https://doi.org/10.1016/j.rse.2018.08.018

Freire, J. G., Castro DaCamara, C. (2018). Using cellular automata to simulate wildfire propagation and to assist in fire prevention and fighting. *Natural Hazards and Earth System Sciences Discussions*, (19), 169–179. https://doi.org/10.5194/nhess-2018-227

Frey, C. M., Kuenzer, C., Dech, S. (2012). Quantitative comparison of the operational NOAA-AVHRR LST product of DLR and the MODIS LST product V005. *International Journal of Remote Sensing*, *33*(22), 7165–7183. https://doi.org/10.1080/01431161.2012.699693

Friedman, J. H. (2001). Greedy Function Approximation: A Gradient Boosting Machine. *The Annals of Statistics*, *29*(5), 1189–1232.

Gabbasova, I. M., Garipov, T. T., Suleimanov, R. R., Komissarov, M. A., Khabirov, I. K., Sidorova, L. V, … Kotlugalyamova, E. Y. (2019). The Influence of Ground Fires on the Properties and Erosion of Forest

Soils in the Southern Urals (Bashkir State Nature Reserve). *Eurasian Soil Science*, *52*(4), 370–379. https://doi.org/10.1134/S1064229319040070

Ganteaume, A., Barbero, R., Jappiot, M., Maillé, E. (2021). Understanding future changes to fires in southern Europe and their impacts on the wildland-urban interface. *Journal of Safety Science and Resilience*, *2*(1), 20–29. https://doi.org/10.1016/j.jnlssr.2021.01.001

Ganteaume, A., Camia, A., Jappiot, M., San-Miguel-Ayánz, J., Long-Fournel, M., Lampin, C. (2013). A review of the main driving factors of forest fire ignition over Europe. *Environmental Management*, *51*(3), 651–662. https://doi.org/10.1007/s00267-012-9961-z

García, M., Chuvieco, E., Nieto, H., Aguado, I. (2008). Combining AVHRR and meteorological data for estimating live fuel moisture content. *Remote Sensing of Environment*, *112*, 3618–3627. https://doi.org/10.1016/j.rse.2008.05.002

Garcia, M., Saatchi, S., Casas, A., Koltunov, A., Ustin, S. L., Ramirez, C., … Balzter, H. (2017). Quantifying biomass consumption and carbon release from the California Rim fire by integrating airborne LiDAR and Landsat OLI data. *Journal of Geophysical Research: Biogeosciences*, *122*, 1–12. https://doi.org/10.1002/2015JG003315.Received

Gasparini, P., Marchetti, M. (2019). Patrimonio forestale. In *RaF 2017-2018 - Rapporto sullo stato delle foreste e del settore forestale in Italia* (pp. 72–91).

Ghisu, T., Arca, B., Pellizzaro, G., Duce, P. (2014). A level-set algorithm for simulating wildfire spread. *CMES - Computer Modeling in Engineering and Sciences*, *102*(1), 83–102. https://doi.org/10.3970/cmes.2014.102.083

Ghisu, T., Arca, B., Pellizzaro, G., Duce, P. (2015). An optimal Cellular Automata algorithm for simulating wildfire spread. *Environmental Modelling and Software*, *71*, 1–14. https://doi.org/10.1016/j.envsoft.2015.05.001

Giglio, L., Boschetti, L., Roy, D. P., Humber, M. L., Justice, C. O. (2018). The Collection 6 MODIS burned area mapping algorithm and product. *Remote Sensing of Environment*, *217*(March), 72–85. https://doi.org/10.1016/j.rse.2018.08.005

Gillies, S. (2013). The Shapely Manual. Retrieved from https://shapely.readthedocs.io/en/latest/manual.html

Glade, T., Nadim, F. (2014). Early warning systems for natural hazards and risks. *Natural Hazards*, *70*(3), 1669–1671. https://doi.org/10.1007/s11069-013-1000-8

Glasa, J., Halada, L. (2008). On elliptical model for forest fire spread modeling and simulation. *Mathematics and Computers in Simulation*, *78*(1), 76–88. https://doi.org/10.1016/j.matcom.2007.06.001

Glasa, J., Halada, L. (2011). A note on mathematical modelling of elliptical fire propagation. *Computing and Informatics*, *30*(6), 1303–1319.

Godinho-Ferreira, P., Azevedo, A., Rego, F. M. C. C. (2005). Carta da Tipologia Florestal de Portugal Continental. *Silva Lusitana*, *13*(1), 1–34. https://doi.org/10.5751/ES-04642-170214

González-Olabarria, J. R., Rodríguez, F., Fernández-Landa, A., Mola-Yudego, B. (2012). Mapping fire risk in the Model Forest of Urbión (Spain) based on airborne LiDAR measurements. *Forest Ecology and Management*, *282*, 149–156. https://doi.org/10.1016/j.foreco.2012.06.056

Gorelick, N., Hancher, M., Dixon, M., Ilyushchenko, S., Thau, D., Moore, R. (2017). Google Earth Engine: Planetary-scale geospatial analysis for everyone. *Remote Sensing of Environment*, *202*, 18–27. https://doi.org/10.1016/j.rse.2017.06.031

Goss, M., Swain, D. L., Abatzoglou, J. T., Sarhadi, A., Kolden, C. A., Williams, A. P., Diffenbaugh, N. S. (2020). Climate change is increasing the likelihood of extreme autumn wildfire conditions across California. *Environmental Research Letters*, *15*(9), 094016. https://doi.org/10.1088/1748-9326/ab83a7

Hantson, S., Pueyo, S., Chuvieco, E. (2015). Global fire size distribution is driven by human impact and

climate. *Global Ecology and Biogeography*, *24*(1), 77–86. https://doi.org/10.1111/geb.12246

Harris, C. R., Millman, K. J., van der Walt, S. J., Gommers, R., Virtanen, P., Cournapeau, D., … Oliphant, T. E. (2020). Array programming with NumPy. *Nature*, *585*(7825), 357–362. https://doi.org/10.1038/s41586-020-2649-2

Hashimoto, H., Dungan, J. L., White, M. A., Yang, F., Michaelis, A. R., Running, S. W., Nemani, R. R. (2008). Satellite-based estimation of surface vapor pressure deficits using MODIS land surface temperature data. *Remote Sensing of Environment*, *112*, 142–155.

Haworth, B. T. (2018). Implications of Volunteered Geographic Information for Disaster Management and GIScience: A More Complex World of Volunteered Geography. *Annals of the American Association of Geographers*, *108*(1), 226–240. https://doi.org/10.1080/24694452.2017.1321979

He, T., Belcher, C. M., Lamont, B. B., Lim, S. L. (2016). A 350-million-year legacy of fire adaptation among conifers. *Journal of Ecology*, *104*(2), 352–363. https://doi.org/10.1111/1365-2745.12513

He, T., Lamont, B. B. (2018). Baptism by fire: the pivotal role of ancient conflagrations in evolution of the Earth's flora. *National Science Review*, *5*(2), 237–254. https://doi.org/10.1093/nsr/nwx041

Hermosilla, T., Ruiz, L. A., Kazakova, A. N., Coops, N. C., Moskal, L. M. (2014). Estimation of forest structure and canopy fuel parameters from small-footprint full-waveform LiDAR data. *International Journal of Wildland Fire*, *23*(2), 224–233. https://doi.org/10.1071/WF13086.The

Hościło, A., Lewandowska, A. (2019). Mapping Forest Type and Tree Species on a Regional Scale Using Multi-Temporal Sentinel-2 Data. *Remote Sensing*, *11*(8), 929. https://doi.org/10.3390/rs11080929

Hoyer, S., Hamman, J. (2017). xarray: N-D labeled Arrays and Datasets in Python. *Journal of Open Research Software*, *5*(1), 10. https://doi.org/10.5334/jors.148

Huang, X., Rein, G. (2017). Downward spread of smouldering peat fire: the role of moisture, density and oxygen supply. *International Journal of Wildland Fire*, *26*(11), 907–918. https://doi.org/10.1071/WF16198

Huesca, M., Riaño, D., Ustin, S. L. (2019). Spectral mapping methods applied to LiDAR data: Application to fuel type mapping. *International Journal of Applied Earth Observation and Geoinformation*, *74*(August 2018), 159–168. https://doi.org/10.1016/j.jag.2018.08.020

Hunter, J. D. (2007). Matplotlib: a 2D Graphics Environment. *Computing in Science and Engineering*, 90–95.

ISPRA. (2019). *Dati sull'ambiente*.

Ivanova, G. A., Kukavskaya, E. A., Ivanov, V. A., Conard, S. G., McRae, D. J. (2020). Fuel characteristics, loads and consumption in Scots pine forests of central Siberia. *Journal of Forestry Research*, *31*(6), 2507–2524. https://doi.org/10.1007/s11676-019-01038-0

Jaffe, D. A., Wigder, N. L. (2012). Ozone production from wildfires: A critical review. *Atmospheric Environment*, *51*, 1–10. https://doi.org/10.1016/j.atmosenv.2011.11.063

Janzing, D., Minorics, L., Blöbaum, P. (2020). Feature relevance quantification in explainable AI: a causal problem. *Proceedings of the 23rd International Conference on Artificial Intelligence and Statistics (AISTATS)*, *108*.

Jolly, W. M., Cochrane, M. A., Freeborn, P. H., Holden, Z. A., Brown, T. J., Williamson, G. J., Bowman, D. M. J. S. (2015). Climate-induced variations in global wildfire danger from 1979 to 2013. *Nature Communications*, *6*(May), 1–11. https://doi.org/10.1038/ncomms8537

Jones, M. W., Smith, A. J. P., Betts, R. A., Canadell, J. G., Prentice, I. C., Le Quéré, C. (2020). Climate Change Increases the Risk of Wildfires. *ScienceBrief Review*. Retrieved from https://tyndall.ac.uk/sites/default/files/publications/wildfires_briefing_note_3.pdf

Jurdao, S., Yebra, M., Guerschman, J. P., Chuvieco, E. (2013). Regional estimation of woodland moisture content by inverting Radiative Transfer Models. *Remote Sensing of Environment*, *132*, 59–70.

https://doi.org/10.1016/j.rse.2013.01.004

Kan, T., Strezov, V., Evans, T. J. (2016). Lignocellulosic biomass pyrolysis: A review of product properties and effects of pyrolysis parameters. *Renewable and Sustainable Energy Reviews*, *57*, 1126–1140. https://doi.org/10.1016/j.rser.2015.12.185

Karafyllidis, I., Thanailakis, A. (1997). A model for predicting forest fire spreading using cellular automata. *Ecological Modelling*, *99*(1), 87–97. https://doi.org/10.1016/S0304-3800(96)01942-4

Keeley, J. E., Pausas, J. G. (2019). Distinguishing disturbance from perturbations in fire-prone ecosystems. *International Journal of Wildland Fire*, *28*(4), 282–287. https://doi.org/10.1071/WF18203

Keeley, J. E., Pausas, J. G., Rundel, P. W., Bond, W. J., Bradstock, R. A. (2011). Fire as an evolutionary pressure shaping plant traits. *Trends in Plant Science*, *16*(8), 406–411. https://doi.org/10.1016/j.tplants.2011.04.002

Keeley, J. E., Syphard, A. D. (2019). Twenty-first century California, USA, wildfires: fuel-dominated vs. wind-dominated fires. *Fire Ecology*, *15*(1), 1–15.

Kelley, D. I., Bistinas, I., Whitley, R., Burton, C., Marthews, T. R., Dong, N. (2019). How contemporary bioclimatic and human controls change global fire regimes. *Nature Climate Change*, *9*(9), 690–696. https://doi.org/10.1038/s41558-019-0540-7

Kellogg, K., Rosen, P. A., Barela, P., Sagi, V. R., Kumar, R., Hoffman, P., … Xaypraseuth, P. (2020). NASA-ISRO Synthetic Aperture Radar (NISAR) Mission. *IEEE*.

Kluyver, T., Ragan-Kelley, B., Pérez, F., Granger, B. E., Bussonnier, M., Frederic, J., … Willing, C. (2016). Jupyter Notebooks—a publishing format for reproducible computational workflows. *Positioning and Power in Academic Publishing: Players, Agents and Agendas - Proceedings of the 20th International Conference on Electronic Publishing, ELPUB 2016*, 87–90. https://doi.org/10.3233/978-1-61499-649-1-87

Knorr, W., Kaminski, T., Arneth, A., Weber, U. (2014). Impact of human population density on fire frequency at the global scale. *Biogeosciences*, *11*(4), 1085–1102. https://doi.org/10.5194/bg-11-1085-2014

Konings, A. G., Rao, K., Steele-Dunne, S. C. (2019). Macro to micro: microwave remote sensing of plant water content for physiology and ecology. *New Phytologist*, *223*(3), 1166–1172. https://doi.org/10.1111/nph.15808

Kotsiantis, S. B. (2013). Decision trees: A recent overview. *Artificial Intelligence Review*, *39*(4), 261–283. https://doi.org/10.1007/s10462-011-9272-4

Krebs, P., Pezzatti, G. B., Mazzoleni, S., Talbot, L. M., Conedera, M. (2010). Fire regime: History and definition of a key concept in disturbance ecology. *Theory in Biosciences*, *129*(1), 53–69. https://doi.org/10.1007/s12064-010-0082-z

Lagouvardos, K., Kotroni, V., Giannaros, T. M., Dafis, S. (2019). Meteorological Conditions Conducive to the Rapid Spread of the Deadly Wildfire in Eastern Attica, Greece. *Bulletin of the American Meteorological Society*, (November), 2137–2146. https://doi.org/10.1175/BAMS-D-18-0231.1

Lainas, S., Sabatakakis, N., Koukis, G. (2016). Rainfall thresholds for possible landslide initiation in wildfire-affected areas of western Greece. *Bulletin of Engineering Geology and the Environment*, *75*(3), 883–896. https://doi.org/10.1007/s10064-015-0762-5

Lam, S. K., Pitrou, A., Seibert, S. (2015). Numba: a LLVM-based Python JIT compiler. *Proceedings of the Second Workshop on the LLVM Compiler Infrastructure in HPC - LLVM '15*, 1–6. Retrieved from http://dl.acm.org/citation.cfm?doid=2833157.2833162

Lanorte, A., Lasaponara, R. (2008). Fuel type characterization based on coarse resolution MODIS satellite data. *IForest*, *1*(FEB), 60–64. https://doi.org/10.3832/ifor0451-0010060

Liu, W., Dugar, S., McCallum, I., Thapa, G., See, L., Khadka, P., … Shakya, P. (2018). Integrated participatory

and collaborative risk mapping for enhancing disaster resilience. *ISPRS International Journal of Geo-Information*, *7*(2), 1–23. https://doi.org/10.3390/ijgi7020068

Liu, Y., Goodrick, S., Heilman, W. (2014). Wildland fire emissions, carbon, and climate: Wildfire-climate interactions. *Forest Ecology and Management*, *317*, 80–96. https://doi.org/10.1016/j.foreco.2013.02.020

Liu, Y., Stanturf, J., Goodrick, S. (2010). Trends in global wildfire potential in a changing climate. *Forest Ecology and Management*, *259*, 685–697. https://doi.org/10.1016/j.foreco.2009.09.002

Lovreglio, R., Leone, V., Giaquinto, P., Notarnicola, A. (2010). Wildfire cause analysis: Four case-studies in southern Italy. *IForest*, *3*(JANUARY), 8–15. https://doi.org/10.3832/ifor0521-003

Lumley, S., Sieber, R. (2019). Web maps for global data visualization: does Mercator matter? In *CEUR Workshop Proceedings - Spatial Knowledge and Information* (Vol. 7, p. 5).

Lundberg, S. M., Erion, G., Chen, H., DeGrave, A., Prutkin, J. M., Nair, B., … Lee, S.-I. (2020). From local explanations to global understanding with explainable AI for trees. *Nature Machine Intelligence*, *2*(1), 56–67. https://doi.org/10.1038/s42256-019-0138-9

Lundberg, S. M., Erion, G. G., Lee, S.-I. (2018). Consistent Individualized Feature Attribution for Tree Ensembles. *ArXiv Preprint*, (2). Retrieved from http://arxiv.org/abs/1802.03888

Lundberg, S. M., Lee, S.-I. (2017). A unified approach to interpreting model predictions. *Advances in Neural Information Processing Systems*, (2), 4766–4775.

Lundberg, S. M., Nair, B., Vavilala, M. S., Horibe, M., Eisses, M. J., Adams, T., … Lee, S.-I. (2018). Explainable machine-learning predictions for the prevention of hypoxaemia during surgery. *Nature Biomedical Engineering*, *2*(10), 749–760. https://doi.org/10.1038/s41551-018-0304-0

Mantero, G., Morresi, D., Marzano, R., Motta, R., Mladenoff, D. J., Garbarino, M. (2020). The influence of land abandonment on forest disturbance regimes: a global review. *Landscape Ecology*, *35*(12), 2723–2744. https://doi.org/10.1007/s10980-020-01147-w

Marino, E., Guillén-Climent, M., Algeet, N., Tomé, J. L., Hernando, C. (2018). Estimation of live fuel moisture content of shrubland using MODIS and Sentinel-2 images. *Advances in Forest Fire Research 2018*, 218–226. https://doi.org/10.14195/978-989-26-16-506_22

Martell, D. L. (2011). The development and implementation of forest fire management decision support systems in Ontario, Canada: Personal reflections on past practices and emerging challenges. *Mathematical and Computational Forestry and Natural-Resource Sciences*, *3*(1), 18–26.

Martin-StPaul, N., Pimont, F., Dupuy, J. L., Rigolot, E., Ruffault, J., Fargeon, H., … Toutchkov, M. (2018). Live fuel moisture content (LFMC) time series for multiple sites and species in the French Mediterranean area since 1996. *Annals of Forest Science*, *75*(3). https://doi.org/10.1007/s13595-018-0744-4

Masad, D., Kazil, J. (2015). Mesa : An Agent-Based Modeling Framework. *Proceedings of the 14th Python in Science Conference*, (Scipy), 51–58.

McKinney, W. (2011). pandas: a Foundational Python Library for Data Analysis and Statistics. *International Journal of RF and Microwave Computer-Aided Engineering*, 1–9. https://doi.org/10.1002/mmce.20381

Mell, W. E., Manzello, S. L., Maranghides, A., Butry, D., Rehm, R. G. (2010). The wildland-urban interface fire problem - current approaches and research needs. *International Journal of Wildland Fire*, *19*(2), 238–251. https://doi.org/10.1071/WF07131

Mendiguren, G., Pilar Martín, M., Nieto, H., Pacheco-Labrador, J., Jurdao, S. (2015). Seasonal variation in grass water content estimated from proximal sensing and MODIS time series in a Mediterranean Fluxnet site. *Biogeosciences*, *12*(18), 5523–5535. https://doi.org/10.5194/bg-12-5523-2015

Miller, C., Ager, A. A. (2013). A review of recent advances in risk analysis for wildfire management. *International Journal of Wildland Fire*, *22*(1), 1–14. https://doi.org/10.1071/WF11114

Miller, R. K., Field, C. B., Mach, K. J. (2020). Barriers and enablers for prescribed burns for wildfire

management in California. *Nature Sustainability*, *3*(2), 101–109. https://doi.org/10.1038/s41893-019-0451-7

Moreira, F., Ascoli, D., Safford, H., Adams, M. A., Moreno Rodriguez, J. M., Pereira, J. M. C., … Fernandes, P. M. (2020). Wildfire management in Mediterranean-type regions: Paradigm change needed. *Environmental Research Letters*, *15*(1). https://doi.org/10.1088/1748-9326/ab541e

Moreira, F., Pe'er, G. (2018). Agricultural policy can reduce wildfires. *Science*, *359*(March), 1001. https://doi.org/10.1126/science.aat1359

Moritz, M. A., Parisien, M.-A., Batllori, E., Krawchuk, M. A., Van Dorn, J., Ganz, D. J., Hayhoe, K. (2012). Climate change and disruptions to global fire activity. *Ecosphere*, *3*(6), art49. https://doi.org/10.1890/es11-00345.1

Muñoz Sabater, J. (2019). ERA5-Land hourly data from 1981 to present [data set]. https://doi.org/10.24381/cds.e2161bac

Murata, T. (1989). Petri Nets: Properties, Analysis and Applications. *Proceedings of the IEEE*, *77*(4), 541–580.

Mutlu, M., Popescu, S. C., Stripling, C., Spencer, T. (2008). Mapping surface fuel models using lidar and multispectral data fusion for fire behavior. *Remote Sensing of Environment*, *112*(1), 274–285. https://doi.org/10.1016/J.RSE.2007.05.005

Mutlu, M., Popescu, S. C., Zhao, K. (2008). Sensitivity analysis of fire behavior modeling with LIDAR-derived surface fuel maps. *Forest Ecology and Management*, *256*, 289–294. https://doi.org/10.1016/j.foreco.2008.04.014

Myoung, B., Kim, S. H., Nghiem, S. V., Jia, S., Whitney, K., Kafatos, M. C. (2018). Estimating live fuel moisture from MODIS satellite data for wildfire danger assessment in Southern California USA. *Remote Sensing*, *10*(1). https://doi.org/10.3390/rs10010087

NASA. (2020). Earth Data Search. Retrieved from https://search.earthdata.nasa.gov/search

Nelson Jr, R. M. (2000). Prediction of diurnal change in 10-h fuel stick moisture content. *Canadian Journal of Forest Research*, *30*(7), 1071–1087. https://doi.org/10.1139/cjfr-30-7-1071

Nelson, K. J., Long, D. G., Connot, J. A. (2016). LANDFIRE 2010—Updates to the national dataset to support improved fire and natural resource management. *Open-File Report 2016–1010*, 48. Retrieved from https://pubs.er.usgs.gov/publication/ofr20161010

Nieto, H., Aguado, I., Chuvieco, E., Sandholt, I. (2010). Dead fuel moisture estimation with MSG-SEVIRI data. Retrieval of meteorological data for the calculation of the equilibrium moisture content. *Agricultural and Forest Meteorology*, *150*(7–8), 861–870. https://doi.org/10.1016/j.agrformet.2010.02.007

Nolan, R. H., Resco de Dios, V., Boer, M. M., Caccamo, G., Goulden, M. L., Bradstock, R. A. (2016). Predicting dead fine fuel moisture at regional scales using vapour pressure deficit from MODIS and gridded weather data. *Remote Sensing of Environment*, *174*, 100–108. https://doi.org/10.1016/j.rse.2015.12.010

Ntinas, V. G., Moutafis, B. E., Trunfio, G. A., Sirakoulis, G. C. (2017). Parallel fuzzy cellular automata for data-driven simulation of wildfire spreading. *Journal of Computational Science*, *21*, 469–485. https://doi.org/10.1016/j.jocs.2016.08.003

NWCG. (2006). Glossary of wildland fire terminology. Retrieved from http://www.nwcg.gov/glossary-of-wildland-fire-terminology

Panda, S. S., Masson, E., Sen, S., Kim, H. W., Amatya, D. M. (2016). Geospatial technology applications in forest hydrology. *Forest Hydrology: Processes, Management and Assessment*, 162–179. https://doi.org/10.1079/9781780646602.0162

Papadopoulos, G. D., Pavlidou, F. (2011). A Comparative Review on Wildfire Simulators. *IEEE Systems Journal*, *5*(2), 233–243.

Parise, M., Cannon, S. H. (2012). Wildfire impacts on the processes that generate debris flows in burned watersheds. *Natural Hazards*, *61*(1), 217–227. https://doi.org/10.1007/s11069-011-9769-9

Parsa, A. B., Movahedi, A., Taghipour, H., Derrible, S., Mohammadian, A. (Kouros). (2020). Toward safer highways, application of XGBoost and SHAP for real-time accident detection and feature analysis. *Accident Analysis and Prevention*, *136*, 105405. https://doi.org/10.1016/j.aap.2019.105405

Pausas, J. G., Keeley, J. E. (2014). Evolutionary ecology of resprouting and seeding in fire-prone ecosystems. *New Phytologist*, *204*(1), 55–65. https://doi.org/10.1111/nph.12921

Pausas, J. G., Paula, S. (2012). Fuel shapes the fire-climate relationship: evidence from Mediterranean ecosystems. *Global Ecology and Biogeography*, *21*(11), 1074–1082. https://doi.org/10.1111/j.1466-8238.2012.00769.x

Pearce, H. G., Anderson, W. R., Fogarty, L. G., Todoroki, C. L., Anderson, S. A. J. (2010). Linear mixed-effects models for estimating biomass and fuel loads in shrublands. *Canadian Journal of Forest Research*, *40*(10), 2015–2026. https://doi.org/10.1139/X10-139

Pechony, O., Shindell, D. T. (2010). Driving forces of global wildfires over the past millennium and the forthcoming century. *Proceedings of the National Academy of Sciences of the United States of America*, *107*(45), 19167–19170. https://doi.org/10.1073/pnas.1003669107

Pedregosa, F., Varoquaux, G., Gramfort, A., Michel, V., Thirion, B., Grisel, O., … Duchesnay, É. (2011). Scikit-learn: Machine Learning in Python. *Journal of Machine Learning Research*, *12*, 2825–2830. https://doi.org/10.1145/2786984.2786995

Pellizzaro, G., Duce, P., Ventura, A., Zara, P. (2007). Seasonal variations of live moisture content and ignitability in shrubs of the Mediterranean Basin. *International Journal of Wildland Fire*, *16*(5), 633–641. https://doi.org/10.1071/WF05088

Pérez, F., Granger, B. E. (2007). IPython: A System for Interactive Scientific Computing. *IEEE Computing in Science and Engineering*, 21–29.

Perry, G. L. W., Sparrow, A. D., Owens, I. F. (1999). A GIS-supported model for the simulation of the spatial structure of wildland fire, Cass Basin, New Zealand. *Journal of Applied Ecology*, *36*(4), 502–518. https://doi.org/10.1046/j.1365-2664.1999.00416.x

Pettinari, M. L., Chuvieco, E. (2020). Fire Danger Observed from Space. *Surveys in Geophysics*, *41*(6), 1437–1459. https://doi.org/10.1007/s10712-020-09610-8

Piñeiro, G., Perelman, S., Guerschman, J. P., Paruelo, J. M. (2008). How to evaluate models: observed vs. predicted or predicted vs. observed? *Ecological Modelling*, *216*(3–4), 316–322. https://doi.org/10.1016/j.ecolmodel.2008.05.006

Plucinski, M. P. (2019). Fighting Flames and Forging Firelines: Wildfire Suppression Effectiveness at the Fire Edge. *Current Forestry Reports*, *5*(1), 1–19. https://doi.org/10.1007/s40725-019-00084-5

Portier, J., Gauthier, S., Bergeron, Y. (2019). Spatial distribution of mean fire size and occurrence in eastern Canada: Influence of climate, physical environment and lightning strike density. *International Journal of Wildland Fire*, *28*(12), 927–940. https://doi.org/10.1071/WF18220

Potapov, P., Li, X., Hernandez-Serna, A., Tyukavina, A., Hansen, M. C., Kommareddy, A., … Hofton, M. A. (2020). Mapping global forest canopy height through integration of GEDI and Landsat data. *Remote Sensing of Environment*, (August), 112165. https://doi.org/10.1016/j.rse.2020.112165

Price, O. F., Gordon, C. E. (2016). The potential for LiDAR technology to map fire fuel hazard over large areas of Australian forest. *Journal of Environmental Management*, *181*, 663–673. https://doi.org/10.1016/j.jenvman.2016.08.042

Quegan, S., Le Toan, T., Chave, J., Dall, J., Exbrayat, J. F., Minh, D. H. T., … Williams, M. (2019). The European Space Agency BIOMASS mission: Measuring forest above-ground biomass from space. *Remote Sensing of Environment*, *227*(March), 44–60. https://doi.org/10.1016/j.rse.2019.03.032

Quill, R., Sharples, J. J., Wagenbrenner, N. S., Sidhu, L. A., Forthofer, J. M. (2019). Modeling Wind Direction Distributions Using a Diagnostic Model in the Context of Probabilistic Fire Spread Prediction. *Frontiers in Mechanical Engineering*, *5*(February), 1–16. https://doi.org/10.3389/fmech.2019.00005

Rego, F. M. C. C., Moreno Rodriguez, J. M., Vallejo Calzada, V. R., Xanthopoulos, G. (2018). *Forest Fires - Sparking firesmart policies in the EU*. Directorate - General for Research and Innovation - Climate Action and Resource Efficiency. https://doi.org/10.2777/248004

Rein, G. (2009). Smouldering Combustion Phenomena in Science and Technology. *International Review of Chemical Engineering*, *1*, 3–18.

Rein, G. (2013). Smouldering Fires and Natural Fuels. In W. and Sons (Ed.), *Fire Phenomena and the Earth System - An Interdisciplinary Approach to Fire Science* (pp. 15–34). https://doi.org/10.1002/9781118529539.ch2

Rein, G., Cleaver, N., Ashton, C., Pironi, P., Torero, J. L. (2008). The severity of smouldering peat fires and damage to the forest soil. *Catena*, *74*(3), 304–309. https://doi.org/10.1016/j.catena.2008.05.008

Resco de Dios, V., Fellows, A. W., Nolan, R. H., Boer, M. M., Bradstock, R. A., Domingo, F., Goulden, M. L. (2015). A semi-mechanistic model for predicting the moisture content of fine litter. *Agricultural and Forest Meteorology*, *203*, 64–73. https://doi.org/10.1016/j.agrformet.2015.01.002

Ribeiro, L. M., Rodrigues, A., Lucas, D., Viegas, D. X. (2020). The Impact on Structures of the Pedrógão Grande Fire Complex in June 2017 (Portugal). *Fire*, *3*(4), 57. https://doi.org/10.3390/fire3040057

Richards, G. D. (1995). A General Mathematical Framework For Modelling Two-Dimensional Wildland Fire Spread. *International Journal of Wildland Fire*, *5*(2), 63–72. https://doi.org/10.1071/WF9950063

Ricotta, C., Di Vito, S. (2014). Modeling the landscape drivers of fire recurrence in Sardinia (Italy). *Environmental Management*, *53*(6), 1077–1084. https://doi.org/10.1007/s00267-014-0269-z

Rimmer, S. M., Hawkins, S. J., Scott, A. C., Cressler, W. L. (2015). The rise of fire: Fossil charcoal in late Devonian marine shales as an indicator of expanding terrestrial ecosystems, fire, and atmospheric change. *American Journal of Science*, *315*(8), 713–733. https://doi.org/10.2475/08.2015.01

Rocklin, M. (2015). Dask: Parallel Computation with Blocked algorithms and Task Scheduling. *Proceedings of the 14th Python in Science Conference*, (Scipy), 126–132. https://doi.org/10.25080/majora-7b98e3ed-013

Rodriguez-Aseretto, D., De Rigo, D., Di Leo, M., Cortés, A., San-Miguel-Ayanz, J. (2013). A data-driven model for large wildfire behaviour prediction in Europe. *Procedia Computer Science*, *18*, 1861–1870. https://doi.org/10.1016/j.procs.2013.05.355

Rodríguez y Silva, F., Molina-Martínez, J. R. (2012). Modeling Mediterranean forest fuels by integrating field data and mapping tools. *European Journal of Forest Research*, *131*(3), 571–582. https://doi.org/10.1007/s10342-011-0532-2

Rosen, P. A., Hensley, S., Shaffer, S., Veilleux, L., Chakraborty, M., Misra, T., … Satish, R. (2015). The NASA-ISRO SAR mission - An international space partnership for science and societal benefit. *IEEE National Radar Conference - Proceedings*, 1610–1613. https://doi.org/10.1109/RADAR.2015.7131255

Rothermel, R. C. (1972). A Mathematical Model for Predicting Fire Spread in Wildland Fuels. *U.S. Department of Agriculture, Forest Service, Intermountain Forest and Range Experiment Station. Research Paper, INT-115*.

Rothermel, R. C. (1983). *How to Predict the Spread and Intensity of Forest and Range Fires*. *USDA Forest Service, Intermountain Forest and Range Experiment Station. General Technical Report* (Vol. INT-143).

Rothermel, R. C. (1991). *Predicting Behavior and Size of Crown Fires in the Northern Rocky Mountains*. *U.S. Department of Agriculture, Forest Service, Intermountain Research Station, Research Paper* (Vol. INT-438).

Ruffault, J., Curt, T., Moron, V., Trigo, R. M., Mouillot, F., Koutsias, N., … Belhadj-Khedher, C. (2020). Increased likelihood of heat-induced large wildfires in the Mediterranean Basin. *Scientific Reports*, *10*(1), 1–9. https://doi.org/10.1038/s41598-020-70069-z

Saarela, S., Wästlund, A., Holmström, E., Mensah, A. A., Holm, S., Nilsson, M., … Ståhl, G. (2020). Mapping aboveground biomass and its prediction uncertainty using LiDAR and field data, accounting for tree-level allometric and LiDAR model errors. *Forest Ecosystems*, *7*(1). https://doi.org/10.1186/s40663-020-00245-0

Saba, F. (2004). Le cause degli incendi boschivi e rurali in Sardegna: dalle ipotesi all'analisi dei dati. In *Atti del Convegno Incendi boschivi e rurali in Sardegna. Dall'analisi delle cause alle proposte d'intervento2*.

Salis, M., Ager, A. A., Arca, B., Finney, M. A., Bacciu, V. M., Duce, P., Spano, D. (2013). Assessing exposure to human and ecological values in Sardinia, Italy. *International Journal of Wildland Fire*, *22*, 549–565. https://doi.org/10.1071/WF11060

Salis, M., Ager, A. A., Finney, M. A., Arca, B., Spano, D. (2014). Analyzing spatiotemporal changes in wildfire regime and exposure across a Mediterranean fire-prone area. *Natural Hazards*, *71*(3), 1389–1418. https://doi.org/10.1007/s11069-013-0951-0

Salis, M., Arca, B., Alcasena, F. J., Arianoutsou, M., Bacciu, V., Duce, P., … Spano, D. (2016). Predicting wildfire spread and behaviour in Mediterranean landscapes. *International Journal of Wildland Fire*, *25*(10), 1015–1032. https://doi.org/10.1071/WF15081

Salis, M., Arca, B., Alcasena, F. J., Massaiu, A., Bacciu, V. M., Bosseur, F., … Duce, P. (2019). Analyzing the recent dynamics of wildland fires in Quercus suber L. woodlands in Sardinia (Italy), Corsica (France) and Catalonia (Spain). *European Journal of Forest Research*, *138*(3), 415–431. https://doi.org/10.1007/s10342-019-01179-1

Salis, M., Del Giudice, L., Arca, B., Ager, A. A., Alcasena-Urdiroz, F., Lozano, O., … Duce, P. (2018). Modeling the effects of different fuel treatment mosaics on wildfire spread and behavior in a Mediterranean agro-pastoral area. *Journal of Environmental Management*, *212*, 490–505. https://doi.org/10.1016/j.jenvman.2018.02.020

San-Miguel-Ayánz, J., Gitas, I., Camia, A., Oliveira, S. (2011). *Advances in Remote Sensing and GIS applications in Forest Fire Management - From local to global assessments*. *JRC Scientific and Technical Reports*.

San-Miguel-Ayánz, J., Houston Durrant, T., Boca, R., Libertà, G., Branco, A., de Rigo, D., … Leray, T. (2018). *Forest Fires in Europe, Middle East and North Africa 2017*. https://doi.org/10.2760/663443

San-Miguel-Ayánz, J., Moreno, J. M., Camia, A. (2013). Analysis of large fires in European Mediterranean landscapes: lessons learned and perspectives. *Forest Ecology and Management*, *294*, 11–22. https://doi.org/10.1016/j.foreco.2012.10.050

Santoro, M., Beer, C., Cartus, O., Schmullius, C., Shvidenko, A., McCallum, I., … Wiesmann, A. (2011). Retrieval of growing stock volume in boreal forest using hyper-temporal series of Envisat ASAR ScanSAR backscatter measurements. *Remote Sensing of Environment*, *115*(2), 490–507. https://doi.org/10.1016/j.rse.2010.09.018

Santoso, M. A., Christensen, E. G., Yang, J., Rein, G. (2019). Review of the Transition From Smouldering to Flaming Combustion in Wildfires. *Frontiers in Mechanical Engineering*, *5*(September). https://doi.org/10.3389/fmech.2019.00049

Sayad, Y. O., Mousannif, H., Al Moatassime, H. (2019). Predictive modeling of wildfires: A new dataset and machine learning approach. *Fire Safety Journal*, *104*(January), 130–146. https://doi.org/10.1016/j.firesaf.2019.01.006

Schelling, T. C. (1971). Dynamic models of segregation. *Journal of Mathematical Sociology*, *1*, 143–186. https://doi.org/10.1080/0022250X.1971.9989794

Schneider, F. D., Ferraz, A., Hancock, S., Duncanson, L. I., Dubayah, R. O., Pavlick, R. P., Schimel, D. S. (2020). Towards mapping the diversity of canopy structure from space with GEDI. *Environmental Research Letters*, *15*(11). https://doi.org/10.1088/1748-9326/ab9e99

Scott, J. H., Burgan, R. E. (2005). *Standard Fire Behavior Fuel Models: A Comprehensive Set for Use with Rothermel's Surface Fire Spread Model*. *U.S. Department of Agriculture, Forest Service, Rocky Mountain Research Station. General Technical Report* (Vol. RMRS-GTR-1).

Scott, J. H., Reinhardt, E. D. (2001). Assessing Crown Fire Potential by Linking Models of Surface and Crown Fire Behavior. *U.S. Department of Agriculture, Forest Service, Rocky Mountain Research Station. Research Paper, RMRS-RP-29*, 59 pp.

Sebastián López, A., San-Miguel-Ayanz, J., Burgan, R. E. (2002). Integration of satellite sensor data, fuel type maps and meteorological observations for evaluation of forest fire risk at the pan-European scale. *International Journal of Remote Sensing*, *23*(13), 2713–2719. https://doi.org/10.1080/01431160110107761

Sebastián López, A., San-Miguel-Ayanz, J., Libertà, G. (2000). An integrated forest fire index for Europe. In M. F. Buchroithne (Ed.), *A Decade of Trans-European Remote Sensing Cooperation* (pp. 83–88).

Shakesby, R. A. (2011). Post-wildfire soil erosion in the Mediterranean: Review and future research directions. *Earth-Science Reviews*, *105*(3–4), 71–100. https://doi.org/10.1016/j.earscirev.2011.01.001

Shapley, L. S. (1953). A value for n-person games. In A. E. Roth (Ed.), *The Shapley Value. Essays in Honor of Lloyd S. Shapley.* (pp. 31–40). https://doi.org/10.2307/2554979

Shu, Q., Quan, X., Yebra, M., Liu, X., Wang, L., Zhang, Y. (2019). Evaluating the Sentinel-2A satellite data for fuel moisture content retrieval. *IGARSS 2019 - 2019 IEEE International Geoscience and Remote Sensing Symposium*, 9416–9419.

Simard, A. J. (1968). *The moisture content of forest fuels*. University of California.

Smith, A. J. P., Jones, M. W., Abatzoglou, J. T., Canadell, J. G., Betts, R. A. (2020). Climate Change Increases the Risk of Wildfires. *ScienceBrief Review*. Retrieved from https://sciencebrief.org/

Spawn, S. A., Gibbs, H. K. (2020). Global Aboveground and Belowground Biomass Carbon Density Maps for the Year 2010 [data set]. https://doi.org/10.3334/ORNLDAAC/1763

Spawn, S. A., Sullivan, C. C., Lark, T. J., Gibbs, H. K. (2020). Harmonized global maps of above and belowground biomass carbon density in the year 2010. *Scientific Data*, *7*(1), 1–22. https://doi.org/10.1038/s41597-020-0444-4

Staver, A. C., Archibald, S., Levin, S. A. (2011). The global extent and determinants of savanna and forest as alternative biome states. *Science*, *334*(6053), 230–232. https://doi.org/10.1126/science.1210465

Stefanidou, A., Dragozi, E., Stavrakoudis, D., Gitas, I. Z. (2018). Fuel type mapping using object-based image analysis of DMC and Landsat-8 OLI imagery. *Geocarto International*, *33*(10), 1064–1083. https://doi.org/10.1080/10106049.2017.1333532

Stevens-Rumann, C. S., Kemp, K. B., Higuera, P. E., Harvey, B. J., Rother, M. T., Donato, D. C., … Veblen, T. T. (2018). Evidence for declining forest resilience to wildfires under climate change. *Ecology Letters*, *21*, 243–252. https://doi.org/10.1111/ele.12889

Stewart, S. I., Radeloff, V. C., Hammer, R. B., Hawbaker, T. J. (2007). Defining the Wildland–Urban Interface. *Journal of Forestry*, (June), 201–207.

Stocker, T. F., Qin, D., Plattner, G.-K., Tignor, M., Allen, S. K., Boschung, J., … Midgley, P. M. (2013). *Climate Change 2013: The Physical Science Basis. Contribution of Working Group I to the Fifth Assessment Report of the Intergovernmental Panel on Climate Change*. Cambridge, United Kingdom and

New York, NY, USA. Retrieved from https://www.ipcc.ch/

Stracher, G. B., Taylor, T. P. (2004). Coal fires burning out of control around the world: thermodynamic recipe for environmental catastrophe. *International Journal of Coal Geology*, *59*(1–2), 7–17. https://doi.org/10.1016/j.coal.2003.03.002

Štrumbelj, E., Kononenko, I. (2014). Explaining prediction models and individual predictions with feature contributions. *Knowledge and Information Systems*, *41*(3), 647–665. https://doi.org/10.1007/s10115-013-0679-x

Stysley, P. R., Coyle, D. B., Clarke, G. B., Frese, E., Blalock, G., Morey, P., … Hersh, M. (2016). Laser production for NASA's Global Ecosystem Dynamics Investigation (GEDI) lidar. *Proceedings of SPIE, Laser Radar Technology and Applications XXI*, *9832*, 983207. https://doi.org/10.1117/12.2239889

Sullivan, A. L. (2009a). Wildland surface fire spread modelling, 1990-2007. 1: Physical and quasi-physical models. *International Journal of Wildland Fire*, *18*(4), 349–368. https://doi.org/10.1071/WF06143

Sullivan, A. L. (2009b). Wildland surface fire spread modelling, 1990-2007. 2: Empirical and quasi-empirical models. *International Journal of Wildland Fire*, *18*(4), 369–386.

Sullivan, A. L. (2009c). Wildland surface fire spread modelling, 1990-2007. 3: Simulation and mathematical analogue models. *International Journal of Wildland Fire*, *18*(4), 387–403.

Taylor, K. E., Stouffer, R. J., Meehl, G. A. (2012). An overview of CMIP5 and the experiment design. *Bulletin of the American Meteorological Society*, *93*(4), 485–498. https://doi.org/10.1175/BAMS-D-11-00094.1

Tedim, F., Leone, V., Amraoui, M., Bouillon, C., Coughlan, M. R., Delogu, G. M., … Xanthopoulos, G. (2018). Defining Extreme Wildfire Events: Difficulties, Challenges, and Impacts. *Fire*, *1*(9), 1–28. https://doi.org/10.3390/fire1010009

Tedim, F., Leone, V., Coughlan, M., Bouillon, C., Xanthopoulos, G., Royé, D., … Ferreira, C. (2020). Extreme wildfire events: the definition. In *Extreme Wildfire Events and Disasters* (pp. 3–29). Elsevier. https://doi.org/10.1016/b978-0-12-815721-3.00001-1

Terrasson, A., McCarthy, N., Dowdy, A., Richter, H., McGowan, H., Guyot, A. (2019). Weather Radar Insights Into the Turbulent Dynamics of a Wildfire-Triggered Supercell Thunderstorm. *Journal of Geophysical Research: Atmospheres*, *124*(15), 8645–8658. https://doi.org/10.1029/2018JD029986

Thompson, M. P., Calkin, D. E. (2011). Uncertainty and risk in wildland fire management: A review. *Journal of Environmental Management*, *92*(8), 1895–1909. https://doi.org/10.1016/j.jenvman.2011.03.015

Trabaud, L. (1994). Postfire Plant Community Dynamics in the Mediterranean Basin. In J. M. Moreno & W. C. Oechel (Eds.), *The Role of Fire in Mediterranean-Type Ecosystems. Ecological Studies (Analysis and Synthesis)* (Vol. 107, pp. 1–15). Springer, New York, NY. https://doi.org/10.1007/978-1-4613-8395-6_1

Trucchia, A., D'Andrea, M., Baghino, F., Fiorucci, P., Ferraris, L., Negro, D., … Severino, M. (2020). Propagator: An operational cellular-automata based wildfire simulator. *Fire*, *3*(3), 1–24. https://doi.org/10.3390/fire3030026

Trunfio, G. A., D'Ambrosio, D., Rongo, R., Spataro, W., Di Gregorio, S. (2011). A new algorithm for simulating wildfire spread through cellular automata. *ACM Transactions on Modeling and Computer Simulation*, *22*(1). https://doi.org/10.1145/2043635.2043641

Turco, M., Bedia, J., Di Liberto, F., Fiorucci, P., Von Hardenberg, J., Koutsias, N., … Provenzale, A. (2016). Decreasing fires in mediterranean Europe. *PLoS ONE*, *11*(3). https://doi.org/10.1371/journal.pone.0150663

Turco, M., Jerez, S., Augusto, S., Tarín-Carrasco, P., Ratola, N., Jiménez-Guerrero, P., Trigo, R. M. (2019). Climate drivers of the 2017 devastating fires in Portugal. *Scientific Reports*, *9*(1), 1–8. https://doi.org/10.1038/s41598-019-50281-2

Turco, M., Rosa-Cánovas, J. J., Bedia, J., Jerez, S., Montávez, J. P., Llasat, M. C., Provenzale, A. (2018).

Exacerbated fires in Mediterranean Europe due to anthropogenic warming projected with non-stationary climate-fire models. *Nature Communications*, *9*(1), 1–9. https://doi.org/10.1038/s41467-018-06358-z

Tymstra, C., Bryce, R. W., Wotton, B. M., Taylor, S. W., Armitage, O. B. (2010). *Development and structure of Prometheus: the Canadian Wildland Fire Growth Simulation Model* (Vol. 417).

UNISDR. (2015). *Sendai Framework for Disaster Risk Reduction 2015-2030. United Nations International Strategy for Disaster Risk Reduction*. Geneva.

USDA Forest Service. (2020). Fire Terminology. Retrieved from https://www.fs.fed.us/nwacfire/

USGS. (2020). Earth Explorer. Retrieved from https://earthexplorer.usgs.gov/

Valdez, M. C., Chang, K.-T., Chen, C.-F., Chiang, S.-H., Santos, J. L. (2017). Modelling the spatial variability of wildfire susceptibility in Honduras using remote sensing and geographical information systems. *Geomatics, Natural Hazards and Risk*, *8*(2), 876–892. https://doi.org/10.1080/19475705.2016.1278404

Van Der Walt, S., Colbert, S. C., Varoquaux, G. (2011). The NumPy Array: A structure for Efficient Numerical Computation. *Computing in Science and Engineering*, *13*(2), 22–30. https://doi.org/10.1109/MCSE.2011.37

van der Werf, G. R., Randerson, J. T., Giglio, L., Van Leeuwen, T. T., Chen, Y., Rogers, B. M., … Kasibhatla, P. S. (2017). Global fire emissions estimates during 1997-2016. *Earth System Science Data*, *9*(2), 697–720. https://doi.org/10.5194/essd-9-697-2017

Van Wagner, C. E. (1977). Conditions for the start and spread of crown fire. *Canadian Journal of Forest Research*, (1), 23–34. https://doi.org/10.16309/j.cnki.issn.1007-1776.2003.03.004

Veraverbeke, S., Rogers, B. M., Goulden, M. L., Jandt, R. R., Miller, C. E., Wiggins, E. B., Randerson, J. T. (2017). Lightning as a major driver of recent large fire years in North American boreal forests. *Nature Climate Change*, *7*(7), 529–534. https://doi.org/10.1038/nclimate3329

Vermote, E., NOAA CDR Program. (2019). NOAA Climate Data Record (CDR) of AVHRR Normalized Difference Vegetation Index (NDVI), Version 5 [data set]. https://doi.org/10.7289/V5ZG6QH9

Vermote, E., Wolfe, R. E. (2015). MOD09GA MODIS/Terra Surface Reflectance Daily L2G Global 1kmand 500m SIN Grid V006 [data set]. https://doi.org/10.5067/MODIS/MOD09GA.006

Viney, N. R. (1991). A review of fine fuel moisture modelling. *International Journal of Wildland Fire*, *1*(4), 215–234. https://doi.org/10.1071/WF9910215

Virtanen, P., Gommers, R., Oliphant, T. E., Haberland, M., Reddy, T., Cournapeau, D., … Vázquez-Baeza, Y. (2020). SciPy 1.0: fundamental algorithms for scientific computing in Python. *Nature Methods*, *17*(3), 261–272. https://doi.org/10.1038/s41592-019-0686-2

Wagenbrenner, N. S., Forthofer, J. M., Lamb, B. K., Shannon, K. S., Butler, B. W. (2016). Downscaling surface wind predictions from numerical weather prediction models in complex terrain with WindNinja. *Atmospheric Chemistry and Physics*, *16*(8), 5229–5241. https://doi.org/10.5194/acp-16-5229-2016

Wan, Z., Hook, S., Hulley, G. (2015). MOD11A1 MODIS/Terra Land Surface Temperature/Emissivity Daily L3 Global 1km SIN Grid V006 [data set]. https://doi.org/10.5067/MODIS/MOD11A1.006

Wang, L., Quan, X., He, B., Yebra, M., Xing, M., Liu, X. (2019). Assessment of the dual polarimetric Sentinel-1A data for forest fuel moisture content estimation. *Remote Sensing*, *11*(13). https://doi.org/10.3390/rs11131568

Watt, D. A. (2006). *Programming language design concepts*. (Wiley, Ed.).

Watts, A. C., Kobziar, L. N. (2013). Smoldering Combustion and Ground Fires: Ecological Effects and Multi-Scale Significance. *Fire Ecology*, *9*(1), 124–132. https://doi.org/10.4996/fireecology0901124

Weichselgartner, J., Pigeon, P. (2015). The Role of Knowledge in Disaster Risk Reduction. *International Journal of Disaster Risk Science*, *6*(2), 107–116. https://doi.org/10.1007/s13753-015-0052-7

Westerling, A. L. R. (2016). Increasing western US forest wildfire activity: Sensitivity to changes in the timing of spring. *Philosophical Transactions of the Royal Society B: Biological Sciences*, *371*(1696). https://doi.org/10.1098/rstb.2015.0178

Wilensky, U., Rand, W. (2007). Making models match: replicating an agent-based model. *Jasss*, *10*(4).

Williams, A. P., Abatzoglou, J. T. (2016). Recent Advances and Remaining Uncertainties in Resolving Past and Future Climate Effects on Global Fire Activity. *Current Climate Change Reports*, *2*(1), 1–14. https://doi.org/10.1007/s40641-016-0031-0

Wolfram, S. (2002). *A New Kind of Science*. Champaign, IL: Wolfram Media.

Yang, H., Yan, R., Chen, H., Lee, D. H., Zheng, C. (2007). Characteristics of hemicellulose, cellulose and lignin pyrolysis. *Fuel*, *86*(12–13), 1781–1788. https://doi.org/10.1016/j.fuel.2006.12.013

Yebra, M., Chuvieco, E. (2009a). Generation of a Species-Specific Look-Up Table for Fuel Moisture Content Assessment. *IEEE Journal of Selected Topics in Applied Earth Observations and Remote Sensing*, *2*(1), 21–26. https://doi.org/10.1109/JSTARS.2009.2014008

Yebra, M., Chuvieco, E. (2009b). Linking ecological information and radiative transfer models to estimate fuel moisture content in the Mediterranean region of Spain: Solving the ill-posed inverse problem. *Remote Sensing of Environment*, *113*(11), 2403–2411. https://doi.org/10.1016/j.rse.2009.07.001

Yebra, M., Chuvieco, E., Riaño, D. (2008). Estimation of live fuel moisture content from MODIS images for fire risk assessment. *Agricultural and Forest Meteorology*, *148*(4), 523–536. https://doi.org/10.1016/j.agrformet.2007.12.005

Yebra, M., Dennison, P. E., Chuvieco, E., Riaño, D., Zylstra, P., Hunt, E. R., … Jurdao, S. (2013). A global review of remote sensing of live fuel moisture content for fire danger assessment: Moving towards operational products. *Remote Sensing of Environment*, *136*, 455–468. https://doi.org/10.1016/j.rse.2013.05.029

Yebra, M., Scortechini, G., Badi, A., Beget, M. E., Boer, M. M., Bradstock, R., … Ustin, S. (2019). Globe-LFMC, a global plant water status database for vegetation ecophysiology and wildfire applications. *Scientific Data*, *6*(1), 1–8. https://doi.org/10.1038/s41597-019-0164-9